UNIVERSITÀ DEGLI STUDI DI CATANIA
Dipartimento di Fisica e Astronomia
Corso di Dottorato in Fisica XXX ciclo

Giuseppe Ferdinando D'Agata

THE $^{19}F(\alpha, p)^{22}Ne$ AND $^{23}Na(p, \alpha)^{20}Ne$ REACTIONS IN ASTROPHYSICAL ENVIRONMENT WITH THE TROJAN HORSE METHOD

Ph.D Thesis

Supervisors:
Prof. Romano Stefano
Prof. Spitaleri Claudio
Dott. Pizzone Rosario Gianluca

academic year 2016/2017

Contents

Introduction

Elements in the universe are mostly produced inside stars. Apart from H, He and Li, partly produced in primordial nucleosynthesis, the heavier elements were in fact produced in stellar environments.

Isotopes with atomic number A<60 can be produced by thermonuclear reactions, given the enhancement of the Coulomb barrier and the consequent fall of the cross-section between charged particles. It is also known that elements belonging to the Fe-group (Fe, Ni, Cr...) have the highest binding energies between nucleons, making fusion reactions disadvantageous for such nuclei.

If A > 60, neutron capture is the main responsible for heavier nuclei production.

One of the two key points of this work will be the study of one of the main destruction channels for ^{19}F, that results to be one of the least abundant elements with $12 < A < 56$. In this atomic number range, it is proven that nucleosynthesis mainly takes place inside AGB-stars, in which the isotopes just synthesized are brought to the surface by a mechanism called *third dredge-up* (TDU). Following the accepted models, at this evolutionary stage a star is composed by a degenerate C-O core, surrounded by a He-shell and a H-shell. The latter are separated by a thin layer called He-intershell ($10^{-2} \div 10^{-3}$ $M_\odot$), while the stellar envelope is composed by dust, that can extend for hundreds of $R_\odot$.

If temperature is high enough in the He-intershell, elements coming from the CNO cycle, such as ^{14}N, can lead to the production of ^{19}F by means of the chain $^{14}N(\alpha, \gamma)^{18}F(\beta^+\nu)^{18}O(p, \alpha)^{15}N(\alpha, \gamma)^{19}F$. Low-mass AGB-stars are the only sites of production observatively confirmed [Santos et al., 2004; Recio-Blanco et al., 2012; Li et al., 2013]. ^{19}F production was also predicted to take place is in Supernovae

and Wolf-Rayet objects, evven if in small quantities.

Fluorine abundance shows a strong dependence from the internal conditions of the star where it is produced: its production and destruction pathways are, in fact strongly linked to temperature, density and to the mixing processes that move the so called *s* elements on the surface of the star, and to the superficial mixing that alters light elements abundances. Moreover, about ^{19}F, its abundance can not still be reproduced by astrophysical models, that strongly underestimates such quantities.

Observative evidences of fluorine production are obtained from an analysis of the electromagnetic spectra of stars. In this way in fact, a study of the distribution of energy as a function of the wavelength is possible, so that information about temperature and chemical composition of the star can be obtained.

If the pathways in which ^{19}F is produced are quite clear, is now important to describe how it can be destroyed. In AGB stars it could happen with the reactions ^{19}F(p, α)^{16}O and ^{19}F(α, p)^{22}Ne, and their relative importance critically depends on the environment where the reaction takes place. It is therefore important to know the reaction rate for ^{19}F(α, p)^{22}Ne. This is not well known in the energy range of astrophysical interest, because direct measurements of the cross-section at the Gamow energy region for a stellar temperature of T = $8{\cdot}10^8$ K should go at energies in the center of mass reference frame between 390 e 800 keV, while the lowest energy for such a measurement is at 1.1 MeV in the laboratory reference frame.

The other main topic of this work will be on ^{23}Na. The reaction ^{23}Na(p, α)^{20}Ne, in particular, is of primary importance for sodium destruction inside the nucleosynthesis path in the A > 20 mass region. This reaction is also involved in the branching point of the Ne-Na cycle, responsible for hydrogen burning at high temperatures. Ne-Na cycle is not well understood, mainly because the branching (p,α) to (p,γ) ratio bears great uncertainties. Only if the first prevail on the second the cycle can be started. From an observative point of view, the anti-correlations O-Na are of utmost importance while observing massive stars: those will be of great help in understanding the action of Ne-Na cycle, giving also a hint on the reaction pathways occurring in stars. The ^{23}Na(p, α)^{20}Ne reaction plays its role in quiescent burning, so in the range temperature between T = $20 \cdot 10^6$ K and T = $80 \cdot 10^6$ K, and in the Hot Bottom Burning occurring in AGB-stars, whose impact needs to be known at between T = $70 \cdot 10^6$ K and T = $100 \cdot 10^6$ K.

The ^{23}Na(p, α)^{20}Ne reaction needs to be studied at energy E = $50 \div 200$ keV, corresponding to the Gamow peak for the temperatures expressed earlier. In this energy

range, the (p,α) channel prevails, allowing the development of the Ne-Na cycle, but measurements are proven to be difficult due to the presence of some resonant states of the intermediate ^{24}Mg nucleus, and as for now there are no clear information about their contribution on the total ^{23}Na(p,α)^{20}Ne reaction rate. These intermediate states were studied, and two resonances at 37 and 138 keV were found, but their large uncertainties make its importance in a Ne-Na closed cycle still not fully understood. It is now clear why the study of such a reaction could be important at astrophysical energies.

Measurements at low energies are in general kind of problematic: astrophysically relevant reactions usually take place at energies of a few tens of keV or lower, while the typical Coulomb barrier has a value of some MeV. In such conditions, the cross-section is strongly reduced (order of magnitude of some picobarn or lower). This makes direct measurements really hard and, in some cases, nearly impossible. For this reason extrapolations are often used and cross-section is calculated starting from values at higher energies, extending its trend in an energy range where, if there are no resonances, its behaviour is strongly decreasing. To make things easier, it is very useful to use the *astrophysical factor* $S(E) = \sigma(E)E \times e^{2\pi\eta}$, in which the decreasing behaviour of the cross-section is compensated by the $e^{2\pi\eta}$, where η is the Sommerfeld parameter. In this way extrapolations are made easier. Such a procedure can sometimes be not much reliable, because it doesn't take into account possible the presence of resonances at low-energy (or below the threshold).

In this energy regions *electron screening* is also important. This phenomenon lowers the effects of the Coulomb barrier between the interacting nuclei, and it is due to electrons, enhancing the probability of interaction between projectile and target. Theoretical models do not reproduce well all these facts, and so the bare nucleus cross-section is not approachable from the one measured with direct methods at very low energies.

For all those reasons, several indirect method were proposed. Their aim is to study the reaction of interest starting from processes that have some kind of link with it, and that make easier to study. Among them, the *Trojan Horse Method* (THM) allows us to measure the cross-section between charged particles - or between charged particles and neutrons - at low energies, avoiding Coulomb barrier and electron screening effects. This method is useful to reduce uncertainties, making models that describe the chemical evolution of stellar objects more accurate.

The idea behind this method is to study the two-body reaction of interest

$$a + x \rightarrow C + c$$

from a three-body reaction in the exit channel:

$$a + A \rightarrow C + c + s$$

where the nucleus A has a cluster-like structure $A = x \oplus s$, with the x particle is the participant and the s one is the spectator, following the nuclear reaction theory for the quasi-free break-up. If quasi-free processes are taking place, the participant nucleus, interacting with the target, will lead to the two-body reaction of interest, while the spectator will continue undisturbed. Furthermore, if the beam energy is high enough to overcome the Coulomb barrier between a e A, then the participant nucleus will be led inside the nuclear field of a, and the reactions will take place without Coulomb suppression and electron screening effects.
In the following work the reactions ^{19}F(α, p)^{22}Ne and ^{23}Na(p, α)^{20}Ne in their respective region of astrophysical interest will be studied with the THM method: for the first reaction, a nucleus of ^{6}Li, that can be considered as a cluster $\alpha \oplus d$, is used as projectile particle impinging on a ^{7}LiF target, with the aim to induce the reaction ^{19}F(^{6}Li, p^{22}Ne)^{2}H, in which the α particle is the spectator and the deuterium is the spectator. In the second one, a ^{23}Na beam impinging on a CD_2 target will be used to study the ^{2}H(^{23}Na, α^{20}Ne)n, with the proton as participant and neutron as spectator. For both reaction, once the detector are calibrated, a particle discrimination was made using the ΔE – E telescope technique. To isolate the three body reaction, kinematic loci were than studied, with the aim to isolate the right $Q-$value. After that, the quasi-free process was identified using the momentum distribution of the spectator particle, and a cross-section in arbitrary units was extracted, using the THM standard approach. Then for the ^{19}F(α,p)^{22}Ne reaction the absolute value cross-section, the S(E)−factor and the reaction rate were calculated, and the astrophysical impact of the new values was also evaluated. Both measurement show the presence of resonant structures in the energetic range of astrophysical relevance.
The following work will consist in:

- CHAPTER 1: Astrophysical problems connected to the reactions.
- CHAPTER 2: Key features to study arguments related to nuclear astrophysics

.

- CHAPTER 3: Brief discussion on indirect methods with a particular focus on THM method (experimental examples).
- CHAPTER 4: Experimental apparatus and calibration procedures.
- CHAPTER 5: Experimental results for the ^{19}F(α,p)^{22}Ne reaction.
- CHAPTER 6: Early experimental results for the ^{23}Na(p,α)^{20}Ne reaction.

CHAPTER 1

Astrophysical background

Main topic of astrophysics is to explain what happens in the universe, applying well-known and verified physical laws. About the physical processes that take place inside stars, we know that those can be considered, in first approximation, as an isotropic system of self gravitating particles, whose equilibrium can be described using the virial theorem:

$$\langle T \rangle = -\frac{1}{2}\langle U \rangle \tag{1.1}$$

with T the kinetic energy and U the gravitational potential. Following eq.1.1 it is possible to say that a star, to stay at thermal equilibrium, has to spend half of the gravitational energy gained by contraction to rise its temperature. The other half is lost by radiation.

While temperature increases, contraction is made slower due to increasing radiation pressure. This is caused by internal energy production (e.g. nuclear fusion). Among the physical inputs for stellar evolution, nuclear processes cross-section or the decay of the produced particles are really important. Nuclear astrophysics studies from a theoretical and experimental point of view the nucleosynthesis of the involved reactions inside stars, trying to minimize the errors with which they are known.

In this work we will focus on the ^{19}F(α,p)^{22}Ne and ^{23}Na(p,α)^{20}Ne reactions. The former is important in ^{19}F abundance in stars, while the latter is of great importance for sodium destruction inside the nucleosynthesis path for A>20.

In the first part of this work we will focus on stellar structure and evolutionary pathways of the star in which the synthesis of those two elements takes place. To do so we will introduce some proper quantities of astrophysics, starting from the

so-called *abundance*.

1.1 Abundances

In astrophysics, abundance is defined as a quantity that indicates the presence of a certain element or isotope inside stars, a cluster, a galaxy, the primordial universe or any other astrophysic environment. This quantity is usually given as the ratio of a certain element i over hydrogen, so $[X^i]/[H]$[1] , where X^i is the number of atoms of a certain element i, and H is the abundance of hydrogen in the observed object[2].

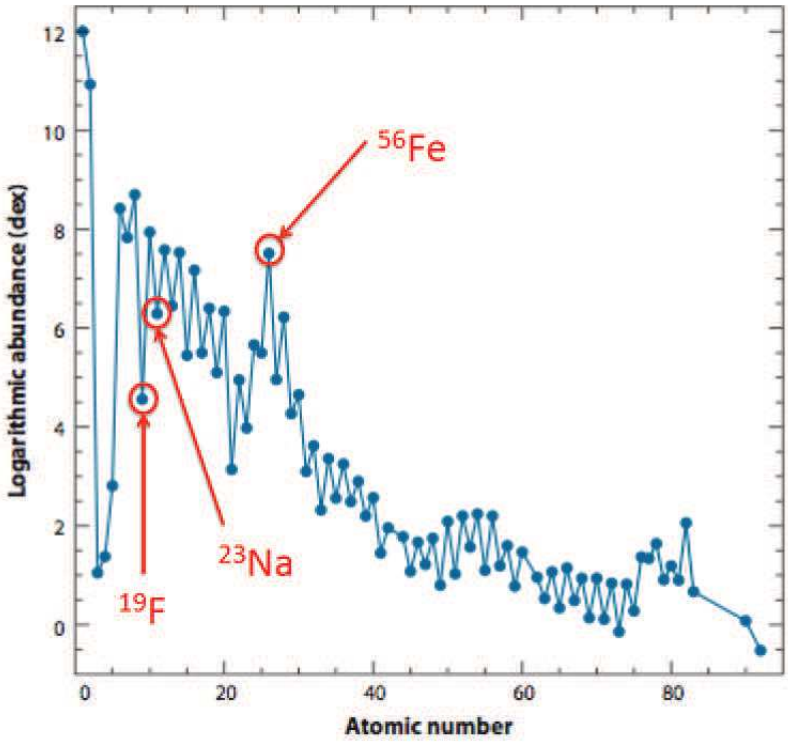

Figure 1.1: Abundances of elements in solar photosphere as a function of A. H and He are the most abundant elements [Asplund et al., 2009]

Looking at Figure 1.1 it results clear that the Sun has elements heavier than A = 8 inside it. Those elements are not produced in *Big Bang* nucleosynthesis but more likely in a earlier generation of stars, that enriched the interstellar medium with those elements. While hydrogen and helium abundances at equilibrium reflect the primordial composition of the universe, all the heavier isotopes with Z>6 are synthesized

[1] When squared parentheses are present, those quantities are referred to the Sun

[2] Sometimes abundance can be expressed as a ratio ove elements other than hydrogen, like for instance Fe, Si or O

by nuclear reactions in stellar environment. So our Sun is not a first-generation star (but a second generation one, at least), given that the protostellar cloud from which the star was produced shows such elements.
Lithium, beryllium and boron are the most fragile nuclear elements[3] in stellar environment. This behaviour explains why in Fig 1.1 they look to be the least abundant light elements. Those with A $\leq$ 56 (^{56}Fe) inside stars are mainly produced by fusion reactions between charged particles. In those cases Coulomb barrier comes to play, reducing fusion probability. This explains the decreasing trend in the abundances of elements between ^{12}C to ^{40}Ca. A peak around Iron in figure 1.1 is also visible, and this is due to the fact that ^{56}Fe - like elements are the ones with the highest binding energy, and so those are the most stable ones (figure 1.2).

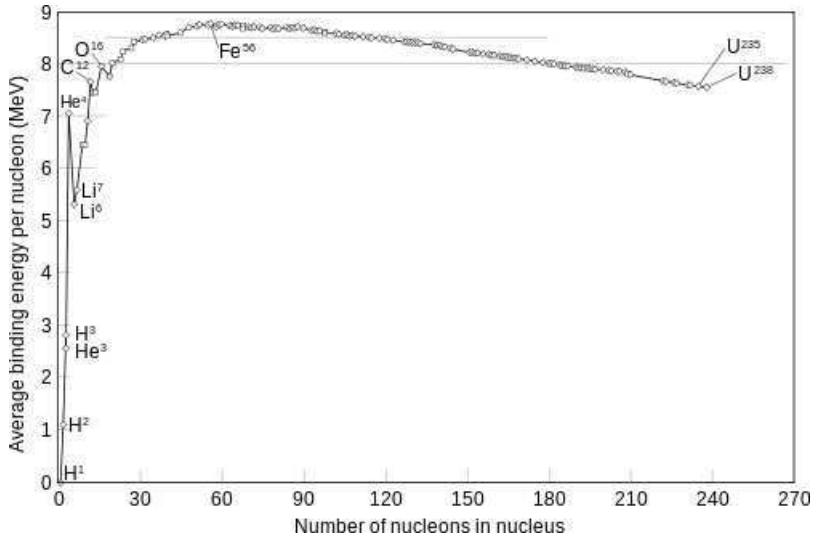

Figure 1.2: Binding energy per nucleon B/A as a function of the mass number A.

Elements heavier than ^{56}Fe cannot be produced by exothermic fusion reactions, because now this kind of interaction is energetically disadvantageous. Those elements are therefore produced by neutron and proton capture [Burbidge et al., 1957].

1.1.1 Essentials on abundance measurements

An analysis of the electromagnetic radiation emitted from a star is a way to ascertain the physical and chemical characteristics of a star: analysing the wavelengtht of the light produced by a star, it is possible to have information on its temperature and chemical composition. A stellar spectrum can be decomposed into two compo-

[3]Those elements have a big destruction cross-section, even at low energies. This key-point will be discussed in chapter II

nents, once temperature is fixed: a discrete part, composed by absorption lines, and a continuum one. Light emitted from inside the star can be assumed as a black-body radiation, and is absorbed by the photosphere and by interstellar clouds, giving rise to absorption lines. Those lines strongly depend on chemical species emitting or absorbing it, and on the temperature of the photosphere. Absorption coefficient of a certain line (e.g. l_v) is defined as the ratio between the intensities of the absorbed line radiation and the continuum, and is proportional to the number of atoms of a certain species X:

$$l_v \propto \frac{fX_i - N_i}{\rho} \tag{1.2}$$

with X_i mass fraction of the $i-$element, ρ its density, N_i the number of atoms able to populate the atomic level responsible for the absorption line and f the oscillator strength [Gray, 2005].
From spectral analysis, along with information about strength and position of absorption lines, it is possible to obtain information about chemical composition.

1.2 Basis of stellar evolution

In stellar environment nuclear reactions can take place in a specific energy range (the so-called *Gamow window*[4]). This is strongly tied to stellar mass and temperature. It is therefore important to describe the characteristics of stars where this reaction can take place. Star classification is based on spectral characteristics, in which stars are ordered by their effective temperature[5], in decreasing order, in spectral types O, B, A, F, G, K, M. Every one of those is than divided into ten sub-categories (B0, B1, B2...B9, A0, A1...), following Tab 1.1[Castellani, 1985].

[4] See Chapter 2.5.

[5] The effective temperature (T_{eff}) of a body such as a star or planet is the temperature of a black body that would emit the same total amount of electromagnetic radiation. Effective temperature is often used as an estimate of a body's surface temperature when the body's emissivity curve (as a function of wavelength) is not known.

Class	Temperature (K)	Mass ($M_\odot$)	Radius ($R_\odot$)	Luminosity ($L_\odot$)
O	≥ 33000	≥ 16	≥ 6.6	≥ 30000
B	$10000 - 33000$	$2,1 - 16$	$1,8 - 6,6$	$25 - 30000$
A	$7500 - 10000$	$1,4 - 2,1$	$1,4 - 1,8$	$5 - 25$
F	$6000 - 7500$	$1,04 - 1,4$	$1,15 - 1,4$	$1,5 - 5$
G	$5200 - 6000$	$0,8 - 1,04$	$0,96 - 1,15$	$0,6 - 1,5$
K	$3700 - 5200$	$0,45 - 0,8$	$0,7 - 0,96$	$0,08 - 0,6$
M	≤ 3700	$0,08 - 0,45$	$\leq 0,7$	$\leq 0,08$

Table 1.1: Spectral classification and reference physical parameters for every class (expressed as a function of solar values)

At the beginning of the XX century, Hertzprung and Russel put stars into their world-famous diagram, organizing them by visual magnitude[6], and its color index (B-V)[7] or temperature (figure1.3). This schematic view is still called H-R diagram in their honour.

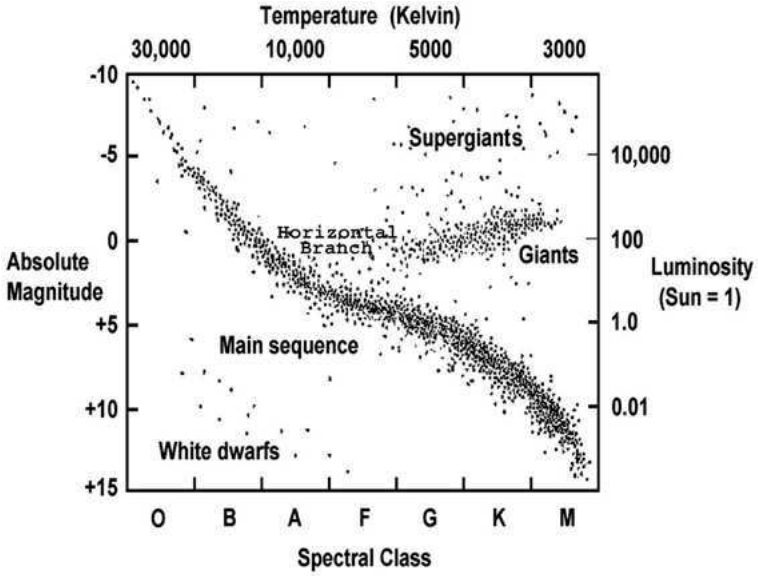

Figure 1.3: Star population based on spectral classification, absolute magnitude and temperature. Absolute magnitude is the apparent magnitude that an object would have if it were to be at a distance of 10 parsecs from the observer. The parsec (pc) is a unit of length used to measure large distances to objects outside the Solar System. One pc is the distance at which one astronomical unit subtends an angle of one arcsecond [Castellani, 1985] and is equal to about 3.26 light-years.

[6]Apparent magnitude is a measurement of luminosity from a certain place (e.g. Earth). It is equal to $m_x - m_{x_0} = -2,5 log_{10} F/F_{x_0}$, where m is the magnitude and F_x is the observable flux in the x-band. If subscript 0 is present, than it is referred to a reference object, like the Sun.

[7]In astronomy, the color index is a simple numerical expression that determines the color of an object. To measure the index, one observes the magnitude of an object successively through two different filters B and V, where B is sensitive to blue light and V is sensitive to visible (green-yellow) light

Looking at this diagram, it can be seen how stars in the so-called *main sequence* corresponds to the longest period of steady nuclear burning inside the core, where hydrogen is converted in helium and accumulates in the core.
He production from H can take place through different reaction networks. At low temperatures, as shown in figure 1.4, the main source of helium (and energy) is the so-called *p-p chain* (typical for stars with mass lower than $\approx 1.2\, M_{\odot}$), while at higher temperatures the *CNO-cycle* (carbon nitrogen oxygen) is dominant [Iliadis, 2007] [Rolfs, 1988].

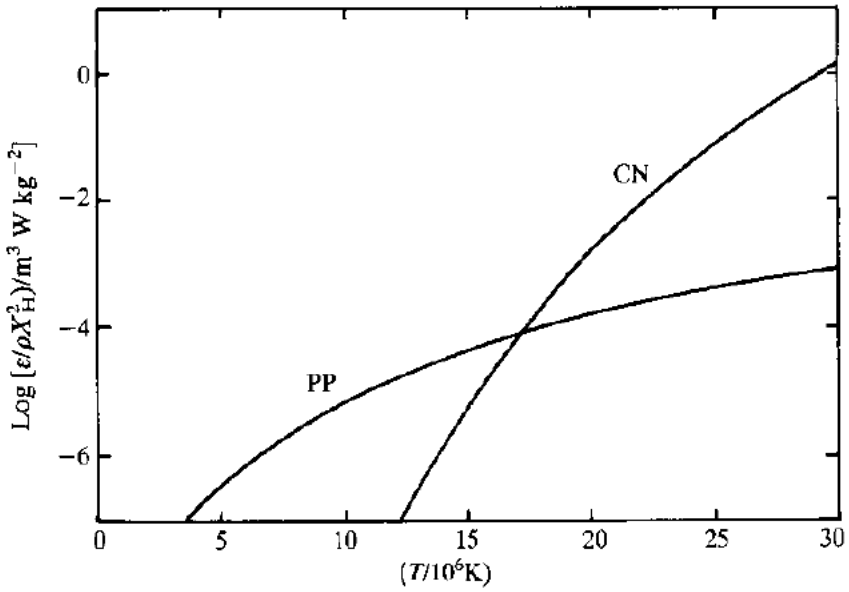

Figure 1.4: Energy production of pp chain and CNO cycle as a function of temperature. If $T < 15 \cdot 10^6$ K the first is dominant, while at higher temperature the latter prevail [Rolfs, 1988].

In the p-p chain four protons are fused to produce a He nucleus. This phenomenon is efficient in stars at temperature of the order at $T = 6 \cdot 10^6$ K , and begins with the reactions: This chain, called PPI, represents the most likely reaction pattern (circa

$$\begin{array}{cc} H + H \rightarrow {}^2H + e^+ + \nu_e & Q{=}1.18\ \text{MeV} \\ d + p \rightarrow {}^3H + \gamma & Q{=}5.49\ \text{MeV} \\ {}^3He + {}^3He \rightarrow {}^4He + 2p & Q{=}12.86\ \text{MeV} \end{array}$$

86%). The other possibilities, called PPII and PPIII chain are proven to be less probable(14%)

$$^{3}\mathrm{He}(^{4}\mathrm{He},\gamma)^{7}\mathrm{Be}(\mathrm{e}^{-},\nu)^{7}\mathrm{Li}(\mathrm{p},\alpha)^{4}\mathrm{He}$$
$$^{3}\mathrm{He}(^{4}\mathrm{He},\gamma)^{7}\mathrm{Be}(\mathrm{p},\gamma)^{8}\mathrm{B}(\mathrm{e}^{+}\nu)^{8}\mathrm{Be}(\alpha)^{4}\mathrm{He}$$

About the CNO-cycle, firstly proposed by the German physicist Hans Bethe in 1938, it consists in the fusion of four H nuclei also to form a He one, producing energy in the process. This cycle, however, needs some catalyst like carbon, nitrogen and oxygen and is composed by two different steps. The first (CN-cycle) goes by the chain reactions:

$$\begin{array}{ll}
^{12}\mathrm{C} + \mathrm{p} \rightarrow ^{13}\mathrm{N} + \gamma & \mathrm{Q}{=}1.94\ \mathrm{MeV} \\
^{13}\mathrm{N} \rightarrow ^{13}\mathrm{C} + \beta^{+} + \nu & \mathrm{Q}{=}1.51\ \mathrm{MeV} \\
^{13}\mathrm{C} + \mathrm{p} \rightarrow ^{14}\mathrm{N} + \gamma & \mathrm{Q}{=}7.54\ \mathrm{MeV} \\
^{14}\mathrm{N} + \mathrm{p} \rightarrow ^{15}\mathrm{O} + \gamma & \mathrm{Q}{=}7.29\ \mathrm{MeV} \\
^{15}\mathrm{O} \rightarrow ^{15}\mathrm{N} + \beta^{+} + \nu & \mathrm{Q}{=}1.76\ \mathrm{MeV} \\
^{15}\mathrm{N} + \mathrm{p} \rightarrow ^{12}\mathrm{C} + ^{4}\mathrm{He} & \mathrm{Q}{=}4.96\ \mathrm{MeV}
\end{array}$$

The ^{15}N+p has also a 0.04% probability to give rise to another chain:

$$\begin{array}{ll}
^{16}\mathrm{O} + \mathrm{p} \rightarrow ^{17}\mathrm{F} + \gamma & \mathrm{Q}{=}0.60\ \mathrm{MeV} \\
^{17}\mathrm{F} \rightarrow ^{17}\mathrm{O} + \mathrm{e}^{+} + \nu & \mathrm{Q}{=}2.22\ \mathrm{MeV} \\
^{17}\mathrm{O} + \mathrm{p} \rightarrow ^{14}\mathrm{N} + ^{4}\mathrm{He} & \mathrm{Q}{=}1.19\ \mathrm{MeV}
\end{array}$$

The CNO-cycle can not take place unless at least one of the catalyst is present [Kippenhahn and Weigert, 1990]. Moreover, the CN-cycle can only take place at temperatures higher than $1.5 \cdot 10^{7}$, K, while the second step needs even higher temperatures ($2 \cdot 10^{7}$ K). It is also important to underline that the low cross-section of the p(p,e$^{+}\nu$)d and ^{14}N(p,γ)^{15}O reactions is the main responsible for the long "life" of the main sequence stage. This stage is called *Main Sequence* (MS), and is indeed a very long period of time (circa 10^{9} year) in which it slowly contracts, producing helium from hydrogen as explained before. In the central region, gravitational pressure is no more balanced out by energy production, given that the $3-\alpha$ process has a higher Coulomb barrier, and therefore the star starts to contract. The star then leaves the MS gradually, and its temperature increases inside the star. Hydrogen present in the layer surrounding the core, called *shell*, starts burning, giving rise to an increase in luminosity, while effective temperature is almost unvaried. As an answer to the contraction of the core, the convective envelope expands. The star has so entered the *Red Giant Branch* (RGB).

In RGB phase, the helium-composed core,which mass is increased by the reactions taking place in the shell, continues to shrink, unless it becomes electron-degenerate matter[8]. The external parts of the star then expand and cool down, until they became convective[9]: convection will enter inside the star, reaching the zone in which hydrogen was previously converted in helium. This mixing, called *first dredge-up*, is able to modify superficial abundances (in particular of carbon and nitrogen). If the stellar core has mass below $0.45 \div 0.55$ $M_\odot$ (depending on the chemical composition) He-core remains inert, and H-burning in shell is activated.

If the star is more massive, in-core He-burning can take place: in the first step, two α can react and form ^{8}Be. Its ground state has a half-life of 10^{-16} sec, long enough with respect respect to the typical time for another α particle to come across the nucleus [Iliadis, 2007] (10^{-19} sec). So ^{8}Be "lives" long enough to capture another helium nucleus and form ^{12}C[10].

At $T = 2 \cdot 10^8$ K carbon can capture another α particle and form ^{16}O emitting a γ ray with the $^{12}C(\alpha,\gamma)^{16}O$ (this reaction is moreover slower than C-production). All this chain can be triggered only in electron-degenerate matter. In such an environment the non-relativistic equation of state is still valid, so pressure P is proportional to density ρ, in particular $P \propto \rho^{5/3}$, and lowly dependent from temperature, unless energy is high enough to remove the degeneracy. This happens due to reactions that take place in the *He-flash*[11]. Now the star has lower luminosity with respect to the one that it had at the end of the RGB, and can be placed in a part of the H-R diagram (figure 1.4) called *Horizontal Branch*: in this evolutionary stage the central He-burning brings to carbon and oxygen formation. Those elements gather at the center of the star, and when all helium is converted in C and O, energy for stellar equilibrium will be provided by in-shell H-burning, unless helium abundance and temperature are not enough to start He-burning again. So an alternate shell burning of hydrogen and helium will take place (figure 1.5).

[8] When matter is compressed to a density of $10^6 \div 10^8$ g/cm^3, electrons start to manifest a quantic repulsion, due to the Pauli exclusion principle. Electrons are fermions, so they can not coexist as a pair in the same quantum state with anti-parallel spin.

[9] Convection is a movement of matter that allows heat transportation. It happens when transport by radiation is not sufficient to bring outside all the produced energy.

[10] This reaction can occur because there is a resonance of ^{12}C near the Q-value (7.68 MeV), that enhances the reaction rate [Rolfs, 1988]

[11] This occurrence is possible because the time necessary to expand the gas is longer than the one necessary for the 3α reaction

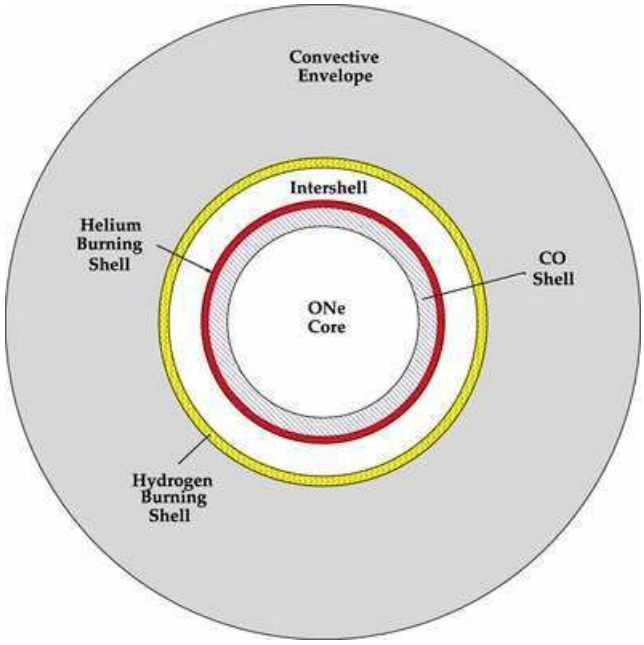

Figure 1.5: Sketch of the shell structure of a AGB star [Lugaro et al., 2012].

In this way the star reaches the so-called *Asymptotic Giant Branch* (AGB) of the H-R diagram, whose name is chosen because of the way in which the evolutionary track of those stars comes near to the Giant Branch (figure 1.6). AGB stars are one of the proposed sites of ^{19}F and ^{23}Na nucleosynthesis, and in those the reaction ^{19}F(α,p)^{22}Ne and ^{23}Na(p,α)^{20}Ne can take place.

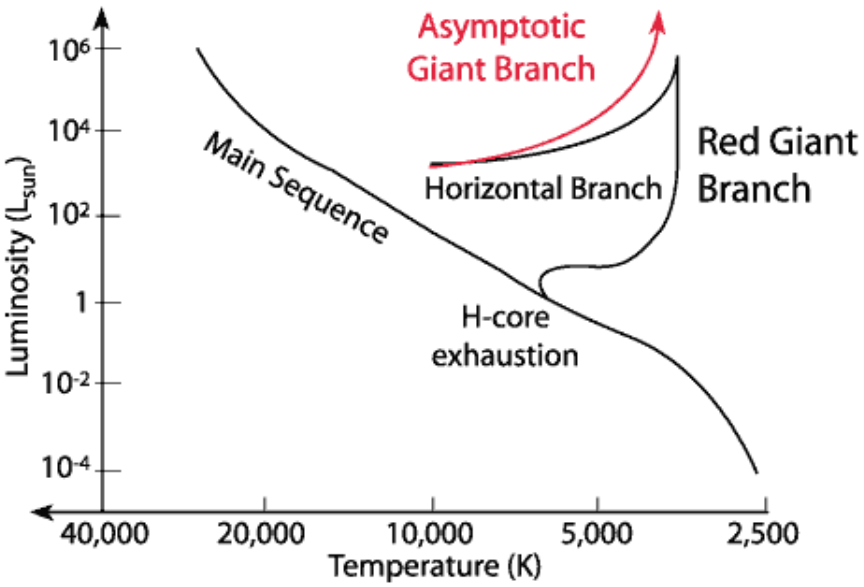

Figure 1.6: H-R diagram of the discussed stellar evolution

Hydrogen and helium shells are divided by a thin zone ($10^{-2} \div 10^{-3}\, M_{\odot}$), called He-intershell. The external part of a star is instead called convective envelope, and is composed by a "cold" and dusty atmosphere made in most part of hydrogen. This zone can extend itself for several hundreds of $R_{\odot}$. In H-shell, when active, He is produced by means of nuclear reactions explained in the previous paragraph. Helium is heavier than hydrogen and it will accumulate in the He-intershell, enhancing density and temperature in the process, unless the physical conditions are good enough to ignite He-burning.

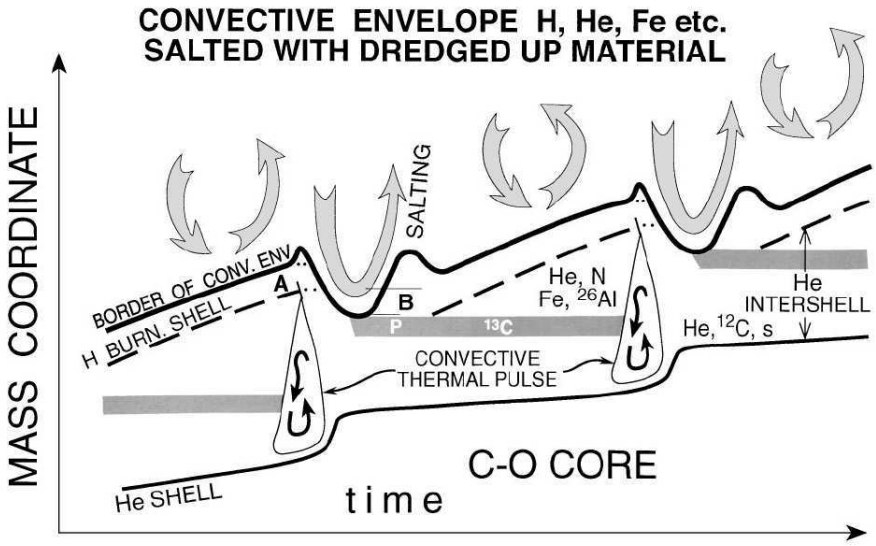

Figure 1.7: Convective episodes. The convective zone, generated by a thermal pulse, covers the He-intershell completely. After 2000 years, external convection penetrates the inner part of the star [Straniero et al., 2006]

Those episodes are called *thermal pulses* (figure1.7) and can be described as follows: when the right conditions of He mass is fulfilled, the shell temperature is high enough to trigger fast processes, giving birth to a *flash*. Due to this, a convective zone will be formed, and it will cover the region from the He-burning shell to the H-shell (this phenomenon is called *thermal pulset*). This phenomenon is responsible for the mixing of the elements coming from the $3-\alpha$ and from H-burning in the intershell region [Straniero et al., 2006].

Energy produced and released in this process results in an expansion of the star, that will cool down in the process. This goes to the point that the hydrogen shell switches off, and the He-shell become more stable. This phase is called *convective burning*: while helium decreases, the shell starts to die out and superficial convec-

tion can penetrate the H-shell and the external part of the He-shell, changing the chemical composition of the surface. This phenomenon is called *third dredge-up*, and the convective envelope penetrates in the deep region of the He-shell, carrying a lot of carbon from the inner part to the surface of the star. it will modify the C/O superficial ratio, now equal to more than one.
After He-burning the star will start to shrink again, rising its internal temperature, while the envelope expands and cools down. In this phase H-shell accumulates helium, until the conditions are right for another pulse. There are lot of thermal pulses in the life of a star, and there are a lot of theoretical models that try to explain that (for example Cristallo et al. [2014] Cristallo et al. [2011]; Cristallo et al. [2009]).

1.3 The fluorine problem

Fluorine origin into our Galaxy is still a matter of debate. There are few spectroscopical observations, due to the scarce abundance of fluorine if compared to other elements (like C, N, O, ...). This fact determines the low intensity of its spectral lines. Fluorine has no spectral lines in the visible part of the electromagnetic spectra: the only atomic lines (transitions from ground state of F_I) can be seen, but only in the deep ultraviolet spectrum. It is therefore convenient to use the transitions of the HF molecule. Those are in the infra-red spectrum (at about 23000 Å), and the HF(1-0)R9 spectral line [Recio-Blanco et al., 2012; D'Orazi et al., 2013] is often used, because it is considered to be the best indicator to ascertain fluorine abundance[12] [Abia et al., 2009; Lucatello et al., 2011].
The production and destruction patterns of fluorine in galactic environment are still not fully understood. In stellar environment characterized by a great presence of hydrogen and helium, ^{19}F, only stable isotope of fluorine, can be destroyed through the reactions ^{19}F(p,α)^{16}O and ^{19}F(α,p)^{22}Ne. Its abundance is the lowest among the light elements with $6 \leq Z \leq 20$ [Abia et al., 2009]. Until today, three main stellar sites are proposed for ^{19}F nucleosynthesis:

- He-Burning in AGB stars whose mass is between $2 \div 4\ M_{\odot}$;
- Type II Supernovae (SNe II);
- H-Burning in Wolf-Rayet objects;

[12]This line was identified, for example, using the CRiogenic high-resolution InfraRed Echelle Spectrograph (CRIRES)[Recio-Blanco et al., 2012]

1.3.1 ^{19}F production in AGB environment

In AGB stars fluorine can be produced by the chain of reactions:

$$^{14}N(\alpha,\,\gamma)^{18}F(\beta^{+}\nu)^{18}O(p,\,\alpha)^{15}N(\alpha,\,\gamma)^{19}F \tag{1.3}$$

in which ^{14}N produced in CNO cycle by proton capture from ^{13}C. This chain, nevertheless, can take place only in the He-rich part of the star. Here is highly possible that a ^{14}N nucleus interacts with an α particle, forming ^{18}F. This nucleus is unstable, with a half-life of 109.8 minutes, and will decay in ^{18}O. It will capture a proton, with the reaction^{18}O(p,α)^{15}N, and after $\alpha-$capture ^{19}F will be produced through the reaction ^{15}N(α,γ)^{19}F [Forestini et al., 1992]. An oxygen-18 nucleus can also absorb an α producing ^{22}Ne[13] in the process. This reaction is furthermore involved in ^{23}Na production via proton capture, and will be discussed later in this work.

A ^{14}N nucleus is now in the He-intershell region of an AGB star, and can be synthesized *in situ* due to the presence of protons brought by the third dredge-up, by means of the chain reactions:

$$^{12}C(p,\,\gamma)^{13}N(\beta^{+}\nu)^{13}C(p,\,\gamma)^{14}N \tag{1.4}$$

This case, called ^{13}C-*pocket* formation, is widely discussed in literature, because the reaction ^{13}C(α,n)^{16}O is, together with the ^{22}Ne(α,n)^{25}Mg reaction, considered to be the main source of neutrons for the so-called *s-process*, typical of AGB-nucleosynthesis for low-mass stars.

Given the high cross section for the reaction ^{14}N + n this isotope is also known as a "poison" for s-processes, because it can absorb a lot of neutrons coming from ^{13}C(α,n)^{16}O, blocking neutron capture from heavier nuclei. However, the ^{14}N(n,γ)^{15}N reaction would be important for ^{19}F production:

$$^{14}N(n,\,\gamma)^{15}N(\alpha,\,\gamma)^{19}F \tag{1.5}$$

but this last chain is not efficient enough. In fact, the ^{14}N(n,γ)^{15}N reaction is approximately ten times slower than the ^{14}N(n,p)^{14}C [Fowler et al., 1967; Brehm et al., 1988].

Another possibility is that a ^{18}O nucleus absorbs a neutron, producing ^{19}O. This will decay in a ^{19}F nucleus through β^{-} decay:

$$^{14}N(\alpha,\,\gamma)^{18}F(\beta^{+}\nu)^{18}O(n,\,\gamma)^{19}O(\beta^{-}\nu)^{19}F \tag{1.6}$$

[13] Neon production via this reaction takes place in the firsts thermal pulses, because it needs higher temperatures [Wasserburg et al., 1995]

The efficiency of this channel of production is, however, strongly tied to the ^{18}O(n,γ)^{19}O reaction: ^{19}O, in fact, has a high neutron capture cross-section[14].
From what discussed so far, it is clear that the chain 1.3 is dominant if compared to the others.
Fluorine, produced at the end of every thermal pulse and brought to the surface by means of the third dredge-up, is very fragile. Three main reactions were proposed as a destruction channel for ^{19}F in AGB environment:

$$^{19}F(\alpha,\ p)^{22}Ne \tag{1.7}$$

$$^{19}F(n,\gamma)^{20}F \tag{1.8}$$

$$^{19}F(p,\ \alpha)^{16}O$$

The dominance of one of those three reaction on the others will be strongly influenced by the presence of protons, neutrons or α particles: the 1.7 reaction is typical of the He-intershell region part that is rich of α particles, while the 1.8 will take place thanks to the neutrons coming from ^{13}C(α,n)^{16}O and ^{22}Ne(α,n)^{25}Mg. The 1.9 reaction will happen in proton-rich environments. In the first part of this work we will focus on 1.7. About 1.9, this reaction was extensively studied in the last years [La Cognata et al., 2015; Lombardo et al., 2015; Indelicato et al., 2017], while about the 1.7 cross-section and reaction rate are almost unknown at astrophysical energies.

1.3.2 Observative evidences

First observations of fluorine in stellar environment were made by Jorissen, Smith and Lambert, tat in 1992 succeeded in measuring its abundance (following the procedure briefly explained at the beginning of the paragraph) in a sample of stars[15], finding it higher than solar abundance. At the same time they found a correlation between ^{19}F and C/O ratio: this correlation is enhanced in correspondence of the Third Dredge-up [Busso et al., 1999]. Examples of fluorine spectra are reported in figure1.8a and 1.8b.

[14] 5.4 mb at 30 keV [Bao and Kappeler, 1987]
[15] Their work was focused on Red Giants [Jorissen et al., 1992]

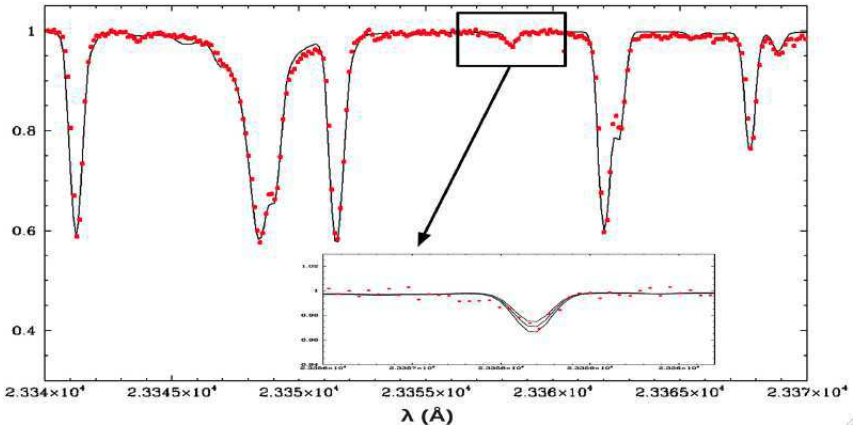

(a)

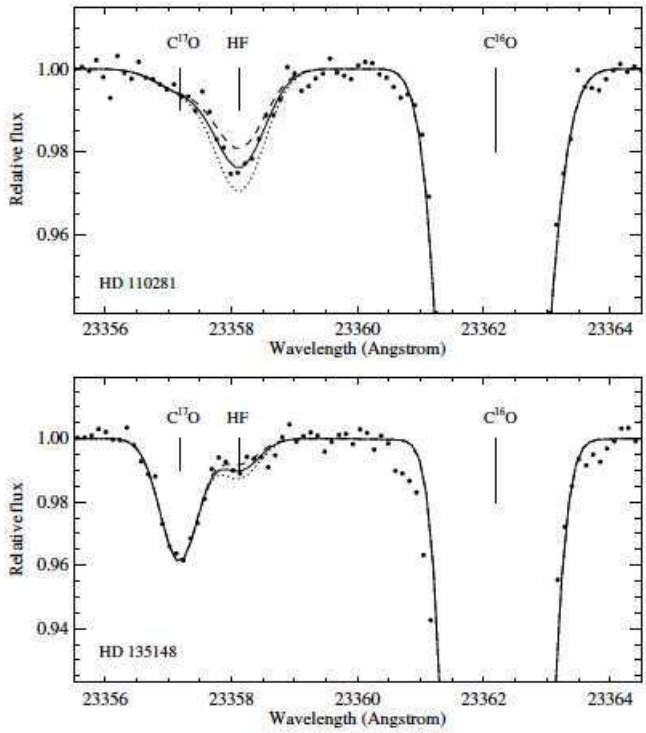

(b)

Figure 1.8: a)Spectrum for the K-type HD 131977 (red dots), belonging to the Libra constellation; in the squared part the zoom for the R9 (1-0) line of the HF molecule at $\lambda \simeq 23358$ Å is reported. In table 1.2 some atmospheric parameters are reported [Santos et al., 2004; Sousa et al., 2006] together fluorine abundances for some stars [Recio-Blanco et al., 2012]
b)Some examples of HF spectra at $\lambda \simeq 2.3358\ \mu m$ for HD 110281 (K-type) belonging to Virgo constellation, and HD 135148, same class, but located in the Serpent constellation [Li et al., 2013]

ID Target	T_{eff}(K)[16]	$log\varepsilon(F)$[17]
HD 50281	4658 ± 56	4.53 ± 0.20
HD 65486	4660 ± 66	4.47 ± 0.20
HD 85512	4505 ± 176	4.73 ± 0.20
HD 101581	4646 ± 96	4.61 ± 0.20
HD 111261	4529 ± 62	4.44 ± 0.20
HD 131977	4693 ± 80	5.16 ± 0.20
HD 156206	4568 ± 94	4.41 ± 0.20
HD 209100	4629 ± 77	4.75 ± 0.20
HD 216803	4555 ± 87	4.64 ± 0.20

Table 1.2: Examples of stars containing fluorine. In figure 1.8a is represented the spectrum of the star HD131977 (in red).

Abundances observed in low-mass AGB-stars, in which fluorine production is confirmed, are in agreement with the galactic one, while observation about stars belonging to the Large Magellanic Cloud (LMC)[18] and *ω Cen* show a decreasing F/O ratio in correspondence of oxygen enhancement.

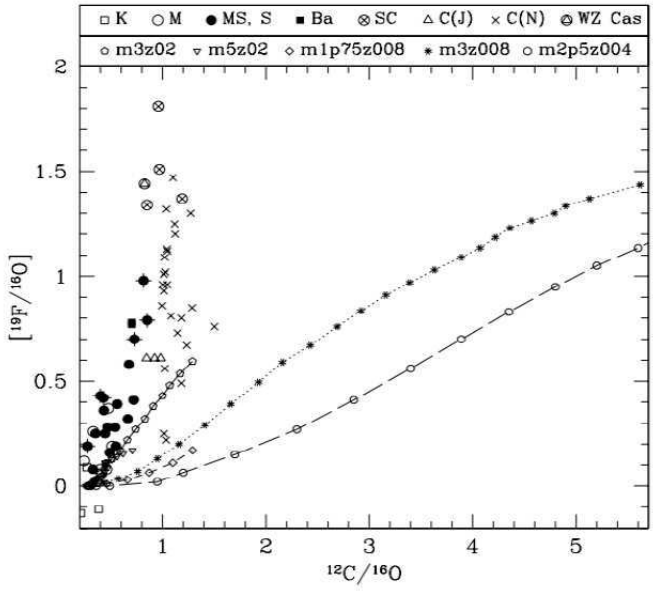

Figure 1.9: Observed abundances made by Jorissen (firs line at top) for various stars, in respect to various models (second line)) [Lugaro et al., 2004]

[16] In astrophysics, the effective temperature T_{eff} of a star is the temperature of a black-body object with the same luminosity for unit of surface of the star.

[17] $log\varepsilon = log\frac{[X^i]}{[H]} - 12$

[18] The Large Magellanic Cloud (LMC) is a satellite galaxy of the Milky Way. The LMC has a diameter of about 14,000 light-years (4.3 kpc) and a mass of approximately 10 billion $M_\odot$, making it roughly 1/100 as massive as the Milky Way. The LMC is the fourth-largest galaxy in the Local Group, after the Andromeda Galaxy (M31), the Milky Way, and the Triangulum Galaxy (M33).

This could be due to an increased ^{19}F production in more massive stars [Cunha et al., 2003; Renda et al., 2005].

Nucleosynthesis pattern earlier discussed can not explain the high measured abundance of fluorine (figure 1.9): if C/O ratio is the same only a small part of it is in fact theoretically justified.

To solve this problem, the presence of processes of extra mixing at the base of the convective envelope were proposed. One of these phenomena, known as *cool bottom processing* (CBP) [Wasserburg et al., 1995; Lugaro et al., 2004], consists in a slow mixing of materials from the base of the convective envelope to the hydrogen shell. During this, there can be elements exposed to proton capture [Nollett et al., 2003]. This process can reduce the ^{12}C/^{13}C and ^{12}C/^{16}O ratios, and enhance ^{14}N [Uttenthaler et al., 2008; Palmerini et al., 2011a,b; Hedrosa et al., 2013] one.

The CBP is typical of low-mass Red Giants ($M < 2.3M_{\odot}$) while for heavier objects ($4 \div 8M_{\odot}$) the base of the convective envelope can reach temperatures $\sim 10^7$ K. In this case, some proton capture reactions are allowed: this event is called *Hot Bottom Burning* (HBB) [Frost and Lattanzio, 1996]. Either HBB or CBP have the effect to modify superficial abundances in stars. In this case ^{12}C and ^{18}O abundance decrease, while ^{14}N and ^{15}N (typical "signs" of CN-burning) abundance increase. Furthermore, ^{17}O abundance varies. Even superficial abundance of ^{19}F can be modified by CBP or HBB. In particular, more fluorine will burn through ^{19}F(p,γ)^{20}Ne and ^{19}F(p,α)^{16}O.

A better understanding of fluorine nucleosynthesis could be really important to understand AGB nucleosynthesis, even for low-metallicity[19] and population II stars[20], as underlined in Lucatello et al. [2011].

Regarding what is stated in Lugaro et al. [2004], recently those measurement were corrected by Abia et al. [2009]. They were able to systematically reduce fluorine abundance, in carbon-rich AGB stars, by a factor of 0.8. Now low-mass, low metallicity AGB stars are in agreement with theoretical calculations. Those results, any-

[19] In astronomy, metallicity of a certain object is a non-dimensional quantity indicating the fraction of mass of a star or other kind of astronomical object that is not in hydrogen or helium. The overall stellar metallicity is often defined using the total Iron-content of the star [Fe/H] = $\log_{10}(\frac{N_{Fe}}{N_H})_{star}$ - $\log_{10}(\frac{N_{Fe}}{N_H})_{Sun}$.

[20] Population II, or metal-poor stars, are those with relatively little metal. The idea of a relatively small amount must be kept in perspective as even metal-rich astronomical objects contain low percentages of any element other than hydrogen or helium; metals constitute only a tiny percentage of the overall chemical make-up of the universe, even 13.8 billion years after the Big Bang. However, metal-poor objects are even more primitive. These objects are formed during an earlier time of the universe.

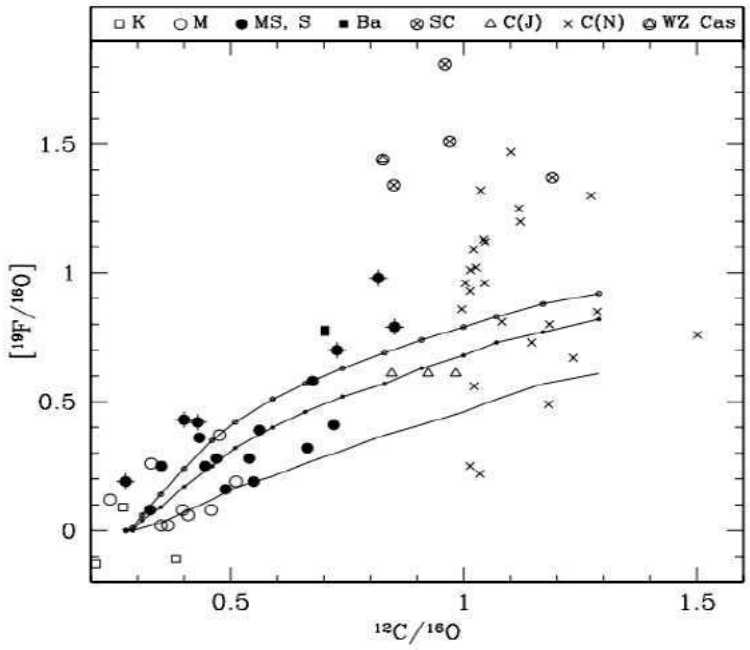

Figure 1.10: fluorine abundance observed by Jorissen taking into account partial mixing zone [Jorissen et al., 1992]

way, do not confute the role that AGB stars play in fluorine production and in any case are not able to reproduce theoretical predictions for more massive stars.

A particular case of AGB stars: C-EMP

Carbon-enhanced metal-poor (C-EMP) gives us an opportunity to directly measure ^{19}F in low-mass, low-metallicity AGB stars. C-EMP stars are chemically peculiar: in fact they are characterized by an over-abundance of carbon with respect to the average cosmic abundance ([C/Fe]>1)[21]. This anomalous abundance, together with the irregular abundances of nitrogen and oxygen (again beside iron), suggests that there is a strong contribution to nucleosynthesis of C and O, cause of the enhancement of nitrogen, carbon and oxygen. Those represent around 10%-20% of stars with $[Fe/H] \leq -2.5$.
Various types of C-EMP are listed in literature [Lucatello et al., 2011]

- C-EMP-s: traces of s-processes in their spectra (circa 80% of the observed ones) [Aoki et al., 2007];
- C-EMP-r: traces of r-processes in their spectra;

[21] Some authors use different cut-off taking into account the evolutionary stage of the star, adopting [C/Fe]≃0.5

- C-EMP-rs: r-processes and s-processes are both present;
- C-EMP-no: no chemical enrichment;

Lucatello et al. [2005] showed that any C-EMP-s star belongs to binary systems, composed by a low-mass star ($M \sim 0.8\,M_{\odot}$) and a slightly bigger one (between 1.2 and 2.5 $M_{\odot}$, the exact range depends on metallicity). Through stellar wind, the more massive, "dying" star passes the processed materials to the companion star. Those elements can be seen on the surface of the remaining star, that often is still not an AGB-star. This allows to perform measurement of abundance of fluorine or other s-elements and s-elements in C-EMPs (figure1.11).

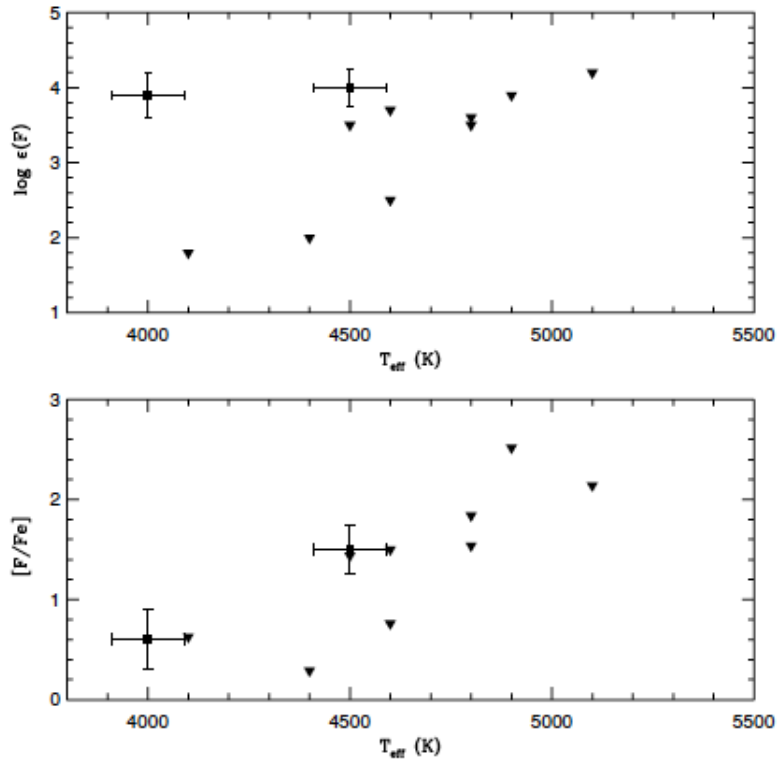

Figure 1.11: Measured abundances as a function of T_{eff} for a sample of stars [Lucatello et al., 2011]. Overturned triangles represent upper limits. The correlation between them and T_{eff}

Anyway, C-EMP stars are still quite peculiar objects. The existence of C-EMP-no, in particular [Fujimoto et al., 2000] suggests that those stars became C-enhanced through self-enrichment due to an anomalous mixing process characteristic for low-metallicity star, without going by the AGB phase. Otherwise Ryan et al. [2005], those stars may have been born from C-rich gases, maybe contaminated by remnants of a previous generation supernova, whose *fall-back* kept heavier elements during

explosive stages.

Another proposed scenario consists in a transfer of heavy elements from low-mass AGB stars before s-processes [Ryan et al., 2005; Masseron et al., 2010], or from AGB stars whose evolution has been interrupted by a binary interaction with its companion (still visible) [Izzard and Tout, 2003].

Measurements about abundance of ^{19}F (1.12) would be crucial in understanding the origin of chemical composition observed in C-EMP-no.

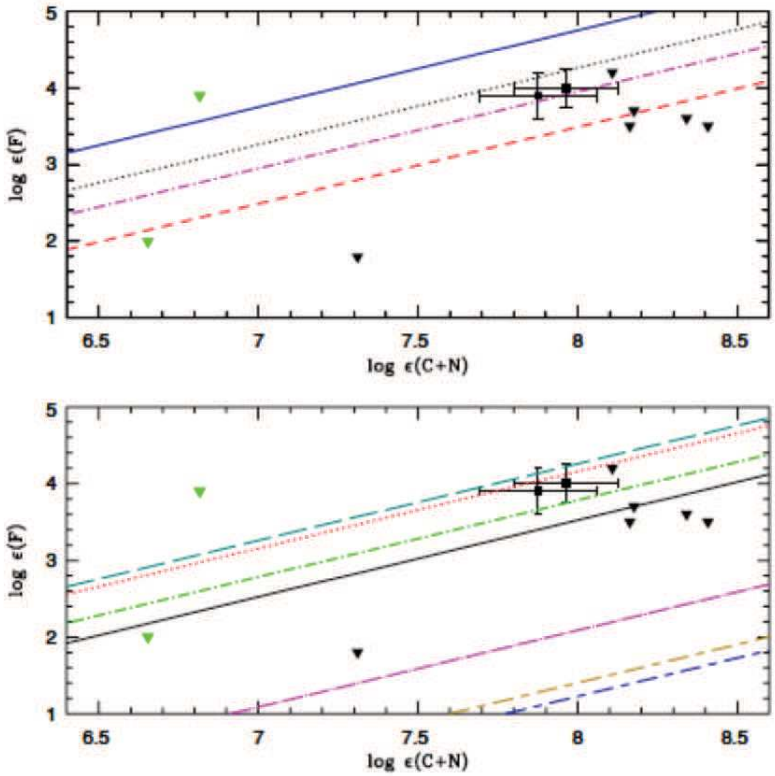

Figure 1.12: Fluorine abundances as a function of C+N for ten C-EMP stars. Reversed triangles are the upper limits, while the green symbols represents C-EMP-no stars. All lines come from theoretical calculations [Lucatello et al., 2011].

1.3.3 Supernovae

A Supernova (SN) is an explosive and extremely energetic event. At its luminosity peak, a typical SN can rise up to 20 magnitudes more than its original state (so one thousand million times brighter), and reach 10^{10} solar luminosities (emitting as much light as an entire galaxy). This phenomenon is indeed destructive: it is revealed by the humongous quantity of energy emitted and the expansion velocity observed (circa 10^4 km/sec).

There are two types of Supernovas:

- Type I Supernovas (SNe I): characterized by the absence of hydrogen lines and a by well defined light curve, with a rapid rise (circa three order of magnitude) and a slow and regular fall (Fig 1.13);
- Type II Supernovas (SNe II): characterized by the presence of hydrogen and by a slow and regular decline (linear SNII), in some cases interrupted by zones in which the fall almost stops (plateau SNII)(Fig 1.14)

Another difference between SNe I and SNe II that the spectrum of the latter has sign of hydrogen, that are not visible in the first.

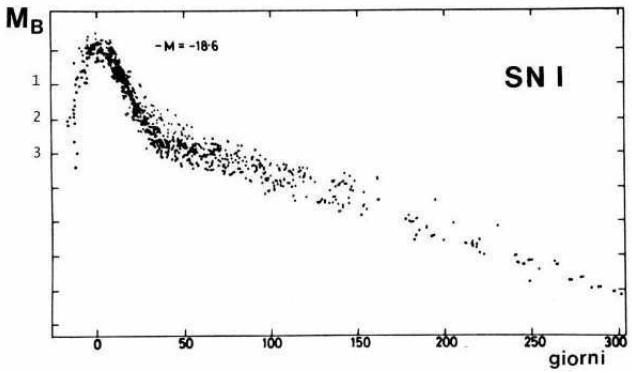

Figure 1.13: Light curve obtained superimposing data from thirty-eight different SNe I [Castellani, 1985].

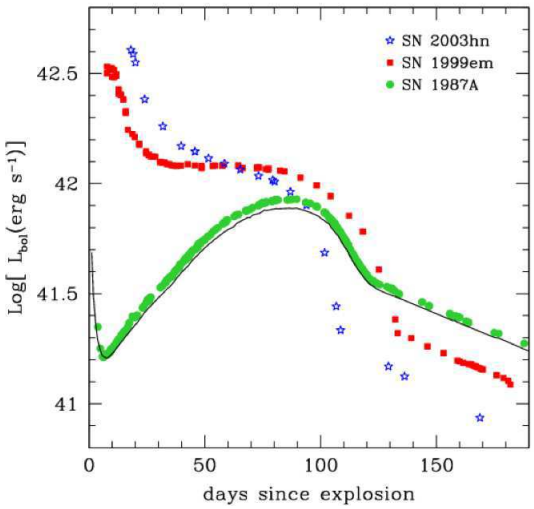

Figure 1.14: Light curve for several Sne II stars (SN 1987a, SN 1999em, SN 2003hh). The solid line represents the measurements made by by Suntzeff e Bouchet (1990) (solid line)

SN II represents the final evolutionary stage of massive objects ($M \gtrsim 10\,M_{\odot}$), and are considered to be among the fluorine production sites. Those stars throw into the interstellar medium the external parts, leaving a Neutron Star or a Black Hole as a remnant.
In this case, a large part of the produced fluorine is made by spallation[22] from ^{20}Ne, with the emission of μ e τ [Woosley and Haxton, 1988; Woosley et al., 1990]. A part of it is produced *in situ*, but the largest part of it is expelled in the interstellar medium (ISM). Another source of ^{19}F can be found in pre-explosive CNO-cycle in the H-shell, but spallation is considered to be dominant. Renda et al. [2004] and Heger et al. [2005] have supposed that the neutrino cross-section should be revised to lower values. If that is true, than fluorine production could be halved in SNe II stars. Anyway, there are still no observative evidences of fluorine production in SN.

1.3.4 Wolf-Rayet stars

At the beginning of this paragraph, while discussing about ^{19}F production sites, we mentioned Wolf-Rayet stars (WR). These objects, discovered in 1867 by Charles Wolf and Georges Rayet that identified three of such stars in Cygnus constellation, are extremely peculiar: their temperature is quite high ($25000\,K \leq T_{eff} \leq 50000\,K$) such as their masses ($M \geq 20\,M_{\odot}$). Another striking feature is that those stars produce really strong stellar winds ($v \geq 2000$ km/sec) [Tuthill et al., 1998]. Even if in a minor part, WR stars contribute to chemical enrichment of galaxies, and are considered to be one of the possible sources of long (usually tied to massive star explosion in a peculiar supernova called *collapsar*) and soft (emitted by highly magnetic neutron stars belonging to our Galaxy) *gamma ray bursts*[23] [Woosley and Bloom, 2006]. Furthermore, the presence of WR stars was also confirmed in the zone of formation of high mass stars [Schaerer and Vacca, 1998].
Regarding WR spectroscopy, these objects show broad and strong emission lines (figure1.15), while the absorption ones are narrow and typical of "normal" star populations. Two types of Wolf-Rayet stars are identified nowadays:

[22] Nuclear spallation is a phenomenon discovered in 1937 by the Nobel-awarded Glenn Theodore Seaborg, while studying neutron inelastic scattering. This is the effect of the bombardment of an atom by high-energy particles (over 100 MeV). After that lighter nuclei are emitted. This easily happens on the surface of stars after the interaction with cosmic rays.

[23] *Gamma ray burst* are gamma ray flashes that can last from some milliseconds to several minutes. Those explosions are the most energetic phenomena observed so far in the universe.

- Stars with strong lines of helium and nitrogen in their spectrum (WN-type);
- Stars with strong lines corresponding to helium, carbon and oxygen (WC- and WO-type);

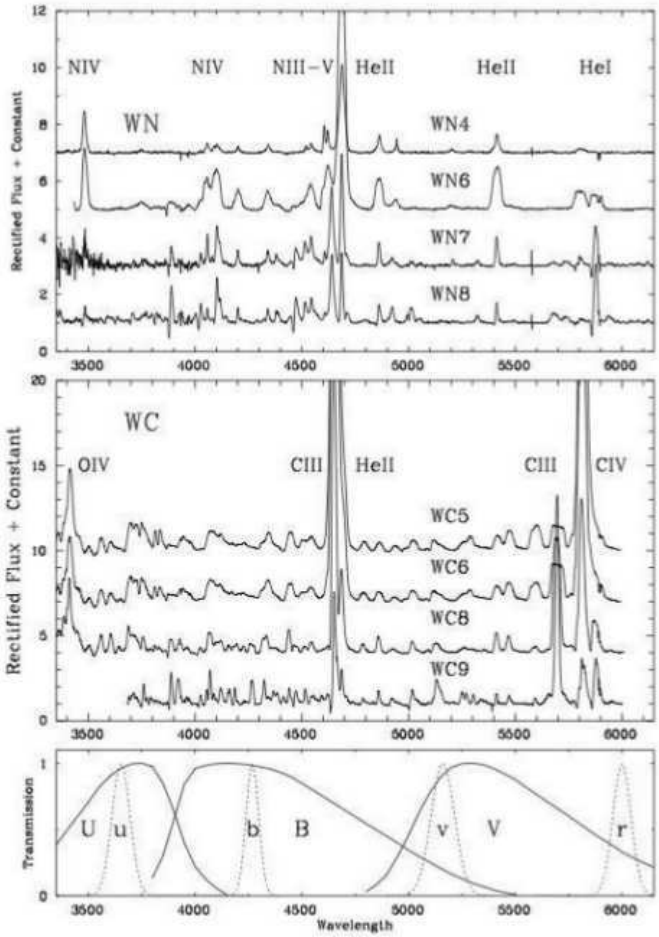

Figure 1.15: WN and WC spectra obtained by Smith [1968]; Massey [1984]; Massey and Johnson [1998] [Crowther, 2007]

The first scientist to suggest that the anomalous composition of WR stars is due to previous nuclear reactions (detectable in the stellar surface) was George Gamow in 1943. This idea was not completely accepted by the scientific community until 1991 [Lamers et al., 1991].

WR stars show CNO products, while WC have traces of He-burning. Wolf-Rayet stars with solar-like metallicity have $\simeq 25 M_{\odot}$, comparable with the mass limit that Humphreys & Davidson found in 1979 for Supergiants (RSG). WR stars could therefore be an evolutionary stage subsequent to red supergiants. Those stars exist

a really narrow mass interval ($25 \div 30 M_{\odot}$) [Crowther, 2007], and, show hydrostatic He-burning that can bring to ^{19}F production (that is expelled afterwards by stellar wind) [Meynet and Arnould, 2000]. The production network is the same as the one explained earlier in 1.3.1.

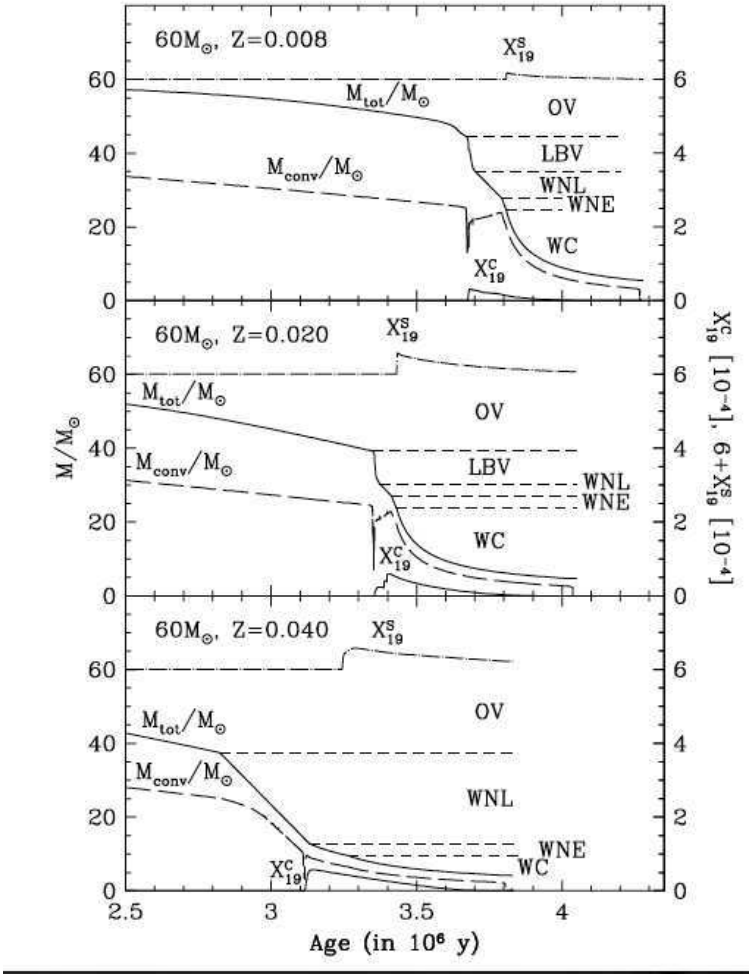

Figure 1.16: Evolution of total mass M_{tot}, of the convective core M_{conv} and of the superficial (X^S_{19}) and central(X^C_{19}) mass fraction of ^{19}F for a 60 $M_{\odot}$ star with Z=0.008, 0.02 and 0.04 metallicity at the end of the H-burning and during He-burning [Meynet and Arnould, 2000]

1.4 Sodium production in stellar environment

As fluorine, sodium presence inside stars has been matter of debate in the last twenty years, but for different reasons. Sodium overabundances has been found in many astrophysical objects: in particular, observation of globular clusters (GCs) have proven to be really interesting. These clusters, in fact, host many different star

populations [Gratton et al., 2012].

Globular clusters usually contains about 10^5 stars, and their distribution is spherical. Stars inside GC are among the oldest ($\sim 10^{10}$ years, composed by population II stars) of the Milky Way, giving to those objects great importance as a "laboratory" to study stellar evolution. In our Galaxy there are about 150 GC.

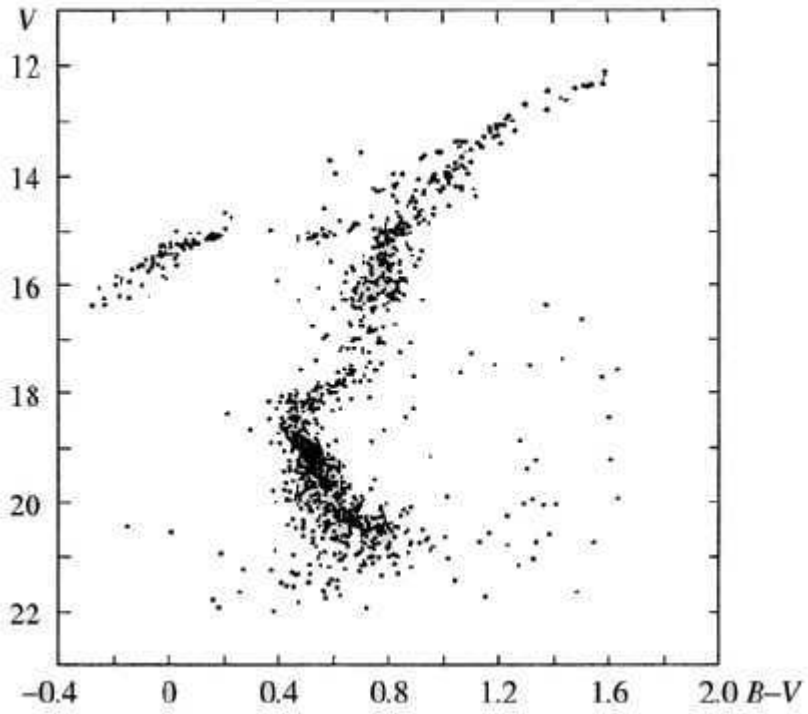

Figure 1.17: Colour-magnitude diagram of the M5 globular cluster. In addition to the main sequence, Giant Branch (the one bending to the right) and the Horizontal branch are also visible [Kartunnen et al., 1987]

The colour-magnitude diagram of a typical (M5) GC (figure 1.17) shows that the main sequence contains only faint red stars, then there is a prominent giant branch, and clear evidences of horizontal and asymptotic branches. Their overall linear size can be calculated in $0.3 \div 10$ pc, and they are surrounded by an envelope that is up to 100 times larger.

GC mass can be estimated from virial theorem, and is at about $10^4 - 10^6\,M_\odot$. In the Milky Way GC are concentrated towards its center and at the plane of the galaxy [Kartunnen et al., 1987]. The first group form a system that rotates along with the general rotation of the galaxy, while the second is spherically distributed in 35 kpc radius. This second group does not rotate as a system: each GC has its own velocity, distributed in every direction. Even elemental abundance is different: disk clusters

have at about 30% of solar value, while halo clusters have only 1% of the solar value (the smallest known value is 10^{-3}).

For all that has been said, it is clear how GC are important to understand the production of elements in the early universe and during Milky Way formation. All Globular Clusters are old, and the halo ones are among the oldest objects known. Their ages should be $13 \div 16 \times 10^9$ years, but a precise estimation is difficult [Kartunnen et al., 1987]. For GC that exhibit a negligible spread in [Fe/H], the various stars can be classified using their light element abundances, in particular considering [O/Fe] and [Na/Fe] ratio [Carretta et al., 2009] (figure 1.18):

- Primordial, first generation stars with compositions similar to metal-poor halo field stars (O-rich, Na-poor).
- Intermediate, second generation stars with lowered [O/Fe] and enhanced [Na/Fe].
- Extreme, like the previous, but with the lowered O and enhanced Na abundances.

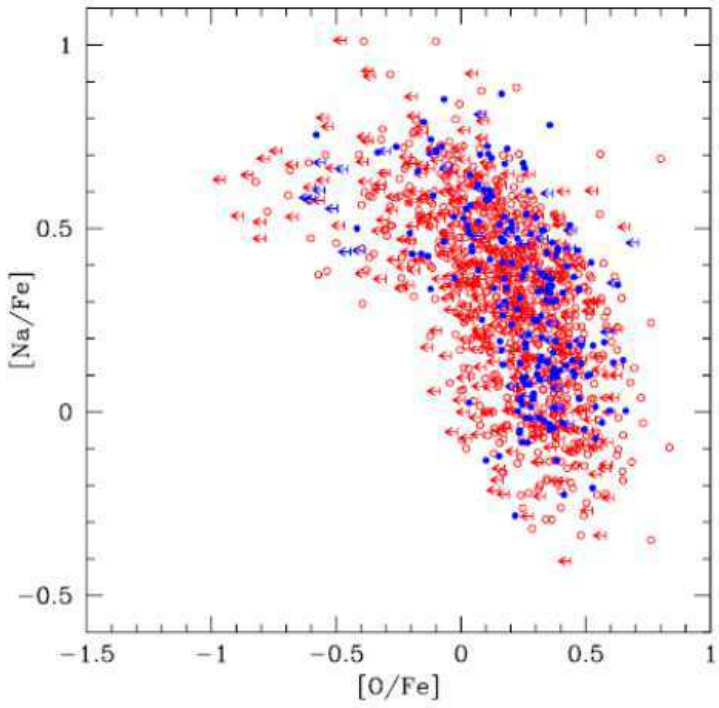

Figure 1.18: Na-O anticorrelation for of 1958 individual red giant stars. [Na/Fe] and [O/Fe] ratios from GIRAFFE spectra are shown as open (red) circles; abundance ratios obtained from UVES spectra are superimposed as filled (blue) circles and show no offset from the GIRAFFE sample. Arrows indicate upper limits in oxygen abundances [Carretta et al., 2009]

About these three, there are evidences [Carretta et al., 2009] that the intermediate population tends to dominate on the other two, with the "extreme" population that can be found only in a bunch of clusters.
The striking feature about ^{23}Na is its widely observable anti-correlation with oxygen. In GC in particular, it is an evidence that elements inside stars atmosphere has gone through a severe proton capture nucleosynthesis [Denisenkov and Denisenkova, 1990; Langer et al., 1993; Prantzos et al., 2007]. While [C/Fe], [N/Fe], and ^{12}C/^{13}C ratios in subgiant (SGB) and red giant branches (RGB) as a function of evolutionary state can be strictly linked to mixing processes [Denissenkov and VandenBerg, 2003], the same thing cannot be said for [Na/O]. Temperatures reached near the bottom of the convective envelope in evolved low-mass RGB stars are in fact too low to significantly alter the abundance of elements (there are possible exceptions to that, see D'Antona and Ventura [2007]).
In the past years, many works were published [Briley et al., 1996; Gratton et al., 2001; Ramírez and Cohen, 2002, 2003; Carretta et al., 2009; Briley et al., 2004a,b; Cohen and Meléndez, 2005; Bragaglia et al., 2010; D'Orazi et al., 2010; Dobrovolskas et al., 2014] that seem to support the idea that the composition differences between the various globular cluster populations are due to difference in the gas from which the GC was formed. About the source of ^{23}Na inside stars, there is still no agreement between scientists. In particular, four solutions seem to be the most promising:

- Intermediate-mass AGB-stars (4-9 $M_\odot$) [Cottrell and Da Costa, 1981; D'Antona et al., 1983; Ventura et al., 2001] or Super-AGB stars[24] [Pumo et al., 2008; Ventura and D'Antona, 2010, 2011];
- Supermassive Stars ($\approx 10^4$ $M_\odot$)[Denissenkov and Hartwick, 2014];
- Fast Rotating Massive Stars (FRMS) [Norris, 2004; Maeder and Meynet, 2006; Prantzos and Charbonnel, 2006; Decressin et al., 2007a,b];
- Massive Binaries [de Mink et al., 2009]

All of this stellar objects, at same point of their evolution, have the right parameters of temperature to efficiently host CNO-cycle, and also the so-called NeNa-cycle and

[24]Super Massive AGB Stars (SMAGBs) are objects with initial masses in the range between 9 $M_\odot$ and 11 $M_\odot$, that undergo off-center carbon ignition in partially degenerate conditions and end up their evolution as O-Ne white dwarfs [Ventura and D'Antona, 2010]

MgAl-cycle: for this reason they are considered to be a good place for ^{23}Na production. Which model is the right one is still matter of debate(see Renzini et al. [2015] and Charbonnel et al. [2013] and references therein), and every model has its flaws. If temperatures are higher than the typical CNO-burning temperatures ($\simeq 2\cdot 10^7$ K), additional cycles can come into play: the NeNa, MgAl, SiP and SCl cycles. We will focus on the first two, given that ^{23}Na looks to be the branching point between NeNa and MgAl cycles (figure 1.19). Both have the result to fuse hydrogen into

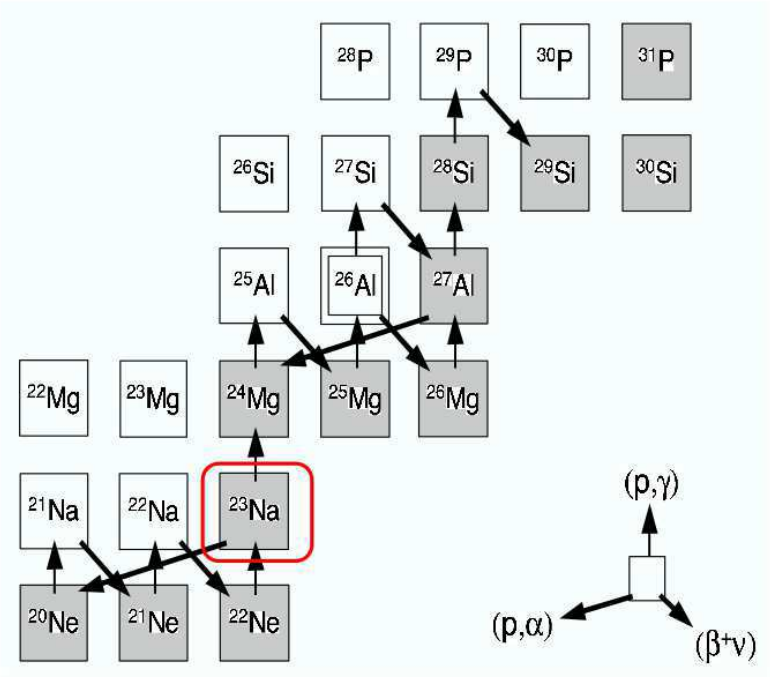

Figure 1.19: NeNa and MgAl cycles. Note that the ^{23}Na(p,α)/^{23}Na(p,γ) branching ratio is really important because it represents the branching point between the two cycles [Iliadis, 2007].

helium, and their importance in stellar energetic production is negligible. Their true relevance lays in the production of heavier elements between ^{20}Ne and ^{27}Al [Rolfs, 1988]. Nuclei in this mass range are mainly produced by β-decay, (p, γ) and (p, α) reactions. The relative importance of one of this three physical processes with respect to the others determines the temperature range at which the two cycles above are possible, and the nucleosynthesis path in the nuclide chart.

Reactions induced by protons involving unstable isotopes do not play an important role in that cycles, since the competing β-decays are much faster. The β-decay typical time range goes form seconds to minutes in most cases, but even long-lived nuclei like ^{22}Na ($T_{1/2}$=2.6 y) β-decay is faster than (p,γ) reaction at temperatures

proper of the non explosive H-Burning. These situation changes at T≥0.065 GK, with the ^{22}Na(p,γ)^{23}Mg reaction that dominates over the β-decay. This temperature is well above the one for non-explosive H-burning. For a mass number $20 \leq A \leq 40$, both (p,α) and (p,γ) channels are open, so those kind of reaction will compete. One of the two cycles in figure 1.19 can be active if the reaction rate branching ratio $B_{p\alpha/p\gamma}=N_A\langle\sigma v\rangle_{p\alpha}/N_A\langle\sigma v\rangle_{p\gamma}$ is large enough. H-burning in the mass range $A \geq 20$ is important to understand Ne, Na, Mg and Al abundances observed in stars: the relative isotopic abundance depends on the temperature and density conditions inside the H-burning region of a certain star. About NeNa-cycle, at temperature $T \sim 10^6$ K, ^{22}Ne is entirely transformed in ^{23}Na. An extra production of this element is predicted at temperatures higher than $3.5 \cdot 10^7$ K, reaching 60% at $T \sim 6 \cdot 10^7$ K. This extra production is provided by ^{20}Ne reaction. In the end ^{23}Na starts burning at $T \geq 6 \cdot 10^6$ K [Mowlavi, 1999]. From an experimental point of view, ^{23}Na detection has proven to be much easier than ^{19}F. Detectable spectral lines are in fact present in the visible spectrum, as the doublets at 5672-88 Å and 6154-60 Å. As an example, in figure 1.20 [Johnson et al., 2015] there is the reduced spectrum for an AGB-star belonging to the Globular Cluster 47-Tuc.

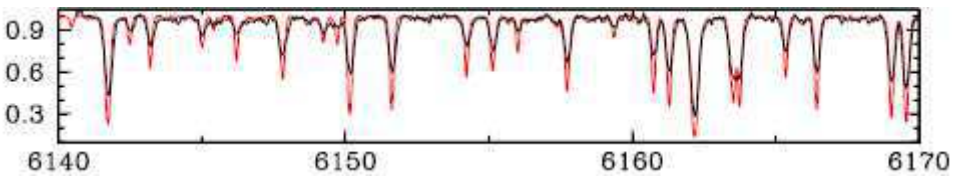

Figure 1.20: Sample spectrum of a 47 Tuc AGB star in the region of interest for Na I. The line at 6154-60 Å [Johnson et al., 2015] is visible

1.4.1 ^{23}Na in AGB and Super AGB Stars

Carbon and s-processes are considered to be the main verifiable examples of He-shell nucleosynthesis and TDU, but there are other elements produced during thermal pulses, like ^{19}F, ^{22}Ne and ^{23}Na. The last two are produced through a combination of helium and hydrogen burning. Fluorine nucleosynthesis is extremely complex, as can be seen in the previous paragraph. Furthermore neon looks to be enhanced in all the models including TDU, because it can be brought to the surface of a star due to the dredge up of freshly synthesized ^{22}Ne during thermal pulses via

the chain reaction [Mowlavi, 1999]:

$$^{14}N(\alpha,\gamma)^{18}F(\beta^{+}\nu)^{18}O(\alpha,\gamma)^{22}Ne \tag{1.9}$$

In 1.9 the way in which nucleosynthesis proceeds is the very same of what was already discussed in Section 1.3.1, with the only difference that the production of ^{22}Ne must take place in the first thermal pulses, because higher temperature are necessary [Wasserburg et al., 1995]. The abundance of ^{22}Ne in the intershell is fairly high ($\approx$2%), because ^{14}N is converted into ^{22}Ne during a thermal pulse [Karakas and Lattanzio, 2014].

If the ^{22}Ne abundance is higher or equal to the ^{20}Ne one, an enhancement in the elemental Ne composition is expected. The intershell is also enriched in ^{23}Na and ^{27}Al, that are not He-burning products but are synthesised in the H-shell during the previous interpulse [Karakas and Lattanzio, 2014]. Those elements are not burned by the subsequent TP and mixed into the envelope by the next TDU episode. In low-mass AGB-stars, sodium can be synthesized via proton captures during the ^{13}*C-Pocket* formation, and through neutron captures during both the radiative burning of the ^{13}*C-Pocket* and the convective ^{22}Ne-burning in the convective shells generated by TPs [Cristallo et al., 2009]. This leads to a notable ^{23}Na surface enhancement especially for low metallicities. In most massive stars, its synthesis is strongly affected by HBB [Ventura and D'Antona, 2006; Karakas and Lattanzio, 2014] through the ^{22}Ne(p,γ)^{23}Na reaction (Fig 1.21).

The sodium produced in this way will then enter the NeNa-cycle.

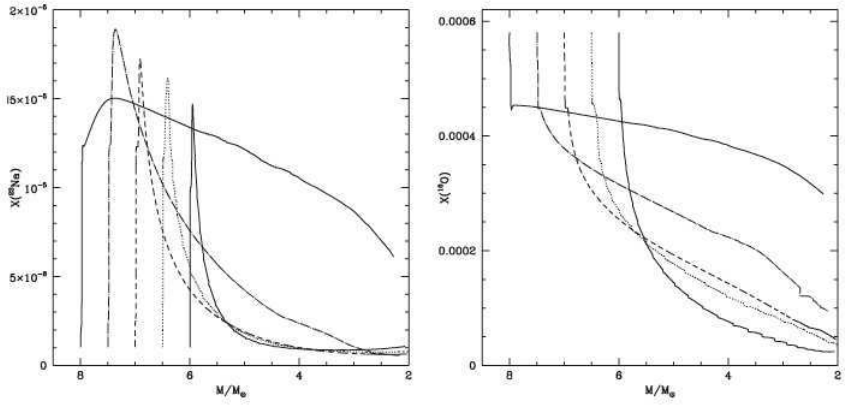

Figure 1.21: Left panel: variation during evolution of sodium abundance at the surface model with initial mass 6 $M_{\odot}$ (light solid line), 6.5 $M_{\odot}$ (dotted), 7 $M_{\odot}$(dashed) 7.5 $M_{\odot}$(dot-dashed) and 8 $M_{\odot}$ (solid).
Right panel: same thing but for oxygen surface mass fraction.[Ventura and D'Antona, 2011]

1.4.2 Supermassive Stars

To solve the [Na/O] anticorrelation, Supermassive stars (SMS) were supposed as a possible site of ^{23}Na production. A supermassive star is a stellar object with a mass more than fifty times the mass of the sun. It was proposed [Denissenkov and Hartwick, 2014] that the more massive stars inside a GC will sink to the center of the cluster and then merge, forming a SMS. Such a star is a fully convective object and has a luminosity that is close or exceeds the Eddington luminosity[25] with T_{eff}=10^5 K. In this condition Denissenkov and Hartwick [2014] postulated that these objects reach central temperature for CNO−, NeNa−, and MgAl−cycles already at the beginning of the main sequence. The star will continue to burn H until He abundance increases by $\Delta Y = 0.15$, which is approximately the largest difference in Y between Na-poor and Na-rich sub-populations of GC stars. After that, the SMS lose the greatest part of its mass as a result of various instabilities and stellar winds. The remaining parts of the SMS eventually collapse to directly form an intermediate mass black hole ($10^2 \div 10^6$ $M_\odot$) if $M_{SMS} \simeq 10^4$ $M_\odot$. This star can likely produce ^{23}Na through the 1.9 and enrich the GC of CNO and p-capture products with its wind. As shown in figure1.22 this model well reproduce experimental data.

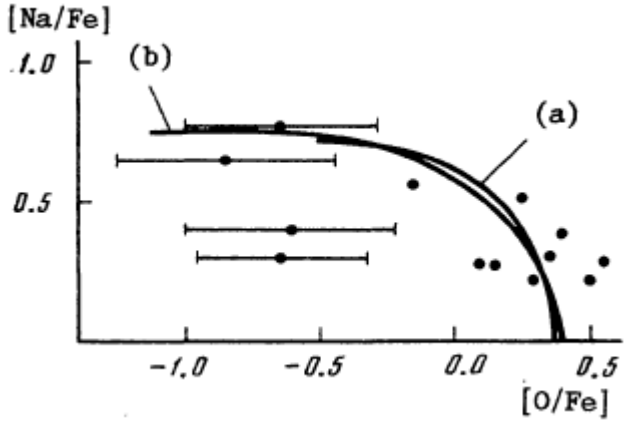

Figure 1.22: Comparison between theoretical [Na/Fe] and [O/Fe] whit observations (full circle) (See Denisenkov and Denisenkova [1990] and references therein)

[25] Eddington limit is the maximum luminosity that a star in hydrostatic equilibrium could reach. It can be calculated as L_{Edd}=$33000\frac{M}{M_\odot}L_\odot$. Once this limit is exceeded, the star will throw a lot of its mass into the interstellar medium through stellar wind, lowering its temperature in the process. Many massive stars with less luminosity than the Eddington limit have a strong wind by the way: in this case it is due to other phenomena. This condition is valid only for stable objects.

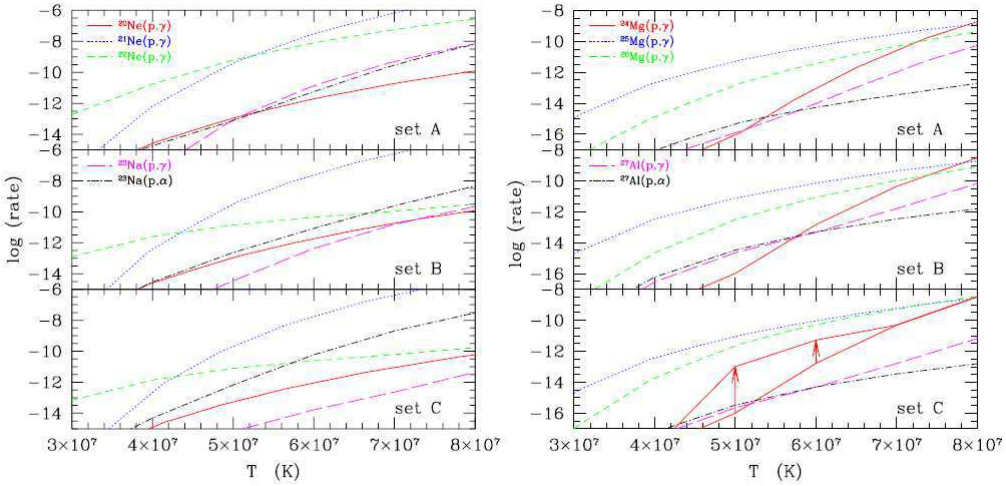

Figure 1.23: Nuclear reaction rate for NeNa (left) and MgAl (right) cycles for three sets of data. Arrows and upper full lines in the lower right panel indicate the increase of ^{24}Mg(p,γ)^{25}Al at 60·10^6 K [Decressin et al., 2007b]

1.4.3 Fast Rotating Massive Stars

Fast rotating Massive Stars are OB stars (≥20 $M_\odot$) characterized by fast rotation (≥100 km/sec) with broad spectral lines, due to rotation. For a star of 60 $M_\odot$, for example [Decressin et al., 2007b], central temperatures on the main sequence vary from $4.8 \cdot 10^7$ K to $7.5 \cdot 10^7$ K. In this condition CNO cycle can reach equilibrium at the beginning of the H-burning after a fast lowering in ^{12}C abundance in favour of a ^{14}N enhancement. ^{23}Na in main sequence shows a three step evolution: it rises rapidly, than there's a progressive increase, and then a rapid decrease (Fig1.23).
The first step is due to proton capture on ^{21}Ne and ^{22}Ne. The second is due to the competition between ^{20}Ne burning and (p,γ) and (p,α) reactions on ^{23}Na. This results in a slow increase of sodium because the first reaction is less efficient than the other two at T<50·10^6 K, while the situation reverses at higher temperatures. Following this model and using NACRE nominal reaction rates, O and Na are respectively depleted and produced, as required by the observations.

1.4.4 Binary objects

An interacting binary star is a type of binary star in which one or both components have filled or exceeded the Roche lobe[26]. When this happens, material will flow from a star towards the other; de Mink et al. [2009] proposed this system as

[26]The Roche lobe is the region around a star in a binary system within which orbiting material is gravitationally bound to the star [Kartunnen et al., 1987].

a source for the internal pollution of GC. Interacting Binaries, in fact, are able to provide large amounts of H-burning ashes into their surrounding. The ejecta of such stars show signatures of CNO processing [Grundstrom et al., 2007]. Evidence of severe mass-loss from interacting binaries comes from many sources, and appears to be a common phenomenon (see de Mink et al. [2007] and references therein), and theoretical considerations support the idea that most interacting binaries shed large amounts of mass.

To follow the nucleosynthesis up to the advanced stages of H-burning, a binary system with initial metallicity $Z = 5 \cdot 10^{-4}$ and masses of 20 and 15 $M_\odot$ for the two stars, with an orbital period of twelve days can be considered [de Mink et al., 2009]. After hydrogen exhaustion in the center, the primary star expands and starts to transfer mass to the companion, that at the beginning grows efficiently, absorbing both mass and angular momentum, spinning faster in the process. After absorbing 1.5 $M_\odot$, the star approaches critical rotation, and the majority of the mass is ejected into the interstellar medium. After transferring almost its entire envelope, the donor star becomes a Wolf-Rayet star, igniting helium. During He-burning, another $1M_\odot$ is transferred and accreted by the companion star. Shortly after this material is ejected by the rotationally enhanced wind. After the primary star ignites carbon, it fills its Roche lobe a third time and then explode as a SNe I.

A stellar system made in this way, according to model [de Mink et al., 2009], shows

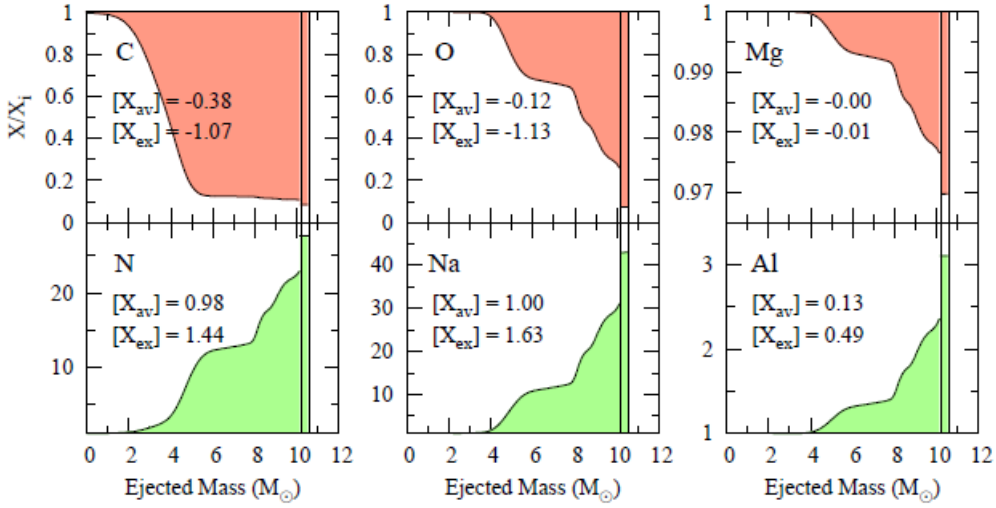

Figure 1.24: Composition of the slow ejecta of the binary system as a function of the ejected amount of mass. Each mass function X is given relative to initial mass X_i, except for Mg where ^{24}Mg, ^{25}Mg, ^{26}Mg are added. The average X_{av} and the most extreme mass-fraction X_{ex} are given in logarithmic scale. The solid vertical line separates between first and second mass fraction [de Mink et al., 2009].

the presence of 2 $M_\odot$ of relatively unprocessed material, that resembles the pristine composition except for a depletion of fragile elements (like lithium). The next 2 $M_\odot$ are processed by CN-cycle, and the next 4 $M_\odot$ show He enrichment and Na-O anticorrelation (figure1.24). After that, a sudden change in slope is visible for all elements except carbon. The layers of the donor star are now exposed, and show part of the convective zone above H-burning shell. Here temperatures are high enough to allow proton capture by ^{25}Mg and ^{26}Mg, leading to an enhancement of Aluminium.

1.5 Final considerations

Now that the overall theoretical framework for fluorine and sodium production has been exposed, some considerations can be made. About the first it is important to underline if the ^{19}F(α,p)^{22}Ne reaction is considered to be one of the responsible for the destruction of a substantial part of it. With the actual reaction rate reported in literature, fluorine abundance detected in AGB-stars is impossible. The only one corresponding to the theoretical predictions are WR stars ($M_i \gtrsim 25$ $M_\odot$ for Z=0.02, $M_i \gtrsim 35$ $M_\odot$ for Z=0.008, see Maeder and Meynet [1994]; Meynet and Arnould [2000]), in which some fluorine is produced in He-burning. A part of it, however, is expelled in the interstellar medium before being destroyed.

About sodium, a big part of the problem lies in the models, as said at the beginning of this paragraph. Sodium production sites are in fact still matter of debate, but it was suggested by D'Antona and Ventura [2016] that a reduction by a factor of five of the ^{23}Na(p, α)^{20}Ne reaction rate would "... put the rate of sodium destruction below the rate of oxygen destruction in the whole range of interest for the AGB envelope p−capture processing. This would allow to reduce the mass loss rates in the models, and achieve a good quantitative agreement also in the magnesium depletion" (figure 1.25). In this way the study of ^{23}Na-related reactions would be of much help to solve the puzzle, even only reducing uncertainties. It is also important to fully understand the ^{23}Na(p,α)^{20}Ne versus ^{23}Na(p,γ)^{24}Mg branching ratio, that will be of much help to fully understand the transition from the NeNa-cycle to MgAl-cycle.

In the following chapters, after some other theoretical considerations necessary to better understand the "nuclear" part of the problem, two experiments about the ^{19}F(α,p)^{22}Ne and ^{23}Na(p,α)^{20}Ne reactions will be explained and results on the experimental cross-section at astrophysical energies and reaction rate will be shown.

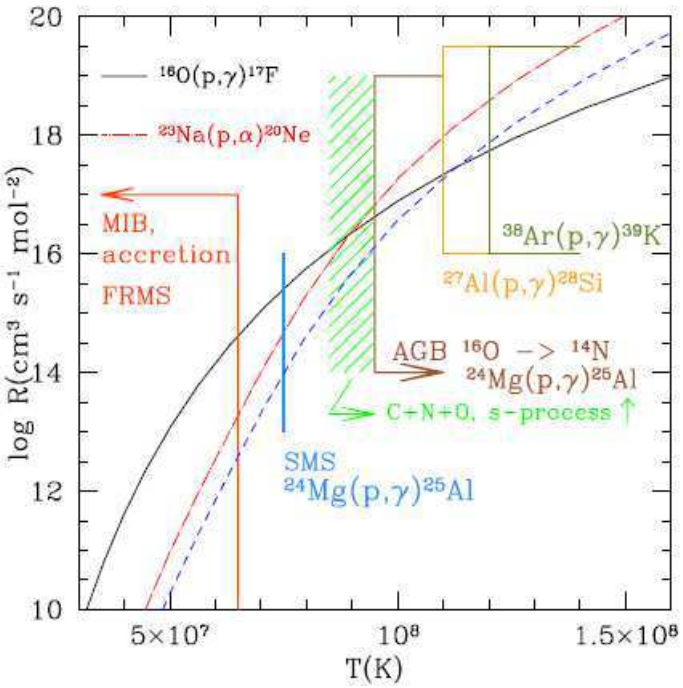

Figure 1.25: Rates of the two reaction that mainly influence Na-O correlation in AGB stars as a function of temperature. Rates for oxygen burning via proton capture are from Angulo et al. [1999], while for sodium burning a value ~25% below the rate recommended by Hale et al. [2004](red line). The blue dashed line correspond to a further reduction by a factor of five. Temperature boundaries for the different scenarios are also marked. Temperatures at which the reaction work efficiently are also reported. The green dashed temperature range is the temperature in AGB models with longer evolutionary time, in which total content of C+N+O and s-process abundances increase due to the third dredge-up [Ventura and D'Antona, 2006] (figure and caption taken from D'Antona and Ventura [2016]).

In both cases those represent the first experimental results on those reactions at such energies, as it will be discussed in Chapter III.

CHAPTER 2

Direct measurements in nuclear astrophysics

Energy production inside stars is mainly caused by nuclear reactions [Kippenhahn and Weigert, 1990]. To understand how and in how much time energy can be produced, it is therefore necessary to introduce some definitions and concepts proper of nuclear physics, starting from the so-called *cross-section*.
At energy of astrophysical interest, particle motion is caused by thermal agitation, corresponding to temperatures of $k_bT \approx 10^7 \div 10^8$ K. At those temperature, the particles have energies that are lower than the Coulomb barrier. In this condition measurements are technically really hard (if not virtually impossible), because the cross-section are very low (some pico-nanobarns).
In the following chapter we will discuss general arguments regarding nuclear physics, paying close attention to nuclear astrophysics, underlining experimental difficulties concerning such measurements.

2.1 Cross-section

In a standard nuclear physics experiment, two particles collide with each other, and a reaction like the following is obtained:

$$A + a \rightarrow b + B \tag{2.1}$$

Here a and A are the impinging and the target particle, while b and B represent the reaction products, respectively. Now let us call J_{inc} the number of particles that

hit the target per unit of time on a unit of surface perpendicular to the beam. We call ρ_{inc} the number of impinging particles per unit of volume, and v the relative velocity between a and A. The flux of incoming particles will therefore be expressed as it follows

$$J_{inc} = \rho_{inc} v \tag{2.2}$$

Let us now suppose that ρ_{inc} is so small that mutual interactions between the particles composing the beam can be considered negligible, and be N the number of particles emitted per unit of time inside a certain interval of solid angle $d\Omega$, proper of a certain detector placed an angle θ from the beam direction. In this situation N can be defined as

$$N = J_{inc} \Sigma(\theta) d\Omega \tag{2.3}$$

$\Sigma(\theta)$ is a physical quantity that has the dimensions of a surface, and represents the probability for a particle of the beam that collides with a particle of the target to be emitted at a certain solid angle $d\Omega$ [Williams, 1991].
Since the target is usually composed by an high number of particles (quantity comparable with the Avogadro number N_A) and the relative distances between them are bigger than the De Broglie wavelength, considering negligible the coherence effects for waves coming from diffusers, $\Sigma(\theta)$ will be equal to

$$\Sigma(\theta) = N\sigma(\theta) \tag{2.4}$$

In equation 2.4 $\sigma(\theta)$ is called *differential cross-section*, and represents the probability for a certain particle to be emitted inside a certain solid angle $d\Omega$, after the reaction 2.1 took place.
The quantity $\sigma(\theta)$ can be calculated using equations 2.3 and 2.4:

$$\sigma(\theta) = \frac{N}{J_{inc} N d\Omega} \tag{2.5}$$

We can now integrate equation 2.5 on the whole solid angle, obtaining the total cross-section for the process:

$$\sigma_{tot} = \int_{\Omega} \sigma(\theta) d\Omega \tag{2.6}$$

Here $\Sigma(\theta)$, $\sigma(\theta)$ and σ_{tot} have the dimensions of a surface, and given that the diffusers are $10^{-13} \div 10^{-14}$ cm wide, those quantities will be expressed in *barns*, so that 1 barn=10^{-24} cm^2

2.2 Reaction rate

Another important quantity in nuclear physics is the *reaction rate*, which represents the number of reactions that take place in the unit of volume and time. It indicates also the number of nuclei created or destroyed by a certain reaction. This quantity depends on the number of involved nuclei (N_a and N_A), on the cross-section σ and on other boundary conditions (like temperature, for instance).
Let us consider a system made by a certain number N_a of a-nuclei and N_A particles of A-nuclei, being $\sigma(v)$ the cross section for the reaction equation 2.1. In this case v is the relative velocity between the two particles. The reaction rate r is defined as the number of reactions per unit of time and volume, and can be calculated as the product of the cross-section times the density of the target particles N_A and the flux of the incoming particles equation 2.2, if ρ is substituted with N_a

$$r = N_a N_A v\sigma(v) \tag{2.7}$$

This quantity can be measured as number of particles per second.
It is important to underline that this equation is valid only if a and A are not identical: in this case another term must be added, due to indiscernible nature of these two particles. So the equation 2.7 will be:

$$r = (1 + \delta_{aA})^{-1} N_a N_A v\sigma(v) \tag{2.8}$$

with δ_{aA} known as Kronecker's delta.
Let us now assume that the relative velocity is included between v and $v + dv$, and that $f(v)dv$ is the probability for the velocity to take a certain value in that range. In this case the reaction rate will be obtained by an integration of the equation 2.8, where at each velocity is assigned a certain weight $f(v)$:

$$r = (1 + \delta_{aA})^{-1} N_a N_A \int v\sigma(v) f(v) dv = (1 + \delta_{aA})^{-1} N_a N_A \langle \sigma v \rangle \tag{2.9}$$

The $\langle \sigma v \rangle$ term is the reaction rate for a pair of particles, while the $(1+\delta_{aA})^{-1} N_a N_A$ is the total number of them.

It is now mandatory to know the energy at which particles inside stars interact with each other: this is indeed possible, considering that the kinetic energy of the nuclei inside a star is mainly due to the thermal agitation. Stellar plasma, in fact, due to the high temperature and low densities, may be considered in fair approximation as a non degenerate and non relativistic gas. So the most probable energy can be calculated as

$$E \approx kT \tag{2.10}$$

with k Boltzmann constant. Such a plasma can be considered as a gas at thermodynamic equilibrium, so the velocity distribution can be expressed as a Maxwell-Boltzmann one, again considering the plasma as a non degenerate gas with almost no electromagnetic interaction between particles:

$$f(v_i)dv_i = 4\pi v_i^2 \left[\frac{m_i}{2\pi kT}\right]^{3/2} exp\left[-\frac{m_i v_i^2}{2kT}\right] dv_i \tag{2.11}$$

In equation 2.11 T is the temperature, while m_i is the i-nucleus mass.
Assuming that equation 2.9 depends only on relative velocity between particles, it is convenient to express velocities of the many particles as a function of the relative and center-of-mass ones ($\mathbf{v}$ and $\mathbf{V}$, respectively)

$$v_a = \mathbf{V} + \frac{m_A}{m_a + m_A}\mathbf{v} \tag{2.12}$$

$$v_A = \mathbf{V} - \frac{m_A}{m_a + m_A}\mathbf{v} \tag{2.13}$$

Let us now introduce the probability for the a-particle to have velocity $\mathbf{v}_a$ in a certain element of volume of the velocity-space d^3v_a and for the A-particle to have velocity $\mathbf{v}_A$ in d^3v_A. This quantity will be calculated as $f(\mathbf{v_a})d^3v_a f(\mathbf{v_A})d^3v_A$, and it is possible to demonstrate that it can be written as a product between the velocity distributions in the center-of-mass reference frame and relative velocity, respectively $exp\left[-\frac{M\mathbf{V}}{2kT}\right]$ and $exp\left[-\frac{M\mathbf{v}}{2kT}\right]$:

$$N_a N_A \left[\frac{M}{2\pi kT}\right]^{3/2} exp\left[-\frac{M\mathbf{V}^2}{2kT}\right]\left[\frac{\mu}{2\pi kT}\right]^{3/2} exp\left[-\frac{\mu\mathbf{v}^2}{2kT}\right] \tag{2.14}$$

where μ e M are the reduced mass and the total mass respectively. Those distributions are however normalized, and the integral with respect to d^3V will be equal to one. So the reaction rate will be

$$\begin{aligned} r &= (1+\delta_{aA})^{-1} N_a N_A \langle\sigma v\rangle \\ &= (1+\delta_{aA})^{-1} N_a N_A 4\pi \left(\frac{\mu}{2\pi kT}\right) \int_0^\infty v^3 \sigma(v) exp\left(-\frac{\mu v^2}{2kT}\right) dv \end{aligned} \tag{2.15}$$

Or, in terms of energy

$$r = (1 + \delta_{aA})^{-1} N_a N_A \left(\frac{8}{\pi\mu}\right)^{1/2} \frac{1}{(kT)^{3/2}} \int_0^\infty E\sigma(E)\, exp\left(-\frac{E}{kT}\right) dE \tag{2.16}$$

About the latter, it is necessary to underline that the integration is extended only on the positive region if the reaction is exothermic. For the endothermic ones, the integration path will start from the threshold energy [Iliadis, 2007].

2.3 Coulomb barrier effects between charged particles

Analysing interactions between nuclei, two things have to be taken into account: centrifugal barrier and Coulomb interaction. The second, in particular, is due to the repulsion between projectile and target. If we consider two nuclei, with atomic number Z_1 e Z_2 interacting with each other, the forces involved will be the Coulomb repulsion and the nuclear force (attractive). Their combination will lead to a potential that goes as in Fig. 2.1.

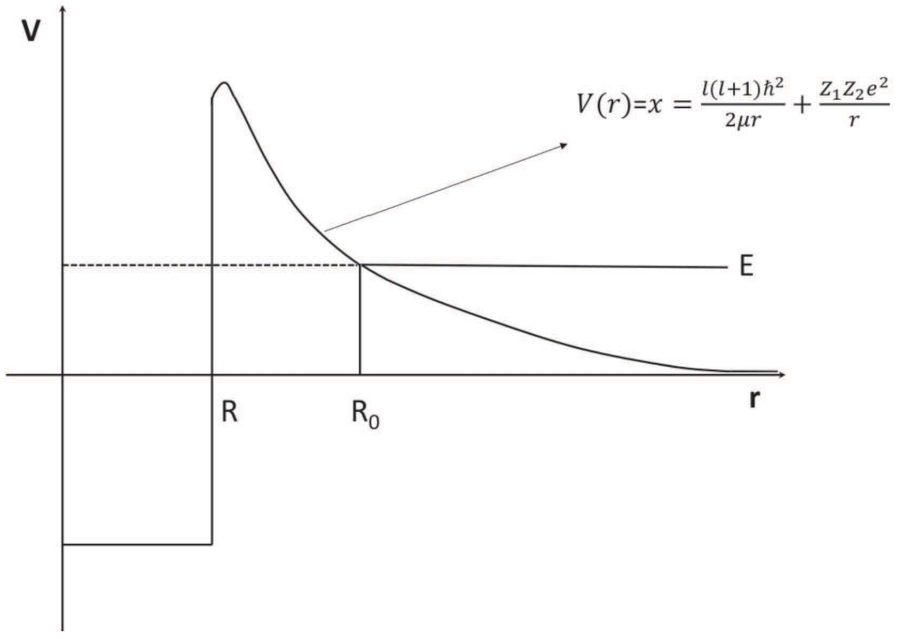

Figure 2.1: Sketch of the complete potential (Coulomb + nuclear) that rules the relative motion of two nuclei

Reaction	E_c
p + p	0.45 MeV
p + ^{7}Li	0.93 MeV
α + ^{12}C	2.78 MeV
α + ^{19}F	3.81 MeV
p + ^{23}Na	2.57 MeV

Table 2.1: Values of the Coulomb barrier (E_c) for a sample of nuclear reaction of interest for nuclear astrophysics and for the two reactions in exam

At big distances Coulomb force will prevail, while going at distances lower than the sum of the two nuclear radii, the lead will be taken by the nuclear force, that can be approximated to a finite potential well with R width and V_0 depth.
In nuclear astrophysics energies are at the order of magnitude of some keV (proper of stellar nucleosynthesis) up to hundreds of keV (primordial nucleosynthesis) (estimations made using equation 2.10). Given that Coulomb barriers are at about $1 \div 10$ MeV (e.g. table 2.1), with a classical approach this reaction should not take place, because the interacting nuclei would not be near enough to trigger the nuclear interaction. This problem is overcome by the so-called *tunnel effect*[1].
The probability for a nucleus to overcome the Coulomb barrier by tunnel effect can be expressed as a penetration factor

$$P_l = \frac{|\chi_l(\infty)|^2}{|\chi_l(R)|^2} \tag{2.17}$$

where χ_l is the wave radial function that solves the Schrödinger equation

$$\left[-\frac{\hbar^2}{2\mu}\frac{d^2}{dr^2} + V_l(r) - E \right]\chi_l(r) = 0 \tag{2.18}$$

and

$$V_l = \frac{l(l+1)}{2\mu r^2} + \frac{Z_1 Z_2}{r^2} \tag{2.19}$$

is the effective potential for the l-wave, sum of the centrifugal potential (that depends on l) and the Coulomb one (independent form it).
Solutions of the equation 2.18 are known and can be expressed as the so-called Coulomb regular and irregular wave functions. The first one, $G_l(r)$, diverges if $l \to 0$ while the second, F_l, is equal to zero at the origin, being the only possible solution if it is included. In our case ($0 \leq r \leq R$), $\chi_l(r)$ can be written as a linear combination

[1] Quantic tunnelling was introduced by George Gamow in 1928, and was proposed while studying α-decay. Following quantum mechanic a finite probability for the incoming particle to tunnel through the barrier exists

of the two, so the penetration factor equation 2.17 will be

$$P_l(kR) = \frac{1}{F_l^2(kR) + G_l^2(kR)} \tag{2.20}$$

where k is the wave number.

By the way, P_l has no analytic form. It is therefore necessary to use known values of $F_l(kR)$ and $G_l(kR)$, or, if $V_l(r)$ is a lot bigger than the impinging energy, to an approximation of P_l based on expansion of $G_l(r)$ as a function of the modified Bessel equations (Semi-classical approximation, or WKB) [Rolfs, 1988]. In this case, if $V >> E$, then $G_l >> F_l$, and so

$$P_l = \left[\frac{E_b - E}{E}\right]^{1/2} exp\left[- \frac{2\sqrt{2\mu}}{\hbar} \int_R^{R_0} \left(\frac{E_c R}{R} \frac{E_l R^2}{R} - E \right) dr \right] \tag{2.21}$$

In this equation E_b is the sum of the Coulomb (E_c) and centrifugal (E_l) barriers heights.

Let us define $-W_l$ the terms in the exponential function in equation 2.21, and try to understand its trend when l changes.

1. $l = 0$: the most common case in nuclear astrophysics, due to the fact that energies are of a few keV. In this case integrating and using power expansion as a function of $\frac{E}{E_c}$, the W_l term will be equal to:

$$W_0 = \frac{2\pi Z_1 Z_2 e^2}{\hbar v} \left[1 - \frac{4}{\pi}\left(\frac{E}{E_c}\right) + \frac{2}{3\pi}\left(\frac{E}{E_c}\right)^{3/2} \right] \tag{2.22}$$

   The first term of equation 2.22 can be written as

$$bE^{-\frac{1}{2}} \tag{2.23}$$

   in which

$$b = 31.28 \cdot Z_1 Z_2 A^{1/2} \tag{2.24}$$

   while the second term is equal to

$$-1.05(ARZ_1Z_2)^{1/2} \tag{2.25}$$

   with A reduced mass of the system, E_c calculated in MeV and R in fm. The third term, which depends on the energy, represents a corrective term in the case of E at the same order of magnitude of the Coulomb barrier, calculated by:

$$\frac{4Z_1 Z_2 e^2}{3\hbar v}\left(\frac{E}{E_c}\right)^{3/2} \tag{2.26}$$

adding up equations 2.23, 2.25, and 2.26, we will obtain:

$$W_0 = bE^{-\frac{1}{2}} - 1.05(ARZ_1Z_2)^{1/2} + \frac{4Z_1Z_2e^2}{3\hbar v}\left(\frac{E}{E_c}\right)^{3/2} \tag{2.27}$$

2. $l \neq 0$: In the hypothesis that $E_c > E_l$, W_l can be obtained using power expansion as a function of R/r:

$$W_l = W_0 + 2\left[\frac{l(l+1)E_1}{E_c}\right]^{1/2}\left[1-\left(\frac{E}{E_c}\right)^{1/2}\right] \tag{2.28}$$

From equation 2.22 and 2.28, stopping the expansion at the first order, P_l will be equal to

$$P_l = \left(\frac{E_c}{E}\right)^{1/2} exp\left[-bE^{-1/2} + 1.05(AZ_1Z_2)^{-1/2} - 7.62l(l+1)(AZ_1Z_2)^{-1/2}\right] \tag{2.29}$$

If $E << E_c$ and the interaction takes place in s-wave, penetrability can be approximated with the *Gamow factor*

$$P_0 = exp\left[-bE^{-1/2}\right] = exp\left[-\frac{2\pi Z_1Z_2e^2}{\hbar v}\right] = exp\left(-2\pi\eta\right) \tag{2.30}$$

in which $\eta = Z_1Z_2\alpha\beta$, where α is the structure constant and β is the velocity in units of c (the speed of light). The η factor, called *Sommerfeld parameter*, gives a measurement of Coulomb interaction, assuming values that grow with the charge of the interacting nuclei, and decrease at higher relative velocities (corresponding to lower interaction times) [Rolfs, 1988].

2.4 Astrophysical factor

As anticipated in previous paragraphs, the experimental study of nuclear reactions in astrophysical conditions is really hard, due to the small reaction rates and to the low energies: the p + p $\rightarrow$ d + e^+ + ν_e reaction, which as shown in table 2.1 has the smallest Coulomb barrier and occurs in the Sun at T $\approx 1.5 \cdot 10^7$ K, has a really low cross-section (mainly due to the fact that energy is not sufficient to overcome the Coulomb barrier and that the cross-section is governed by weak interaction), $\sigma = 10^{-47}$ cm^2 = 10^{-23} b (Q = 1.44 MeV). It is therefore clear that an experiment meant to reproduce this reaction in solar environment with direct methods would obtain an event every 1000000000 years! This is just one of the many cases in which experiments aimed to reproduce reaction of astrophysical interest are impossible. The study of such reaction in fact, is normally possible at higher energies,

and some kind of extrapolation near or below the Coulomb barrier based on measurements at higher energies is necessary. In this procedure, even a trivial error in sub-threshold estimation could be catastrophic. It is therefore necessary to optimize the system and the experimental set-up for low-energies measurements in a way that maximizes the signal-to-noise[2] ratio, that represents a limit for those measurements. Such a measure is then almost impossible with direct methods.
From equation 2.5 is clear that the number of detected particles N is proportional to the number of incoming particles N_{inc}, in portion of width equal to δ of the target and at the solid angle subtended by the detectors:

$$N \propto N_{inc}\delta\Delta\Omega \tag{2.31}$$

From equation2.31 it is clear that three independent parameters can be changed, even if the increasing rate will bring forth other issues that lower data accuracy:

- Increasing beam intensity a spatial charge will be generated and the target will heat up, modifying its structure (density and chemical composition variations) or destroying it
- Increasing the density of the target will lead to an enhancement of the interaction between particles, but straggling and energy loss will reduce resolution.
- Increasing the solid angle range (for example using wide detector placed near the target), can be useful, but this operation have some limits regarding the beam direction and the high count rates.

Another way to enhance the signal-to-noise ratio is to reduce the background coming from cosmic rays, environmental radioactivity or from electric devices: in the first case, material able to absorb neutrons or γ can be used, or the measurements can be done in underground laboratories (like in Laboratori Nazionali del Gran Sasso[3]).
Regarding extrapolation, the cross-section is strongly related with the geometrical factor $\pi\lambda\!\!\!^{-2} \propto\left(\frac{1}{P_l}\right)^2 \propto \frac{1}{E}$, where $\lambda\!\!\!^{-}$ is the De Broglie reduced wavelength and P_l is the penetrability factor. Those are both strongly varying with energy. To overcome those difficulty one can adopt a representation for the interaction probability at high energies that allows to separate the purely nuclear effects and the geometrical and

[2]The signal is made by the particles incoming in the detectors from the reaction of interest, while noise comes from background or from other competing reactions
[3]LUNA experiment [Broggini et al., 2010]

electromagnetic ones: for such a reason the so-called Astrophysical Factor, or S(E), was introduced:

$$S(E) = E\sigma(E)\, exp\,(2\pi\eta) \tag{2.32}$$

This quantity represents the nuclear component of the probability for a certain reaction to occur and, if there are no resonances in the extrapolation region, it allows to obtain more accurate low-energies extrapolation. Trends of $\sigma(E)$ and S(E), for non-resonant reactions, are shown in Fig. 2.2. From it is possible to understand that the second one is almost a constant, while the first has an exponential decreasing.

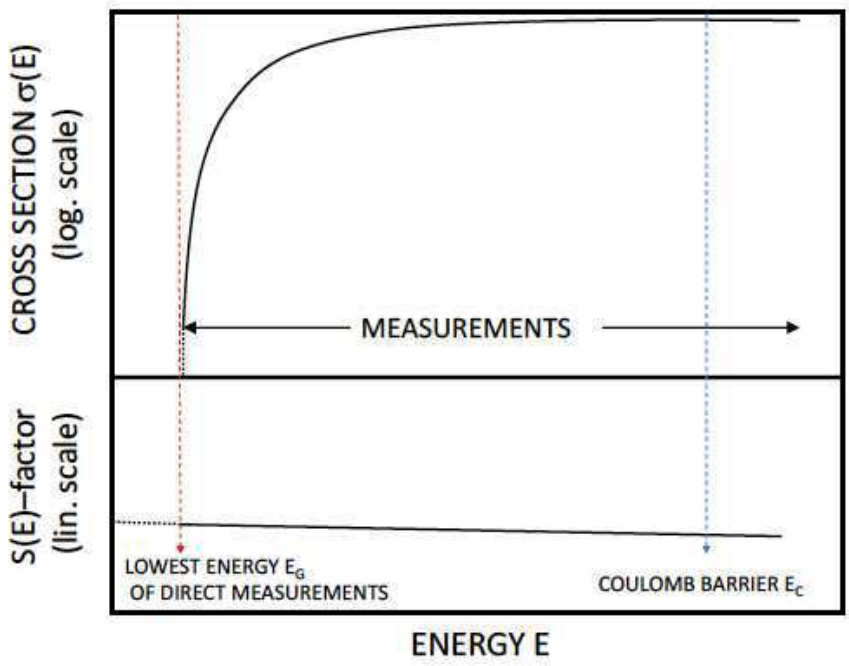

Figure 2.2: Comparison between cross-section and astrophysical factor, both as a function of energy and for charged particle reactions without resonances.

This procedure allows to make extrapolations at low energies, normally by means of polynomial fit. A more complex method is the so-called *R-Matrix* [Lane and Thomas, 1958], that will be used later in this work, in particular regarding the ^{19}F(α,p)^{22}Ne reaction (see Chapter 5.5).

2.5 Charged Particle Reactions

Substituting equation 2.32 in equation 2.16, and taking into account equation 2.30 and dividing by $N_a N_A (1 + \delta_{aA})^{-1}$, one can obtain the reaction rate for a couple

of interacting particles

$$\langle \sigma v \rangle = \left(\frac{8}{\mu\pi}\right)^{1/2} \frac{1}{(kT)^{3/2}} \int_0^\infty S(E) exp\left(-\frac{E}{kT} - bE^{-1/2}\right) dE \qquad (2.33)$$

The argument of the integral in equation 2.33 is essentially dependent on the exponential part, that is a function of energy. Furthermore, as it can be seen in figure 2.3, the term $exp(-E/kT)$ shows a decreasing trend as a function of energy, while the tunnel probability increases. The biggest contribution to the integral is then coming from intermediate energies.

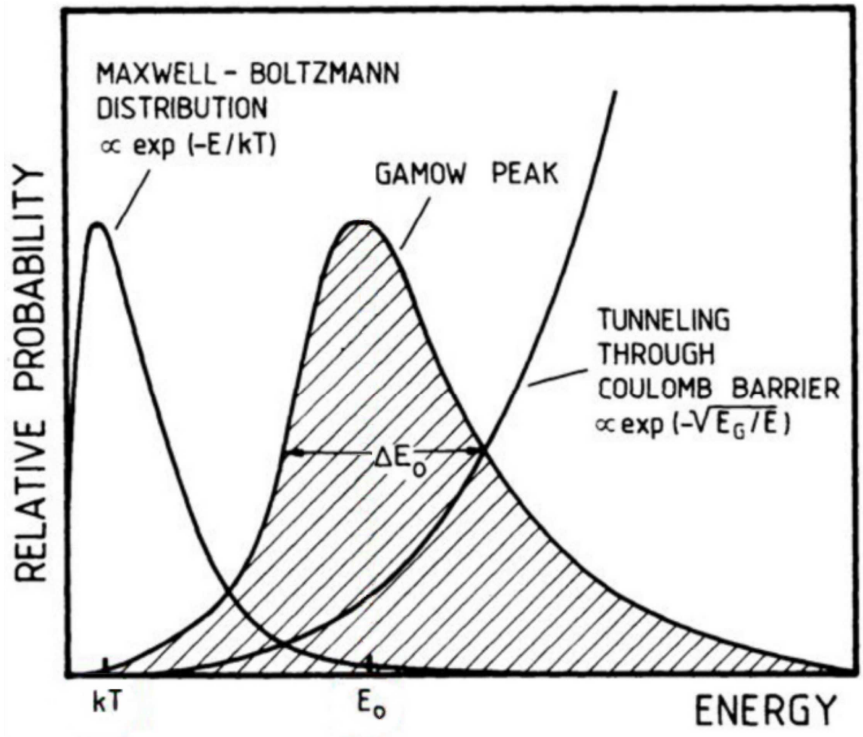

Figure 2.3: Representation of the exponential terms that determine the trend of the reaction rate for resonant processes. The product of those two (Gamow factor an Maxwellian tail) originates the so-called Gamow peak (strongly magnified in picture). It indicates the energy range at which the probability for a reaction to occur is maximized. The E_G factor in figure is called Gamow energy, and in the adopted notation for this work corresponds to b^2 [Clayton, 1983].

For non-resonant reactions in stellar environment, the energetic range in which they take place is so narrow that the astrophysical factor can be accounted as constant (figure 2.2). This region is called “Gamow window”.

It is clear that a good approximation of equation 2.33, again in the case of non-resonant reactions, can be made considering S(E) as a constant, with the value that it would have at E_0, at which the exponential shows its peak. Than $S(E) \approx S(E_0) \approx$

S_0, and so

$$\langle \sigma v \rangle = \left(\frac{8}{\pi\mu}\right)^{1/2} \frac{S_0}{(kT)^{3/2}} \int_0^\infty exp\left(-\frac{E}{kT} - bE^{-1/2}\right) dE \tag{2.34}$$

This result can be further evaluated by approximating the function inside the integral to a Gaussian function with E_0 as its centroid and the same slope of the original function. Considering now the minimum for the $g(E) = E/kT + bE^{-1/2}$ function, and after Taylor expansion around E_0, we will obtain:

$$g(E) = g(E_0) + \frac{1}{2}(E - E_0)^2 g''(E_0) + ... \tag{2.35}$$

From equation 2.35 it is possible to acquire the energy corresponding to the Gamow peak:

$$E_0 = \left(\frac{bkT}{2}\right)^{2/3} = 1.220\,(Z_a^2 Z_A^2 \mu T_6^2)^{1/3}\ \text{keV} \tag{2.36}$$

where $T_6 = T/10^6$ K, and μ is the reduced mass for the two-body process. At E_0 the probability for a certain nuclear reaction to occur is strongly enhanced, given a certain temperature T. From equation 2.36, and considering the case for a couple of light particles ($Z < 6$) at temperature of tenth of millions degree, values of $E_0 \approx 1 \div 30$ keV can be obtained. Those values are clearly bigger than $kT = 0.086T_6$ keV: this fact makes us understand how Coulomb barrier penetrability trend enhances the probability for reactions at the high-energy tail of the Maxwell-Boltzmann function. By substitution of g(E) with equation 2.35, and taking into account equation 2.36, it is possible to obtain:

$$exp\left(-\frac{E}{kT} - bE^{-1/2}\right) \approx C\, exp\left[-\frac{(E - E_0)^2}{2\Delta^2}\right] \tag{2.37}$$

where

$$C = exp\left(-\frac{E}{kT} - bE_0^{-1/2}\right) = exp\left(-\frac{3E_0}{kT}\right) \tag{2.38}$$

The equation equation 2.37 is, in the end, simply an approximation to a Gaussian function of the original exponential one, with Δ as the full-width of the Gaussian function that can be determined from the second derivative of $g(E)$.

$$\Delta = 2.31(E_0 kT)^{1/2} = 0.75(Z_a^2 Z_A^2 \mu T_6^5)^{1/6}\ \text{keV} \tag{2.39}$$

From equation 2.39 is clear that the Gamow window width is related to the average of the peak energy E_0 and the maximum value for the Maxwell-Boltzmann distribution.

$$\Delta E_G = E_0 \pm \frac{\Delta}{2} \tag{2.40}$$

By substituting what found so far in the expression of the reaction rate for a couple of particles, we will obtain:

$$\langle \sigma v \rangle = \left(\frac{8}{\mu\pi}\right)^{1/2} \frac{S_0}{(kT)^{3/2}} e^{-\tau} \int_{-\infty}^{\infty} exp\left[-\frac{(E-E_0)^2}{2\Delta^2} \right] dE \tag{2.41}$$

Where $\tau = 3E_0/kT$. Resolving the integral:

$$\begin{aligned} r_a A &= (1+\delta_a A)^{-1} N_a N_A \langle \sigma v \rangle \\ &= (1+\delta_a A)^{-1} N_a N_A \frac{7.20 \cdot 10^{-19}}{A Z_a Z_A} S_0 \,(\text{keV b})\, \tau^2 e^{-\tau} \,\text{cm}^3/\text{sec} \end{aligned} \tag{2.42}$$

In this last equation the dependence from the temperature is contained in the term τ. From equation 2.42 it is clear that the reaction rate will depend mainly on $e^{-\tau}$.

Reactions	$e^{-\tau}$
p + p	$1.1 \cdot 10^{-6}$
p + ^{14}N	$1.8 \cdot 10^{-27}$
^{4}He + ^{12}C	$3.0 \cdot 10^{-57}$
p + ^{23}Na	$1.6 \cdot 10^{-105}$
α + ^{19}F	$9.1 \cdot 10^{-138}$
^{16}O + ^{16}O	$6.2 \cdot 10^{-239}$

Table 2.2: Values of $e^{-\tau}$ for some important reactions of astrophysical interest at T = $15 \cdot 10^6$ K. This factor determines the trend of the reaction rate

In table 2.2 some values of this factor are reported as examples. All those reactions (apart from ^{16}O+^{16}O) take place inside the solar core ($T_6 = 15$). At this temperature the p + p reaction has been shown to be the most efficient. It will contribute strongly to energy production inside the Sun.
At a certain value of temperature, only some nuclear species will experience nuclear fusion. The core will start to contract, rising its temperature, unless it will be high enough to trigger new reactions.

2.6 Resonant reactions induced by charged particles

In the case of resonant reactions between two nuclei, an excited state of the compound nucleus is formed. This process occurs when the energy of the entrance channel matches the energy of a certain excited state in the compound nucleus. This compound nucleus will subsequently decay to lower-lying states.
If resonances are taking place inside the energy region of interest, the astrophysical

factor S(E) is no more slowly varying with energy, and cannot be considered as a constant value. In this case the reaction rate is dominated by such resonances.
Resonant reactions are those in which the temporary formation of an exited state of a compound nucleus occurs between the entrance and the exit channel [Satchler, 1990]. In this case, an intermediate state composed by fusing projectile and target will form:

$$a + A \longrightarrow C^* \longrightarrow b + B \tag{2.43}$$

In 2.43 C^* represents the intermediate system. Populating this state, resonances will affect the excitation function for the reaction of interest.
Let us suppose that a nucleus can be formed in an excited state during the collision between projectile and target particles. This new-born nucleus will be left in an excited state, and than will decay emitting γ radiation. The energy at which this state is formed is called "resonance". A resonance is called narrow when its width (Γ) is a lot smaller that the peak energy (E_r). This condition usually corresponds to $\frac{\Gamma}{E_r} \leq 10\%$. If it does not happen, the resonance is called broad.

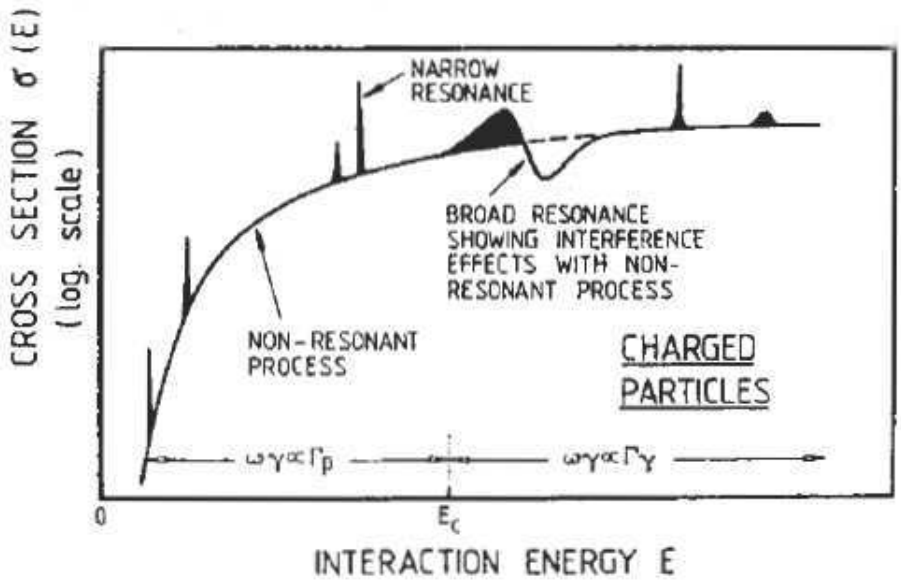

Figure 2.4: Examples of narrow, broad and isolated resonances [Rolfs, 1988].

In case of a isolated resonance, where the energy gap between different levels is bigger than the width of the states, the cross-section can be calculated using the Breit-Wigner formula:

$$\sigma_{BW}(E) = \pi\lambda\!\!\!^{-2}\omega\frac{\Gamma_1\Gamma_2}{(E-E_r)^2 + (\Gamma/2)^2} \tag{2.44}$$

in which E_r is the energy of the resonance, $\pi\lambda\!\!\!^{-2}$ represents a geometrical factor typical for the quantic process, and ω is a statistical factor that can be calculated as

$$\omega = \frac{2J+1}{(2J_a+1)(2J_A+1)}(1+\delta_{aA}) \tag{2.45}$$

In 2.45 J, J_a and J_A are the spins of the compound nucleus and of the interacting particles respectively, and $(1+\delta_{aA})$ is meant to take into account the case for identical particles.

In the total Γ width, all the possible decays of the compound nucleus are considered, while Γ_1 and Γ_2 are the probability amplitudes of the compound nucleus formation from the particles in the entrance channel and of the decay to the particles in the exit channel, respectively.

If $\Gamma \ll E_r$ (narrow resonances), the reaction rate for a pair of particles equation 2.33 will be equal to [Clayton, 1983]:

$$\langle\sigma v\rangle = \left(\frac{8}{\pi\mu}\right)^{1/2}\frac{1}{kT}\int_0^\infty \sigma_{BW}(E)E\,exp\left(-\frac{E}{kT}\right)dE \tag{2.46}$$

In this case the exponential function will be nearly constant, given that it acts in a tight energy interval ($\approx \Gamma$), and can be written as

$$\langle\sigma v\rangle = \left(\frac{8}{\pi\mu}\right)^{1/2}\frac{1}{kT}E_r\int_0^\infty \sigma_{BW}(E)\,dE \tag{2.47}$$

If one ignores the energy dependence for Γ, Γ_1 and Γ_2, the integration in equation 2.47 will be equal to

$$\int_0^\infty \sigma_{BW}(E)\,dE = 2\pi^2\lambda\!\!\!^{-2}_r\omega\gamma \tag{2.48}$$

where $\gamma = \Gamma_1\Gamma_2/\Gamma$, and $\omega\gamma$ is the resonance strength. Combining equation 2.48 and equation 2.47 we obtain

$$\langle\sigma v\rangle = \left(\frac{2\pi}{\mu kT}\right)^{3/2}\hbar(\omega\gamma)_r\,exp\left(-\frac{E_r}{kT}\right) \tag{2.49}$$

For reactions that occur thanks to narrow resonances, nuclear combustion takes place at the energy of the resonance E_r, and the Gamow peak will correspond to the resonance one [Iliadis, 2007].

For broad resonances ($\Gamma/E_r \geq 10\%$), instead, the energy dependence of the cross-section and of the Γ width must be taken into account. In this case the cross-section σ(E) will be:

$$\sigma(E) = \sigma_r\frac{E_r}{E}\frac{\Gamma_1(E)}{\Gamma_1(E_r)}\frac{\Gamma_2(E)}{\Gamma_2(E_r)}\frac{(\Gamma_r/2)^2}{(E-E_r)^2+[\Gamma(E)/2]^2} \tag{2.50}$$

with $\sigma_r = \sigma(E = E_r)$ and $\Gamma_r = \Gamma(E = E_r)$.
If the level spectrum of the compound nucleus has an energy state below the Q_{value}[4], the resonance will be addressed as sub-threshold resonance for the channel b + B. This state cannot decay in b + B, and the excited state can not be populated using this reaction channel, given that $E_r = E_R - Q$ is negative. Nevertheless such an excited state, to be formed needs at least one allowed decay channel. This implies that this level must be characterized by a Γ and certain half-life. If the width of the resonance is large enough to have a tail at energies higher than Q-E_R, then the resonance will be "visible", and will lead to an enhancement of the cross-section σ with respect to the expected value. In this case the cross-section will be:

$$\sigma(E) = \pi\lambda^2\omega\frac{\Gamma_1(E)\Gamma_2(E + Q)}{(E - E_r)^2 + [\Gamma(E)/2]} \tag{2.51}$$

2.7 Electron screening

Up to now we assumed that both projectile and target are completely electron-less objects. This allows us to easily consider the Coulomb barrier.

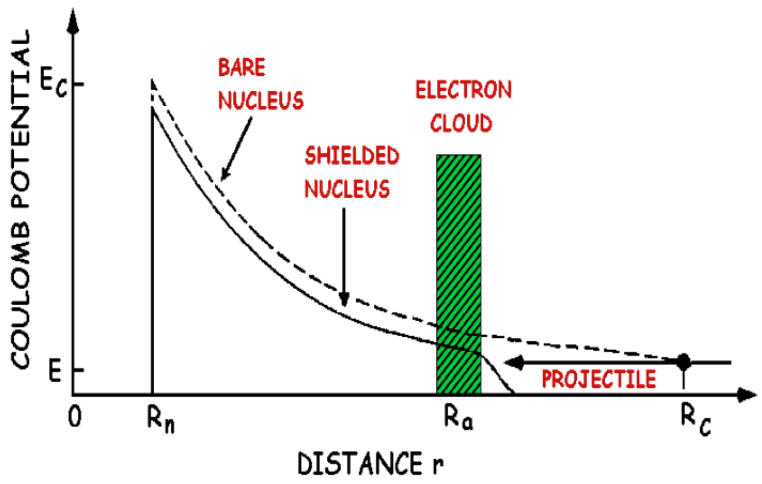

Figure 2.5: Sketch of the Coulomb potential modified by electrons. The dashed line represents the *bare nucleus* condition. R_a, R_n, E_c and R_c are the atomic radius, the nuclear interaction radius, the height of the barrier for a classical bare nucleus and the classical turning point for a particle with a certain energy E

[4]The Q_{value} for a certain reaction can be defined as mass-defect that can be detected between the entrance and the exit channels. For a certain reaction A + a → b + B it will be $Q_{value} = (m_a + m_A - m_b - m_B)c^2$

In experiments with charged particles performed in laboratory, however, projectile and target particles are in form of ions and atoms (or atom and molecules) respectively, so electrons will shield both charges. Let us therefore now the target nucleus is considered as an atom: for distances above the atomic radius R_a, the electrostatic potential is zero (figure 2.5), and so the the projectile nucleus will not experience Coulomb repulsion until it does not surpasses the electron "nebula".
For high-energy reactions, this effect is negligible, but at astrophysical energies it is not the case. In Born-Oppenheimer approximation, the atomic and nuclear degrees of freedom can be treated separately, and the dynamical effects (polarization and deformation of the nebula), can be overlooked. It is possible to calculate the so-called *screening potential* U_e between interacting nuclei:

$$U_{eff}(r) = \frac{Z_a Z_A}{r} - U_e \tag{2.52}$$

Where a and A are the projectile and target nuclei, respectively.
Let us consider electrons as distributed on a surface with R_a radius, the projectile as completely ionized and the target as globally neutral. In this case the shielding potential U_e can be determined using a simplified model [Assenbaum et al., 1987]: the potential generated by the electron nebula at a distance comparable with R_a can be accounted as a constant value $V_a = Z_a e/R_a$ [Rolfs, 1988]. So the barrier that the projectile must overcome is equal to:

$$U_{eff}(R_n) = U_{coul}(R_n) - U_e(R_n) = \frac{Z_a Z_A e^2}{R_n} - \frac{Z_a Z_A e^2}{R_a} \tag{2.53}$$

with R_n radius of nuclear interaction, equal to the sum of the radii of the incoming and target nuclei. Equation 2.53 gives informations about the *electron screening*: for distances smaller than the atomic radius the screening potential is $U_e = Z_a Z_A e^2/R_a$, and it will reduce the fusion barrier, enhancing the cross-section in the process with respect to the the bare nucleus one.
Now that this potential is known, a correction factor f_{lab} can be calculated, with the aim to obtain the shielded nucleus cross-section $\sigma_s(E)$ from the bare nucleus one $\sigma_b(E)$ [Fiorentini et al., 1995]

$$f_{lab} = \frac{\sigma_s(E)}{\sigma_b(E)} \tag{2.54}$$

The reaction rate for a couple of particles $\langle \sigma v \rangle$ for shielded nuclei can be calculated by substituting energy E with $E_s = E + U_e$ in the equation 2.33. In this condition, it is like the barrier penetration is occurring at higher energies [Assenbaum

et al., 1987]. The value $\sigma_s(E)$ must be replaced with $\sigma_b(E_s)$, and the astrophysical factor must be a constant for U_e « E. So f_{lab} is :

$$f_{lab} = \frac{\sigma_b(E + U_e)}{\sigma_b(E)} = \frac{E}{E + U_e} exp\left(\frac{\pi\eta U_e}{E}\right) \tag{2.55}$$

The quantity f_{lab} is also dependent from U_e/E, and as can be seen in table 2.3, for U_e/E = 0.01, the electron screening is not negligible [Assenbaum et al., 1987].

Reaction	$U_e(keV)$	$f_{lab}(U_e/E = 0.1)$	$f_{lab}(U_e/E = 0.01)$	$f_{lab}(U_e/E = 0.001)$
$d + d$	0.027	16.5	1.10	1.003
$d + {}^3He$	0.11	20.9	1.11	1.003
${}^3He + {}^3He$	0.22	131	1.18	1.006
$p + {}^7Li$	0.24	14	1.09	1.003
$\alpha + {}^12C$	2.0	868	1.25	1.007

Table 2.3: Some values of f_{lab} for different reactions: even for U_e/E = 0.01 the discrepancy is relevant (E≈ 3 - 30 keV)[Assenbaum et al., 1987]

More accurate approximations of this phenomenon exist. Those take into account dynamical effects. At lower energies, where relative velocities of the interacting nuclei are smaller than the typical velocities for atomic electrons, the so-called *adiabatic approximation* can be used [Fiorentini et al., 1995]: in this case the electron screening potential is equal to

$$U_e = E_a + E_A - E_c \tag{2.56}$$

where E_a, E_A, and E_c are the binding energies of the projectile, the target and the compound nucleus respectively. In this approximation the fact that the nuclei are a lot slower that the electrons is assumed. In this way, a wave function can be assigned to the electrons for every instantaneous configuration of the interacting nuclei. Those can be chosen as one that does not differs too much from the one obtained considering the nuclei static in their instantaneous positions. In table 2.4 some results of electron screening calculations for some reactions are reported, along with theoretical predictions coming from adiabatic model.

Reaction	*Experimental U_e (eV)*	References	U_e^{ad} *(eV)*
^{6}Li(p,α)^{3}He	470 ± 150	Engstler et al. [1992]	175
^{6}Li(d,α)^{4}He	380 ± 250	Engstler et al. [1992]	175
^{7}Li(p,α)^{4}He	300 ± 280	Engstler et al. [1992]	175
^{3}He(d,p)^{4}He	219 ± 7	Aliotta et al. [2001]	119
d(d,p)t	25 ± 5	Greife et al. [1995]	20.4

Table 2.4: Comparison between screening potential values for some reactions of astrophysical interest. Those are obtained through best-fits on experimental data. Discrepancies with theoretical values gave rise to the electron screening problem. This is one of the biggest uncertainties in the astrophysical factor extraction at the Gamow peak.

2.7.1 Electron screening in stellar environment

In stars, atoms are completely ionized, due to high temperatures. In principle, it would be reasonable to think that the electron screening is not important in such environment. It is not right: nuclei, in fact, are surrounded by a "sea" of free electrons, that tend to cluster around them, with effects similar to the ones generated by atomic electrons.

Such a region is called Debye-Hückel sphere, and is characterized by a parameter called Debye-Hückel radius, R_D:

$$R_D = \left(\frac{kT}{4\pi e^2 \rho N_A \xi} \right)^{1/2} \tag{2.57}$$

with N_A the Avogadro number, ρ the density of the stellar plasma and ξ defined by

$$\xi = \sum_i \left(Z_i^2 + Z_i \right) \frac{X_i}{A_i} \tag{2.58}$$

In equation 2.58 X_i, Z_i and A_i represents the mass fraction, the nuclear charge and the atomic mass of the i-th ion, respectively [Rolfs, 1988].

Therefore in stars, the presence of the negatively-charged Debye-Hückel sphere, generates the reduction of the Coulomb potential, making the barrier penetration easier. So even in stellar environment, a factor that ties $\langle \sigma v \rangle_s$ observed in presence of electron screening and the bare nucleus $\langle \sigma v \rangle_b$ must be introduced:

$$f_{plasma} = \frac{\langle \sigma v \rangle_{screen}}{\langle \sigma v \rangle_b} \tag{2.59}$$

This factor is strongly tied to equation 2.57 with the operation [Adelberger et al., 1998]

$$f_{plasma} = exp\left(\frac{Z_a Z_A e^2}{kTR_D} \right) \tag{2.60}$$

From equation 2.60 it is clear that while stellar density grows, the reaction rate must grow too: the Debye-Hückel sphere, in fact, is reduced and the electron shielding grows [Rolfs, 1988].
From an experimental point of view the bare nucleus cross-section cannot be measured directly, but we can gain information on the shielded one. It is therefore necessary to perform measurements of the latter cross-section, to calculate the f_{plasma} term applying the Debye correction equation 2.60, and then calculate the bare nucleus cross-section. This is mandatory for direct measurements.

CHAPTER 3

Indirect Measurements: The Trojan Horse Method

In the previous chapters of this thesis we focused on the difficulties to overcome when measuring physical quantities of astrophysical relevance. A way to succeed consists in using indirect methods. Those take advantage of reactions that are different from the ones of interest, but have some kind of connection with those, above all in its cross-section.
In this chapter we will briefly discuss three indirect methods, among the most used ones:

- Coulomb Dissociation (CD);
- Asymptotic Normalization Coefficient (ANC);
- Trojan Horse Method (THM);

The first two methods are useful in studying radiative capture reactions, while the third one, to whom is dedicated the most extensive description (the measures discussed later in this work are made using it), has proven to be useful for reactions involving charged particles or neutrons in the entrance and exit exit channel.

3.1 Coulomb dissociation

The CD method is an indirect procedure meant to study radiative capture at energies corresponding to the Gamow peak. It was used for example for the $^{12}C(\alpha,\gamma)^{16}O$ reaction [Bertulani, 1994], important in heavy elements nucleosynthesis in massive stars, in particular in the phases after ^{4}He burning. Another example could be found in $^7Be(p,\gamma)^8Be$ [Motobayashi et al., 1994; Bertulani, 1994], fundamental to study solar neutrino problem.
This method uses a three-body reaction, with the aim to study a radiative capture reaction at astrophysical energies, analysing the projectile nucleus (a) break-up, induced by virtual photons: those mediate the Coulomb field generated by a heavy nucleus (Z_T):

$$a + Z_T \rightarrow b + c + Z_T \tag{3.1}$$

In 3.1, the a nucleus can be described as a cluster $a = b \oplus c$. The break-up is the way to study the photo-disintegration reaction

$$a + \gamma \rightarrow b + c \tag{3.2}$$

Studying it with the detailed balance method, the cross-section for the reaction of interest

$$b + c \rightarrow a + \gamma \tag{3.3}$$

can be measured. This method shows two main advantages:

- The adequate selection of the kinematic conditions allows to precisely measure the 3.1 reaction at low energies, using beams at higher energies with respect to Coulomb barrier. This fact makes the detection of projectile fragments easier, and allows to use thicker targets, enhancing the reaction rate, given that the straggling in it is low [Baur and Rebel, 1994];

- The reaction rate is enhanced with respect to direct radiative capture or photo-disintegration measurements. This happens because the a particle is hit by a lot of virtual photons due to the presence of Z_T, that has a high atomic number.

This rate enhancement is clear if differential cross-section for projectile break-up of a defined multipole $\pi\lambda$ is considered [Baur and Rebel, 1994]:

$$\frac{d^2\sigma}{d\Omega dE_\gamma} = \frac{1}{E_\gamma}\frac{dn_{\pi\lambda}}{d\Omega}\sigma_{\pi\lambda}^{photo} \tag{3.4}$$

The equation 3.4 is the product of three terms: a kinematic factor ($1/E_\gamma$), the virtual photon number for a unit of solid angle $\frac{dn_{\pi\lambda}}{d\Omega}$, and the off-energy shell photodisintegration cross-section $\sigma_{\pi\lambda}^{photo}$. The second term, called equivalent photon spectrum, is purely kinematic, and is responsible for an enhancement (some orders of magnitude) of the cross-section for the three-body process, with respect to the radiative capture [Baur and Rebel, 1994].
The 3.3 reaction, that is the real aim for the measurement, is a on-energy shell process, so it implies real photon exchange, so the equation 3.4 is valid only as an approximation [Baur and Rebel, 1994].
The relation 3.4 can only be applied if the process is a purely Coulomb one. In this case the interaction between the projectile and the target must be peripheral, or else the strong nuclear interactions must be taken into account.

3.1.1 Experimental examples

The CD method is useful when radiative capture are studied, because it allows to explore the low relative energy region of the two fragments (nearly parallel emission).
It is necessary to underline, however, that the break-up can occur as an effect of the Coulomb field and via strong nuclear interaction. Those processes can not be distinguished, so interference will be observed. For example, the ^{7}Be(p,γ)^{8}B, studied using the three-body reaction ^{208}Pb(^{8}B,p^{7}Be)^{208}B [Bertulani, 1994; Motobayashi et al., 1994] shows the presence of interference phenomena between the two reaction channels in the cross-section (figure 3.1a) .
Coulomb Dissociation was also used used to study the cross-section of the ^{7}Be(p,γ)^{8}B because the binding energy of ^{8}B is really low (0.1375 MeV), and in this case the dissociation cross-section is three orders of magnitude higher than the purely nuclear contribution [Bertulani, 1994; Motobayashi et al., 1994].

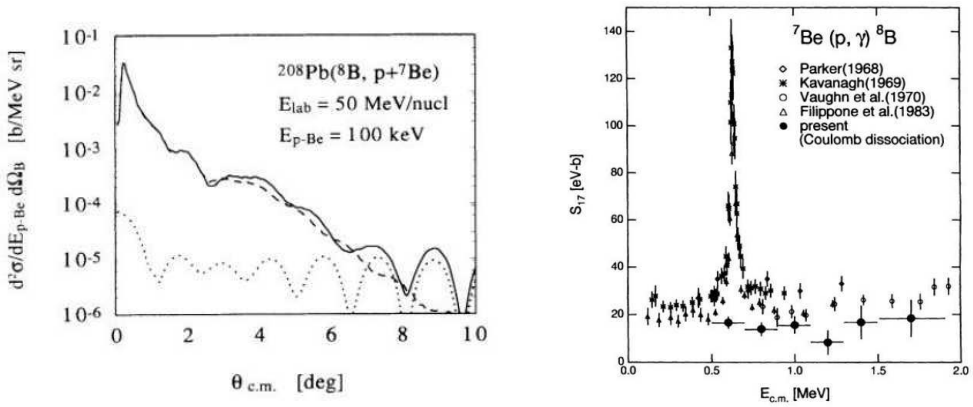

(a)

Figure 3.1: a) Angular distribution for the ^{8}B+^{208}Pb→p+^{7}Be+^{208}Pb at the energy of 50 MeV/A, with relative energy of the fragments at 100 keV: The dotted and dashed lines are the cross-section for a purely Coulomb process and for a purely nuclear one, respectively. The continuous curve mixes the two processes through interference [Bertulani, 1994]
b)Comparison between the astrophysical factor of the $S_{p-^{7}Be}$ extracted via Coulomb dissociation of ^{8}B with previous measurements. Horizontal bars indicate the E_{rel} range in which S(E) is mediated [Motobayashi et al., 1994]

3.2 Asymptotic Normalization Coefficient method

The Asymptotic Normalization Coefficient allows to evaluate the cross-section for (p, γ) and (α, γ) reactions at astrophysical energies form the so-called normalization coefficient C, related to the low-bound systems B = A + p or B = A + α, so in cases where the nucleus is composed by a core A and a proton or a α particle tied to it [Trache et al., 1998].

The coefficient, obtained from measurements of the cross-section for peripheral transfer processes, will represent the probability for a certain B particle to be in the A + p or A + α configuration, at distance bigger than the strong interaction range. In this way the wave function trend in the asymptotic region is essentially determined by the Coulomb interaction. In this way an accurate measure of the rate can be made, once the tail amplitude is known [Azhari et al., 2001].

Let us consider the peripheral transfer reaction

$$A + X \rightarrow B + Y \tag{3.5}$$

where $X = Y + a$ and $B = A + a$, with a the transferred particle (figure 3.2). In Distorted Wave Born Approximation (DWBA) the amplitude for the process 3.5, that we call M, under the hypothesis that the interaction between the particles is

peripheral, is equal to [Mukhamedzhanov et al., 1997]

$$M(E_i, \cos\theta) = \sum M_a \langle \chi_f^{(-)} I_{Aa}^B(\mathbf{r}_{Aa}) | \Delta V | I_{Ya}^X(\mathbf{r}_{Ya}) \chi_i(+) \tag{3.6}$$

In equation 3.6, E_i represents the relative energy of the two nuclei A and X, θ is the diffusion angle in the center-of-mass reference frame, and $\chi_i^{(+)}$ and $\chi_f^{(-)}$ are the distorted waves for the entry and exit channel respectively, while ΔV is the transition operator, and $I_{\beta\gamma}^{\alpha}(\mathbf{r}_{\beta\gamma})$ is the overlapping function for the β and γ nuclei that constitutes the $\alpha = \beta + \gamma$ state: α, β and γ represent the X, Y and a nuclei in the right part of equation of equation 3.6 (entrance channel) and B, A and a in the left one (exit channel), respectively.

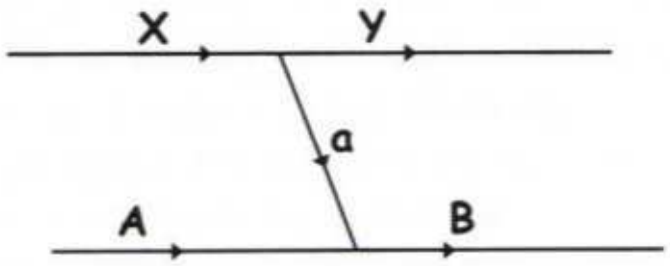

Figure 3.2: Schematic diagram for the $A + X \rightarrow B + Y$ reaction, where $X = Y + a$ and $B = A + a$. The a particle is transferred from the X nucleus to the A one

The validity of this method is based on the fact that the overlapping function $I_{\beta\gamma}^{\alpha}(\mathbf{r}_{\beta\gamma})$ of the equation 3.6 is the same in case of direct capture:

$$M_{DC} = \lambda \langle I_{aA}^B(\mathbf{r}_{Aa}) | O | \Psi_i^+(\mathbf{r_A a}) \rangle \tag{3.7}$$

In equation 3.7 λ is a kinematic factor, O is the electro-magnetic transition operator, and Ψ_i^+ represents the scattering wave function in the entry channel.
If the diagram in figure 3.2 describes the transfer reaction, the DWBA cross-section can be factorized using the initial and final spectroscopic factors as it follows [Mukhamedzhanov et al., 1997]:

$$\frac{d\sigma}{d\Omega} = \sum_{j_B j_X} S_{Aal_B j_B} S_{Yal_X j_X} \sigma^{DW}_{l_B j_B l_X j_X} \tag{3.8}$$

If evaluated following this approximation, those nevertheless are strongly dependent on the used model, due to the behaviour of the wave function inside the nucleus (unlike the normalization coefficients). This fact makes the uncertainties on the geometrical parameters of the potential a strong source of errors in calculations.

The asymptotic normalization coefficient is tied to the behaviour of the wave function at distances above the nuclear interaction range. This makes the coefficient less model-dependent with respect to the spectroscopic factor [Mukhamedzhanov et al., 1997].

Let us now write down the radial part of the overlapping function

$$C_{\beta\gamma l_\alpha j_\alpha} = S^{1/2}_{\beta\gamma l_\alpha j_\alpha} b_{\beta\gamma l_\alpha j_\alpha} \tag{3.9}$$

In equation 3.9 $b_{\beta\gamma l_\alpha j_\alpha}$ is the normalization constant of the wave function related to the intercluster motion of β and γ, that is involved in the radial part of the overlapping function.

The equation 3.9 is useful to define the behaviour of the overlapping function for $r_{\beta\gamma}$ bigger than the nuclear interaction range. By substituting the equation 3.8 in the 3.9, the cross section is equal to:

$$\frac{d\sigma}{d\Omega} = \sum_{j_B j_X} (C^B_{Aal_B j_B})^2 (C_{Yal_X j_X})^2 R_{l_B j_b l_X j_X} \tag{3.10}$$

where $R_{l_B j_B l_X j_X}$ can be calculated as:

$$R_{l_B j_B l_X j_X} = \frac{\sigma_{l_B j_B l_X j_X}}{b^2_{Aal_B j_B} b^2_{Yal_X j_X}} \tag{3.11}$$

The equation 3.10 is weakly sensible to nuclear parameter variations (unlike σ^{DW}) for peripheral reactions.

To apply the ANC method, the transfer contribution must be isolated from other mechanisms, with the aim to normalize the differential cross-section, calculated with the DWBA approach, to the experimental values at small angles, where transfer process is considered to be dominant.

3.2.1 Experimental examples

The ANC method was used for example to study the ^{8}Be $\rightarrow$ ^{7}Be + p reaction using the ^{10}B(^{7}Be,^{8}B)^{9}Be proton transfer. The astrophysical factor for the capture reaction ^{7}Be(p,γ)^{8}B was than determined using the normalization coefficient for the virtual decay ^{10}B $\rightarrow$ ^{9}Be + p, given that in equation 3.6 overlapping coefficient are present. From an experimental point of view, the ANC for the ^{10}B $\rightarrow$ ^{9}Be + p reaction must be extracted first, by means of another transfer reaction, and using the ^{9}Be(^{10}B,^{9}B)^{10}Be to avoid a third ANC use. In this way the overlapping function for the two vertices are known and other ANC are avoided.

This method was successfully used to evaluate the values of $S_{p-^7Be}(0)$ equal to 17.3± 1.8 eVb [Azhari et al., 2001], averaging on different determinations obtained analysing the transfer reactions ^{10}B(^{7}Be,^{8}B)^{9}Be and ^{14}N(^{7}Be,^{8}B)^{13}C. This result is in agreement with the one adopted in literature, equal to 19^{+4}_{-2} eVb [Adelberger et al., 1998]. This is also consistent with the most recent values of $S(0)_{p-^7Be}$ obtained with direct measurements [Hass, 1999] and CD method [Iwasa et al., 1999].

3.3 The Trojan Horse Method (THM)

3.3.1 Quasi-free processes

The THM is based on direct reaction theory, and in particular on the quasi-free break-up [Satchler, 1990]. Let us consider the $A + a \rightarrow c + C + s$ reaction, in which the a nucleus can be described as a cluster a=$x \oplus$s, and that the intercluster motion can occur mostly in s-wave: this implies that the momentum distribution for that motion has a maximum at 0 MeV/c. In this conditions the break-up can be considered as a quasi-free one if the spectator particle s has the same momentum distribution inside a and in the exit channel. Under such constraints the s particle acts as a spectator for the virtual process A(x,c)C [Satchler, 1990] (figure 3.3), and the validity for polar approximation can be assumed.

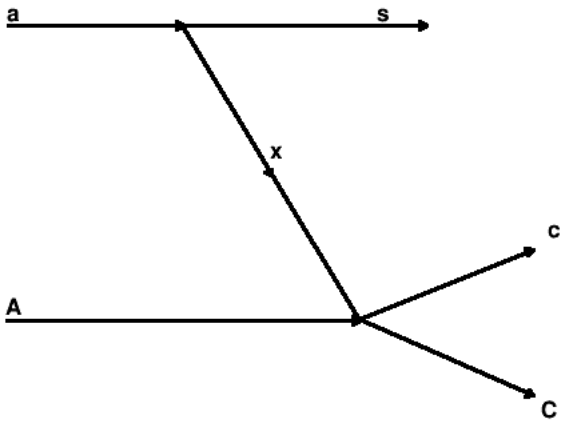

Figure 3.3: Feynman pseudo-diagram for the $A + a \rightarrow c + C + s$ process. In the superior pole the target (a) breaks-up into the two clusters x and s. The particle x does interact with the beam (A), giving rise to the virtual reaction $A + x \rightarrow C + c$, while s acts as a spectator for the reaction, preserving the momentum that it had before the break-up inside a (polar approximation)

It is necessary to underline that this method is valid whether the break-up takes place inside the projectile or inside the target, and even if the relative cluster motion x - s does not take place in s-wave.

3.3.2 THM

The THM is often used to study nuclear reactions with charged particles or neutrons in the entrance and in the exit channel, in the energy range of astrophysical interest. Using this method, an indirect measurement of the cross section of a two-body reaction is possible from the study of a quasi-free three-body reaction. In this process, the wave function associated to the Trojan Horse (TH) nucleus has a dominant amplitude for cluster configuration. Under such kinematic conditions, the angles at which the c and C particles of the figure 3.3 are emitted are called quasi-free angles. They can be determined considering that the s particle must remain with momentum equal to $\mathbf{k_s}$ before and after the interaction between x and A. If the condition E_{beam}>E_{Coul} is chosen, the viability of this method is legitimate and it makes possible to avoid Coulomb suppression of the cross-section. To do so, the energy of the projectile particle is chosen to be higher than the A - a Coulomb barrier, while the A - x interaction can take place at very low energies, even zero. The binding energy between x and s, in fact, compensates the kinetic energy of the relative motion A - x, giving rise to the so-called quasi-free energy [Tumino et al., 2003]. This energy can be considered as the minimum energy necessary to maximize the quasi-free contribution, given that the momentum distribution has a peak around p_s = 0. This quantity can be calculated as:

$$E_{qf} = E_{Ax} - B_{x-s} \tag{3.12}$$

In equation 3.12 E_{Ax} is the beam energy in the center-of-mass reference frame for the A - x system and B_{x-s} is the binding energy for the x - s bound system. Under these conditions the intercluster motion of the x particle inside the a nucleus has the "duty" to fix the energy range that can be explored around the quasi-free energy for the process.

Furthermore the $E_{beam} > E_{coul}$ relation makes the electron screening effects negligible.

3.3.3 Plane Wave Impulse Approximation

Let us describe now the THM in a more detailed way. From a theoretical point of view, the quasi-free mechanism can be approached using the impulse approximation [Chew and Wick, 1952]:

- the A nucleus does not interact at the same time with the two particles composing the cluster, x and s. This is true if the De Broglie wavelength of the projectile A momentum is less than the average distance between x and s;
- the probability for the interaction between A and x is the same that x should have in case of a free particle. This also means that s does not participate to the reaction;
- the binding energy of the system x - s is negligible if compared with the interaction energy between A and x.

Under such hypothesis, and introducing the plane-wave approximation formalism, a simplified approach to the quasi-free break-up can be used: the Plane-Wave Impulse Approximation (PWIA). To do so, two more assumptions must be made:

- the incoming and outgoing particles must be describable as plane waves;
- the momentum distribution of the spectator particle can be calculated as the Fourier transformation of the wave function of the relative motion between the x and s nuclei.

Let us assume now, to further simplify the problem, that the involved particles have all spin equal to zero, and that the projectile nucleus wave function can be written as the product of the wave functions of the cluster components x and s, which are in their fundamental state. If ψ_x and ψ_s are such functions, the relative motion of the cluster components can be written as it follows [Jain et al., 1970]:

$$\psi_a = \psi_x(\mathbf{r_x})\psi_s(\mathbf{r_s})\psi(\mathbf{r_x} - \mathbf{r_s}) \tag{3.13}$$

The equation 3.13 is an approximation to the lowest order of a series expansion. The complete expression implies the sum on the different excited levels of the cluster components, introducing c_i coefficients, strongly tied to the probability for a certain configuration to happen:

$$\psi_a = \sum_i c_i\psi_{x_i}(\mathbf{r_{x_i}})\psi_{s_i}(\mathbf{r_{s_i}})\psi(\mathbf{r_x} - \mathbf{r_s}) \tag{3.14}$$

Let us now suppose that the TH nucleus is in the target, and define $\mathbf{k_C}$, $\mathbf{k_c}$, $\mathbf{k_s}$, $\mathbf{q}$ and $\mathbf{p}$ as the momenta of the particles C, c, s, x and A in the laboratory reference frame. Here $\mathbf{k_{xs}} = (m_s\mathbf{q} - m_x\mathbf{k_s})/m_a$ is the relative momentum of the cluster components inside the target nucleus a and $\psi(\mathbf{k_{xs}})$ is the Fourier transform of the wave function of the relative motion $\psi(\mathbf{r_x} - \mathbf{r_s})$ [Jain et al., 1970].
In this notation, the wave function for the a nucleus in the momentum space can be written as it follows:

$$\langle \mathbf{k_s}, \mathbf{q} | a \rangle = \phi(\mathbf{k_{xs}})\delta(\mathbf{q} + \mathbf{k_s}) \tag{3.15}$$

In equation 3.15 $|a\rangle$ is the intrinsic state of the target, while the Dirac's delta is there because it takes into account the fact that the target is at rest in the laboratory reference frame. Now the momentum for the target must be equal to zero, and so

$$\mathbf{k}_a = \mathbf{k}_s + \mathbf{q} \;\Rightarrow\; \mathbf{q} = -\mathbf{k}_s = \mathbf{k}_{xs} \tag{3.16}$$

Here the x momentum before the collision with the projectile A is equal and opposed to the s one. This means that it can be experimentally measured, because s will show up in the exit three-body channel. The initial and final state wave function will be respectively equal to

$$|i\rangle = |\mathbf{p}, a\rangle \tag{3.17}$$

$$|f\rangle = |\mathbf{k}_C, \mathbf{k}_c, \mathbf{k_s}\rangle \tag{3.18}$$

equations 3.17 and 3.18 are true if the incoming and outgoing particles can be described as plane-waves. So said, the transition element between the initial and final state of the system will be [Jain et al., 1970]:

$$T_{fi} = \langle f | \hat{T} | i \rangle = \langle \mathbf{k}_C, \mathbf{k}_c, \mathbf{k}_s | \hat{T}^{3B} | \mathbf{p}, a \rangle \tag{3.19}$$

where $\hat{T}^{3B}$ is the operator $\hat{T}$ referred to the three-body reaction.
If the PWIA hypotheses are satisfied, then $\hat{T}^{3B}$ of equation 3.19 can be substituted with $\hat{T}^{2B}$, referred to the two-body reaction, and the spectator wave function will not change under the influence of such operator

$$\langle \mathbf{k}_s | \hat{T}^{2B} = \langle \mathbf{k}_s |$$

Taking into account what was said so far, the transition element of the equation 3.19 matrix can be written as it follows:

$$T_{fi} = \langle \mathbf{k}_C, \mathbf{k}_c, \mathbf{k}_s | \hat{T}^{2B} | \mathbf{p}, a \rangle = \int \langle \mathbf{k}_C, \mathbf{k}_c | \hat{T}^{2B} | \mathbf{p}, \mathbf{q} \rangle \langle \mathbf{q} | a \rangle d^3\mathbf{q} \tag{3.21}$$

Now, the equations 3.15 and 3.16 can be used to obtain the following result:

$$\begin{aligned} T_{fi} &= \int \langle \mathbf{k}_C, \mathbf{k}_c \left| \hat{T}^{2B} \right| \mathbf{p}, -\mathbf{k}_s \rangle \langle \mathbf{k}_s, \mathbf{q} | a \rangle d^3\mathbf{q} \\ &= \int \langle \mathbf{k}_C, \mathbf{k_c} \left| \hat{T}^{2B} \right| \mathbf{p}, -\mathbf{k}_s \rangle \phi(\mathbf{k}_{xs}) \delta(\mathbf{q} + \mathbf{k}_s) d^3\mathbf{q} \\ &= \langle \mathbf{k}_C, \mathbf{k}_c \left| \hat{T}^{2B} \right| \mathbf{p}, -\mathbf{k}_s \rangle \phi(-\mathbf{k}_s) \end{aligned} \tag{3.22}$$

In equation 3.22 the matrix element

$$T_{fi}^{2B} = \langle \mathbf{k}_C, \mathbf{k}_c \left| \hat{T}^{2B} \right| \mathbf{p}, -\mathbf{k}_s \rangle \tag{3.23}$$

is the matrix element of the two-body reaction that describes the transition form the initial state $\left|\mathbf{p}, -\mathbf{k}_s\right\rangle$ to the final one $\left|\mathbf{k}_C, \mathbf{k}_c\right\rangle$.
In the center-of-mass reference frame and in the coordinate of relative momentum of the two-body system, the T_{fi}^{2B} can be written as [Jain et al., 1970]:

$$T_{fi}^{2B} = \delta(\mathbf{p} - \mathbf{k}_s - \mathbf{k}_C - \mathbf{k}_c) t_{fi}^{2B} \tag{3.24}$$

where

$$t_{fi}^{2B} = \langle \mathbf{k}_f | \hat{T}^{2B} | \mathbf{k}_i \rangle \tag{3.25}$$

is the reduced matrix element proper of the two-body process, $\mathbf{k}_i$ and $\mathbf{k}_f$ are the relative momenta of the a and A particles in the entry channel and of c and C in the exit one, respectively. The Dirac's delta stands for momentum conservation.
Using now equations 3.24 and 3.25, the matrix transition element becomes:

$$T_{fi} = \delta(\mathbf{K}_i - \mathbf{K}_f) t_{fi}^{2B} \phi(-\mathbf{k}_s) \tag{3.26}$$

In equation 3.26 the quantity $\mathbf{K_i} = \mathbf{p}$ and $\mathbf{K}_f = \mathbf{k}_s + \mathbf{k}_C + \mathbf{k}_c$ are the momenta of the center-of-mass reference frame, before and after the collision.
Let us rewrite T_{fi} in terms of the reduced matrix element referred to the three-body process:

$$T_{fi} = \delta(\mathbf{K}_i - \mathbf{K}_f) t_{fi}^{3B} \tag{3.27}$$

with

$$t_{fi}^{3B} = \phi(-\mathbf{k_s}) t_{fi}^{2B} \tag{3.28}$$

This last equation has great importance: in fact, it allows to write down the transition amplitude for the three-body system that appears in the break-up cross-section expression in terms of the reduced matrix element of the two-body system. The differential cross section in the laboratory reference frame for a reaction with three

bodies in the exit channel, in fact, can be written, using natural unities ($\hbar = c = 1$) as [Berggren and Tyren, 1966]:

$$d\sigma = \frac{(2\pi)^4}{\left|v_{rel}\right|} d^3\mathbf{k}_C d^3\mathbf{k}_c d^3\mathbf{k}_s \delta(\mathbf{K}_i - \mathbf{K}_f)\delta(E_i - E_f)\left|t_{fi}^{3B}\right|^2 \tag{3.29}$$

where E_i and E_f represent the total energies for the initial and final state of the system, and $\mathbf{v}_{rel}$ stands for the relative energy between the incoming particle and the target. By substitution of the expressions for $\mathbf{K}_i$ and $\mathbf{K}_f$, and the equation 3.28 in place of t_{fi}^{3B} in equation 3.29, one can obtain

$$\begin{aligned} d\sigma = {} & \frac{(2\pi)^4}{\left|\mathbf{v}_{rel}\right|} k_C^2 dk_C d\Omega_C k_c^2 dk_c d\Omega_c d^3\mathbf{k}_s \\ & \times \delta(\mathbf{p} - \mathbf{k}_s - \mathbf{k}_C - \mathbf{k}_c)\delta(E_i - E_f)\left|\phi(-\mathbf{k_s})\right|^2 \left|t_{fi}^{2B}\right|^2 \end{aligned} \tag{3.30}$$

After an integration in $d^3\mathbf{k}_s$ (given that the spectator is usually not detected[1]) and in $d\mathbf{k}_c$, an explicit expression for the differential cross section can be written, under the hypothesis that only one l contributes [Jain et al., 1970]:

$$\frac{d^3\sigma}{dE_C d\Omega_C d\Omega_c} \propto (KF)\left|\phi(-\mathbf{k}_s)\right|^2 \left(\frac{d\sigma^N}{d\Omega}\right)_l^{off} \tag{3.31}$$

In equation 3.31 KF is a kinematic factor, that depends on the same variables that define equation 3.31, $|\phi(-\mathbf{k_s})|^2$ is the momentum distribution of the spectator nucleus s inside the a cluster and $\left(\frac{d\sigma^N}{d\Omega}\right)_l^{off}$ is the differential cross section *off-energy-shell* [Joachain, 1987] for the A-x reaction.

In our case the kinematic factor can be written as it follows:

$$KF = \frac{\mathbf{k}_C \mathbf{k}_c^2 E_S E_{C.M.}^2}{\mathbf{p} E_{xi} \mathbf{k}_c E_S + E_c[\mathbf{k}_c - \mathbf{p}\cos\vartheta_c + \mathbf{k}_C \cos(\vartheta_C - \vartheta_c)]} \tag{3.32}$$

In equation 3.32 the angles of the particles are measured with respect to the beam direction, $E_{C.M.}$ is the total energy in the center-of-mass system of the two-body reaction, and $E_{xi}^2 = m_c + k_S^2$.

The equation equation 3.31 should be multiplied by a spectroscopic factor, tied to the probability for the a nucleus to be described as composed by the two cluster components x and s. This factor is however unknown, and that is a limit for THM, due to the fact that it does not provide information on the cross-section in absolute units, and normalization to direct data are necessary. The method in fact needs a

[1] This will not be the case for the $^{19}F(\alpha,p)^{22}Ne$ reaction, see Chapter V)

confrontation with direct measurements, and also a normalization to them, at energies above the Coulomb barrier or around it.

Let us now assume that the momentum distribution $|\phi(-\mathbf{k}_s)|^2$ is known theoretically or experimentally studied. After the calculation of the KF, it will be possible to know the differential off-energy-shell,two-body cross section $\left(\frac{d\sigma^N}{d\Omega}\right)_l^{off}$ for the process, if the three-body one is known, using equation 3.31:

$$\left(\frac{d\sigma^N}{d\Omega}\right)_l^{off} \propto \frac{d^3\sigma}{dE_C d\Omega_C d\Omega_c}\left[KF|\phi(-\mathbf{k_S})|^2\right]^{-1} \tag{3.33}$$

If the TH nucleus is in the projectile − like in the ^{19}F(α,p)^{22}Ne − the process can be treated in the same way, taking into account that in this case the wave function of the TH nucleus in the momentum space will be equal to:

$$\langle \mathbf{k}_s, \mathbf{q}|A\rangle = \phi(\mathbf{k}_{xs})\delta(\mathbf{q} + \mathbf{k}_s - \mathbf{p}) \tag{3.34}$$

In equation 3.34, $|A\rangle$ is the intrinsic state of the projectile, and from it we can obtain the two-body amplitude transition. It will lead to a formulation that is identical to equation 3.31, if a factor $\frac{E_A}{E_a}$ is multiplied for it [Slaus et al., 1977], where A is the projectile (that this time acts as a TH nucleus) and a is the target .

It is now important to underline that $\left(\frac{d\sigma^N}{d\Omega}\right)^{off}$ represents only the nuclear contribution, given that the beam energy is deliberately chosen to overcome the Coulomb barrier in the entry channel. In this way the x particle can be brought inside the nuclear interaction field by the TH nucleus. In this way the desired reaction can be triggered.

As said before, this measurements needs a comparison with direct data. For such reason it is necessary to multiply the indirect two-body cross-section by a penetrability coefficient, that stands for the effects of Coulomb and centrifugal barrier related to the l-th partial wave:

$$\frac{d\sigma}{d\Omega} = \sum_l P_l\left(\frac{d\sigma^N}{d\Omega}\right)_l^{off} \tag{3.35}$$

After integration of equation 3.35 over the solid angle $d\Omega$, the total cross-section σ_{tot} is obtained. The S(E)-factor can also be obtained from it (chapter 2 equation 2.33). Both σ_{tot} and S(E) are not affected by electron screening. It is now possible to normalize to direct measurements.

A most refined formalization of the Trojan Horse Method considers as a starting

point not the PWIA, but the Distorted-Wave Impulse Approximation (DWIA). This new formalism introduces some quantitative variations to the cross-section, keeping the factorization equation 3.31 unchanged. This approximation also justifies in a most rigorous way the equation 3.35 with respect to to the PWIA. The DWIA was introduced with the aim to study a peculiar class of issues, called two potential scattering. In this case we suppose that the potential of interaction V can be decomposed into two parts:

$$V = U + W \tag{3.36}$$

Of these two, only the U part will be the exact solution searched, while the W effects are considered only at the first-order solutions.

In this condition the so-called two potential formula can provide the expression for the diffusion amplitude form the potential V as a sum of terms depending on U and W:

$$T_{fi} = \langle \phi_f \big| U \big| \chi_i^+ \rangle + \langle \chi_f^- \big| W \big| \psi_i^+ \rangle \tag{3.37}$$

In equation 3.37 $|\chi_i^+\rangle$ and $|\chi_f^-\rangle$ are the distorted waves of the U potential in the initial and final state, while $|\phi_f\rangle$ is the plane wave representing the final state and $|\psi_i^+\rangle$ is the exact solution of the scattering problem.

Let us now consider a two-body reaction of astrophysical interest obtained using the THM. In general the differential cross-section for a three-body reaction can be rewritten as it follows:

$$\frac{d^3\sigma}{dE_C d\Omega_C d\Omega_c} = KF \big| T_{fi} \big|^2 \tag{3.38}$$

Where again KF is the kinematic factor. Introducing the reduced masses, μ_{Aa} and μ_{Bb}, the momenta $\mathbf{K}_C$ and $\mathbf{K}_c$, the relative momenta $\mathbf{k}_{Cc}$, $\mathbf{k}_{Bs}$ e $\mathbf{k}_{Aa}$, where B stands for the "participants" system[2], the KF factor will be equal to:

$$KF = \frac{\mu_{Aa} m_c}{(2\pi)^5 \hbar^7} \frac{K_C K_c^3}{k_{Aa}} \left[\left(\frac{\mathbf{k}_{Bs}}{\mu_{Bs}} \right) - \frac{\mathbf{k}_{Cc}}{m_c} \cdot \frac{\mathbf{K}_c}{K_c} \right]^{-1} \tag{3.39}$$

In DWIA the three-body cross section can be written as [Typel and Wolter, 2000]:

$$\frac{d^3\sigma}{dE_C d\Omega_C d\Omega_c} = KF \big| W(\mathbf{Q_{Bs}}) \big|^2 \frac{v_{Cc}}{v_{Ax}} P_l^{-1} C_l \frac{d\sigma_l}{d\Omega_{Ax}}(Cc \rightarrow Ax) \tag{3.40}$$

In equation 3.40, $\frac{d\sigma_l}{d\Omega_{Ax}}$ represents the on-shell cross section for the two-body reaction, C_l is a normalization constant and $\mathbf{Q_{Bs}}$ is a probability amplitude tied to

[2]The other letters are like in figure 3.3

the wave function of the a nucleus in the momentum space at its fundamental state $\Phi(\mathbf{Q}_{Bs})$. This link is expressed in the following equations:

$$\mathbf{Q}_{Bs} = \mathbf{k}_{Bs} - \frac{m_s}{m_s + m_x}\mathbf{k}_{Aa} \tag{3.41}$$

$$W(\mathbf{Q}_{Bs}) = -\left(\varepsilon_a + \frac{\hbar^2 Q_{Bs}^2}{2\mu_{xs}}\right)\Phi_a(\mathbf{Q_{Bs}}) \tag{3.42}$$

Here ε_a is the threshold energy for the $a \rightarrow x + b$ decay [Typel and Wolter, 2000]. Moreover, in equation 3.40 the reciprocal of the penetrability factor appears. It compensates for the on-shell cross-section suppression due to the Coulomb barrier.
It is now important to underline that the surface approximation, along with the C_l factor, although it allows us to analyse the two-body cross-section $\frac{d\sigma_l}{d\Omega_{Ax}}$ dependence from the energy, does not give us a result in absolute units. It is therefore necessary some kind of normalization of the two-body cross-section to direct data, in an energy region where the latter is not affected by Coulomb suppression or electron screening.

3.4 Experimental examples

The THM has been used in the past twenty years to study many reactions of astrophysical interest, and in many cases those measurements are in fair agreement with the direct ones. Many studies about the validity of the method have also been made, and experiments on individuation and separability of quasi-free processes have been performed [Jacob and Maris, 1966; Zadro et al., 1989]. They aimed to verify that the quasi-free process is allowed at low energies, and so that the THM is applicable in the range of astrophysical interest.

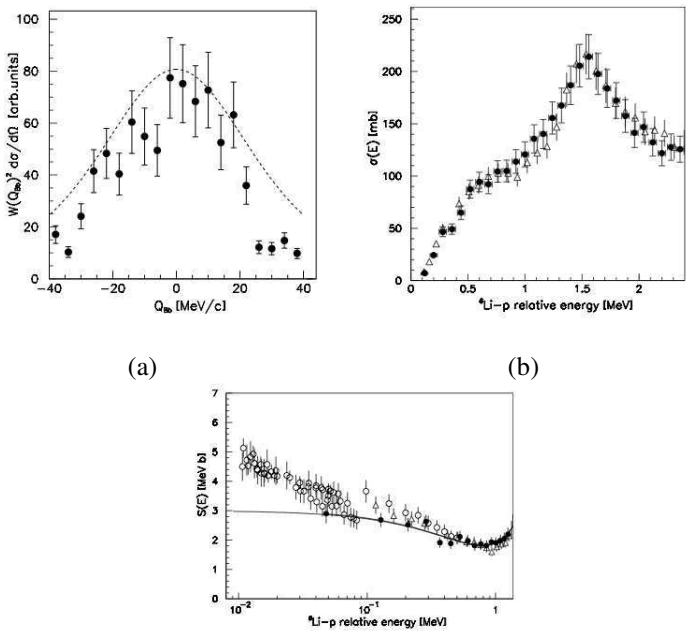

Figure 3.4: Study of the reaction ^{6}Li(p,α)^{3}He via the ^{2}H(^{6}Li, $\alpha\,^{3}$He)n [Tumino et al., 2003].
a)Experimental momentum distribution for the spectator (a neutron), compared with the Hultén function, that is the theoretical trend for neutron distribution inside deuterium (see Chapter 6.2).
b)Indirect two-body cross-section (full circles, compared with direct data at $E_{beam} > E_{coul}$).
c) Experimental astrophysical factor (full circles) compared with direct data. The solid line represents a second order polynomial function that fits the data.

In figure figure 3.4 some results regarding the validity check of quasi-free contribution of the H(^{6}Li,α)^{4}He two-body reaction to the ^{2}H(^{6}Li,$\alpha\,^{3}$He)n three-body one [Tumino et al., 2003], in which the neutron acts as the spectator, are shown.
Experimental evidences underline that the quasi-free mechanism can be separated from the others, and how the excitation function obtained in this way exactly reproduces the direct data, inside the experimental errors. Such a result is a validity test for the polar approximation (paragraph 3.3.1) at energies higher than the Coulomb barrier. An experimental evidence like this constitutes a necessary step to use the THM in nuclear astrophysics measurements.
About the validity of the THM, in figure 3.4 is clear that the ^{2}H nucleus can be used as a TH one. So the method can be applied (figure 3.4a), and the cross section is in good agreement with direct measurements (figure 3.4b). At low energies instead, the astrophysical factor (figure 3.4c) is not influenced by the electron screening.

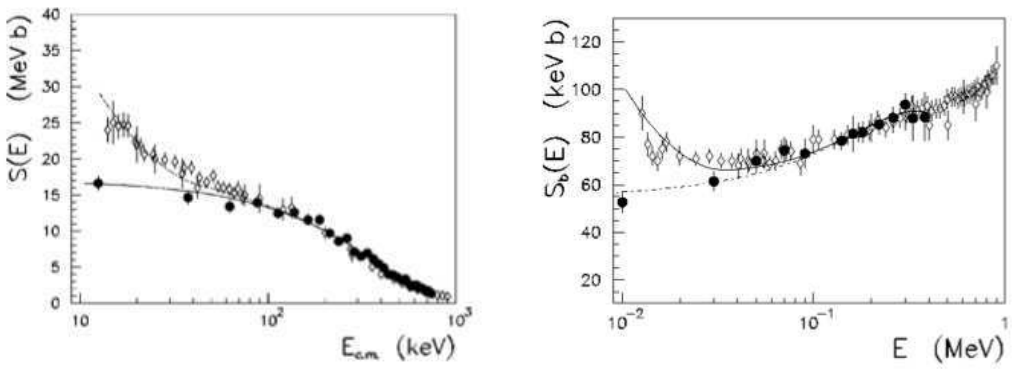

(a) (b)

Figure 3.5: (a) Astrophysical factor for the ^{6}Li + d $\longrightarrow$ $\alpha + \alpha$ reaction extracted using the THM method [Spitaleri et al., 2001] (full circles), and compared with direct data [Engstler et al., 1992] (white diamonds).
(b) Astrophysical factor for the ^{7}Li + p $\longrightarrow$ $\alpha + \alpha$ reaction obtained with the THM [Lattuada et al., 2001] (full circles) compared with direct measurements [Engstler et al., 1992] (white diamonds). In both figures the solid line is the best-fit used to extrapolate the astrophysical factor of bare nucleus at zero energy $S_b(0)$

In figure 3.5 the astrophysical factor for the ^{6}Li(d,α)^{4}He studied via the three-body ^{6}Li(^{6}Li,$\alpha\alpha$)^{4}He are shown (black circles) [Spitaleri et al., 2001], along with the direct measurement at low energies (white diamonds) [Engstler et al., 1992], while in figure 3.5b the astrophysical factor for the ^{7}Li(p,α)^{4}He extracted via ^{2}H(^{7}Li,$\alpha\alpha$)n (black circles) [Lattuada et al., 2001] and the direct measurements (white diamonds) [Engstler et al., 1992] are reported.

Given that the deuteron and the α particle inside ^{6}Li and the proton and the neutron inside ^{2}H are weakly-bound (E_B 1.47 MeV and 2.22 MeV, respectively), in the experimental application of the THM for α and d-induced (^{6}Li), and for proton or neutron induced (^{2}H) reactions, those nuclei can be used. In the present work we will use a ^{6}Li beam impinging on a ^{7}LiF target to study the ^{19}F(α,p)^{22}Ne, starting from the three-body reaction ^{6}Li+^{19}F$\longrightarrow$p+d+^{22}Ne (in which the deuterium acts as a spectator) and a ^{23}Na beam colliding with a CD_2 target to study the ^{23}Na(p,α)^{20}Ne via the ^{23}Na+d$\longrightarrow$ ^{20}Ne+α+n reaction, where this time the spectator is the neutron. As can be easily understood from the results shown until now, the THM is a really useful and a powerful experimental technique for cross-section determination at astrophysical energies.

CHAPTER 4

Preparation of the experiments

In the first part of the following chapter the experimental features for Trojan Horse (TH) application will be explained. After that, a more specific explanation of the experiments meant to study the $^{19}F(\alpha,p)^{22}Ne$ and $^{23}Na(p,\alpha)^{20}Ne$ reactions using the THM will be made, paying attention to the reasons that led us to choose which nuclei to use as projectile and target, where to place our detectors and the two different experimental set-up used.

4.1 Experimental conditions

The first thing to ascertain when TMH can be used is to verify a certain number of conditions, involving the nuclear structure of the TH nucleus and the status of the outgoing particles.
The necessary conditions about nuclear structure are:

- The TH nucleus must show an evident cluster structure;
- The binding energy of the particles composing the cluster must be negligible if compared with the beam energy;
- The momentum distributions of the particles inside the cluster must be known [Pizzone et al., 2005];

To apply the THM, a nucleus that can be described as A= x$\oplus$s must be chosen as TH nucleus, in which x is the participant and s the spectator. If those conditions are

satisfied, a two-body reaction like the one below

$$a + x \rightarrow C + c \tag{4.1}$$

can be studied using the three-body process

$$A + a \rightarrow C + c + s \tag{4.2}$$

Among the nuclei with evident cluster structure, a favorable choice can be to use the one that has the smallest binding energy. In this way, the QF probability to occur can be maximized. In our cases ^{6}Li, that shows a well-known cluster structure $\alpha \oplus$ d with binding energy E_b=1.47 MeV, and ^{2}H that can be described as a system p $\oplus$ n with binding energy E_b=2.22 MeV. Those were therefore chosen as THM nuclei. All four particles distributions inside the respective clusters are well known [Barbarino et al., 1980; Zadro et al., 1987; Cherubini et al., 1996; Spitaleri et al., 2001; Pizzone et al., 2005].

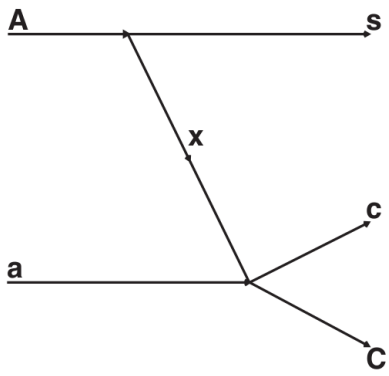

Figure 4.1: Feynman pseudo-diagram for the three-body reaction.

In figure 4.1 a three-body process is sketched, under the hypothesis that the break-up is in the beam particle (if the TH nucleus is in the target, the figure is just tilted upside-down). The total momentum of the TH nucleus is equal to $\mathbf{p_A} = \mathbf{p_s} + \mathbf{p_x}$, and its momentum before the collision must be considered: if the break-up takes place inside the target, the momentum distribution of the spectator particle is equal to $\mathbf{p_x} = -\mathbf{p_s}$. In both cases, the momentum of the x particle composing the cluster can be in principle experimentally measured, given that it is one of the three particles in the exit channel.

The THM will be applied to the ^{6}Li(^{19}F,p^{22}Ne)d reaction with the aim to study the ^{19}F(α,p)^{22}Ne two-body process, and the ^{23}Na(d,α ^{20}Ne)n to study the ^{23}Na(p,α)^{20}Ne:

in the first case the TH nucleus is in the beam (^{6}Li = $\alpha \oplus$ d) and the spectator particle (d) will be detected, while in the second the TH nucleus is in the target (^{2}H = p $\oplus$ n) and the spectator particle (n) characteristics will be reconstructed from the detected ones (^{20}Ne and α).

The next step in the preliminary considerations is to look for some conditions in which the Coulomb barrier effects in the entrance channel can be overcome. Moreover the two-body reaction would take place inside the energy range of astrophysical interest, taking into account that the relative kinetic energy between the two particles in the entrance channel must be compensated by the binding energy between them. Therefore, to choose the beam energy, overcoming the Coulomb barrier is only the first step condition. The center-of-mass energy in QF conditions (E_{qf}), in fact, must lie as near as possible to the Gamow energy range (b factor in 2.24, if squared):

$$E_{qf} = E_A - E_{B(x-s)} \approx E_{Gamow} \tag{4.3}$$

Here $E_{B(x-s)}$ is the binding energy for the spectator particle inside the TH nucleus, and E_A is the energy of the beam for the two-body process in the center-of-mass reference frame. By means of 4.3, the beam energy E_{beam} can be extracted, in the laboratory reference frame:

$$E_{beam} = [E_{B(x-s)} + E_{qf}]\left(\frac{m_x + m_a}{m_a}\right) \tag{4.4}$$

4.1.1 Selection of the kinematic conditions

The THM needs the detection of at least two out of the three outgoing particles: in a three-body reaction, once the emission angles of two out of three particles and the energy of one of those are known, emission angle and energy of the third particle in the exit channel is univocally determined.

The quasi-free contribution will be maximum for p_s=0, where the momentum distribution of the spectator inside the TH nucleus shows its peak. This must be true whether the TH nucleus is in the target or in the projectile, and in the second case the energy of the beam must be taken into account. Using the classic energy and momentum lconservation aws for such a case, a system composed by three equations

in four variables can be established:

$$\begin{aligned} E_A + Q &= E_c + E_C + \frac{p_s^2}{2m} \\ p_A &= p_c cos\vartheta_c + p_C cos\vartheta_C + p_s \\ 0 &= p_c sin\vartheta_c + p_C sin\vartheta_C \end{aligned} \tag{4.5}$$

where E_A and p_A are the energy and the momentum of the TH particle, and E_C, E_c, p_C, p_c, ϑ_C and ϑ_c are energies, momenta and angles of the particles coming from the a(x,c)C reaction (see figure 4.1). Fixing energies and one of the two angles, the other one is determined univocally. If the momentum distribution has $p_s \neq 0$ (i.e. the break-up is in the projectile), angles are chosen in a way that leaves the p_s unchanged before and after the reaction. Finding the right couple of angles is important to maximize QF contribution, thus helping its identification and discrimination form all the other processes occurring.

Once the kinematic conditions are determined, the energy trend in the center-of-mass reference frame must be calculated using the post-collision prescriptions (E_{CM}=E_{c-C}-Q^{2B}_{value}) of the particles coming from the QF process versus p_s: this procedure is useful because it allows us do ascertain that, in these kinematic conditions, measurement in the energy region of astrophysical interest can be performed. This calculation will be compared to the experimental data with the aim to verify if there is agreement between those and the predicted momentum distribution of the spectator particle. Once the angles are chosen, a prediction of the emission energies of the fragments of interest can be made, again using a Monte Carlo simulation, and this is useful to determine the number and the thickness of the detectors[1].

It is obvious that an optimal calibration, both in energy and in angle, is fundamental, due to the narrowness of the region of interest. It is also necessary that all noises coming from parasite reactions are removed. It is also important to understand if there are parasite reactions that share the same two bodies in the exit channel, and in affirmative case this condition must be carefully examinated, and avoided if possible.

[1] In order to maximize resolution, the detected particles must stop inside the detectors

4.2 Detectors and Electronics

In every TH experiment, energy and position of the impinging particles are really important. Detectors with good position and energy resolution (less than 1 mm and less than 1% spacial and energy resolution) even for small values are therefore needed. Our choice was to use Position Sensitive Detectors (PSDs). Those must be placed following some angular conditions (explained in 4.3.3 and 4.6.3), and must have an adequate thickness to detect the incoming particle. With the aim to identify their charge and mass, ΔE-E technique was also used, but using different kind of detectors: silicon detectors for the ^{19}F(α,p)^{22}Ne reaction and ionization chambers for the ^{23}Na(p,α)^{20}Ne. The reasons behind it will be explained in the continuation of this paragraph.

4.2.1 Position Sensitive Detectors

The PSDs are solid-state detectors sensitive to the position where particles hit them.

This achievement is performed using the so-called charge division method. This kind of detector is composed by a diode, with a resistive electrode on the opposite face of the silicon buffer (figure. 4.2). From any event two signals will be produced: one proportional to the energy and another to the position. The former comes from the low-resistance electrode, while the latter passes through the high-resistance one, and it depends from the point where the particle is revealed. If a charged particle comes across the detector, it will be revealed at one of the extremities of it. This signal is proportional to the energy and to the resistance of the electrode produced by the material between the far end of the detector and the point where the particle has struck it. Therefore the P signal will be dependent also one the E one. On the other electrode the signal will be proportional only to the energy. Those two informations allowed us to identify the position where the signal has been produced. If, for example, a particle hit the detector at the position P, naming x as the distance between P and A (4.2), the charge collected at B will be equal to

$$Q_{x_1} = \frac{R_2}{R_{tot}} Q_E \tag{4.6}$$

with Q_E total charge produced by the diode-particle interaction (extracted from the low-resistance electrode), $R_2=\rho x/L$ and $R_{tot}=\rho L/s$ (being ρ the resistivity and s the

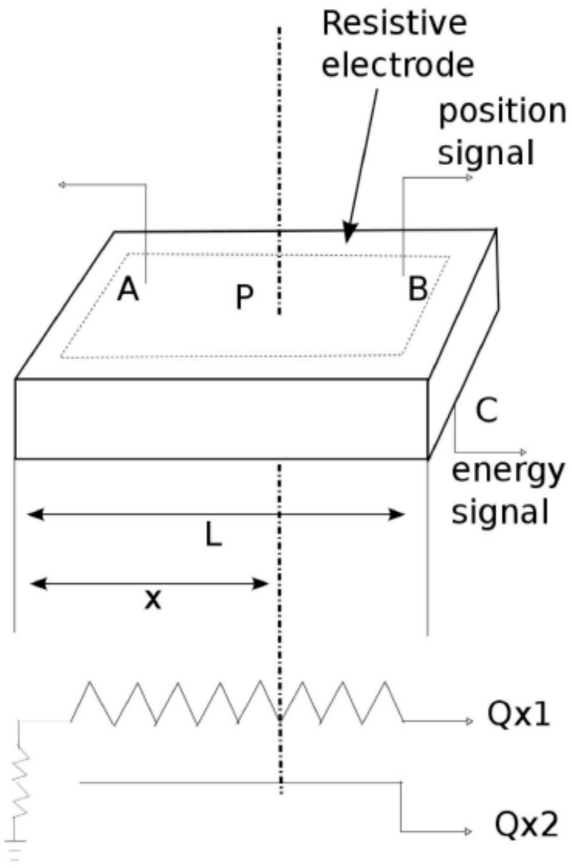

Figure 4.2: Operational scheme of a typical PSD: the incoming particle arrives on the P part, giving rise to a signal that is proportional to the energy and to the position (x) between A and B. On the C part the signal is proportional only to the energy.

surface area of the electrode). So the equation 4.6 can be written as

$$Q_{x_1} = \frac{x}{L} Q_E \tag{4.7}$$

and then

$$P \propto \frac{x}{L} E \tag{4.8}$$

Therefore a calibration in position of the signal is needed. The PSDs used for this experiment, produced by Micron Semiconductors, have a 1×5 cm^2 active area, and a scheduled spacial and energy resolution equal to 0.8 mm and 0.8%.

4.2.2 The ΔE-E tehchnique

Any charged particle, passing through some material, loses energy, ionizing the surrounding nuclei in the process. A formula that takes into account classic and

quantistic effects for particles different from electrons, and for velocities higher than some hundredth of the speed of light was proposed by Bethe and Block in 1930, and for a particle passing through a material made by nuclei with atomic number Z, mass number A and density ρ has the following expression:

$$-\frac{dE}{dx} = 2\pi\frac{N_A Z\rho}{A} r_e^2 m_e c^2 \frac{z^2}{\beta^2}\Big(\ln\frac{2m_e\gamma^2 v^2 W_{max}}{I^2} - 2\beta^2 - \delta - 2\frac{C}{Z}\Big) \tag{4.9}$$

In this formula:

- N_A is the Avogadro number;
- r_e is the classic radius of the orbit of an electron;
- m_e is the mass of the electron;
- z is the atomic number of the incoming particle;
- $\beta = \frac{v}{c}$, with v speed of the incoming particle and c speed of light;
- I is the mean ionization potential;
- $\gamma = \dfrac{1}{\sqrt{1-\beta^2}}$;
- W_{max} is the maximum energy transferred to an electron in a collision;
- δ is the so-called density correction, that compensate for the rapid increase of the logarithm for high values of γ.
- C is the shell correction, important at low energies

So the energy per unit of distance lost by a charged particle in the traversed material $\left(-\frac{\mathrm{dE}}{\mathrm{dx}}\right)$ is proportional to

$$-\frac{dE}{dx} \propto z^2\rho\frac{1}{\beta^2}\ln\beta\gamma \tag{4.10}$$

From equation 4.10 it appears clear that different charged particles at the same energy will lose different amounts of energy in the same material: for example an α particle will lose four times more energy than a proton of the same energy [Leo, 1994]. Using a detector thin enough to not stop the particle but able to measure the energy that the particle has lost in in correlation with a thick one behind that measures its residual energy, particle discrimination by their charge is possible: different particles in fact will lie on different curves depending on it. Plotting the the energy

loss (retrieved by the thin detector) versus the residual energy (measured used the thick one), different hyperboles depending on z^2 will rise. This is the so called ΔE-E technique for particle discrimination.

In the ^{19}F(α,p)^{22}Ne, 3 mm radius silicon detectors were used as ΔE stages, and a signals proportional to energy were xacquired (all the reasons behind this choice will be explained later in this chapter). The way they work is the same of the resistive part of the PSDs, with the difference that in this case energy loss is measured.

For the ^{23}Na(p,α)^{20}Ne, ionization chambers were used, because in this second experiment the identification of the heavy fragment was decided[2], and those had too low energies to pass through solid ΔE stages.

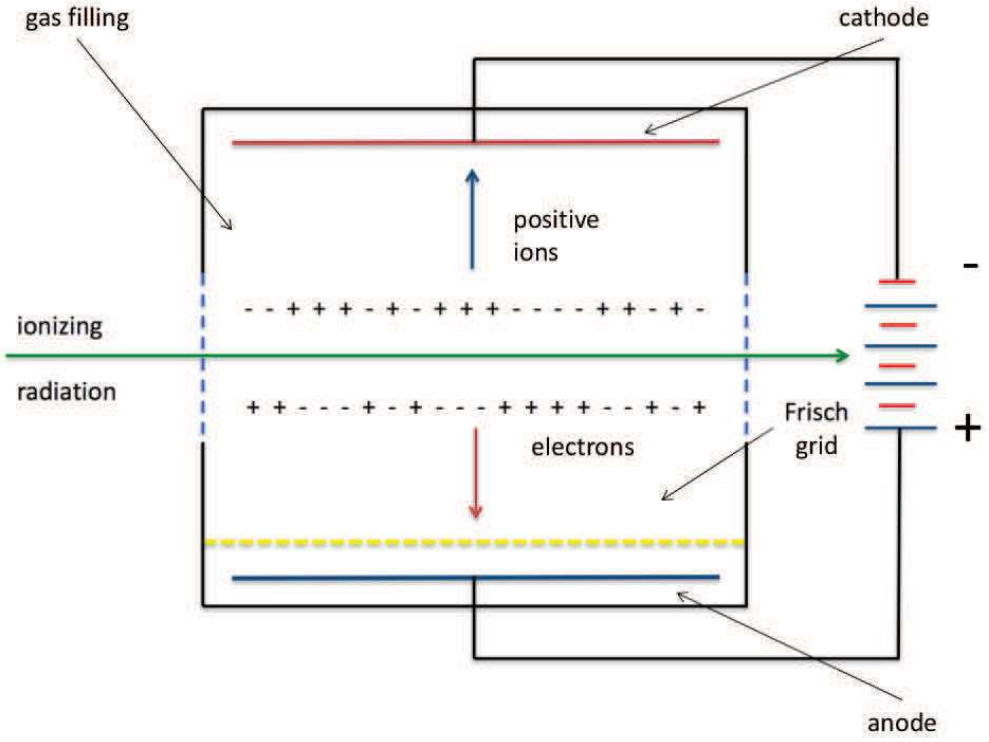

Figure 4.3: Cartoon of a ionization chamber.

The ionization chamber is a device usually used to detect any kind of ionizing radiation, by measuring the amount of charge liberated by the interaction of it with suitable gases [Knoll, 2010]. It is sketched in figure 4.3, and it is composed by two conducting electrodes put inside a container filled with a certain gas. Those are connected to a power supply that maintains an electric field between the anode (positive, blue solid line) and the cathode (negative, red solid line). When the radiation (in this

[2] see Chapter 4.6

case charged particles) penetrates the chamber from a window of suitable thickness (light blue dashed line), its interaction with matter generates ion-electron couples, and the electric field present in the chamber will change due to induction: a ΔV signal is generated by the changing of the electrostatic energy coming from the drift of the charges towards the electrodes. This ΔV signal is proportional to the number of generated charges, therefore to the energy of the particle, and to the distance of the particle track from the electrodes, if the track is parallel to these. That means that for a fixed particle energy, the detector response is strongly dependent on the position of the track. To avoid this, a grid with intermediate potential between the electrodes and transparent to the electrons (called "Frisch grid", yellow dashed line in figure) is placed in front of the anode: this eliminates the dependence from the position. The drift velocity of the ion-electron couples due to the electric field will instead determine the fall time of the ΔV signal.
Ionization chambers are really versatile objects: the pressure of the gas inside it can in fact be widely variated, according to the energy loss of the particle of interest and to the resistance of the window. Increasing pressure, energy loss will also rise, and separation between different Z will be wider. If the ionization chamber has also an exit window, another detector can be placed behind it, and so the ΔE-E technique can be used, with the ΔE stage that measures the energy loss of particles inside it, and the back detector that can be used to measure the final energy of those particles. Proper simulations showed how Isobutane (C_4H_{10}) was the best solution to energy loss measures, because it provided the the best separation between different isotopes at a favorable pressure (50 mb in our case). To avoid gas contamination, it must circulate from the gas bottle to the chamber, and then in an appropriate system for gas disposal.

4.2.3 Electronics

Let us now discuss in a really schematic way how the electronic chain operated. For this reason let us imagine the simplest nuclear physics experiment: an incoming beam, and two detectors, placed at the opposite sides of the beam at certain angles.

Such experiment is represented in figure 4.4: here a ΔE-E telescope and a single-stage detector are present. This is, indeed, really similar to the experimental set-up for both the ^{19}F(α,p)^{22}Ne and ^{23}Na(p,α)^{20}Ne, with the difference that in those two

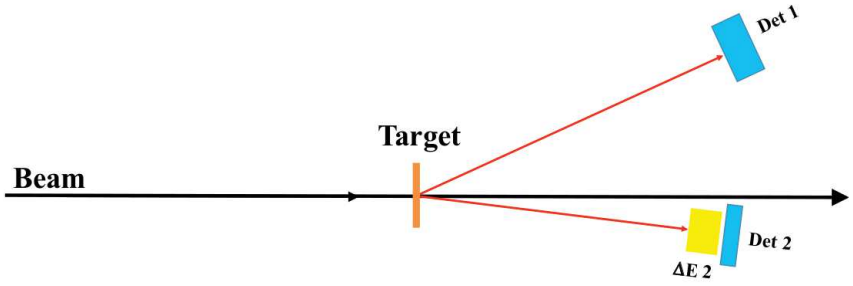

Figure 4.4: Sketch of a simplified experiment of nuclear physics

there are five PSDs (two telescopes) in the first and four PSDs (two telescopes) in the second. The only difference between the case sketched in figure 4.4 and the "real" set-up of the two experiments will be the number of channels that will go to the acquisition system. The way they will be delivered and processed is almost the same. The electronics used for the basic experiment can then be sketched as in figure 4.5.

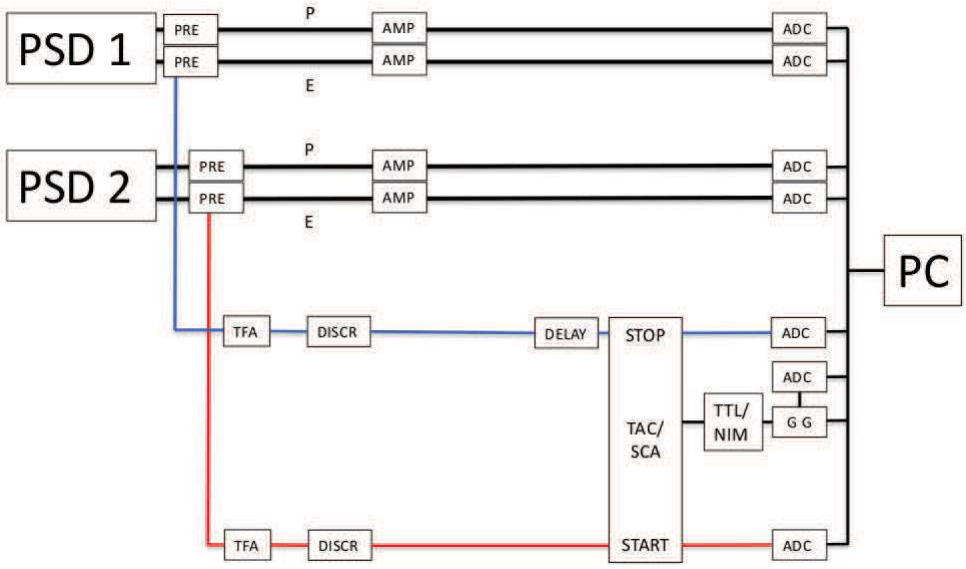

Figure 4.5: Sketch of the used electronic framework: pre-amplifiers (PRE), slow amplifiers (AMP), fast amplifiers (TFA), delays (DELAY), gate generator (GG), discriminators (DISCR), time to amplitude converter (TAC), TTL-NIM-TTL converter (TTL-NIM) and ADC.

For PSDs, two signals are delivered by the detector: one proportional to the energy and the other to the position. The energy signal coming from the amplifier was duplicated into two components: one is sent to the ADC (slow component), and the other followed the other path of the electronics (fast component). Position and ΔE

signals (not reported in figure) were treated in the same way as the slow component of the energy. All the signals coming from PSDs and ΔE stage are delivered from the pre-amplifiers (that increased the signal-to-noise ratio) to the amplifiers, with the aim to shape it in the best possible way, improving resolution. The acquisition trigger[3] is given by the signals of the two E detectors, and the first one to arrive to the START/STOP module opens the coincidence window, a period of time in which the event will be acquired. Once the second signal arrives the acquisition window will be closed and the TAC/SCA module will communucate with the ADC (Analogic to Digital Converter): processed signals are then collected by the ADC and then digitalized and stored in the PC disk. This situation corresponds to the case in which a particle crosses the telescope, and another is detected by the other. About the fast component, it will follow the other path of the electronics and is used to generate the acquisition trigger and gate.
Regarding the two different experiments argument of this thesis, ^{19}F(α,p)^{22}Ne and ^{23}Na(p,α)^{20}Ne, the electronics are not so different: the only thing to keep in mind is that there are a lot more parameters (thirteen for the first, ten for the second). Another difference is that an OR module is present in both experimentsthat is used to discriminate between different detectors operating in coincidence: this coincidence can be one-to-many (PSD1/PSD2-PSD3 in the first experiment) and and one-to-one (PSD1-PSD4 and PSD2-PSD3 in the second one).

4.3 Detectors Calibration

In paragraph 4.2.1 the way how the signal depends from energy was explained. From equation 4.8, it is possible to obtain energy and position information coming from the detectors, but they still need to be calibrated. To do so, some measurements in which the trigger is given by the logic OR of every signal coming from detector were performed: in this way every event detected was aso stored. In this phase every detector had a equally spaced grid with slits placed in front of it (figure 4.6). During calibrations for the ^{19}F(α,p)^{22}Ne, the ΔE detectors were removed, while in the other experiment both calibration with and without the ionization chamber were performed.

[3] Events that start the acquisition

Figure 4.6: PSD holder and grid.

Using a theodolite, the measure of the central positions of any detector and of any of the eighteen spacings was performed. The arm on which the detectors are fixed moves on a graduate ferrule with a 0.1° precision, while the spacings of the grids are 1 mm large. These positions are then compared with the geometrical positions expected for the central values of the spacings, that are already known. Their presence in the calibration phase was fundamental, because it allowed us to establish a correspondence between measured angles and position signals. Calibrations were made using elastic scattering (in the present cases ^{6}Li at 6 MeV and ^{23}Na at 58 MeV on ^{197}Au and CD_2 targets) , standard α-source, or some well known two-body reactions.

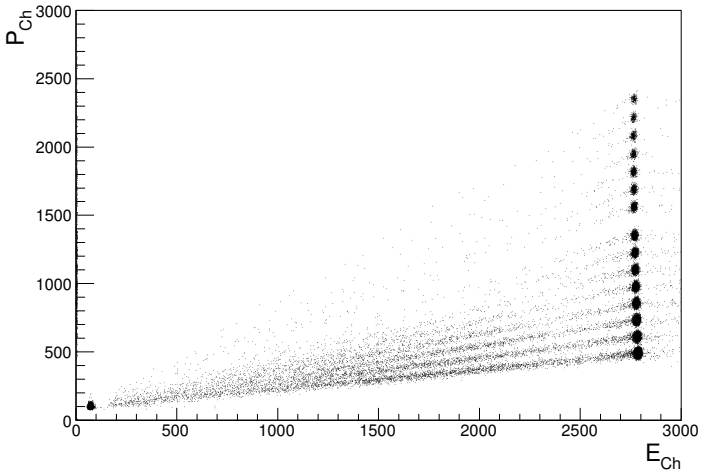

Figure 4.7: Not calibrated typical position versus energy 2D-spectrum (hydrogen beam on ^{197}Au, E_b=5 MeV). Some of the spacings are not visible.

4.3.1 Position Calibrations

To eliminate the dependency of position from energy, the following relation, based on equation 4.8, must be used:

$$x_i = \frac{P_i - P_0}{E_i - E_0} \tag{4.11}$$

with 1<i<n (n=number of spacings), while P_0 and E_0 are constant values to be determined with fit procedures.
The spacings gave rise to the not calibrated 2D-spectrum in figure 4.7, where P_{Ch} and E_{Ch} are the channel signals linked to position and energy, respectively. Once i is fixed, a linear dependency between position and energy is established, and a linear fit procedure can be performed.

$$P_{Ch} = a(\vartheta) + b(\vartheta)E_{Ch} \tag{4.12}$$

Now our aim was to obtain a correspondence between the signals coming form the detector and the angle ϑ corresponding to the position at which it was generated. So linear fits on the $a(\vartheta)$ and $b(\vartheta)$ parameters were performed

$$\begin{aligned} a(\vartheta) &= p_1\vartheta_i + p_2 \\ b(\vartheta) &= p_3\vartheta_i + p_4 \end{aligned} \tag{4.13}$$

The (4.13) gave rise to two functions that, by substitution in (4.12), allowed us to obtain an angle-channel correspondence. This procedure in the end associated any position peak to an angular value. The so obtained calibration function has the following form

$$P_{Ch} = [p_1\vartheta + p_2] + [p_3\vartheta + p_4]E_{Ch} \tag{4.14}$$

and finally

$$\vartheta[deg] = \frac{P_{Ch} - p_2 - p_4E_{Ch}}{p_1 + p_3E_{Ch}} \tag{4.15}$$

This equation finally ties the detection angle with energy and position signals.

4.3.2 Energy Calibration

About energy, it is related to signals by a linear relation:

$$E_{PSD}[MeV] = a + bE_{Ch} \tag{4.16}$$

To obtain *a* and *b* from a best-fit procedure one must be able to identify peaks in the P(ch) versus E(ch) 2D-spectrum, and to associate those peaks with proper energy values. Those are calculated using simulation codes for two-body reactions, taking into account energy loss of the beam particles and of the outgoing ones. Emission angles must be also considered, to better ascertain how much energy the outgoing particles are losing, given that every particle has a different path for different detection angles. This procedure was also made using LISE++ [Tarasov and Bazin, 2008].

Now the best-fit procedure (equation 4.15 and 4.16) must be applied, and the result is the 2D-spectrum in figure 4.8. The fact that the dependence of the position from the energy has been removed can be easily ascertained considering that now spots at different energies share the same position (angle, in this case) of detection, giving rise to a certain linearity in ϑ.

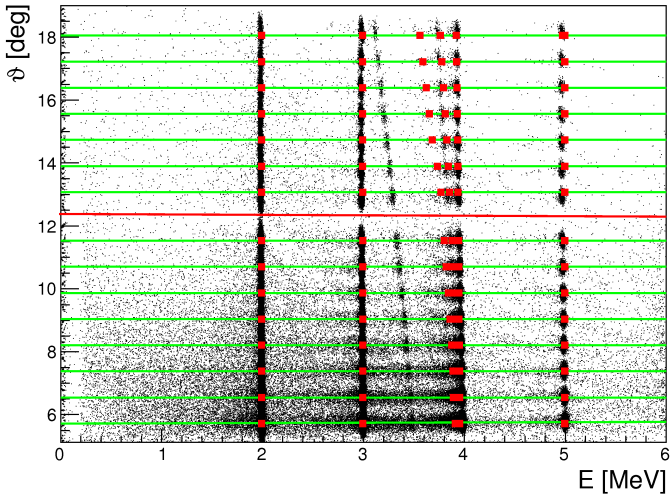

Figure 4.8: Calibrated 2D-spectrum. The green lines represents the central angular values for every spacing, and the red one the central angle of the detector. Red squares represents the theoretical values of energy and position for the i H+^{197}Au and H+CD_2 reactions at different energies[Tarasov and Bazin, 2008].

It is now important to take into account the different energy loss of particles while crossing the target at different angles, the ΔE and the absorbers (the last two if present). It is therefore utterly important to take into account those elements when the association between the signal and the "true" energy is made. This can be made after some calculations, made in this case using LISE++ [Tarasov and Bazin, 2008]: with this program one can calculate how much energy a certain particle loses in

every crossed layer, even considering the different angle of emission, and so the different paths, as a function of the revealed energy, ΔE=f(E$_{res}$). To explain this procedure let us consider a particle crossing two different materials before reaching the detector. For the first material crossed by the incoming particle, a calculation of energy loss is made at different energies. Those are chosen taking into account the energy range of the outgoing particles previously calculated by means of theoretical calculations. After that a best-fit using a proper function (polynomial, exponential or $f(x)$=ax^n function) is performed on the energy of the incoming particles versus energy loss plot. In this way a theoretical trend of energy loss in the material with respect to the energy of the incoming particle can be extracted. The outgoing energies of the particle are then used as impinging ones for the second layer, and with the same procedure the final values are calculated. At last, to take into account energy loss, the final step is to take the energies coming from calibrated detectors and use this last function to calculate the energy that the particle had before the layer, using the fitting function found so far, so E=ΔE+E$_{res}$. This energy will then be used to do the exact same thing for the first layer. In this way a calculation of the "true" energy of an incoming particle can be made.
This concludes the general part of this chapter. In the following all the specifics of the two different experiments will be explained.

4.4 The ^{19}F(α, p)^{22}Ne reaction: preparation of the experiment

Now that all the general features of a THM experiment are known from both a theoretical and experimental point of view, let us discuss the first key point of this thesis: the ^{19}F(α,p)^{22}Ne reaction studied via the ^{6}Li(^{19}F,p^{22}Ne)d by means of the Trojan Horse Method. But first let us discuss the state of the art for the two-body reaction

4.4.1 State of the art

The ^{19}F(α,p)^{22}Ne reaction, as stated in Chapter I, is one of the main destruction channels in AGB-stars. For such stars, whose temperature is at about $0.2\cdot10^9$ K, the Gamow window lies between 200 keV and 760 KeV, while the Coulomb barrier for the two-body reaction of interest is 3.81 MeV. It is therefore obvious that the ^{19}F(α,p)^{22}Ne reaction occurs at energies far below the Coulomb barrier. This kind of

reactions can take place only if quantum mechanics via tunnel effect is considered. In fact this reaction has not been studied with direct method at astrophysical energies: the cross-section measurement at lowest energies near the Coulomb barrier arrived at E_{lab}=1100 keV for a α particle impinging on a fluorine target. Those were then used to perform *R-Matrix*[4] calculations by Ugalde et al. [2005, 2008] (figures 4.9 and 4.10).

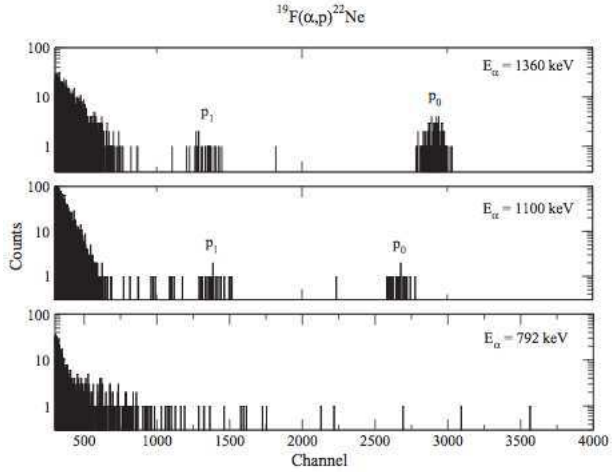

Figure 4.9: Proton spectrum at 135° for three different α beam energies (written in the figure). Groups of protons can be detected at 1360 keV and 1100 keV, while no evidences can be found at 792 keV.

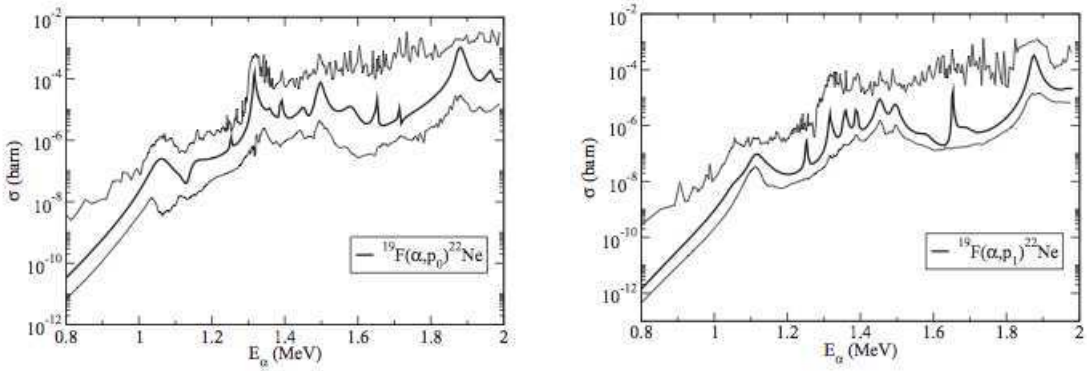

(a) (b)

Figure 4.10: Cross-section extracted with *R-Matrix* calculations for the $^{19}F(\alpha,p)^{22}Ne$ reaction. Both $^{19}F(\alpha,p_0)^{22}Ne$ (panel a) and $^{19}F(\alpha,p_1)^{22}Ne$ (panel b), corresponding to ^{22}Ne ground and first excited state respectively, are shown along with their uncertainties.

[4]See Chapter 5.5

The authors also tried to measure at E_{lab}=792 keV, but no experimental evidences came out whatsoever.

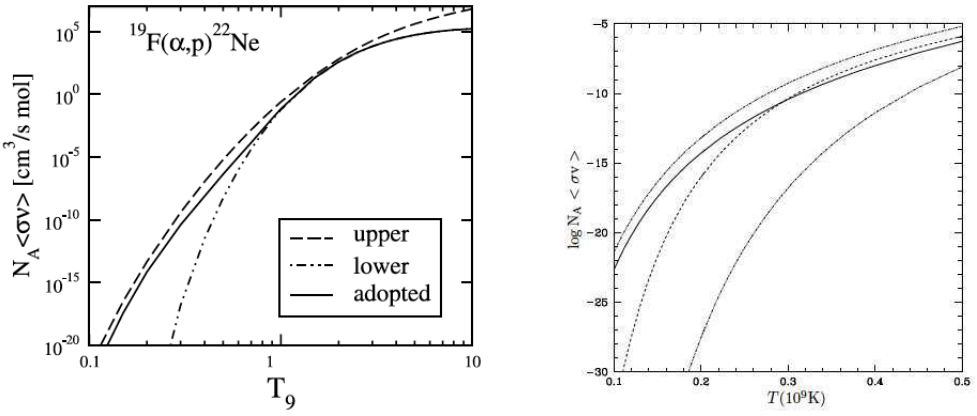

(a) (b)

Figure 4.11: a)Upper and lowers limit for the $^{19}F(\alpha,p)^{22}Ne$ reaction rate for an AGB-star (solid line).[Lugaro et al., 2004]
b)Upper and lower limits for the $^{19}F(\alpha,p)^{22}Ne$ in a WR-star (solid line). The limits are reported as pointed lines, while the dashed one is the $^{22}Ne(\alpha,n)^{25}Mg$ [Stancliffe et al., 2005]

From the two panels in figure 4.11 it appears clear how at T=0.2÷1 T_9 the uncertainties in the reaction rate are huge (circa ten orders of magnitude). It is therefore necessary to have a measurement of the reaction rate at lower energies.
In this work, a indirect measurement of the $^{19}F(\alpha,p)^{22}Ne$ reaction via the three-body one $^6Li(^{19}F,p^{22}Ne)d$ (Q=0.199 MeV) was performed using the Trojan Horse Method (THM).
An accurate measurement of the cross-section of the reaction in the Gamow window energy range would be of great importance to understand fluorine nucleosynthesis inside stars. The following experiment was built with this task.

4.4.2 Preparation of the experiment: experimental conditions

For the case under investigation a ^6Li beam impinging on a ^7LiF target was used. Given the well-known binding energy of the cluster (1.47 MeV), if the energy E_{qf} is equal to the Gamow peak (≈430 keV if T=0.2 T_9), equation 4.4 gives the value E_{beam} ≈2.3 MeV, far lower than the Coulomb barrier previously calculated. Then the experiment was performed using a ^6Li beam with energy equal to 6 MeV, so slightly above the Coulomb barrier for the three-body one (5.42 MeV). This is the lowest

energy at which such a beam with enough focusing[5] (1 mm) could be delivered in Ruđer Bošković Institute (Zagreb). This choice allowed us to have useful events for normalization purposes. Furthermore the beam energy in equation 4.4 is referred to the condition p_s=0, that is not reachable with our experimental set-up: this value, in fact, corresponds to zero degrees in the laboratory reference frame, making it impossible to measure with silicon detectors that would be destroyed by the beam. The minimum spectator momentum for this case is at 25 MeV/c, value low enough to have the presence of QF processes.

Another choice would have been to go to sub-barrier energies, but the cross-section for those reactions is very low, making such a measure too expensive in terms of time.

4.4.3 Selection of the kinematic conditions

Using the (4.6), it is possible to get a precise idea of the angles at which the three body reaction will be detectable. From a kinematic analysis made by means of Monte Carlo simulations, the optimal choice would be at small angles, but this could be a problem if elastic scattering of ^{6}Li on ^{19}F is considered: the rate of incoming particles would be too high to manage for the detectors, that would eventually burn out.

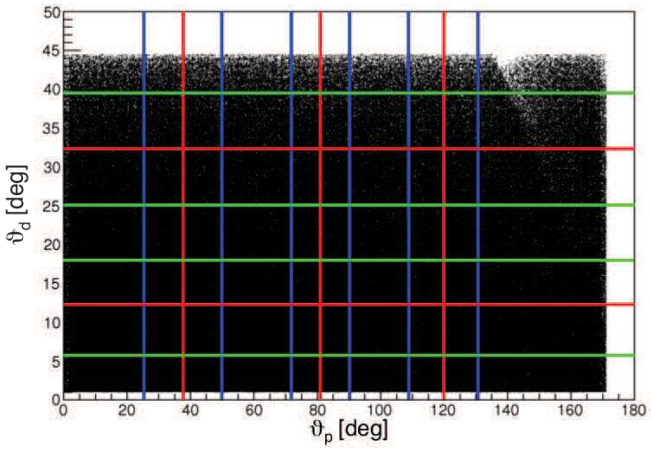

Figure 4.12: Angular range for the two detected particles (exact angular ranges are reported in table 4.2). The red lines represent the central values of the detectors, while the blue and green ones the extremities. In this simulation, only events with p_s <60 MeV/c are considered

[5]Focusing is really important due to the necessity to reconstruct the exact angle of the outgoing particles, as stated in chapter 4.1

The positions of the detectors were chosen taking this fact into account, along with the obstacles coming form the supports. The final angular ranges covered by the experimental set-up are sketched in 4.12: now that angular ranges are decided an idea of the trend of $\mathbf{p_s}$ versus $E_{C.M.\,(p-^{22}Ne)}$ and of the energies of the detected particles are useful, again to ascertain the energy range where parasite reaction can occur and at which momentum values, and to choose the right detectors.

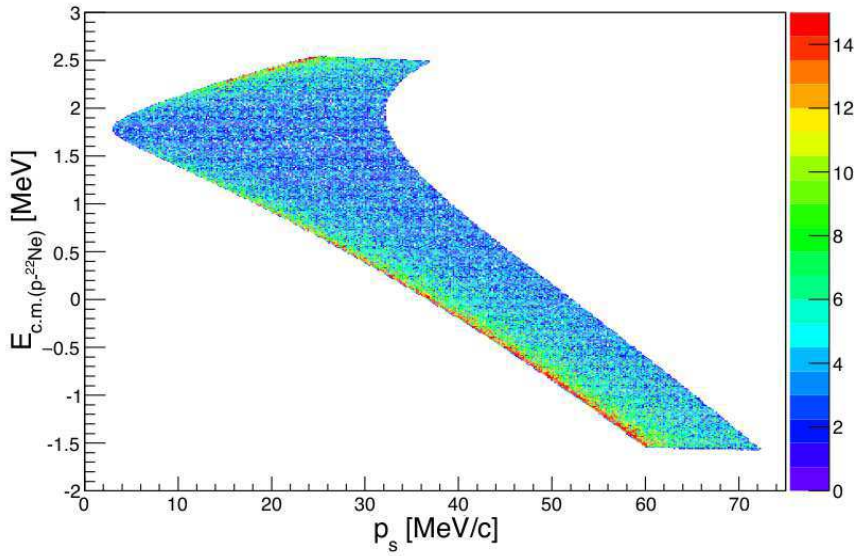

Figure 4.13: Predicted 2D-spectrum $E_{C.M.}$ versus $p_s$for $23° < \vartheta_p < 54°$ and $2° < \vartheta_d < 22°$. As can be seen, all the QF contribution is inside the preferred region.

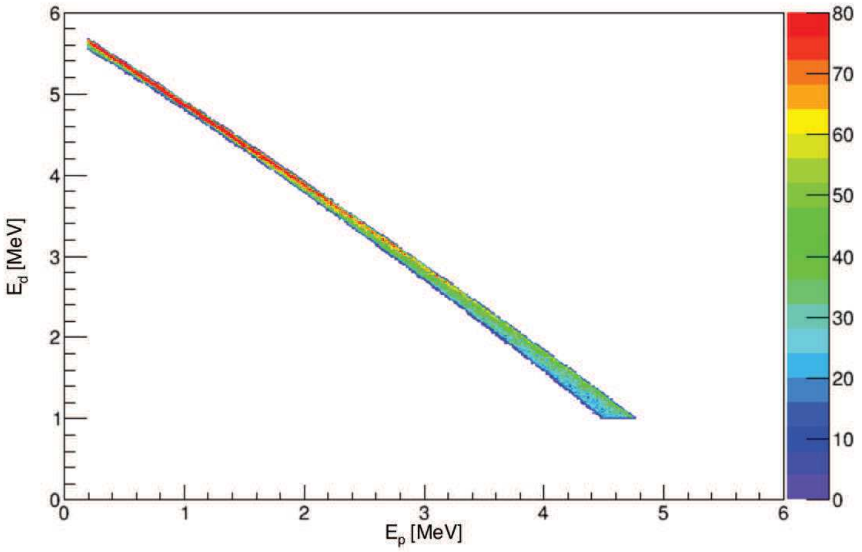

Figure 4.14: 2D-spectrum proton energy versus deuteron energies, with the same cuts reported in figure 4.13.

Given the maximum energy values for protons and deuterons (cfr. figure 4.13) at the designed angles, 500 μm thick PSDs where chosen for energy measurements, while two silicon detectors (round, 81.7 mm^2 active surface) 15 μm thick were chosen as ΔE stages.

4.4.4 Sequential mechanisms

The studied QF reaction is not the preferential channel in the three-body reaction: there are in fact sequential mechanisms[6] that have a much higher cross-section (several orders of magnitude). This makes quasi-free processes hard to detect, due to the fact that the outgoing particles are the same. It is therefore necessary to verify if those reactions can be isolated in some way from the QF process. The reaction used in this experiment is the three-body one in the exit channel

$$^{19}F + {}^{6}Li \rightarrow {}^{22}Ne + d + p \tag{4.17}$$

This reaction can be hindered by some background coming from sequential mechanisms. The reaction 4.17 can occur through three main channels that share the same particles in the exit channel of the reaction of interest:

$$\begin{aligned} {}^{19}F + {}^{6}Li &\rightarrow {}^{22}Ne + {}^{3}He^{*} \rightarrow {}^{22}Ne + d + p \\ {}^{19}F + {}^{6}Li &\rightarrow {}^{24}Na^{*} + p \rightarrow {}^{22}Ne + d + p \\ {}^{19}F + {}^{6}Li &\rightarrow {}^{23}Na^{*} + d \rightarrow {}^{22}Ne + d + p \end{aligned} \tag{4.18}$$

Among those three, the first one is not accessible: in literature there are no excited levels of the ^{3}He particle in the explored energy range [Firestone, 2007a]. About the second mechanism of (4.18), there are no levels reported in literature in the $E_{^{22}Ne-d}$ relative energy range spanned by this experiment (0.5$\div$4.5 MeV, corresponding to 14$\div$20 MeV, see figure 4.15): the highest energy level of ^{24}Na is in fact at 12.5 MeV [Firestone, 2007a] (figure 4.15), so there should not be any detectable interferences coming from this channel. About the third reaction of 4.18, it can not be disentangled from the QF process if not after some considerations about the momentum distribution of the spectator particle for the QF process itself. Some resonant contributions from ^{23}Na are therefore expected.

[6] A *sequential mechanism* is a process that goes through the formation of a compound nucleus that will decay after some time producing some other particles.

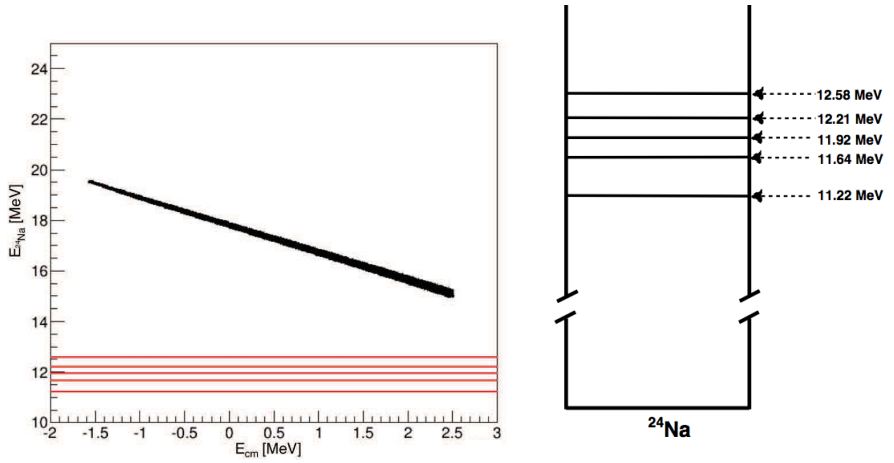

(a) (b)

Figure 4.15: a)2D-plot obtained by Monte Carlo simulation for the ^{19}F +^{6} Li $\rightarrow^{24}$ Na + p. The red solid lines represent the last excited states of ^{24}Na that can be populated by sequential mechanism.
b)Not-in-scale diagram of the levels corresponding to the red lines.

4.5 The ^{19}F(α, p)^{22}Ne via the THM: experimental set-up and calibration

Taking into account what was discussed before, an experiment was performed at Ruđer Bošković Institute (Zagreb), where a ^{6}Li beam with enough collimation is available, as stated earlier in this chapter. This beam collided into a ^{7}LiF target with a ^{12}C backing (produced at LNS-Laboratori Nazionali del Sud). This chemical composition was chosen because it allowed us to well separate the three-body reaction of interest from parasite reactions coming from ^{7}Li and from the carbon backing. ^{6}Li is a good candidate to be a TH nucleus, because of its well-known cluster structure. For this experiment two targets 106 μg/cm^2 and 141μg/cm^2 were used, with 29μg/cm^2 and 23μg/cm^2 ^{12}C backing respectively. The beam had 5 enA intensity and, if one presumes that the reaction is taking place in the middle of the target, the beam energy loss are 0.04 MeV and 0.09 MeV respectively.

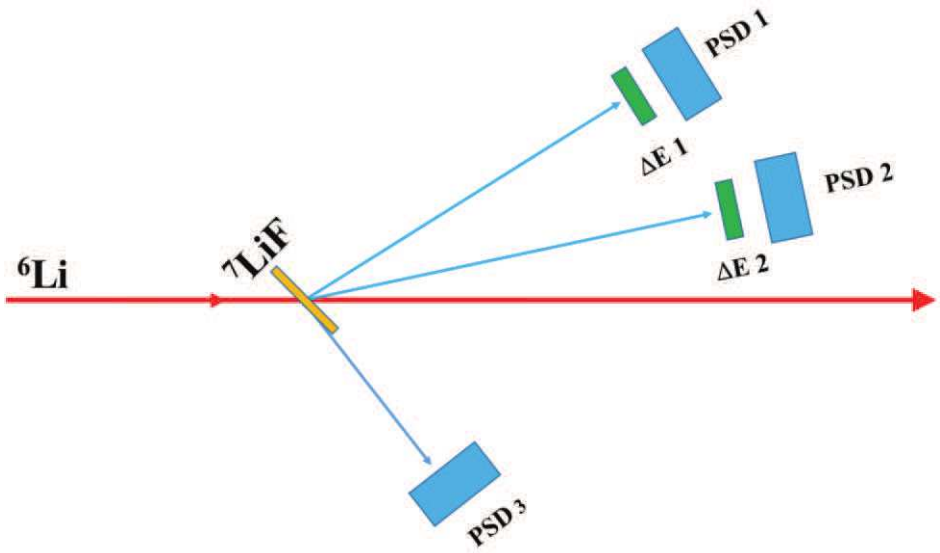

Figure 4.16: Sketch of the experimental set-up

The experimental apparatus is reported in figure 4.16: three position sensitive detectors (PSDs) made by a 500 μm silicon thick buffer were used. Those worked in coincidence (PSD1 and PSD2 with PSD3) and were centred at definite quasi-free angles, as reported in table 4.1).

Before PSD1 and PSD2 two thin silicon detectors (15 μm) are placed at 6 cm and 7.5 cm: those are used for particle identification by means of the ΔE-E technique, with the aim to discriminate deuterium nuclei. A coincidence window of 250 ns was also established to reduce the background. Elastic scattering of ^{6}Li on ^{19}F is a great problem for this experiment. Its rate on PSD2 was calculated using simulations, and it appeared to be ≥ 4kHz (for a 6 MeV ^{6}Li beam with 5enA current impinging on a ^{7}LiF target, calculations made using LISE++ [Tarasov and Bazin, 2008]), but such a quantity would rapidly damage the detector. For this reason, a thin aluminium foil (15 μm) was placed in front of PSD2.

About the target, it is tilted at 45° with respect to the beam direction: this was useful to maximize the counting rate of deuterons on PSD1 and PSD2. In this way in fact the target length that particles must pass through after the reaction is shorter, and this has proven to be crucial given the low energies of deuterons involved. About protons, those have enough energy to punch through the tilted target without any significant reduction in its number.

Det.	Angle [deg]	Distance[cm]	Range [deg]	$\Delta\Omega$[mSr]
PSD1	32.3	17.63	±7.21	16
PSD2	12.3	20.61	±6.58	12
PSD3	-37.7	10.3	±12.4	47
ΔE1	32.3	6	±9.65	89
ΔE2	12.3	7.5	±7.74	57

Table 4.1: Experimental features of the set-up described in the text

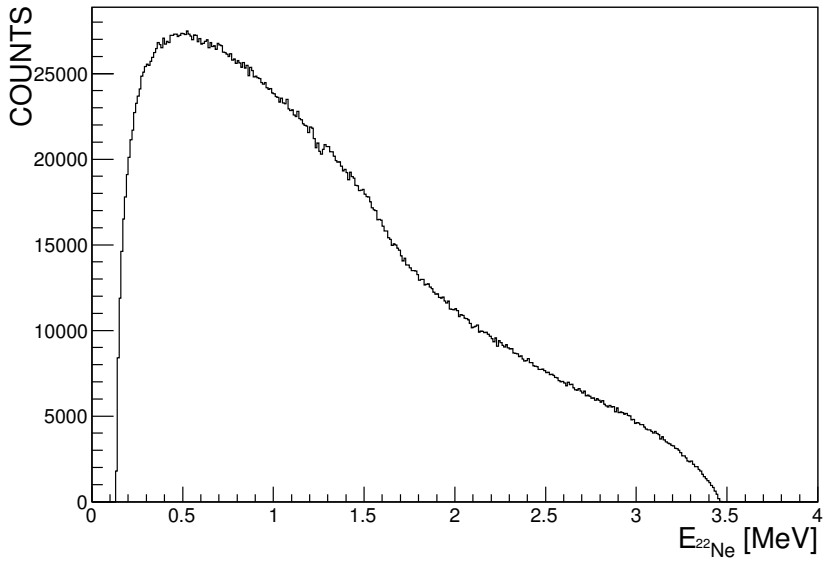

Figure 4.17: ^{22}Ne energy distribution derived using a Monte Carlo simulation

To our purpose it is necessary to detect at least two particles in the exit channel, so protons, deuterons or ^{22}Ne particles. Among those three, ^{22}Ne is impossible to detect: from a proper Monte Carlo simulation, in fact appears clear that it is emitted at forward angles ($0 \leq \vartheta_{^{22}Ne} \leq 6$) and with maximum energy at about 3.5 MeV (figure 4.17). At such low angles the contribution of the elastic scattering would be too great (even with absorbers), while energy loss and angular struggling of the ^{22}Ne particle in the solid target would make its detection virtually impossible. Moreover, using thin silicon detectors for particle discrimination would have been impossible in this case, given that the ^{22}Ne particle would need at least 11 MeV to pass through them, and ionization chambers would be too bulky to be installed at the chosen angles.

For this experiment, PSD1, PSD2 and PSD3 were calibrated using the procedure explained in section 3, by means of standard three-peaks α-source (^{239}Pu, ^{241}Am and ^{244}Cm) and by several scattering reactions:

- H on ^{197}Au 104 μg/cm^2 thick target at different energies (5, 4, 3, and 2 MeV)
- H on CD_2 97 μg/cm^2 thick target at different energies (5, 4, 3, and 2 MeV)

The linear relations for calibration are reported in the following table (table 4.2), and have the form expressed in section 3.

Detector	Position parameters [deg]	Energy parameters [MeV]
PSD1	$p_2 = 151.8$, $p_4 = -1.17$ $p_1 = -3.3685$, $p_3 = 0.052815$	$a = 0.0019247$ $b = -0.11463$
PSD2	$p_2 = 97.665$, $p_4 = -0.17381$ $p_1 = -3.3443$, $p_3 = 0.055534$	$a = -0.11291$ $b = 0.0018355$
PSD3	$p_2 = 129.12$, $p_4 = -0.62465$ $p_1 = -2.2984$, $p_3 = 0.029514$	$a = -0.12998$ $b = 0.0018423$

Table 4.2: Fit parameters for the calibrated detectors

Taking into account the presence of the absorber in front of PSD2, and of the ΔE detectors in front of PSD1 and PSD2, energy losses are evaluated following the prescription briefly explained in section 3, and the total energy of the incoming particles can now be measured. In the following analysis, only PSD2-3 coincidence will be reported: this is due to the fact that only this coincidence bears signs of QF processes.

4.6 The ^{23}Na(p, α)^{20}Ne reaction: preparation of the experiment

As stated in Chapter 1, the ^{23}Na(p,α)^{20}Ne has raised the interest of the scientific community due to Na anticorrelation with oxygen in GC, and one of the many sites proposed for its formation are intermediate-mass AGB or Super-AGB stars. In those scenarios the destruction of sodium becomes really important because the reactions ^{23}Na(p,γ)^{24}Mg and ^{23}Na(p,α)^{20}Ne are the turning point between NeNa and MgAl-cycles. Their relative branching ratio is therefore utterly important, but there are no available data about the cross-section and the S(E)-factor in the temperature range proper of the quiescent burning (20$\div$80 T_6) and hot bottom burning (70$\div$100 T_6). At those temperatures, the Gamow window lies between 50 keV and 200 keV, while the Coulomb barrier for the reaction is 2.57 MeV, so the reaction (as usual) in stellar environment takes place well below the Coulomb barrier thanks to the tunnel effect.

4.6.1 State of the art

As for the ^{19}F(p,α)^{22}Ne, even the ^{23}Na(p,α)^{20}Ne has not been studied at astrophysical energies with direct methods in the energy range of astrophysical interest. Several states of ^{24}Mg were however studied by Hale et al. [2004], via the ^{23}Na(^{3}He,d)^{24}Mg transfer reaction (figure 4.18): a 20 MeV ^{3}He beam was delivered on two separate NaBr targets (49 and 102 μg/cm^2 respectively), with intensity between 100 and 150 pnA. The outgoing particles were momentum-analysed using a Split-Pole spectrometer and detected with an avalanche counter, at angles between 5° and 22.5° in the laboratory reference frame in 2.5° steps and between 25° and 35° in 5° steps.

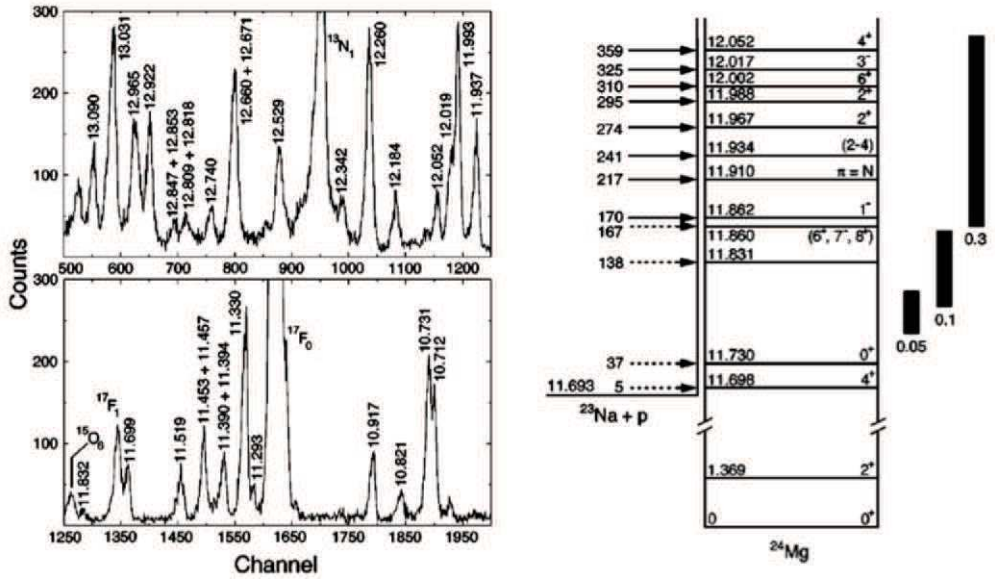

Figure 4.18: Left panel: deuteron spectrum at θ_{lab}=12.5°. The peaks are labelled by energy in ^{24}Mg or by the final state formed from a contaminant in the target [Hale et al., 2004]
Right panel: level scheme for ^{24}Mg. The Gamow windows corresponding to 50 T_6, 100 T_6 and 300 T_6 are shown to the right [Hale et al., 2004].

A resonant state at $E_{C.M.}$=1398 keV has been found. This critically enhanced the ^{23}Na+p reaction rate. Another unexpected 37 keV resonant state has been found, but its low cross-section did not allowed the authors to study it. Anyway the reaction rate maximum contribution for the (p,α) reaction at 37 keV was reduced by a factor of 515, reducing the rate uncertainties for 45 T_6. Now the biggest source of uncertainties is the 138 keV resonance, that near 70 T_6 has an overall uncertainty by a factor of 12 [Hale et al., 2004] (figure 4.19, third pane, shaded area).

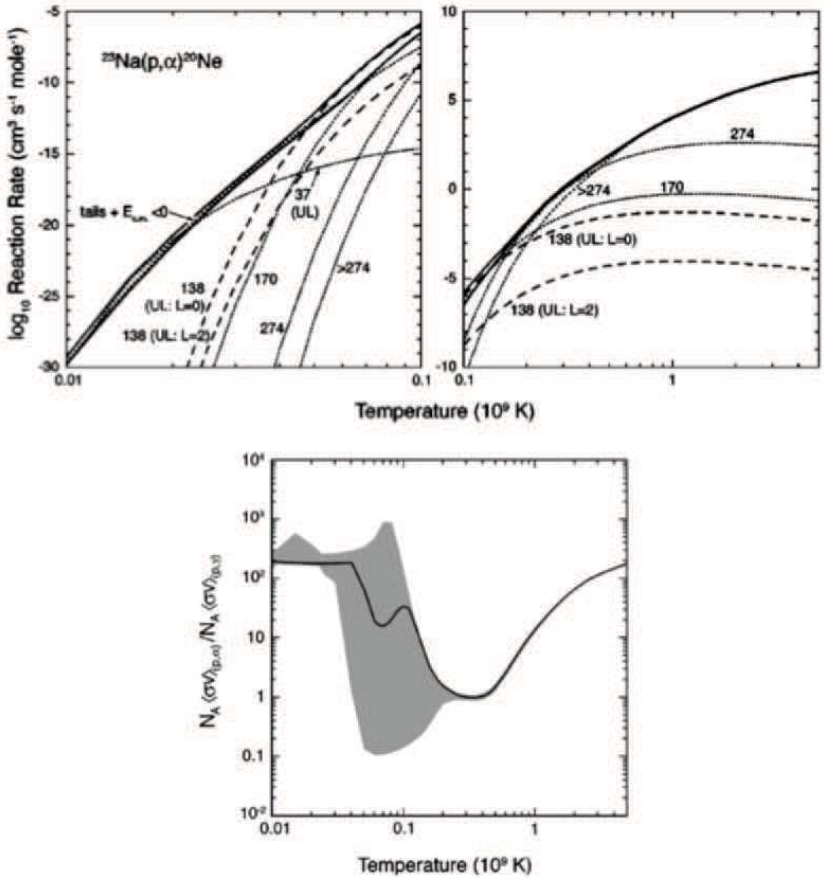

Figure 4.19: Upper panel: total reaction rate (solid line) and contribution of each resonance (dotted lines) for the ^{23}Na(p,α)^{20}Ne reaction. The dashed lines represents the upper limit for l=0,2 capture in the 138 keV state [Hale et al., 2004]
Lower panel: ratio between the (p,γ) and (p,α) reactions. The solid line are made using the recommended rate, and the grey zone denotes the uncertainties in the ratio (correlations in the uncertainties for the two reactions are also considered) [Hale et al., 2004]

The impact of the 138 keV resonance has been evaluated Rowland et al. [2004] in the region of temperatures interesting for Nova nucleosynthesis (0.2÷0.4 T$_9$). To do so, an experiment was carried out delivering a proton beam at energies between 130 and 400 keV with 100 μA current on a Na_2WO_4 evaporated on a tantalum backing. The aim of this experiment was to reduce the uncertainties of the (p,γ) channel and to understand if closed NeNa cycle in Nova explosion is possible or not (figure 4.20): Rowland et al. [2004] concluded that in the 0.2÷0.4 T$_9$ temperature range the branching ratio is close tu unity, so almost 50% of the ^{23}Na is lost after each cycle. So the all ^{23}Na will disappear after a fair number of NeNa and MgAl cycles: almost no NeNa cycle exists at those stellar temperatures, but only below (T≤0.1 T$_9$) and above (T≥0.6 T$_9$) . The large uncertainties about the ^{23}Na(p,α)^{20}Ne do not allow to understand the action of a closed NeNa cycle, and precise information are needed.

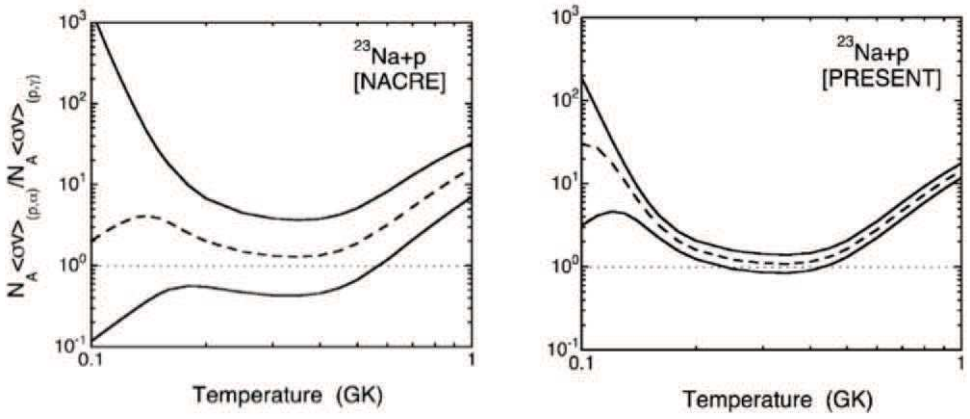

Figure 4.20: Left panel: ratio between ^{23}Na(p,α)^{20}Ne and ^{23}Na(p,γ)^{24}Mg before the work of Rowland et al. [2004]. The dashed line is the ratio of the recommended value, with the zone between the two solid line as uncertainties.
Right panel: same as the left panel, but with the data from Rowland et al. [2004]

4.6.2 Preparation of the experiment: experimental conditions

To study the ^{23}Na(p,α)^{20}Ne reaction via the application of THM, a ^{23}Na beam was produced at Laboratori Nazionali del Sud (LNS). This was the first time that such a beam was produced and accelerated by the TANDEM accelerator at LNS. About the production, it is made using NaOH in inert environment, using a glove box[7] filled with argon, and then mixed with silver to maximize thermal conductivity. This choice was made because sodium hydroxide is an hygroscopic material, and the presence of water inside the ion source must be avoided to prevent the presence of oxygen flashes inside it [Marchetta and Marletta, 2016]. Such a beam impinged on a CD_2 target, with the aim to obtain the three body reaction ^{23}Na(d,α ^{20}Ne)n to study the ^{23}Na(p,α)^{20}*Ne* two body reaction.

Given the well known binding energy of the p-n system inside deuterium (E_b=2.22 MeV) and the l=0 momentum distribution, which can be described in terms of a radial Hulthén function, the beam energy was decided with the same procedure introduced in this chapter so far: the Gamow peak for the reaction of interest at T=10^8 K is $E_G \approx$130 keV, and using the equation 4.4 (with E_{qf}=-E_G) the beam energy is $E_{beam} \approx$ 57 MeV. The beam energy as derived now is not strictly determined but allows us to select the phase-space region where the QF process is expected to be dominant. Energy loss inside the target must also be considered: for this experiment a 150 μg/cm^2 target was used, and the the beam energy was chosen to be E_{beam} = 58

[7] A *glove box* is a sealed container designed to allow the manipulation of objects, where a separate atmosphere is designed. On one side of it there are gloves, arranged in a way that the user can place its hands inside it and perform tasks inside the box without breaking the container.

MeV.

4.6.3 Selection of the kinematic conditions

Using the 4.6, as was already made for the ^{19}F(α,p)^{22}Ne, angular positions for the PSDs can be chosen, using an appropriate Monte Carlo simulation (figure 4.21).

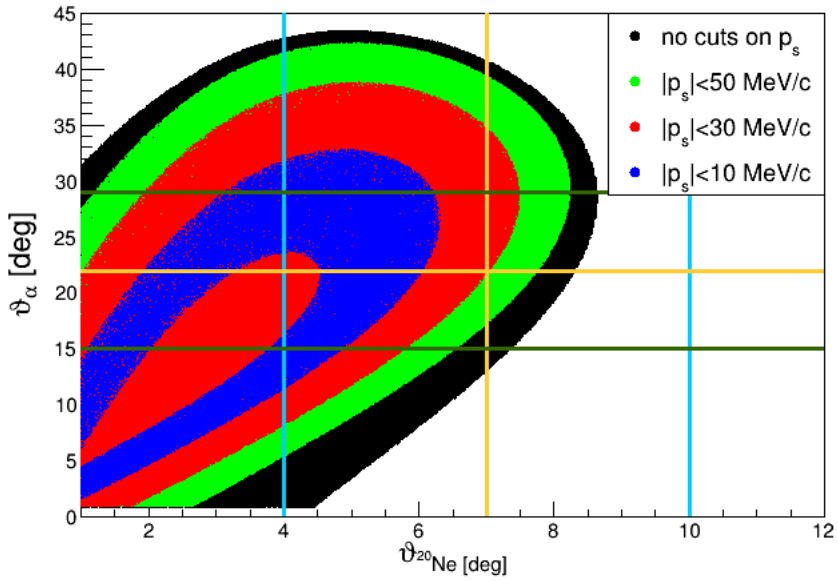

Figure 4.21: Angular range for ^{20}Ne and alpha particles (exact angular ranges are reported in table 4.3). The orange lines represent the central values of the detectors while the dark green and light blue lines are the extremities. This simulation takes also into account different p_s values, with the aim to understand where to place the detectors to get the p_s=0 contribution as big as possible.

Det.	Angle [deg]	Distance[cm]	Range [deg]	ΔΩ[mSr]
PSD1	7.2	47	±3	2.3
PSD2	-7.5	47	±3	2.3
PSD3	21.5	20	±7	12.5
PSD4	-23.1	20	±7	12.5
ΔE1	7.2	40	±3.5	28.34
ΔE2	-7.5	40	±3.5	28.34

Table 4.3: Experimental features of the set-up described in the text

Again, the best choice for ^{20}Ne detection would be at small angles ($\vartheta_{^{20}Ne}$<6°), but a condition at which the PSD spans angles lower than 4° is virtually impossible, given the high scattering rate at those angles (≥3 kHz), and detectors encumbrance inside the chamber. To be able to place the detectors at the angular range of figure

4.21, the beam had a very low intensity (i_{beam} ≈0.6 pnA).

From figure 4.21 it is also clear that, at those angular conditions the QF contribution at p_s=0 is also covered, and this fact is strengthened by the figure 4.22 (where a general idea of the spanned $E_{C.M.}$ range is also reported) and as can be seen the energy range of astrophysical relevance is fully covered.

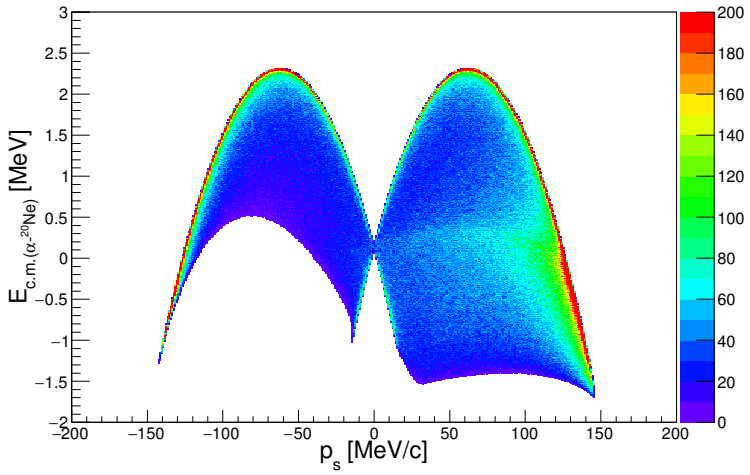

Figure 4.22: Predicted 2D-spectrum $E_{C.M.}$ versus p_s for the designed angular conditions 15° < ϑ_α <29° and 4° < $\vartheta_{^{20}Ne}$ <10°. As can be seen, the maximum QF contribution lies inside the region of astrophysical interest.

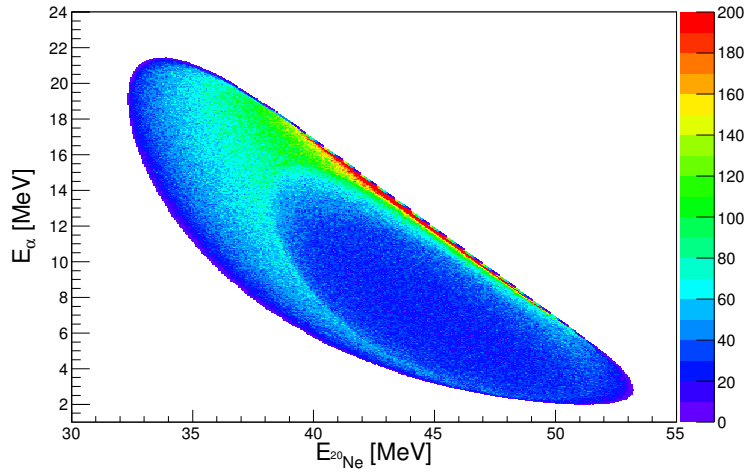

Figure 4.23: Predicted 2D spectrum $E_{^{23}Na}$ versus E_α, with the same angular cuts reported in figure 4.21.

Given the maximum theoretical values for the energies of the two detected particles

(cfr. figure 4.23) at the designed angles, IC chambers were used to discriminate ^{20}Ne, two PSDs 500 μm thick were chosen for neon detection at small angles, and two 1000 μm ones for ^{4}He detection.

4.6.4 Sequential mechanisms

Even for ^{23}Na(p,α)^{20}Ne the presence of sequential mechanisms with the same three particles in the exit channel (p,n and ^{20}Ne) is far more probable than the QF process

$$^{23}Na + d \rightarrow {}^{20}Ne + \alpha + n \tag{4.19}$$

In particular, the parasite reactions that can hinder the detection of the QF process are

$$\begin{aligned} ^{23}Na + d &\rightarrow {}^{20}Ne + {}^{5}He^{*} \rightarrow {}^{20}Ne + \alpha + n \\ ^{23}Na + d &\rightarrow {}^{21}Ne^{*} + \alpha \rightarrow {}^{20}Ne + \alpha + n \\ ^{23}Na + d &\rightarrow {}^{24}Mg^{*} + n \rightarrow {}^{20}Ne + \alpha + n \end{aligned} \tag{4.20}$$

Among those three, the first two show some level right inside the relative energy spanned by our experiment: in literature, in fact, ^{5}He has only one level reported, and ^{21}Ne has several that can hinder our measurement [Firestone, 2007a].
About the third of 4.20, this one can not be disentangled from the QF process now, but only after some considerations about the momentum distribution of the spectator for the QF process. Some contribution from levels of ^{24}Mg is therefore expected.

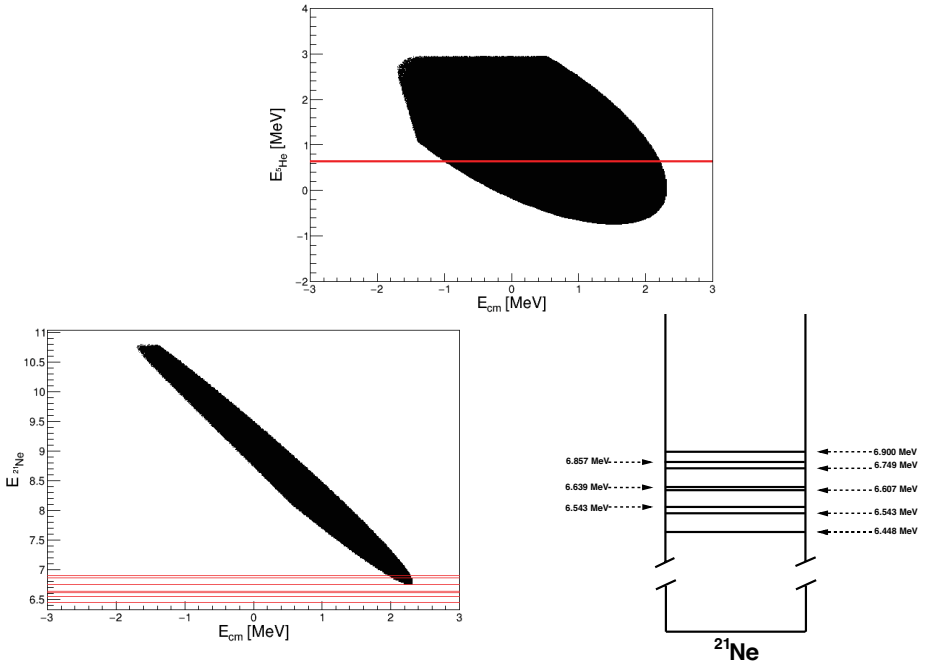

Figure 4.24: Upper panel: 2D plot obtained by means of Monte Carlo simulations for the first reaction of 4.20: the red solid line represent the only possible state of ^{5}He in the explored energy range that can be populated by sequential mechanism.
Lower panel, left: 2D plot obtained by means of Monte Carlo simulations for the second reaction of 4.20: the red solid lines represent the possible states of ^{21}Na in the explored energy range that can be populated by sequential mechanism. The last of them could give some contribution.
Lower panel, right: Not-in-scale diagram of levels corresponding to the red lines of of the figure on the left.

4.7 The ^{23}Na(p, α)^{20}Ne via the THM: experimental set-up and calibration

Now that all the positions of the detectors are known, it is possible to perform the experiment. The ^{23}Na beam impinged on a CD_2 target, also produced at Laboratori Nazionali del Sud. For this experiment, two targets 208 μm/cm^2 and 136 μm/cm^2 thick respectively were used. The beam had very low intensity (0.6 pnA) due to the forwardness of the two thinner detectors, and assuming that the reactions are taking place in the middle of the target, its energy loss is 1.28 MeV and 0.78 MeV respectively.

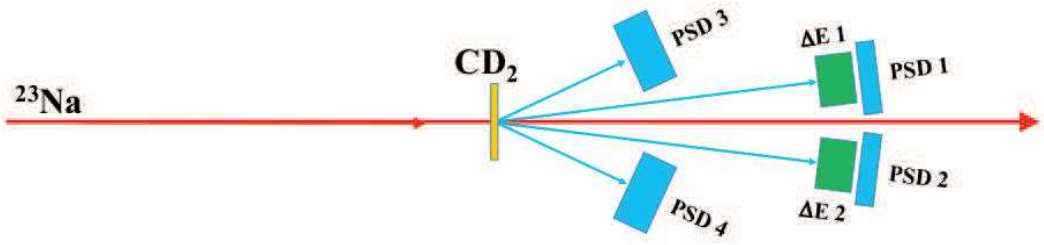

Figure 4.25: Sketch of the experimental set-up

The experimental apparatus is sketched in figure 4.25: it was composed by two ΔE-E telescopes made by two ionization chambers and two 500 μm thick detectors for ^{20}Ne discrimination, and two 1000 μm thick PSDs devoted to α detection. Those worked in a one-to-one coincidence (PSD1-PSD4 and PSD2-PSD3) and were centred at certain defined quasi-free angles, as reported in table 4.3 along with the distances between the various parts of the apparatus.
The reaction ^{23}Na(d,α ^{20}Ne)n was used to study ^{23}Na(p,α)^{20}Ne. This time ^{20}Ne and alpha particles were detected, and energy and angle of the spectator particle was calculated from energy and angle of the other two. All the detectors were calibrated: the ones at forward angles (devoted to heavy emitted particles) by means of elastic scattering of ^{23}Na on a gold target (81 μg/cm^2 thick), while the ones at higher angles were calibrated using standard α-source (^{228}Th, eight peaks) and detecting the α particles coming from the well-known ^{6}Li(^{12}C,α)^{14}N reaction. Both ^{23}Na(^{197}Au,^{197}Au)^{23}Na elastic scattering and ^{6}Li(^{12}C,α)^{14}N two-body reaction (made using a ^{6}Li beam impinging on a 136 μg/cm^2 CD_2 target) were made at several energies:

- ^{23}Na beam at 30, 35, 40, 45, 50 and 58 MeV
- ^{6}Li beam at 14 and 20 MeV

About the first, in this phase measurements both with gas-filled and empty ionization chambers were preformed, to have several calibration points at different energies. About the second, its fairly high Q-value (8.8 MeV) and the number of excited levels of ^{14}N present in the energy range provided us a lot of α particles at different energies between 5 and 25 MeV, similar to the expected energy range for the ones coming from the ^{23}Na(p,α)^{20}Ne reaction. The coefficients for the linear relations for calibration are reported in table 4.4.

Detector	Position parameters [deg]	Energy parameters [MeV]
PSD1	$p_2 = 75.997$, $p_4 = -0.7858$ $p_1 = -7.0656$, $p_3 = 0.1545$	$a = 0.0146$ $b = 0.636$
PSD2	$p_2 = 142.15$, $p_4 = -0.8562$ $p_1 = -10.032$, $p_3 = 0.1557$	$a = -0.0158$ $b = 0.2768$
PSD3	$p_2 = 112.59$, $p_4 = -0.7648$ $p_1 = -2.9477$, $p_3 = 0.0544$	$a = 0.0099$ $b = -0.5707$
PSD4	$p_2 = 81.245$, $p_4 = -0.8079$ $p_1 = -1.8838$, $p_3 = 0.0536$	$a = 0.0101$ $b = -0.3953$

Table 4.4: Fit parameters for the calibrated detectors

Even in this case, energy loss was evaluated, taking into account the presence of the ionization chamber, with two Mylar foils as windows (1.5 μm thick) and 50 mb isobutane inside it.

CHAPTER 5

Data Analysis for the ^{19}F(α,p)^{22}Ne reaction

Once calibration procedures are completed, it is possible to gain information about energies and positions of the incoming particles using the PSDs, and in particular PSD2 and PSD3 (optimized for deuterons and protons detection, respectively), that during the data analysis have been proven to be the the only ones useful to detect the reaction of interest.
The next steps are to select deuterons using the ΔE-E technique, identify the three-body reaction of interest, and isolate the QF contribution. Once data are properly reduced, the two-body cross-section for the ^{19}F(α,p)^{22}Ne reaction can be extracted from the ^{6}Li(^{19}F,p^{22}Ne)d three-body one using the THM. With that the astrophysical factor and the reaction rate will be calculated, and the astrophysical implication will be discussed at the end of the chapter.

5.1 Reaction channel selection

Several reactions can occur after the interaction between the beam and the target components. Some kind of selection is therefore needed. Our experimental apparatus allowed us to select one of the outgoing particles by means of ΔE-E technique explained in the previous chapter: in a ΔE-E typical 2D-spectrum, different particles lie on different hyperbole branches depending on their charge and mass, allowing a separation between different elements and different isotopes, if resolution is high enough.

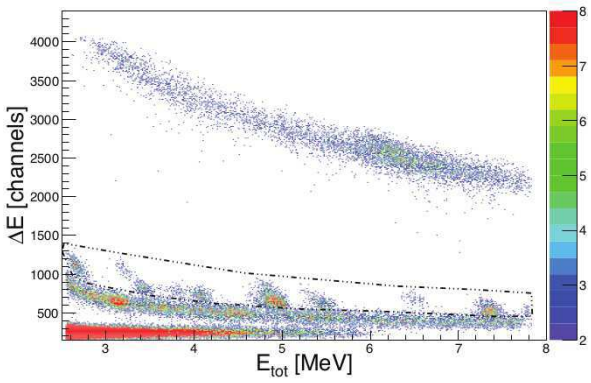

Figure 5.1: ΔE-E identification for deuterons in PSD2 (central angle of the detector 12.3°). As can be seen ^{2}H discrimination with respect to H is really difficult. The selected events lie in the black dashed graphical cut.

In figure 5.1 such a procedure is used in our case, and different particles are visible and distinguishable. In this case resolution is not high enough to easily discriminate between different isotopes of hydrogen, even if the presence of particles with the same atomic number Z=1 and different mass number can be guessed. The applied selection of particles impinging on PSD2 is reported in 5.1, and as can be seen in the selected spectrum some bumps arise: those are evidences of several two bodies parasite reactions.

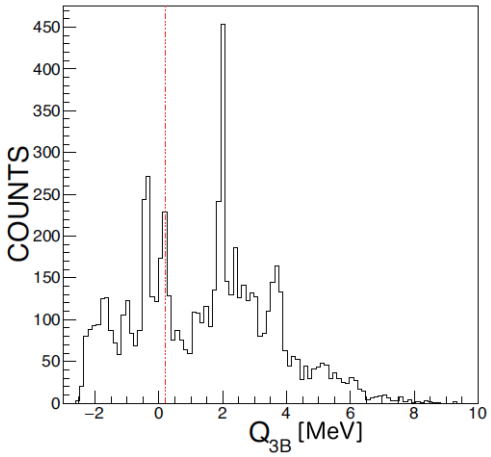

Figure 5.2: Q_{value} from the events selected in 5.1. It clearly shows the presence of several parasite reaction, but a structure around the theoretical value for the ^{6}Li(^{19}F,p^{22}Ne)d (Q_{3B}=0.199 MeV) is also visible.

This is also supported by the Q_{value} spectrum (figure 5.2), where different peaks can be seen for the selected condition. The Q_{value} spectrum is built by means of the measured energies and positions of the particles detected in PSD2 and PSD3, that are

also used to reconstruct energy and position of the not detected third particle.
In figure 5.2 there is also an evidence of some structure around Q_{value}=0.199 MeV, theoretical value for the ^{6}Li(^{19}F,p^{22}Ne)d reaction Q_{value}, but further data reduction is needed. To do so some properties of the Q_{value} were used: for example it has to be independent from the kinematic variables involved in the experiment. A Q_{value} versus ϑ_d or ϑ_p two-dimensional spectrum for the events selected so far must therefore show to be uncorrelated.

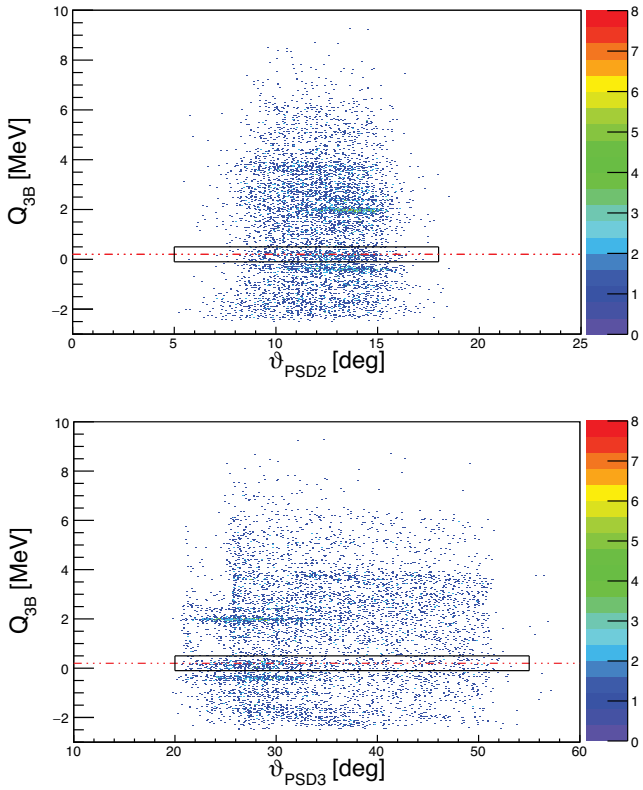

Figure 5.3: Three-body Q_{value} versus angular distributions for PSD2 (upper panel) and PSD3 (lower panel). If the ^{6}Li(^{19}F,p^{22}Ne)d reaction is taking place, then events must lie around y=0.199 MeV, corresponding to the Q_{3B} value for the reaction of interest. In the following analysis only the data contained in the black boxes will be used [D'Agata et al., submitted].

In figure 5.3 it is obviously the case. So a graphic cut on data clustering around Q_{3B}=0.199 MeV was made, and the final Q_{value} for the ^{6}Li(^{19}F,p^{22}Ne)d three-body reaction shows its agreement with theoretical value (figure 5.4).

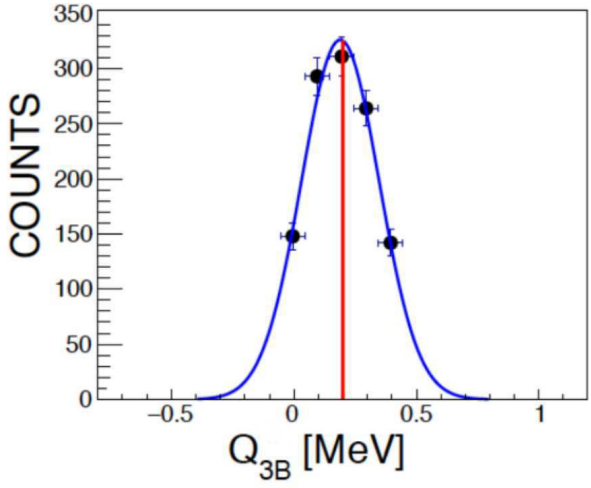

Figure 5.4: Q_{value} spectrum for the ^{6}Li(^{19}F,p^{22}Ne)d reaction. A Gaussian fit to the experimental data is also reported (blue line, centred at Q_{3B}^{exp}=0.19 MeV), along with the position of the theoretical value (red line, Q_{th}^{3B} ≃0.199 MeV) [D'Agata et al., submitted].

As a further proof of the selection of the ^{6}Li(^{19}F,p^{22}Ne)d reaction, a comparison between experimental kinematic locus and a proper Monte Carlo simulation was made. This procedure is reported in figure 5.5: it can be seen experimental data and theoretical predictions are in agreement.

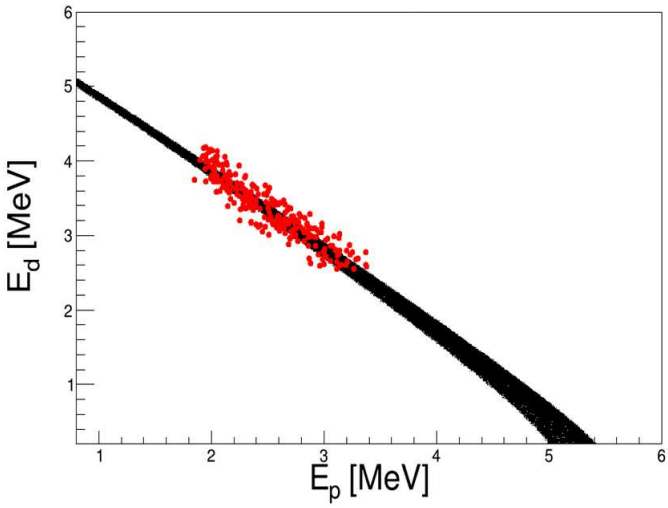

Figure 5.5: E_d-E_p matrix. Events related to the reaction of interest and selected according to the text above (red points) are compared with proper Monte Carlo simulations (black area). The experimental data are spread around the simulation, and this is due to the energy straggling in the absorber and in the thin silicon detector used as ΔE stage of the telescope.

This procedure minimizes the possibility that different processes taking place along with the one of interest are considered, and data coming from the three-body reaction are isolated. The cuts above will be used in the following analysis.

5.2 Quasi-free channel contribution

Next step in data analysis is to isolate the quasi-free contribution. Such a procedure is crucial for THM application: the extraction of the two-body cross-section is in fact possible only after the separation of the QF process from any other (sequential decay, break-up,...) occurring in the target. For this reason, as already done in the previous chapter, 2D-spectra relative energy were studied: E_{p-d} vs. $E_{p-^{22}Ne}$ and $E_{d-^{22}Ne}$ vs. $E_{p-^{22}Ne}$. Analysing those spectra it is possible to check the presence of excited states of ^{3}He, ^{23}Na and ^{24}Na: the presence of horizontal and/or vertical loci will in fact indicate the presence of correlation, and therefore of excited states.

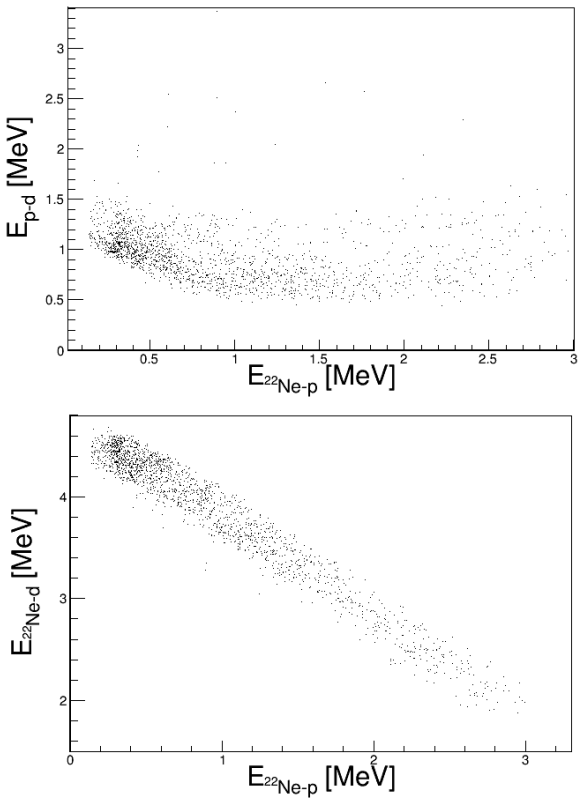

Figure 5.6: Relative energies matrix. In the upper panel the proton-neutron relative energy is potted against the ^{22}Ne-p one, while in the second in the y-axis the ^{22}Ne-d one is plotted. The absence of horizontal loci shows the lack of correlation between ^{22}Ne and deuterium (levels of ^{24}Na compound nucleus) or between protons and deuterons (levels of ^{3}He compound nucleus)

Both the 2D-spectra in figure 5.6 show no horizontal loci, and so no excited states of ^{3}He and ^{24}Na are present in our energy range: this is in agreement with what seen in chapter 4. On the other hand, there is evidence of a structure at $E_{p^{22}Ne}$=0÷0.5 MeV, corresponding to excited levels of ^{23}Na (figure 5.10).

It is now important to understand if those levels are populated via QF or sequential processes. Under the conditions explained in chapter 3, the cross-section can be factorized as it follows (equation 3.33):

$$\frac{d^3\sigma}{d\Omega_c d\Omega_C dE_c} \propto KF \cdot |\Phi(p_s)|^2 \left(\frac{d\sigma}{d\Omega}\right)^{off} \tag{5.1}$$

and so:

$$\frac{d^3\sigma}{d\Omega_c d\Omega_C dE_c} \cdot \frac{1}{KF} \propto |\Phi(p_s)|^2 \left(\frac{d\sigma}{d\Omega}\right)^{off} \tag{5.2}$$

From equation 5.2 it is possible to conclude that a QF process, if present, has a coincidence yield that must change with the momentum distribution $|\Phi(p_s)|^2$, as discussed in chapter 4. So the maximum contribution to the yield must be at $p_s \approx 0$, and must decrease while going away from it.

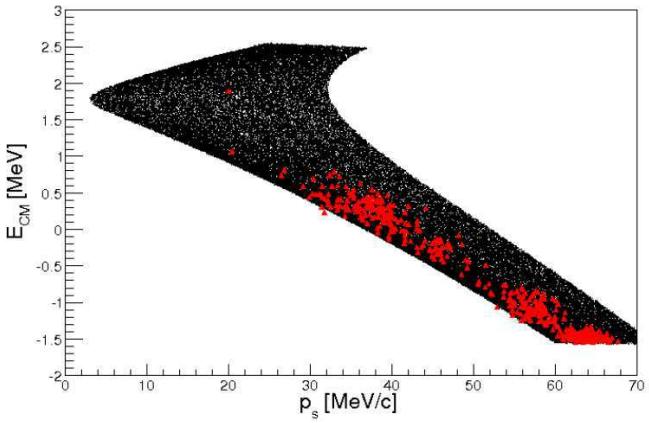

Figure 5.7: Comparison between the 2D spectrum in figure 4.13 and experimental data. In the energetic region of interest those are in agreement. The definition of the quantity E_{CM} is reported in chapter 4

A way to ascertain the presence of QF process is to study this momentum distribution of the spectator inside the cluster, that in our case are deuterium and ^{6}Li. The $|\Phi(p_s)|^2$ can be calculated using the equation 5.2, if the energy region is narrow enough to consider $\frac{d\sigma}{d\Omega}$ as a constant value

$$|\Phi(p_s)|^2 \propto \frac{d^3\sigma}{d\Omega_c d\Omega_C dE_c \left[KF\left(\frac{d^2\sigma}{d\Omega^2}\right)^{off}\right]} \tag{5.3}$$

if QF is present, the momentum distribution should reproduce the distribution of deuterium inside ^{6}Li, within the experimental errors, once coincidence yield is known from the experiment and KF factor from theoretical calculations: for this reason a comparison between the experimental data and a proper Monte Carlo simulation was made, and there was agreement between them (cfr. figure 5.7) .
If the observed process is a QF one, then the momentum distribution of deuterium inside ^{6}Li must follow a certain trend, which is given by an Hänkel function [Barbarino et al., 1980]:

$$|\Phi(\mathbf{p_s})|^2 = N\frac{1}{(k_s^2+\beta^2)^2}\left[\frac{sink_sR_c}{k_s}+\frac{cosk_sR_c}{\beta}\right] \tag{5.4}$$

where $k_s = p_s/\hbar$, R_c is the cut-off radius, and $\beta = (2\mu E_B/\hbar^2)^{1/2}$, with μ reduced mass and E_b binding energy of the system. As can be seen in figure 5.8, this looks to be the case.

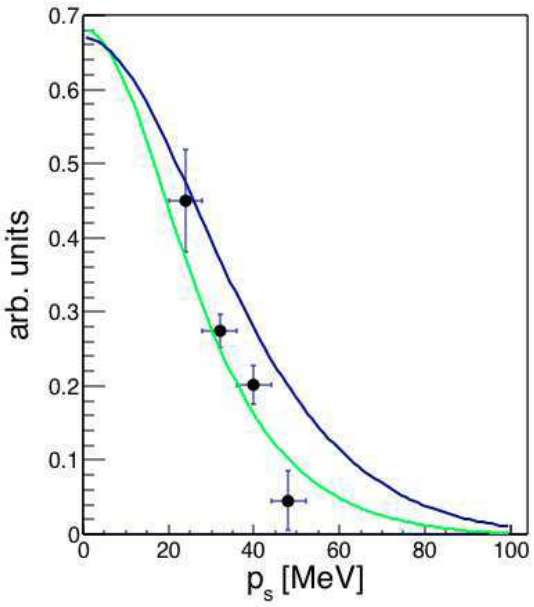

Figure 5.8: Spectator momentum distribution: the experimental data are fitted with an Hänkel function (green line) and compared with the theoretical one [Pizzone et al., 2009] (blue line) [D'Agata et al., submitted].

From literature it is known that the width of the Hänkel function that represents the deuterium cluster distribution inside inside ^{6}Li must follow the following trend [Pizzone et al., 2009] as a function of the the transferred momentum q_t

$$W(q_t) = f_0[1 - exp(-q_t/q_0)] \tag{5.5}$$

with

$$q_t = p_{beam} - \frac{p_p + p_{^{22}Ne}}{2} \tag{5.6}$$

where p_{beam} and $p_{^{22}Ne}$ are the projectile and ^{22}Ne momenta, respectively. In equation 5.5 f_0 = 73 MeV is the asymptotic value of the function and q_0 = 122±3.5 MeV is a fit parameter. In our case, taking into account that q_t=190 MeV/c, from equation 5.5 W(q_t)≈53 MeV/c ± 7 MeV (as reported in figure 5.9).
For further analysis only events with p_s <60 MeV/c are considered.

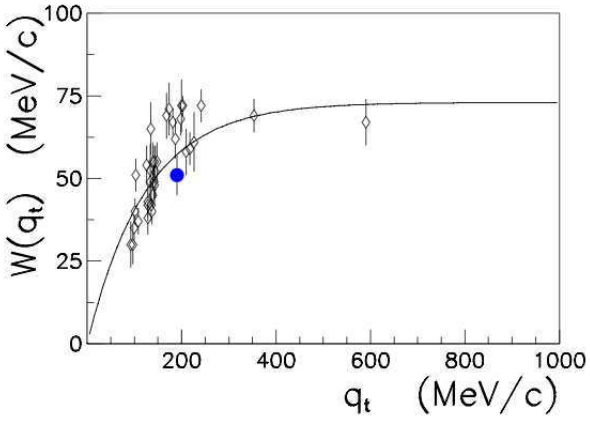

Figure 5.9: FWHM of the momentum distribution for deuteron inside ^{6}Li as a function of the transferred momentum q_t [D'Agata et al., submitted]. The blue circle represents the value obtained in this experiment while the diamonds represent values from literature [Pizzone et al., 2005].

In figure 5.9 the trend of the W(q_t) versus the transferred momentum is reported. As shown in Pizzone et al. [2005], distortions of momentum distribution width arise with decreasing q_t. That should be taken into account in the following analysis.

5.3 Excitation function

Let us now consider the levels of the ^{22}Ne-p compound nucleus: to do so the $E_{^{22}Ne-p}$ relative energy spectra (as anticipated in figure 5.6) is considered. This quantity can be extracted from the relative energy for the ^{22}Ne-p system as it follows:

$$E_{ecc}^{^{23}Na} = E_{p-^{22}Ne} + Q_{ecc} \tag{5.7}$$

where Q_{ecc}=8.794 MeV is the Q_{value} for the formation of the compound nucleus starting from a ^{22}Ne and a proton (as reported in figure 5.10). It is useful to understand that, if $E_{^{22}Ne-p}$ is equal to zero E_{ecc}^{Na}=8.794 MeV.

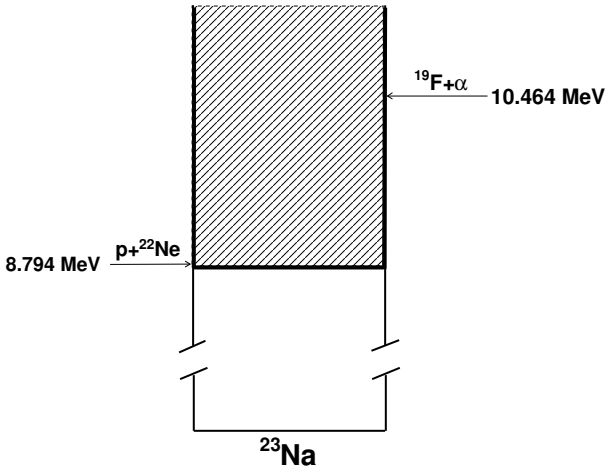

Figure 5.10: Levels scheme for the ^{23}Na compound nucleus: the shaded zone indicates the region explored by this experiment.

In the energy region spanned by the experiment, some resonant structures are detected in the mono-dimensional $E_{^{22}Ne-p}$ relative energy spectrum (figure 5.11), resembling excited states of the ^{23}Na compound nucleus.

A fit on the experimental data (figure 5.11) was made by adding many Gaussian with the same σ. The centroids of these functions were compared with the levels of ^{23}Na available in literature [Firestone, 2007a].

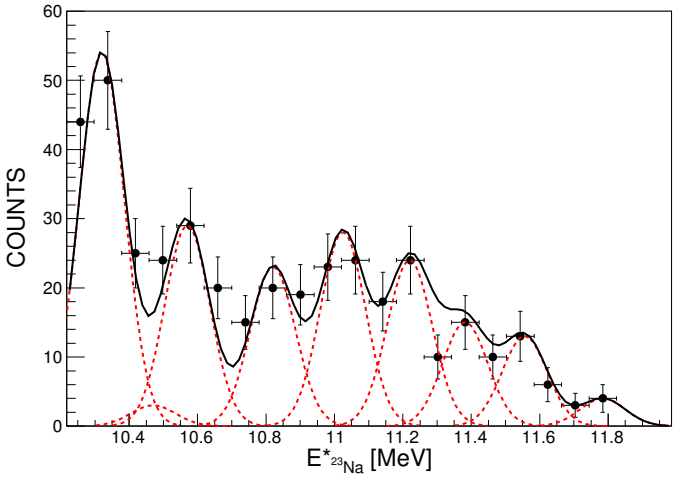

Figure 5.11: Excitation function of the ^{23}Na compound nucleus. The centroids of the used Gaussian are reported in table 5.1, while the σ was fixed as 60 keV

$E^{*exp}_{^{23}Na}$ [MeV]	$E^{*lit}_{^{23}Na}$[Firestone, 2007a] [MeV]	J^π	l_{min}	$\Delta E_{lit-exp}$ [keV]
10.320	10.318	$3^-/2$	1	2
10.470	10.477	$3^+/2$	2	7
10.570	10.575	$3^-/2$	1	5
10.820	10.823	$3^+/2$	2	3
11.025	11.038	$1^+/2$	0	13
11.220	11.238	$3^-/2$	1	18
11.382	11.355	$1^+/2$	0	-27
11.556	11.554	$1^+/2$	0	2
11.784	not present	////	////	////

Table 5.1: Levels used as centers for the Gaussian functions (red dashed lines) in figure [Firestone, 2007a]. The sum of those Gaussian functions makes our fit (black solid line). In the last column the difference between the centroids and the theoretical values are reported.

In figure 5.11, there are evidences of five groups of possible levels, centred near the resonances reported in table 5.1. Experimental resolution, obtained in this case by propagating the experimental errors on energy obtained by means of a three peak α-source and scattering of ^{6}Li on gold and CD_2, is about 60 keV, and it is far greater than the proper width of the levels, that is of the order of magnitude of few keV, or lower [Firestone, 2007a].
This procedure is just a first step for level identification, and the angular momentum of interaction and the J^π of the resonances is still far from being assumed: in the following analysis a more refined method involving *R-Matrix* approach will be used.

5.4 Angular distributions

The triple differential cross-section $\frac{d^3\sigma}{d\Omega_p d\Omega_d dE_{CM}}$ is linked to the energy of the center-of-mass in the post-collision prescription. In this case it can be calculated as it follows:

$$E_{C.M.} = E_{p-^{22}Ne} - Q^{2B}_{value} \tag{5.8}$$

Another variable to consider is the $\vartheta_{C.M.}$ (the emission angle of the proton in the center-of-mass reference frame), that involves the velocity of all the particles after the emission [Slaus et al., 1977]:

$$\vartheta_{C.M.} = \arccos \frac{(\mathbf{v_{^{19}F}} - \mathbf{v}_\alpha) \cdot (\mathbf{v_{^{22}Ne}} - \mathbf{v_p})}{|\mathbf{v_{^{19}F}} - \mathbf{v}_\alpha| \cdot |\mathbf{v_{^{22}Ne}} - \mathbf{v_p}|} \tag{5.9}$$

Looking at the $\vartheta_{C.M.}$ versus $E_{C.M.}$ 2D-spectrum (figure 5.12), the spanned region of $\vartheta_{C.M.}$ is between 120° and 160°.

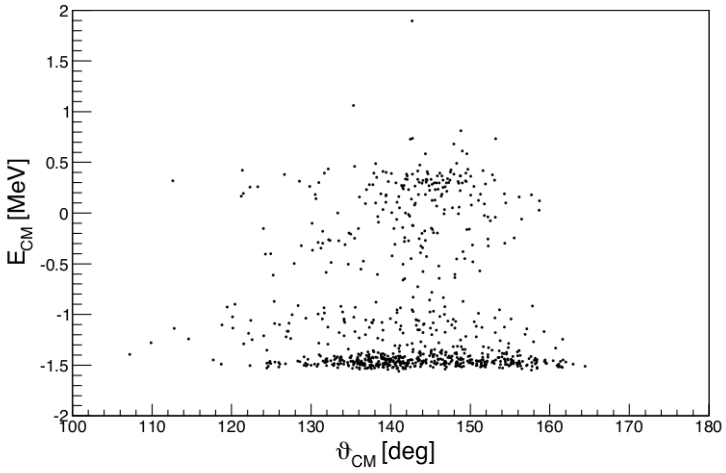

Figure 5.12: 2D-matrix $\vartheta_{C.M.}$ vs $E_{C.M.}$.

Angular distributions have great importance in nuclear spectroscopy: their trend in restricted regions of $E_{C.M.}$, in fact, is of utmost importance to understand the spin-parity J^{π} of a certain resonance.

In the experimental region of $E_{C.M.}$ covered by the experimental set-up there are more resonances than the ones of table 5.1 [Firestone, 2007a]. Different values of the J^{π} of a resonance corresponds to different quantum angular momentum in the entrance channel. In Ugalde et al. [2008] all the levels informations in the energy region of $E_{C.M.}$ are reported, and a predominance of l=2 can be detected: this information is really important for *R-Matrix* calculations, but needs further validation. To do so, mono-dimensional spectra of the variable $\vartheta_{C.M.}$ were analysed, dividing the energy region into three parts ($0<E_{C.M.}<0.3$ MeV, $0.3<E_{C.M.}<0.6$ MeV and $0.6<E_{C.M.}<0.9$ MeV). In this way the statistics and energy interval were respectively high and narrow enough to proceed with the analysis. The spectra obtained so far were than divided by a proper Monte Carlo simulation for the $\vartheta_{C.M.}$, that takes into account the kinematics for the system and the momentum distribution trend extracted earlier: in particular, the experimental fit made using 5.4 on p_s mono-dimensional spectrum was used to modulate the Monte Carlo simulation. The resulting angular distributions are reported in figure 5.13, along with the respective statistical error. The experimental results are then fitted by means of a linear combination of the two spin-parity $3/2^+$ and $5/2^+$, both corresponding to a l=2 configuration [Blatt and Biedenharn, 1952; La Cognata et al., 2015] (figure 5.13).

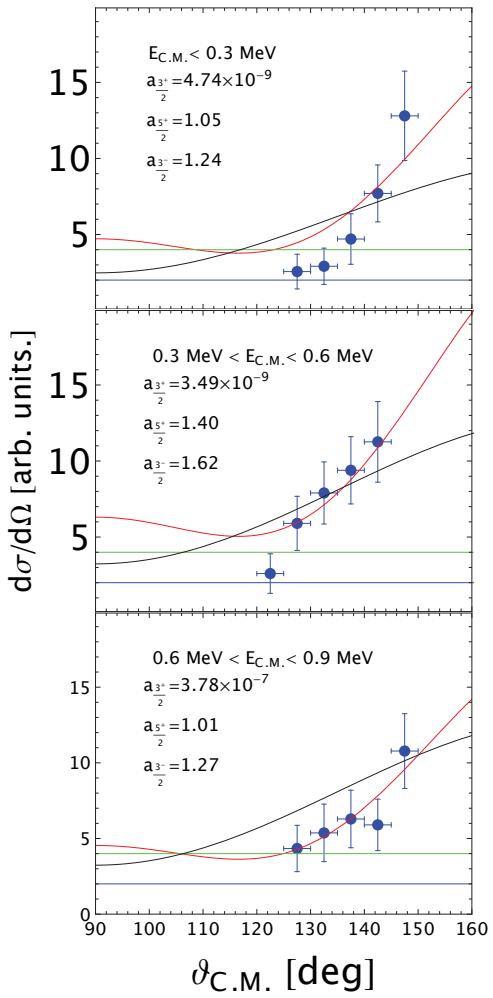

Figure 5.13: Experimental angular distribution vs. $\vartheta_{C.M.}$, that is the emission angle of the proton in the center-of-mass reference frame, versus half-off-energy-shell cross-section: the blue points are the experimental data, while the blue, green and red lines represent best-fits on data made by means of the equations given in Blatt and Biedenharn [1952] and La Cognata et al. [2015] and with J^π equal to $3/2^-$ (with $a_{3/2^-}$ as normalization coefficient), $1/2^+$ and $1/2^-$ (multiplied by a factor of of two to separate it from the previous). Regarding the black line, it represents a best-fit made by means of a linear combination of $J^\pi=3/2^+$ and $J^\pi=5/2^+$ angular distributions.

This combination, reported in figure 5.13, is in fair agreement with the experimental errors, pointing out a dominant contribution of *d*-wave for the resonances detected in the $E_{C.M.}$<0.9 MeV region.

To further stress this last point, many different tries were attempted, and are also reported in figure 5.13: in particular *p*-wave angular distribution with $J^\pi=3/2^-$, $1/2^+$ and $1/2^-$ (green, black and blue lines in figure 5.13) were tested, but those choices did not fit the data. Moreover, looking at the coefficients for the linear combination of $J^\pi=3/2^+$ and $J^\pi=5/2^+$ angular distribution fit ($a_{3/2^+}$ and $a_{5/2^+}$, respectively), it ap-

pears clear that the second dominates over the first by seven orders of magnitude. Now that l=2 is ascertained, the arbitrary units cross-section can be fitted by means of modified *R-Matrix* calculations.

5.5 The modified *R-Matrix* approach: a brief introduction

The *R-Matrix* approach is a way to parametrise the properties of compound nucleus reactions. First of all, let us underline that the *R-Matrix* theory is not a predictive theory, but it is a framework that needs inputs from experimental data, in order to have physical significance. The more accurate the data are, the more the nuclear wave functions are constrained, and the more reliable the *R-Matrix* calculations are, especially when attempting to use it to extrapolate the cross-section at nearly unobserved energies.
This analysis usually starts with a simpler approach (like in our case) with the aim to get informations about energies, J^{π}, and partial widths of the resonances. Those, called level parameters, are then used as a starting point to perform a least-squares fitting of the *R-Matrix* parameters on experimental data. In this way, more accurate level parameters are extracted, and interference signs between resonances wave functions can be obtained.
The assumptions at the base of *R-Matrix* reported in Lane and Thomas [1958] and are:

- non-relativistic quantum physics must be applicable to the reaction. This approximation is reasonable at low energies in nuclear physics, because the kinetic energies of the particles inside nuclei are smaller than their respective rest-masses;
- there are only two nuclei in the entrance and in the exit channels;
- there are no important processes of creation and destruction of particles. The main effect of this assumption is that no photons are produced;
- a certain radius a can be defined as the minimum radial distance at which the nuclei interact with each other. It represents the division between the internal and the external regions. In the first region (r<a), only short range nuclear force is considered and the nuclear potential has an effect (in this

region the physics of the system is described by the *R-Matrix* parameters), while in the second region (r>a) no strong nuclear force acts and the only considered potential derives from the Coulomb force.

Starting from those assumptions and following the formalism given by Lane and Thomas [1958], a mathematical framework to describe the internal and external wave function separately can be made. For first, the aim of *R-Matrix* theory is, as usual, to solve the Schrödinger equation

$$H\Psi = E\Psi \tag{5.10}$$

This equation can be solved by the separation of variable technique, and solution can be obtained for the internal region and for the external one of the configuration space. After deriving under the assumption that the two solution match each other it is possible to obtain the desired relations. Let us now simplify the problem to the scattering of a spinless particle by a central potential V(r), with the aim to obtain the wave functions and properties of the compound nucleus to the *R-Matrix* parameters. In the internal region a complete set of stationary states are made to represent the wave function:

$$\Psi = \sum_{\lambda} A_{\lambda} X_{\lambda} \tag{5.11}$$

where A_λ has the form

$$A_{\lambda} = \int_{V} X_{\lambda} \Psi \, dV \tag{5.12}$$

In 5.12 the integration is on the whole internal volume.
These stationary states satisfy the Hamiltonian $HX_\lambda=E_\lambda X_\lambda$, with E_λ and X_λ energy eigenvalues and eigenvectors of the system. These states must be directly related to the quasi-stationary states at the nuclear surface: it is then necessary to impose a boundary condition, satisfied on the nuclear surface at the channel radius. This condition can be expressed as

$$\frac{dX_{\lambda}}{dr} + bX_{\lambda}|_{r=a} = 0 \tag{5.13}$$

By substitution and integration, it is possible to obtain the following equation:

$$-\frac{\hbar^2}{2m}\left(\Psi\frac{dX_{\lambda}}{dr} + X_{\lambda}\frac{d\Psi}{dr}\right)_{r=a} = (E - E_{\lambda})\int_{0}^{a} X_{\lambda}\Psi \, dr \tag{5.14}$$

and using the equation 5.12

$$A_{\lambda} = -\frac{\hbar^2}{2m}X_{\lambda}(a)\frac{\Psi'(a) + b\Psi(a)}{E - E_{\lambda}} \tag{5.15}$$

Finally, by substituting the equation 5.15 in 5.11

$$\Psi(r) = G(r,a)[\Psi'(a) + b\Psi(a)] \tag{5.16}$$

where $G(r,a)$ is the Green function

$$G(r,a) = -\frac{\hbar^2}{2m}\sum_{\lambda}\frac{X_\lambda^2(a)}{E_\lambda - E} \tag{5.17}$$

and the R-function can be defined as the value of the Green function at $r = a$

$$R = G(a,a) = -\frac{\hbar^2}{2m}\sum_{\lambda}\frac{X_\lambda^2(a)}{E_\lambda - E} \tag{5.18}$$

The equation 5.18 can be simplified introducing a new parameter, γ_λ, such as $\gamma_\lambda^2 = \frac{\hbar^2}{2m}X_\lambda^2$, and

$$R = \frac{\gamma_\lambda^2}{E - E_\lambda} \tag{5.19}$$

In this last equation E is the energy of the particles and E_λ is the eigenvalue, associated with an energy level in the compound nucleus.

Regarding now the external region (where only the Coulomb force is present), the total wave function can be written as the superimposition of the incoming I and the outgoing O waves:

$$\Phi_l = I_l - U_l O_l \tag{5.20}$$

where l is the orbital angular momentum of the system and U_l the collision function. The incoming and outgoing waves are related to the regular and irregular Coulomb functions:

$$I_l = (G_l - iF_l)e^{i\omega_l} \tag{5.21}$$

$$I_l = (G_l + iF_l)e^{-i\omega_l} \tag{5.22}$$

with ω_l Coulomb phase shift $\omega_l = \sum_{n=1}^{l}\tan^{-1}\frac{\eta_l}{n}$, where η_l is the Sommerfeld parameter expressed in chapter 2.3. Using now equation 5.20, the nuclear scattering amplitude can be expressed, along with the differential cross-section $\frac{d\sigma(\vartheta)}{d\Omega}$:

$$A(\vartheta) = \frac{1}{2}ik^{-1}\sum_{l}(2l+1)(1-U_l)P_l(\cos\vartheta) \tag{5.23}$$

$$\frac{d\sigma(\vartheta)}{d\Omega} = |A(\vartheta)|^2 = \frac{1}{4}k^{-2}\Big|\sum_{l}(2l+1)(1-U_l)P_l(\cos\vartheta)\Big|^2 \tag{5.24}$$

where P_l are the Legendre polynomials and U_l is the collision function. The U_l function can be expressed in terms of the R-function, using the boundary conditions and equating the logarithmic derivatives of the internal and external wave functions at the nuclear surface r=a. In this way $U_l = e^{2i\delta_l}$, where

$$\delta_l = \tan^{-1}\left(\frac{P_l R_l}{1 - R_l S_l} - \phi_l\right) \tag{5.25}$$

In equation 5.25 ϕ_l, P_l and S_l are the hard-sphere phase-shift, the penetrability and the energy-shift function, respectively

$$\phi_l = \tan^{-1}\left(\frac{F_l}{G_l}\right) \tag{5.26}$$

$$P_l = \left.\frac{kr}{F_l^2 + G_l^2}\right|_{r=a} \tag{5.27}$$

$$S_l = P_l(F_l F_l' + G_l G_l') \tag{5.28}$$

Finally the differential cross-section depends on the phase-shift ω_l, the hard-sphere phase-shift ϕ_l and the reaction scattering R-function. In the R-function, all the information about the stationary states are contained, and these states are related to the physical reality by the boundary constant b.

In many cases there are multiple states and channels that are open, and many combinations of spin that can contribute to the formation of a certain state of fixed J^π. The collision and R functions then become the collision matrix and *R-Matrix*, depending in general on the indices C=[$\alpha svlm$]. Those represent the channel (α), the channel spin (s), the channel spin component (v), the orbital angular momentum (l) and the orbital angular momentum component (m).

In this representation, the *R-Matrix* can be written as:

$$R_{cc'} = \sum_\lambda \frac{\gamma_{\lambda c'}\gamma_{\lambda c}}{E_\lambda - E} \tag{5.29}$$

In equation 5.29 the difference between primed and unprimed indices is that the first indicates entrance, while the second the exit channel. The collision matrix is related to the *R-Matrix* by the relation:

$$U_{cc'} = \frac{(k_c r_c)^{1/2}(1 - RL^*)I_{c'}}{(k_{c'} r_{c'})^{1/2} O_c(1 - RL)} \tag{5.30}$$

where L_c=S_c-B−c+IP$_c$, with B_c matrix form of the boundary constant.

This theoretical framework introduces a set of parameters, called *poles*, characterized by a certain energy E_λ and reduced width γ_λ. Such quantities are then varied

using a minimization routine to best match the data. In this way, partial widths and levels can be extracted. This procedure can be applied to both resonant and non-resonant reactions. In this second case it is possible to simulate it via a high-energy pole (called *background contribution*), that makes the R-Matrix almost independent from energy [Lane and Thomas, 1958].

The quantities E_λ and γ_λ are associated with physical quantities, but not strictly equal to them. Those are in fact parameters that directly influence the strength of the resonant cross-section, but are identified only as eigenvalues and eigenstates of the stationary wave functions used to describe the internal region of the compound nucleus. The contribution of this part is also combined with the one coming from the external part to calculate the collision matrix and cross-section in a way that makes them independent from the channel radius or boundary condition. So the final cross-section over a certain resonant state can be described with a certain experimental width related to the internal eigenstate parameter (γ_λ), again via channel radius and boundary conditions. This makes the *R-Matrix* a phenomenological approach that describes the observed resonances in terms similar to the Breit-Wigner one, without giving informations on the real wave functions of the compound. The γ_λ parameters are caller *reduced width* and are expressed in terms of $\sqrt{E}$. Those are related to the Γ coming from the Breit-Wigner approach via the following relation

$$\Gamma_\lambda = 2P(E)\gamma_\lambda^2 \tag{5.31}$$

that is the formal width of the resonance. The observed one is then given by

$$\Gamma_\lambda^0 = \frac{2P(E)\gamma_\lambda^2}{1 + \gamma_\lambda^2 S'(E)|_{E=E_r}} \tag{5.32}$$

When the general state energy E_λ is such that the boundary condition is equal to the shift function, the pole energy and resonance energy are the same.

All this formalism has proven to be useful as a feature to fit the experimental cross-section and to extrapolate its behaviour down to the astrophysical energies. In that case the formal values E_λ and γ_λ are considered as adjustable parameters. In particular, in THM application, all this framework must be updated to consider the half-of-energy-shell character of the TH cross-section [La Cognata et al., 2011]. Using the same notation for the incoming and outgoing particles of the three-body reaction used in chapter 3, the TH reaction amplitude is given by an expression similar to the one expressed so far, with the introduction of an overlap function for the internal wave function of the system F=x+A=c+C excited to the level τ, and the

bound-state wave function of A. This function takes the form $I^F_{A\tau} = \left\langle \Phi_\tau \middle| \phi_A \right\rangle$, and can be parametrized in terms of the boundary condition in the x+A channel and of the reduced width $\gamma_{xA\tau}$. Assuming non-interfering resonances, the TH cross section can be obtained in the plane-wave approximation:

$$\frac{d^2\sigma}{dE_{xA}d\Omega_s} = NF \sum_\tau (2J_\tau + 1) \times \left| \sqrt{\frac{k_f(E_{xA})}{\mu_{cC}}} \frac{\sqrt{2P_{l\tau}(k_{cC}R_{cC})}M_\tau(p_{xA}R_{xA})\gamma_{cC\tau}\gamma_{xA\tau}}{D_\tau(E_{xA})} \right|^2 \tag{5.33}$$

Here NF is a normalization factor, J_τ is the spin of the τ-th resonance, $k_f(E_{xA}) = \sqrt{2\mu_{cC}(E_{xA} + Q)}/\hbar$ (with Q as the Q_{value} for the reaction in exam and E_{xA} the relative energy for the x-A system), $P_{l\tau}$ the penetration factor in L_τ-th wave, and R_{xA} and R_{cC} the channel radii.
In equation 5.33 the $M_\tau(p_{xA}R_{xA})$ factor is equal to

$$M_\tau(p_{xA}R_{xA}) = \left[(B_{xA\tau} - 1) j_{l\tau}(\rho) - \rho \frac{\partial j_{l\tau}(\rho)}{\partial \rho} \right]_{\rho = p_{xA}R_{xA}} \tag{5.34}$$

where $j_{l\tau}(\rho)$ is the Bessel spherical function $p_{xA} = \sqrt{2\mu_{xA}(E_{xA} + B_{xs})}/\hbar$ (with B_{xs} the binding energy of the $x \oplus s$ system), and $B_{xA\tau}$ is an arbitrary boundary condition. In the end, the term $D_\tau(E_{xA})$ in equation 5.33 is the standard *R-Matrix* denominator [Lane and Thomas, 1958], containing shift and penetration functions, besides the boundary condition.

5.6 Cross-section

Now that $l = 2$ is ascertained, after studying the experimental angular distributions, the arbitrary unit cross-section can be fitted by means of the *R-Matrix* approach discussed before. The imposition of quantum angular momentum can be made because of the large uncertainties that affect the experimental data: those are in fact not precise enough to allow a more sophisticated use of the *R-Matrix* theory that involves interference in a many channel approach. We then considered all the levels reported in table 5.2 and performed an *R-matrix* fit assuming the proton channels p_0 and p_1 (corresponding to the ground state and to the first excited state of ^{22}Ne) as the dominant one, as pointed out in Ugalde et al. [2008]; Pizzone et al. [2017]; D'Agata et al. [submitted].

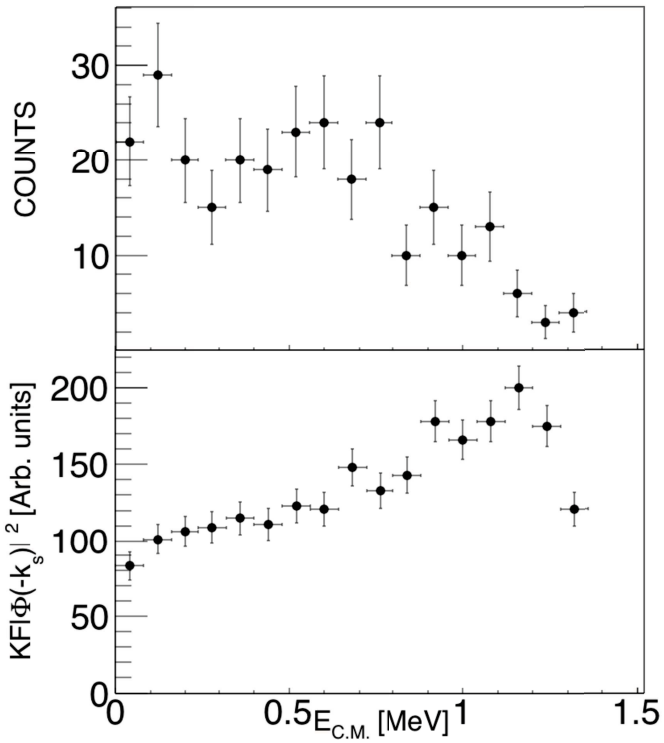

Figure 5.14: Upper panel: Three-body coincidence yield as a function of $E_{C.M.}$.
Lower panel: Kinematic factor times the momentum distribution for the α-d relative motion inside ^{6}Li [D'Agata et al., submitted].

To do so, the arbitrary units coincidence yield (in units of $E_{C.M.}$, figure 5.14 upper panel) must be for first divided by a proper Monte Carlo simulation that takes into account the momentum modulation (brought by the Hänkel function, figure 5.14, lower panel), taking into account distortions discussed in section 5.2. The half-off-energy shell cross section, $\sigma(E_{C.M.})$ has been extracted and fitted by means of one level, three-channel modified R-Matrix calculations, with all the features expressed earlier, and is reported in figure 5.15.

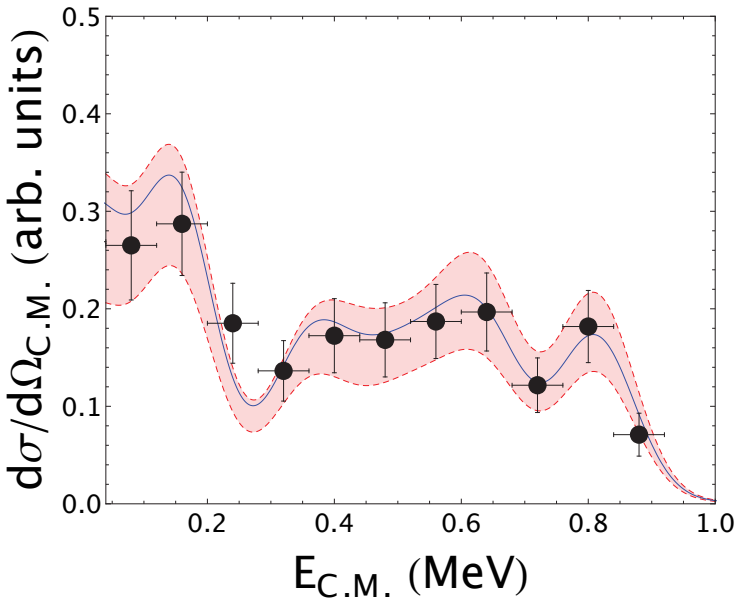

Figure 5.15: Half-of-energy-shell for the ^{19}F(α,p)^{22}Ne reaction in arbitrary units. The blue line with red band represents the R-Matrix fit along with its error. All the resonances parameters are reported in table 5.2 [Pizzone et al., 2017; D'Agata et al., submitted].

E_R [MeV]	$E_{C.M.}$ [MeV]	J^π	γ_α [MeV$^{1/2}$]	γ_p [MeV$^{1/2}$]	$\gamma_{p'}$ [MeV$^{1/2}$]
10.477	0.01	$3/2^+$	$0.0010^{+0.00005}_{-0.00019}$	0.124	0.342
10.616	0.149	$5/2^+$	$0.0055^{+0.00025}_{-0.0080}$	0.087	0.327
10.823	0.356	$3/2^+$	$0.0070^{+0.0001}_{-0.0010}$	0.131	0.417
10.907	0.44	$5/2^+$	$0.0007^{+0.00013}_{-0.00018}$	0.054	0.350
10.972	0.505	$5/2^+$	$0.0090^{+0.00017}_{-0.00090}$	0.044	0.184
10.994	0.527	$3/2^+$	$0.0050^{+0.00017}_{-0.00100}$	0.011	0.079
11.038	0.571	$3/2^+$	$0.0027^{+0.00017}_{-0.00050}$	0.049	0.179
11.109	0.642	$5/2^+$	$0.0120^{+0.00150}_{-0.00150}$	0.016	0.096
11.273	0.806	$3/2^+$	0.003*	0.045	0.279
11.280	0.812	$3/2^+$	0.003*	0.127	0.320
11.303	0.836	$3/2^+$	0.003*	0.105	0.148

Table 5.2: Energies of the ^{23}Na states included in the present analysis. The measured centroid is reported in the first column, as well as the J^π of the levels and the reduced widths involved in the *Modified R-Matrix* fit calculations discussed in Pizzone et al. [2017]; D'Agata et al. [submitted]. Values marked with an asterisk are taken from Ugalde et al. [2008], and have to be considered as upper limits.

About the red band in figure 5.15, it represent the uncertainty band relative to the *Modified R-Matrix* fit, evaluated changing the values of the reduced partial width γ_α to fit the upper and lower limits of the experimental data. This procedure also gave us the possibility to evaluate the errors on γ_α. The fitting procedure (χ^2=0.04) had the aim to extract a trend for the cross-section, but also to deduce the reduced widths of the levels, and to correct for HOES effects and energy resolution. This

was also done for normalization purposes. After angular integration and the evaluation of centrifugal and Coulomb barrier penetration, using the very same parameters and experimental data an on-energy-shell measure for the cross-section has been deduced (figure 5.16), and the contribution of each resonance was evaluated. Then, those data and fitting function were used to evaluate the on-energy-shell cross-section $\sigma(E_{C.M.})$ in absolute units.

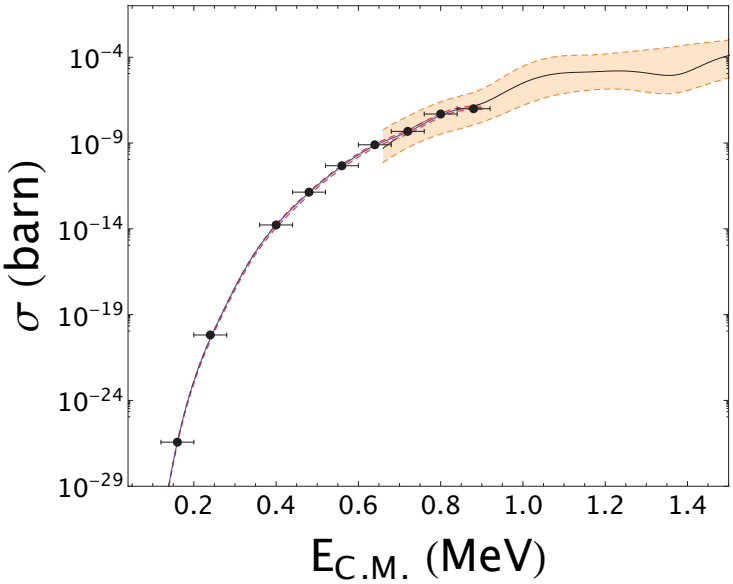

Figure 5.16: Cross-section in absolute units, obtained evaluating penetrability and normalizing data reported in figure 5.15 to direct data [Ugalde et al., 2008]. In this figure, the blue line with red band are the same as in figure 5.15 [D'Agata et al., submitted].

In figure 5.16, error coming from the normalization to data coming from Ugalde et al. [2008] is also added, and a comparison with existing data was performed (black line with orange band).

5.7 Astrophysical Factor and reaction rate

The on-energy-shell $S(E_{C.M.})$-factor, was determined with the parameters extrapolated from the *Modified R-Matrix* calculations and reported in table 5.2. In figure 5.17, the comparison with the present measurement and existing data [Ugalde et al., 2008] was also performed, but this time the comparison is also made with theoretical prediction at lower energies (inside the Gamow window): in this case it was made by Ugalde et al. [2005] and Ugalde et al. [2008] just imposing the known energies and partial width for the resonances of the ^{23}Na compound nucleus [Keyworth et al.,

1968] in a standard *R-Matrix* calculation, for the not experimentally covered energy region ($E_{C.M.}$<0.7 MeV, reported in figure 5.17as a black line with a green band as error). Data above 0.7 MeV are taken from experimental measurements made by Ugalde et al. [2008], and brought in the center-of-mass reference frame for comparison with our experimental data (reported in figure 5.17 as a black line with a orange band as error).

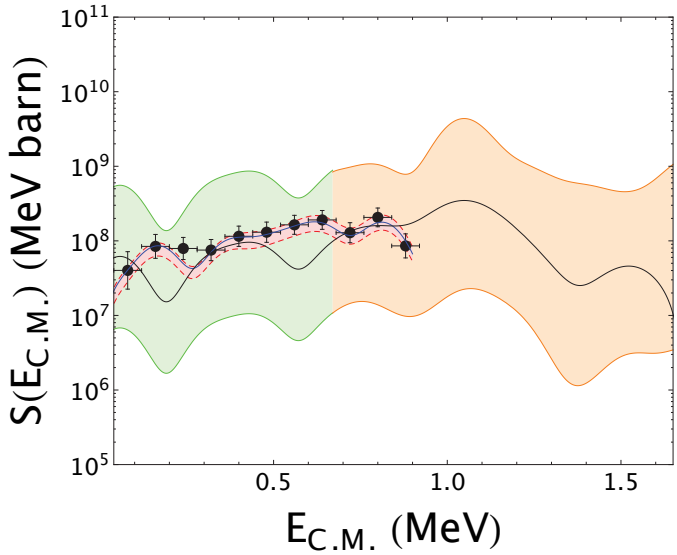

Figure 5.17: Experimental S($E_{C.M.}$)-factor for the ^{19}F(α,p)^{22}Ne reaction [Pizzone et al., 2017]. Here the black line represents the data available in literature [Ugalde et al., 2008] smeared to our experimental resolution using the procedure described in La Cognata et al. [2010], while the green and orange bands are the experimental errors and the average uncertainties in the extrapolation at lower energies reported in Ugalde et al. [2008]. The black dots represent the experimental data from the present measurements, along with the present *Modified R-Matrix* fit (blue line) ant its average uncertainties (red band).

Using now the equations reported in chapter 2, the reaction rate for a couple of charged particles i and j can be calculated as

$$R_{ij} = \frac{N_i N_j}{1+\delta_{ij}}\langle\sigma v\rangle = \frac{N_i N_j}{1+\delta_{ij}}\left(\frac{8}{\pi A}\right)^{1/2}\left(\frac{1}{k_B T}\right)^{3/2} \times \\ \times \int_0^\infty S(E_{C.M.}) exp\left[-\left(\frac{E_{C.M.}}{k_B T} + 2\pi\eta(E_{C.M.})\right)\right] dE_{C.M.} \tag{5.35}$$

where σ is the cross-section for the process, v is the relative velocity of the ij couple of interacting particles and N_i and N_j is the number of nuclei of the two kinds. As can be seen in equation 5.35, the reaction rate is critically dependent on temperature, and in principle any energy of interaction has a role at every value of temperature. To correctly evaluate the reaction rate is then necessary to use some properties of

the reaction rate formula, in particular the properties of additivity of the integral present in equation 5.35: thanks to this property, in fact, it is possible to simply substitute our measure of the reaction rate in the energy range 0<$E_{C.M.}$<0.9 MeV to the existing one, and then calculate the rate in a wide range of temperature. To apply this procedure, a parametrization of the existing reaction rate [Ugalde et al., 2008] is needed.

The following equation represents a parametrization of the existing reaction rate [D'Agata et al., submitted]:

$$\begin{aligned} R_{lit} = \quad & Exp[-a_1 - \tfrac{a_2}{T_9} - \tfrac{a_3}{T_9^{1/3}} - a_4 \cdot T_9^{1/3} + a_5 \cdot T_9 - a_6 \cdot T^{5/3} - a_7 \cdot LogT_9] \\ & + Exp[-b_1 - \tfrac{b_2 \cdot 10^2}{T_9} + \tfrac{b_3}{T^{1/3}} - b_4 \cdot T_9^{1/3} + b_5 \cdot T_9 - b_6 \cdot T_9^{5/3} + b_7 \cdot LogT_9] \\ & + Exp[-c_1 + -\tfrac{c_2}{T_9} + \tfrac{c_3}{T_9^{1/3}} + c_4 \cdot T_9^{1/3} - c_5 \cdot T_9 + c_6 \cdot T_9^{5/3} + c_7 \cdot LogT_9] + \\ & + Exp[d_1 + \tfrac{d_2}{T_9} + \tfrac{d_3}{T_9^{1/3}} - d_4 \cdot T_9^{1/3} + d_5 \cdot T_9 - d_6 \cdot T_9^{5/3} + d_7 \cdot LogT_9] \end{aligned} \tag{5.36}$$

where the constants $a_{1,2,...7}$, $b_{1,2,...7}$, $c_{1,2,...7}$ and $d_{1,2,...7}$ are reported in table 5.3.

Equation 5.36 coefficients			
a_1=1309.18	b_1=15.3885	c_1=844.952	d_1=170.849
a_2=2568.22	b_2=15.7730	c_2=16.3666	d_2=1.80825
a_3=520.290	b_3=432.940	c_3=431.058	d_3=37.3312
a_4=188.174	b_4=418.860	c_4=634.938	d_4=222.838
a_5=5870.34	b_5=12.8279	c_5=240.061	d_5=13.6220
a_6=1286.14	b_6=36.6741	c_6=31.2061	d_6=7.37999
a_7=6374.60	b_7=270.212	c_7=104.777	d_7=88.7584

Table 5.3: Values of the constants in equation 5.36 [D'Agata et al., submitted].

Once the parametrization is done, the reaction rate in the energy region 0<$E_{C.M.}$<0.66 MeV (R_1) and 0.66<$E_{C.M.}$<0.88 (R_2) was calculated from the S-factor already present in literature (figure 5.17). Using now the additivity properties of integrals, those values were subtracted to the parametrization 5.36, and then the measure of the reaction rate performed (R_{THM}) in this work was added to it:

$$R_n = R_{lit} - R_1 - R_2 + R_{THM} \tag{5.37}$$

This results in a an enhancement of the reaction rate at temperature of astrophysical interest ($0.1<T_9<0.6$) up to a factor of four (figure 5.18 ad table 5.4).

Temperature $[10^9 K]$	R_{lit} $\left[\frac{cm^3}{mol \times sec}\right]$	R_{THM} $\left[\frac{cm^3}{mol \times sec}\right]$	Upper R_{THM} $\left[\frac{cm^3}{mol \times sec}\right]$	Lower R_{THM} $\left[\frac{cm^3}{mol \times sec}\right]$	Ratio $\frac{R_{THM}}{R_{lit}}$
0.04	4.259×10^{-34}	4.247×10^{-34}	4.248×10^{-34}	4.245×10^{-34}	0.997
0.05	8.725×10^{-32}	9.376×10^{-32}	9.437×10^{-32}	9.196×10^{-32}	1.075
0.06	8.640×10^{-30}	1.422×10^{-29}	1.474×10^{-29}	1.270×10^{-29}	1.646
0.07	4.940×10^{-28}	1.637×10^{-27}	1.737×10^{-27}	1.325×10^{-27}	3.314
0.08	4.193×10^{-26}	1.310×10^{-25}	1.384×10^{-25}	1.061×10^{-25}	3.125
0.09	5.066×10^{-24}	8.628×10^{-24}	8.912×10^{-24}	7.560×10^{-24}	1.703
0.10	3.297×10^{-22}	3.297×10^{-22}	3.369×10^{-22}	3.003×10^{-22}	1.373
0.11	5.096×10^{-21}	6.709×10^{-21}	6.847×10^{-21}	6.136×10^{-21}	1.316
0.12	6.298×10^{-20}	8.511×10^{-20}	8.719×10^{-20}	7.691×10^{-20}	1.352
0.13	5.550×10^{-19}	7.921×10^{-19}	8.169×10^{-19}	7.027×10^{-19}	1.427
0.14	4.002×10^{-18}	6.017×10^{-18}	6.252×10^{-18}	5.249×10^{-18}	1.504
0.15	2.507×10^{-17}	3.905×10^{-17}	4.085×10^{-17}	3.368×10^{-17}	1.557
0.16	1.379×10^{-16}	2.189×10^{-16}	2.304×10^{-16}	1.875×10^{-16}	1.591
0.18	2.742×10^{-15}	4.559×10^{-15}	4.853×10^{-15}	3.855×10^{-15}	1.663
0.20	3.312×10^{-14}	5.970×10^{-14}	6.438×10^{-14}	4.968×10^{-14}	1.803
0.25	3.727×10^{-12}	9.629×10^{-12}	1.078×10^{-11}	7.655×10^{-12}	2.583
0.30	1.259×10^{-10}	4.572×10^{-10}	5.316×10^{-10}	3.522×10^{-10}	3.632
0.35	2.413×10^{-09}	9.429×10^{-09}	1.136×10^{-08}	7.084×10^{-09}	3.908
0.40	3.377×10^{-08}	1.065×10^{-07}	1.324×10^{-07}	7.805×10^{-08}	3.152
0.45	3.644×10^{-07}	7.976×10^{-07}	1.011×10^{-06}	5.793×10^{-07}	2.188
0.50	3.041×10^{-06}	4.670×10^{-06}	5.875×10^{-06}	3.489×10^{-06}	1.535
0.60	1.018×10^{-04}	1.063×10^{-04}	1.234×10^{-04}	9.034×10^{-05}	1.045
0.70	1.461×10^{-03}	1.399×10^{-03}	1.970×10^{-03}	1.292×10^{-03}	0.957
0.80	1.103×10^{-02}	1.048×10^{-02}	1.430×10^{-02}	1.004×10^{-02}	0.950
0.90	5.639×10^{-02}	5.405×10^{-02}	7.410×10^{-02}	5.272×10^{-02}	0.958
1.00	4.179×10^{-01}	4.110×10^{-01}	5.570×10^{-01}	4.078×10^{-01}	0.983
1.25	$5.762\times10^{+00}$	$5.719\times10^{+00}$	$5.736\times10^{+00}$	$5.704\times10^{+00}$	0.992
1.50	$3.948\times10^{+01}$	$3.935\times10^{+01}$	$3.939\times10^{+01}$	$3.931\times10^{+01}$	0.997
1.75	$1.772\times10^{+02}$	$1.769\times10^{+02}$	$1.770\times10^{+02}$	$1.768\times10^{+02}$	0.998
2.00	$5.921\times10^{+02}$	$5.916\times10^{+02}$	$5.918\times10^{+02}$	$5.915\times10^{+02}$	0.999

Table 5.4: Values for the parametrization (R_{lit}) of the reaction rate and for the obtained values of the present work (R_{THM}). Upper and lower limits of R_{THM} come from the error on *Modified R-Matrix* fit and on normalization, and are between 1% and 21% with respect to the recommended value. In the ratio is possible to see the factor of four enhancement.

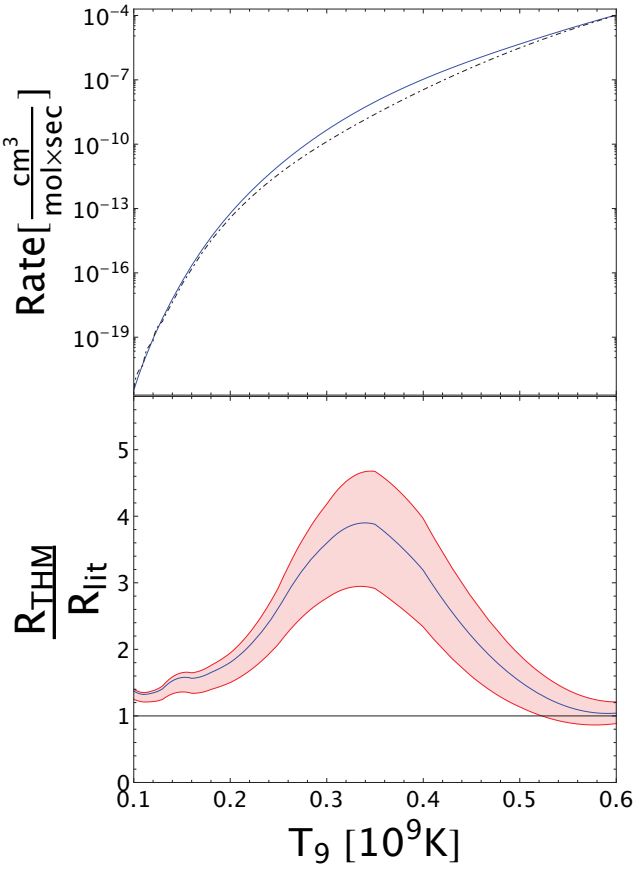

Figure 5.18: Upper panel: comparison between the reaction rate, parametrized from the one present in literature [Ugalde et al., 2008](black dashed line) and the one from the present work (blue line) [Pizzone et al. 2017; D'Agata et al., submitted].
Lower panel: ratio between the reaction rate from Ugalde et al. [2008] and the one from the present work (blue line) along with its errot (red band) [D'Agata et al., submitted].

5.8 Astrophysical implications

Now that the reaction rate is properly calculated, its impact on low-mass AGB-stars nucleosynthesis can be evaluated. As it was already pointed out in Chapter 1, fluorine nucleosynthesis is a quite complicated matter; in particular, it can be destroyed by means of the ^{19}F(p,α)^{16}O, ^{19}F(n,γ)^{20}F and ^{19}F(α,p)^{22}Ne reactions, with the third one that mainly operates during the TP[1], being the abundance of protons in the He-shell quite poor.

The extracted reaction rate was introduced in a state-of-the-art code for fluorine nucleosynthesis: the NEWTON code [Trippella et al., 2014]. Such a feature was used to study fluorine nucleosynthesis in stars of 1.5, 3 and 5 $M_{\odot}$ with solar metallicity.

[1] Thermal pulse, see Chapter 1.2

Profile for proton injection at the TDU[2] and the resulting budget of ^{13}C and ^{14}N in the He-rich region were adopted from Trippella and La Cognata [2017], along with the same cross sections for neutron capture reactions. The cross section for proton and α production were instead adopted from Trippella and La Cognata [2017]; Iliadis et al. [2010]; Caughlan and Fowler [1988]; Adelberger et al. [2011]; Palmerini et al. [2013]; Sergi et al. [2015]; Best et al. [2013a]; La Cognata et al. [2010]; Best et al. [2013b]; Couture et al. [2008]; Ugalde et al. [2008]; Pizzone et al. [2017].

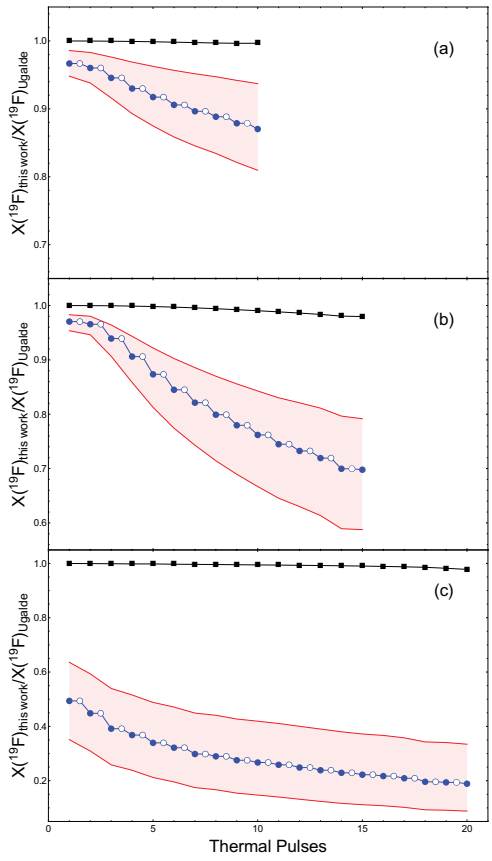

Figure 5.19: Temporal evolution of the ratio abundance obtained using THM data and and the one from Ugalde et al. [2008]. In abscissa there are the thermal pulses that follow through the whole AGB phase, indicated as integer numbers, while the half-integers represent the inter-pulses. In this notation the time increases from left to right. Panels (a),(b) and (c) are made using models of solar metallicity and with mass of 1.5M$_\odot$, 3M$_\odot$ and 5M$_\odot$. The black lines represent the evolution of ^{19}F surface abundance, while the solid black marks indicate the surface composition after each TP and the subsequent TDU. About blue lines, those represent the ratio between fluorine abundance in He-rich stellar region at each TP (blue dots), and before the on-set of the next He-burning episode at the end of the inter-pulse (white dots). Finally the red areas represent the spread of nucleosynthesis code after adopting the upper and lower limits of the R-Matrix calculation shown above [D'Agata et al., submitted].

[2]Third Dredge-Up, see Chapter 1.2

Moreover, other phenomena that are involved in ^{19}F destruction, like cool bottom process (see Palmerini et al. [2011b] and references therein) or hot bottom burning (for 5$M_\odot$ stars, Lattanzio [2003] model), were neglected with the aim to better appreciate the impact of this new measurement of the ^{19}F(α,p)^{22}Ne cross-section and reaction rate [Pizzone et al., 2017; D'Agata et al., submitted]. In figure 5.19 the temporal evolution during the whole AGB phase of the ^{19}F ratio, obtained with the present THM experimental data for the ^{19}F(α,p)^{22}Ne, and the one obtained by using the rate published in Ugalde et al. [2008] are reported: at the typical temperatures value for the He-shell burning (a few 10^8 K) - with the present rate fluorine - is easily destroyed during TP, and its abundance in the stellar interior is lowered.
In (c) panel, where a 5$M_\odot$ AGB-star is considered, the effect of the enhancement of the rate is more visible: ^{19}F abundance is reduced down to a factor of four in the last pulses, due to the fact that in these conditions the temperature is of 3.8×10^8 K, corresponding to the energy at which the difference with the present rate and the one present in literature, is at its maximum. Differences are smaller for 1.5$M_\odot$ and 3$M_\odot$ because temperatures do not exceed 3×10^8K.
When the ashes of He-burning are brought to the stellar surface by the TDU, all the products of stellar nucleosynthesis are mixed and diluted with the envelope materials: so the effect of the ^{19}F(α,p)^{22}Ne reaction becomes negligible (as can be guessed from the black curves in figure 5.19), and the difference between the calculations made by using THM reaction rate or the one from Ugalde et al. [2008] are less than 5%.

5.9 Conclusions

With the experimental analysis presented in this chapter, the study of the ^{19}F(α,p)^{22}Ne using the THM can be considered completed at astrophysical energies. Until this measure, in the region of interest of the Gamow window, there were no experimental measurements for cross-section, S($E_{C.M.}$)-factor or reaction rate. This measurement, performed at Ruđer Bošković Institute (Zagreb), is the first one that succeeded in determining such values at low energies of astrophysical interest. As said earlier, the ^{6}Li(^{19}F,p^{22}Ne)d three-body reaction in the exit channel was used to to study the ^{19}F(α,p)^{22}Ne, that is the main destruction channel of fluorine in α-rich environment, using THM. The excitation function for 10.3<$E_{^{23}Na}$<12 MeV was studied, and many resonances corresponding to ^{23}Na levels [Firestone, 2007a] were

found. The two-body cross-section and S($E_{C.M.}$) were extracted at 0<$E_{C.M.}$<0.88 MeV, and many levels were identified and fitted using the *Modified R-Matrix approach*. This fit was also useful to calculate the reaction rate, that was then used to evaluate the astrophysical impact of this measurement.

With the aim to strengthen the results, more statistics would be needed to reduce errors and clarify if there are interference phenomena between the resonances, along with a better experimental resolution. Furthermore, while it appears clear that $l = 2$ is the dominant angular momentum of interaction, there is no reason why other l could not play any role in the ^{19}F(α,p)^{22}Ne reaction, and measurement of the THM at higher energies ($E_{C.M.}$>1.1 MeV) would allow to have a more efficient normalization. For all this reasons, repeating this experiment would be useful, possibly using a magnetic spectrometer to detect ^{22}Ne[3] or deuterons at small angles: this would allow a better reconstruction of the spectator momentum distribution p_s, improving the quasi-free process separation. Using a spectrometer would also allow to use higher energy ^{6}Li beam, or even a ^{19}F one.

[3]but using a different experimental approach, like a ^{19}F beam impinging on a ^{6}Li target.

CHAPTER 6

Data Analisys for the ^{23}Na(p,α)^{20}Ne reaction

As stated in the previous chapters, energy and position calibration are a necessary step to analyze any nuclear reaction. For the ^{23}Na(d,α ^{20}Ne)n reaction, PSD1 and PSD2 were optimized for neon detection, while PSD2 and PSD4 for α detection: using the ΔE-E technique, the heavy particles for the reaction of interest were selected, and then the QF events were isolated. Once data are properly reduced, excitation function was studied and the two-body half-off-energy-shell cross-section in arbitrary units was extracted. Further analysis will be made in the future.

6.1 Reaction channel selection

Like for ^{19}F(α,p)^{22}Ne, there are many reaction channels that could hinder the ^{23}Na(p,α)^{20}Ne reaction measurement. Careful data selection is therefore needed. The experimental apparatus was mounted to identify particles by means of the ΔE-E technique, at angles that are favorable for ^{20}Ne detection. Looking at equations 4.9 and 4.10, it is clear how energy loss is poorly dependent from the number of neutrons of the incoming particles. In this case the experimental set-up did not allow to disentangle between ^{20}Ne and ^{21}Ne entirely, and a strong contribution from both elastic and inelastic scattering of ^{23}Na on deuterium and ^{12}C was expected.

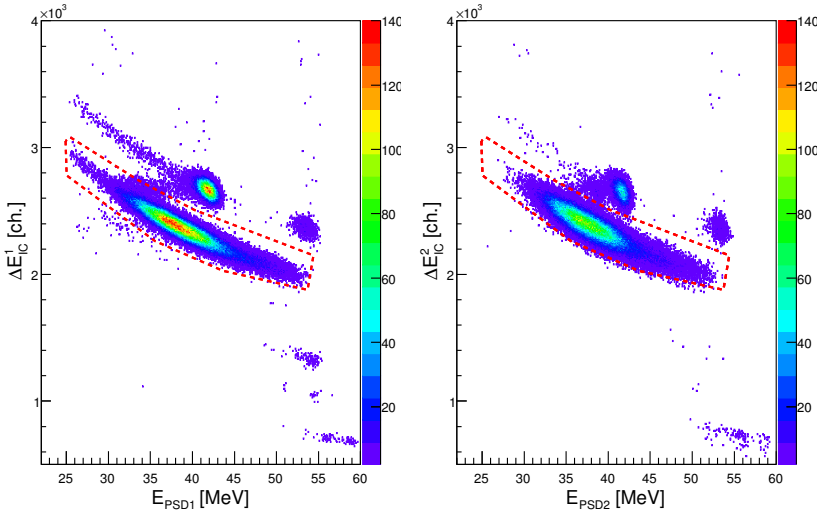

Figure 6.1: 2D-spectra for both ΔE -E telescopes. A large contribution of scattering can be detected for both spectra, and ^{21}Ne presence can not be excluded at this point. In the red dashed boxes, the hyperboles considered to be proper of neon-like particle are selected

As can be seen in figure 6.1, a contribution coming from ^{23}Na scattering falls right inside the neon-like hyperbole, and it must be eliminated in some way. ^{21}Ne coming from the direct two-body reaction ^{23}Na(d,α)^{21}Ne can be also present, and this fact must be taken into account. To eliminate (or reduce to a minimum) both contributions, a comparison between E_{PSD1} vs E_{PSD4} and E_{PSD2} vs. E_{PSD3} with a proper Monte Carlo simulations for the three-body reaction was attempted.

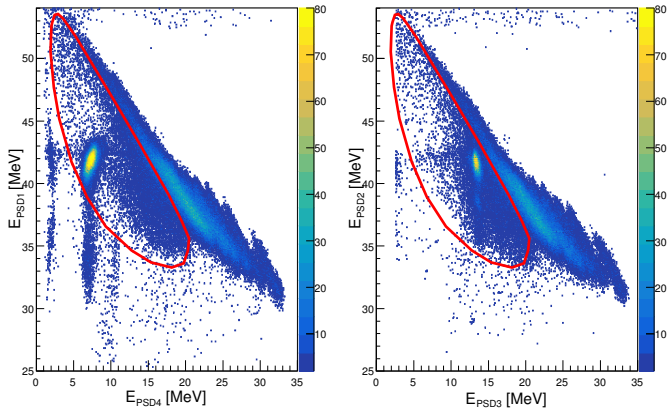

Figure 6.2: E_{PSD1} vs. E_{PSD4} and E_{PSD2} vs. E_{PSD3} 2D-spectra (for PSD1-4 and PSD2-3 coincidences, respectively). The red loci represent the extremities of a proper Monte Carlo simulation of the energies of ^{20}Ne and α nuclei in the examined three-body reaction ^{23}Na(d,α ^{20}Ne)n: those will be used as kinematic cut for further analysis.

This procedure has been proven to be useful for data reduction: in this way, in

fact, it is possible to strongly reduce the contribution coming for ^{21}Ne, but a strong contribution coming from elastic scattering is still present (brighter zones inside the red boxes in figure 6.2). From now on, only data lying inside the red boxes in figure 6.2 will be used: those show a better separation between Ne isotopes and beam, and the contribution form ^{21}Ne is strongly reduced.

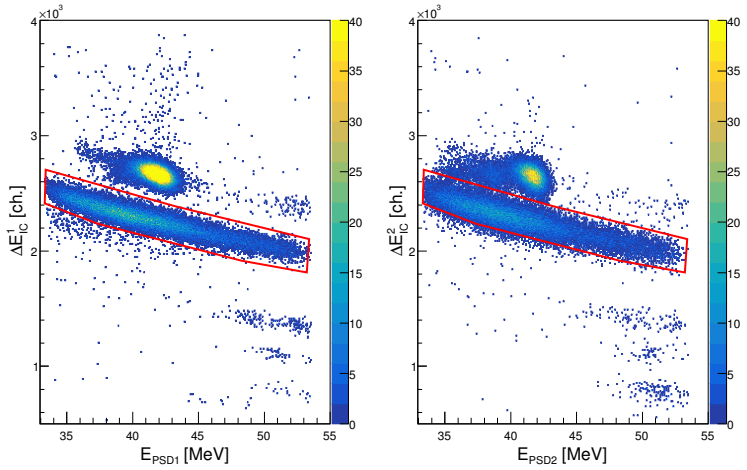

Figure 6.3: ΔE-E 2D-spectra for PSD1 and PSD2 (left and right panel, respectively) after the graphical cuts of figure 6.1 and 6.2. Data shown a better separation from elastic scattering, and the ^{20}Ne hyperbole seems to be more resolved.

Both those facts are evident looking at figure 6.3: the separation of ^{23}Na from Ne-like particles appear to be more pronounced, and the typical contaminations from the beam scattering is way less evident, along with the contribution from ^{21}Ne. The last of those facts can be guessed looking at the hyperbole thickness: it is in fact thinner in the higher part, and according to the Bethe-Bloch formula (eq. 4.9) nuclei with the same Z and different N must lie on curves that are higher when N rises. In this case, results are much better of the one reported in the previous chapter at this stage, and this fact reflected itself in a better refined Q_{value} spectrum. The red boxes of 6.3 will be used as further selection for the following analysis.

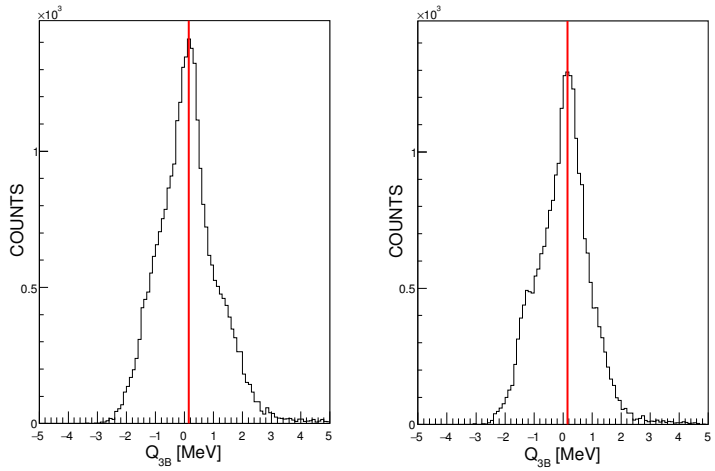

Figure 6.4: Q_{value} of the three body reaction for both coincidences (left and right panel are the same of the previous figures): the red line indicates the theoretic value for the three body reaction (Q_{value}=0.152 MeV)

In figure 6.4 the better refinement is evident, but contaminations are also clearly shown in the unlikely shape of the two peaks. To remove parasite reaction contribution still hindering data analysis, an approach different from the previous chapter was used: a new variable, Q_{2B}=E_{beam}-$E_{^{20}Ne}$-E_{α}, was reconstructed and plotted against the three-body Q_{value}, Q_{3B}=E_{beam}-$E_{^{20}Ne}$-E_{α}-E_n. Using it, if two-body reactions (in particular reactions involving ^{21}Ne contamination) are present, vertical loci must rise, and this should happen even if other two-body reactions different from the ^{23}Na(p,α)^{21}Ne are taking place. From figure 6.5 this looks to be the case, and data

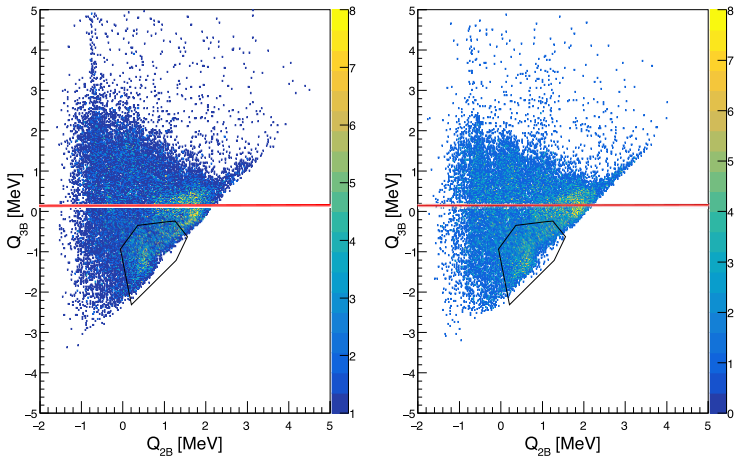

Figure 6.5: 2D-spectra Q_{3B} vs. Q_{2B}. As can be seen in the black boxes, vertical loci are present, underlining the presence of two-body parasite reactions. Those (inside the black boxes) will not be considered in the following analysis. There are evidences of another vertical locus at Q_{2B}=-0.6 MeV, but its contribution is far from the Q_{3B} of interest

"inside" the black boxes will not be considered for further analysis. In this way, the largest amount of the data coming from two-body reactions is eliminated.
Another experimental procedure that was applied in this work is the one coming from Costanzo et al. [1990]. As said before, the experimental set-up was made to detect only two out of the three emitted particles. Energy and angle of the third particle are then reconstructed event by event, applying the conservation principles, under the hypothesis that the third particle is a neutron (A=1). Such an assumption can be made studying two quantities:

$$y = E_{beam} - E_{^{20}Ne} - E_{\alpha} \tag{6.1}$$

$$x = \frac{p_n^2}{2u} \tag{6.2}$$

where u is the atomic mass unit in Mev/c^2. Plotting equations 6.1 versus 6.2, a 2D-spectrum was made (figure 6.6): the events of interest must gather around a straight line:

$$y = \frac{1}{A_n}\frac{p_n^2}{2u} - Q_{value} \tag{6.3}$$

in which A_n is the mass of the spectator particle (a neutron in this case). This line crosses the ordinate axis at y=Q_{value}, that for this case is equal to 0.152 MeV.

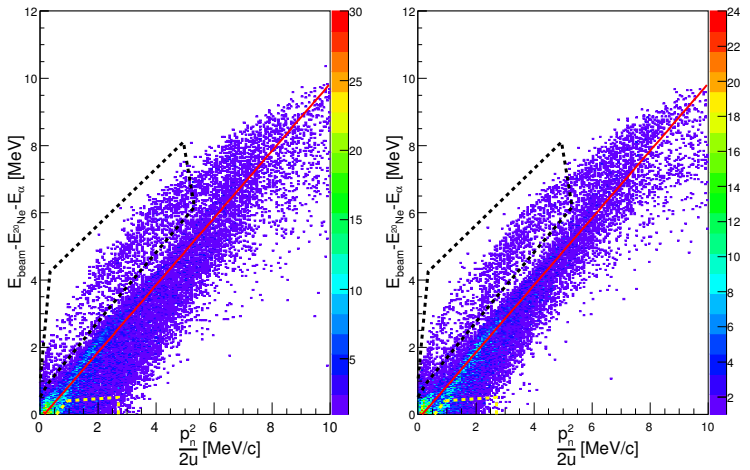

Figure 6.6: Spectator particle identification of the remaining events after the selection made in figure 6.5, using the procedure explained in Costanzo et al. [1990]. The red line represents where the data with the expected Q_{value} should gather. The black and yellow dashed boxes in the left (coincidence PSD1-4) and right panel (coincidence PSD2-3) represent data that will not be considered in further analisys. Data with $\frac{p_n^2}{2u}$ <5 MeV will also be discarded.

Now a possibility would be to cut around the red line in figure 6.6, but this had been proven to be a too big restriction on data: a better choice would be to discard data that did not surely belong to the reaction of interest, ^{23}Na(d,$\alpha\,^{20}Ne$)n. In particular, the black dashed boxes in figure 6.6 should belong to the two-body reaction ^{23}Na(p,α_1)^{20}Ne reaction: the so-called α_1 channel corresponds to the configuration where the heavy nucleus is emitted in the first excited state, in this case ^{20}Ne*. This possibility is also of great interest, and its analysis is left for a future work. After all those selections of data to analyse and discard, a new Q_{value} spectrum was plotted (figure 6.7).

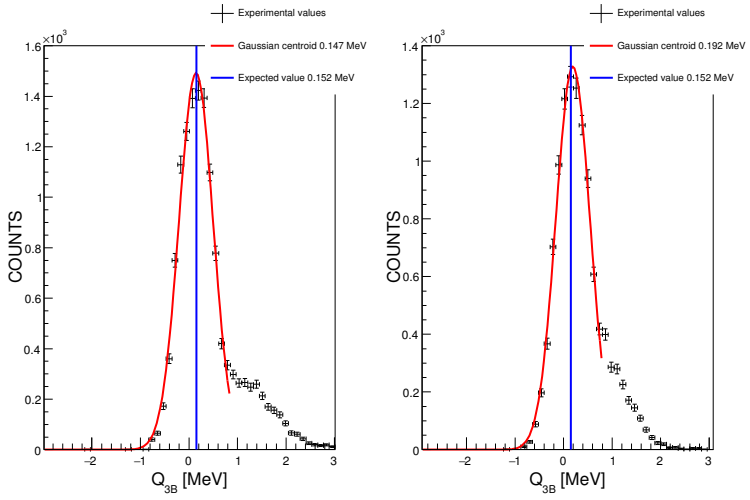

Figure 6.7: Q_{value} for the ^{23}Na(d,$\alpha\,^{20}$Ne)n reaction for both coincidences (PSD1-4 on the left, PSD2-3 on the right), with all the kinematic selections mentioned above. All informations are in the legend

As can be seen in figure 6.7, for both coincidences data are in fair agreement with experimental data. The Gaussian fit is limited to Q_{3B} $\leq$1 MeV, and the contamination at higher values has an unknown origin, but is probably due to some beam contamination. In the following analysis this unknown contamination will be erased (so only events with Q_{3B} $\leq$1 MeV will be considered), imposing some limitation on p_s and $\vartheta_{^{20}Ne}$. This second statement, in particular, was made considering the so called quasi-free angles: the expected angle of emission of the ^{20}Ne particle, $\vartheta_{^{20}Ne}$, in the range where the QF contribution is expected to be maximum (-50 MeV/c $\leq p_s \leq$50 MeV/c), and considering the angular range covered by the α detectors (see table 4.3), in fact, has its maximum between 1° and 6.5 ° (figure 6.8).

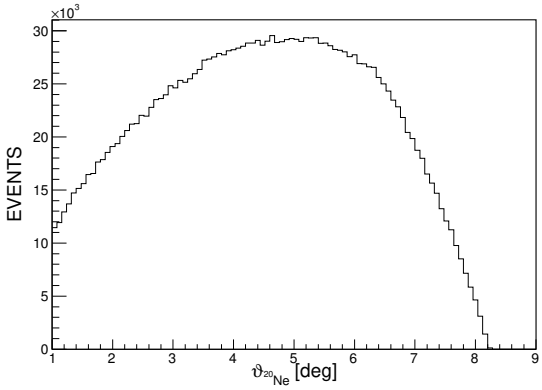

Figure 6.8: Emission angle of the heavy ^{20}Ne particle, guessed from Monte Carlo calculation, considering the p_s range where it is expected to be maximum (-50 MeV/c≤p_s ≤50 MeV/c).

6.2 Quasi-free channel contribution

As in the previous chapter, the three-body reaction channel is now isolated. In the following paragraph, the QF contribution will be evaluated, with the aim to use the THM: to use the method, in fact, is fundamental to eliminate all the contribution from sequential decay, direct break-up, and any other process that can occur with the same particles in the exit channel. As it has already been done for the ^{19}F(α,p)^{22}Ne reaction, it is useful to look at the relative energy 2D-spectra. Plotting the $E_{\alpha-n}$ versus $E_{^{20}Ne-\alpha}$ and $E_{^{20}Ne-n}$ versus $E_{^{20}Ne-\alpha}$, the presence of horizontal and vertical loci is a sign of the presence of ^{5}He (horizontal loci), ^{21}Ne (horizontal loci) or ^{24}Mg (vertical loci) excited states.

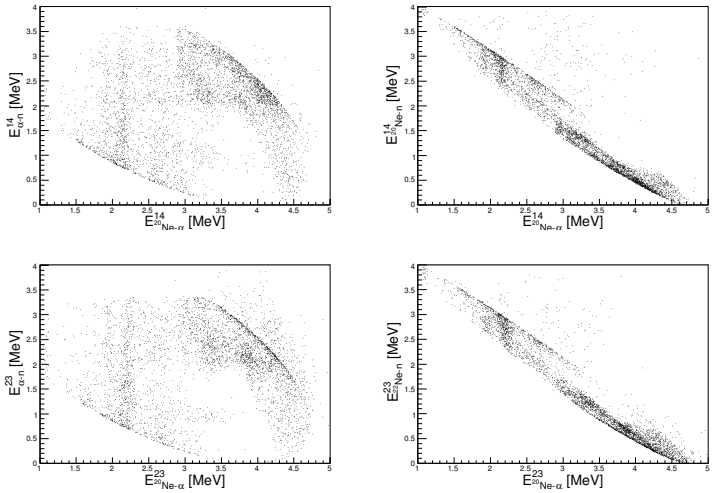

Figure 6.9: Left panels: relative energy 2D spectra for the PSD1-4 coincidence.
Right panels:relative energy 2D-spectra for the PSD2-3 coincidence.

In figure 6.9 there are no signs of horizontal loci in none of the four panels. This indicates the absence of levels coming from excited states of ^{21}Ne or ^{5}He related to sequential decays. Some vertical loci are instead detectable, and this was expected and, in a way, favourable: it in fact underlines the presence of excited states of ^{24}Mg. Among those data, the presence of QF process was investigated. Under the conditions already explained in chapter 3, and from equation 5.2, if QF processes are present the coincidence yield must change with the momentum distribution $|\Phi(p_s)|^2$, and it must show its peak at $p_s \approx 0$. Using now equation 5.3, the presence of those will be revealed by its trend: in this case it must reproduce the neutron distribution inside deuterium, once the yield is known from the experiment and the KF factor from theoretical calculations. From an experimental point of view, this can be applied only in a favourably small region of energy of the center-of-mass system (defined as in the previous chapter). This happens because in this small region the two-body cross-section can be considered as a constant.

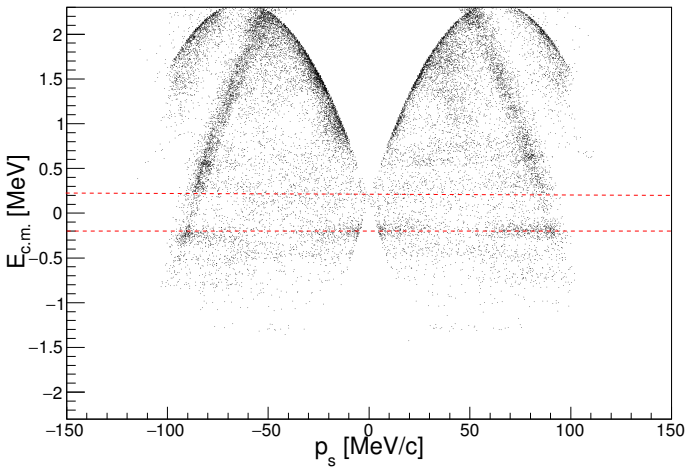

Figure 6.10: E_{CM} versus p_s for both coincidences. The red dashed lines indicate the chosen energy region.

For this case, the choice to take -0.2 MeV<E_{CM} <0.2 MeV(red dashed lines in figure 6.10). Then the experimental p_s was compared with theoretical Monte Carlo calculations, that take into account all the kinematics for the problem (i.e. the KF factor present in eq. 5.3). By dividing the two spectra it is possible to get the trend of the $|\Phi(p_s)|^2$ momentum distribution.

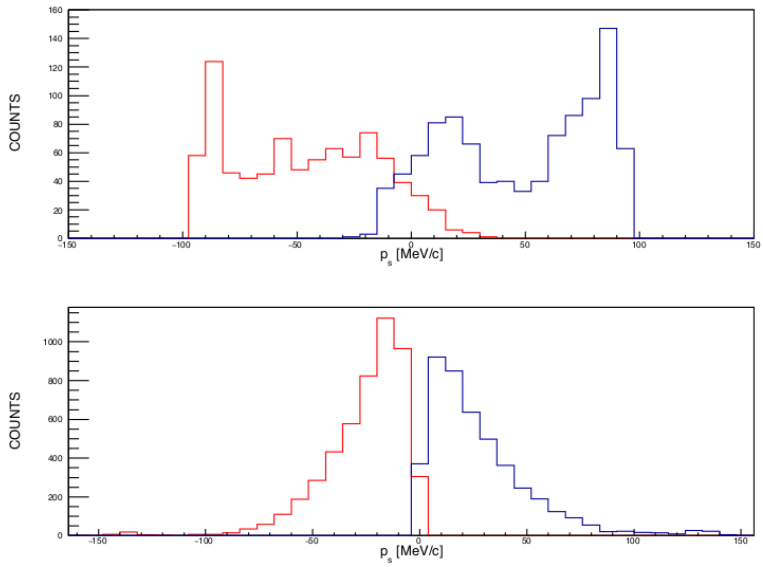

Figure 6.11: Neutron momentum for both coincidences (PSD1-4 in blue and PSD2-3 in red). In the upper panel experimental data are reported, while in the lower there are the theoretical Monte Carlo simulation for the reaction with the corresponding angular restriction (red PSD1-4, blue PSD2-3)

The two distributions (experimental and theoretical) are reported in figure 6.11: as can be seen in the upper panel, for both coincidences there is a strong contribution around $|p_s|$=100 MeV/c (this is also visible in figure 6.10), and this can be due to compound nucleus decay of ^{24}Mg. For this reason the angular cut on $\vartheta_{^{20}Ne}$ was applied ($1° \leq \vartheta_{^{20}Ne} \leq 6.5°$), and the momentum distribution for the two coincidences left is reported in figure 6.12

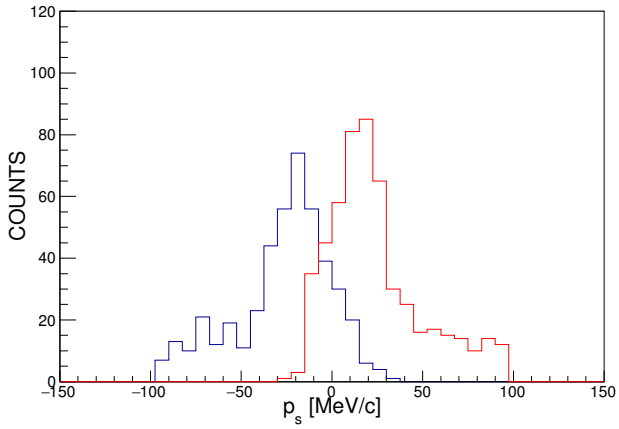

Figure 6.12: Neutron momentum after the angular cut (colors as in figure 6.11). Now the strongest contribution comes from $|p_s| \leq 50$ MeV/c: the peaks at higher $|p_s|$, present in figures 6.10 and 6.11, are removed.

In this new configuration a division between the two histograms (experimental coming from figure 6.12 and theoretical from 6.11) was made, and finally the momentum distribution $|\Phi(p_s)|$ was obtained. In these conditions, the formalism briefly recalled earlier can be used, and if the observed process is a quasi-free one, then the momentum distribution of a neutron inside a deuterium cluster must follows the trend of a Hulthén function [Pizzone et al., 2009]:

$$\Phi(\mathbf{p_s}) = \frac{N}{\pi}\frac{ab(a+b)}{(a-b)^2}\left(\frac{1}{a^2+b^2} - \frac{q}{b^2+FWHM}\right) \tag{6.4}$$

where N is a normalization factor, a=0.2317 fm^{-1} and b=1.202 fm^{-1} are parameters known from literature [Zadro et al., 1989; Pizzone et al., 2009] and FWHM is the experimental full width at half maximum of the fitting curve. Then the absolute values coming from the earlier obtained momentum distributions for the two coincidences were mediated, and the results were best-fitted with the Hulthén function (equation 6.4).

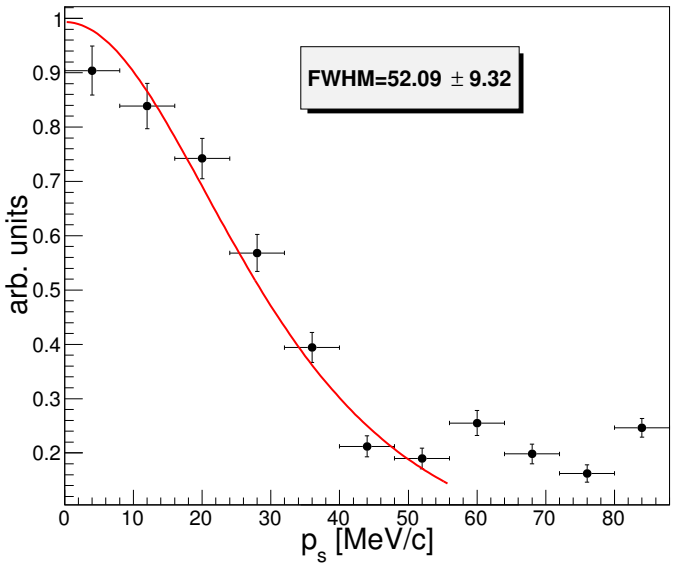

Figure 6.13: Momentum distribution obtained with the procedure explained in the text. The red line represents the Hulthén function that best-fits the experimental data. The FWHM, W(q_t) of this best-fit is reported in figure. Form now on, data will have $|p_s| \leq 40$ MeV/c

Now the anticipated selection over the p_s variable appears clear: it is the limit at which the Hulthén function best-fits the data (figure 6.13). It also is in agreement with the maximum value that the neutron can take in QF reactions ($p_s \leq 60$ MeV/c)[Shapiro et al., 1965].

In the fitting procedure using the Hulthén function, FWHM was calculated and it is FWHM=52.09±9.32 MeV/c. Neutron full-width distribution inside deuterium follows, if plotted as a function of the transferred momentum q_t, a trend similar to the case of ^{6}Li treated in the previous chapter [Pizzone et al., 2009]: in this case equation 5.5 is still valid, with the difference that for this case f_0=58 MeV/c, q_0=60±12 MeV/c, q_t=230 MeV/c, and W(q_t)≈52.09±9.32. About equation 5.6, it is still valid, but p_p and $p_{^{22}Ne}$ must be substituted with p_α and $p_{^{20}Ne}$. The results of this calculation are presented in figure 6.14.

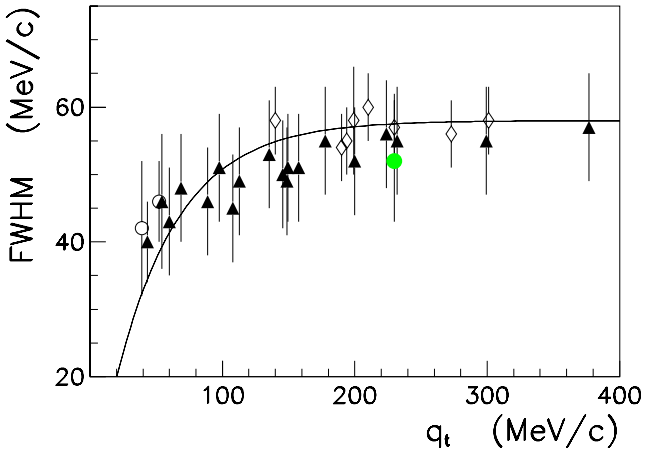

Figure 6.14: FWHM of the momentum distribution of neutron inside deuterium, as a function of the transferred momentum q_t. The green circle represents the value obtained in this experiment, while the black and white diamonds and the white circles are taken from literature [Pizzone et al., 2005, 2009].

6.3 Excitation function

As in chapter 5.3, the levels of the compound nucleus formed by the ^{23}Na+p reaction were considered: The relative energy spectra $E_{^{20}Ne+\alpha}$ were therefore analysed. This quantity can be extracted from experimental data by manipulation of the ^{20}Ne$-\alpha$ system as made in eq. 5.7:

$$E_{ecc}^{^{24}Mg} = E_{^{20}Ne-\alpha} + Q_{ecc} \tag{6.5}$$

In this case Q_{ecc}=9.316 MeV is the Q_{value} for the formation of the ^{24}Mg compound nucleus from a α particle and a ^{20}Ne nucleus (see figure 6.15). Also for this case if $E_{^{20}Ne-\alpha}$ is equal to zero, $E_{ecc}^{^{24}Mg}$ will be equal to 9.316 MeV.

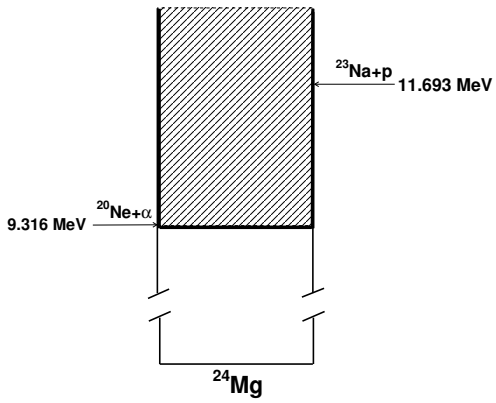

Figure 6.15: Level scheme for the ^{24}Mg compound nucleus: the shaded zone indicates the region explored by the experiment

In the energy region spanned by the experiment (figure 6.15), many resonant structures are detected, using the mono-dimensional energy spectrum extracted from eq. 6.5. Even in this case, a fit on the experimental data was made by adding many Gaussian all with the same width σ=0.05 MeV (corresponding to the experimental resolution, see in the text beyond for further details). All the centroids were then compared with the levels of ^{24}Mg available in literature [Firestone, 2007b].

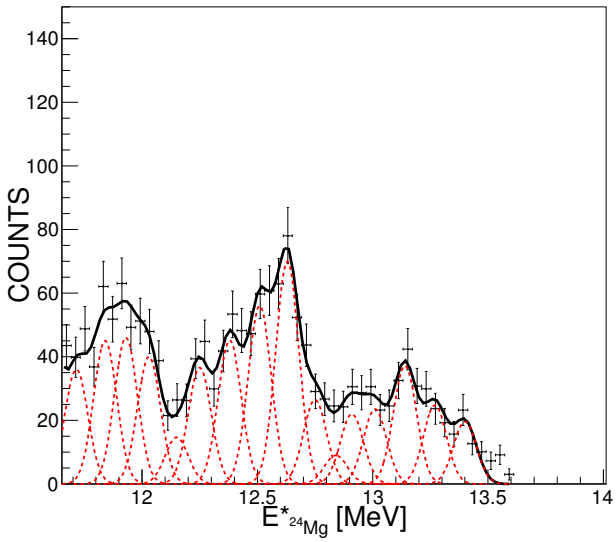

Figure 6.16: Excitation function of the ^{24}Mg compound nucleus. The centroids of the Gaussian are reported in the table 6.1, while the σ are fixed at 0.05 MeV.

In figure 6.16, there is evidence of many groups of blended resonances, really near to

$E^{*exp}_{^{24}Mg}$ [MeV]	$E^{*lit}_{^{24}Mg}$[Firestone, 2007b] [MeV]	J^{π}	l_{min}	$\Delta E_{lit-exp}$ [keV]
11.715	11.728	0^+	2	13
11.830	11.862	////	////	32
11.930	11.969	2^+	2	39
12.030	12.049	4+	2	19
12.150	12.160	4+	2	10
12.250	12.257	3^-	1	7
	12.258	2^+	2	8
12.380	12.339	2^+	2	-41
		3^-	1	
		4^+	2	
	12.403	2^+	2	23
12.510	12.504	4^+	2	-6
12.630	12.636	1^-	1	6
		2^+	2	
12.750	12.737	2^+	2	-13
	12.776			16
12.840	12.845	3^-	1	5
		4^+	2	
12.910	12.919	2^+	2	9
		3^-	2	
		4^+	2	
13.010	12.972	4^+	2	-38
	13.027	2^+	2	17
		3^-	1	
13.140	13.137	////	////	-3
13.270	13.253	////	////	-17
13.400	13.365	////	////	-35
	13.417	////	////	17

Table 6.1: Levels used as centroids for the Gaussian functions (red dashed lines) in figure 6.16 and levels reported in literature [Firestone, 2007b]. The sum of those Gaussian makes our fit (black solid line). In the last column the difference between the centroids and the theoretical values are reported.

each other. In this case, experimental resolution and experimental errors are evaluated from α-source and elastic scattering of ^{23}Na on gold and CD_2 (as in the previous experiment): after the standard error propagation procedure, the experimental resolution has been fixed in 0.05 MeV, and the experimental error in 0.04 MeV. Both are far greater than the proper width of the levels, that is of the order of magnitude of some keV or lower [Firestone, 2007b], as in the case treated in chapter 5. Again, this procedure is just a first step for level identification: angular momentum of interaction and the J^{π} proper of the resonance are still not uniquely assumed: more refined methods are needed.

6.4 Cross-section: preliminary approach

The triple-differential cross-section $\frac{d^3\sigma}{d\Omega_{^{20}Ne} d\Omega_\alpha dE_{CM}}$ is strictly tied to the energy of the light particle in the center-of-mass reference frame of the two-body reaction, under the post-collision prescription. As in the previous chapter it is defined as:

$$E_{C.M.} = E_{^{20}Ne-\alpha} - Q^{2B}_{value} \tag{6.6}$$

It is now useful to calculate the trend of the $\vartheta_{C.M.}$ variable, corresponding to the angle of emission of the light particle in the center-of-mass reference frame of the two-body reaction, following the prescription of Slaus et al. [1977] (similarly to equation 5.9 of the previous chapter):

$$\vartheta_{C.M.} = \arccos \frac{(\mathbf{v_{^{23}Na}} - \mathbf{v_p}) \cdot (\mathbf{v_{^{20}Ne}} - \mathbf{v}_\alpha)}{|\mathbf{v_{^{23}Na}} - \mathbf{v_p}| \cdot |\mathbf{v_{^{20}Ne}} - \mathbf{v}_\alpha|} \tag{6.7}$$

where **v** is the velocity of the different particles.

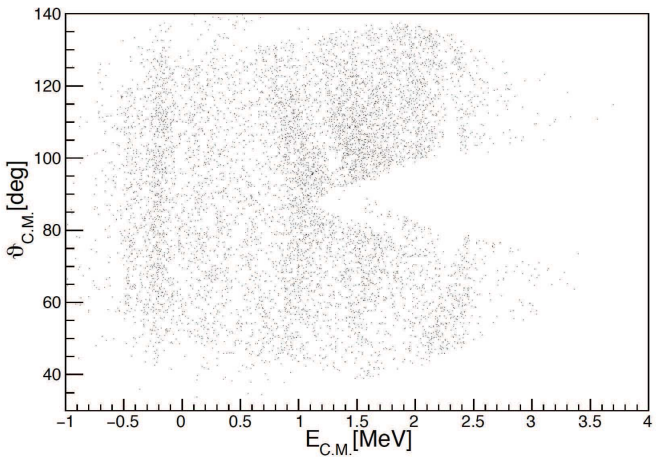

Figure 6.17: 2D-spectrum $\vartheta_{C.M.}$ versus $E_{C.M.}$ for both coincidences

If a 2D-spectrum $\vartheta_{C.M.}$ versus $E_{C.M.}$ is sketched, the region covered by the experimental apparatus can be easily deduced: for this case it is between 40° and 140°. As can be seen in figure 6.17, the spectrum is quite populated, so an angular distribution similar to what has been done in chapter 5 for the $^{19}F(\alpha,p)^{22}Ne$ reaction will be performed in the future. The triple differential cross-section can be extracted considering the variable $E_{C.M.}$ calculated using equation 6.6.

In chapter 3 and chapter 5 it was already stated that the THM is useful to derive the two-body cross-section from a three-body measurement in the exit channel. Using the PWIA, the cross section can be calculated using the equation 3.31, with the same procedure used in chapter 5.

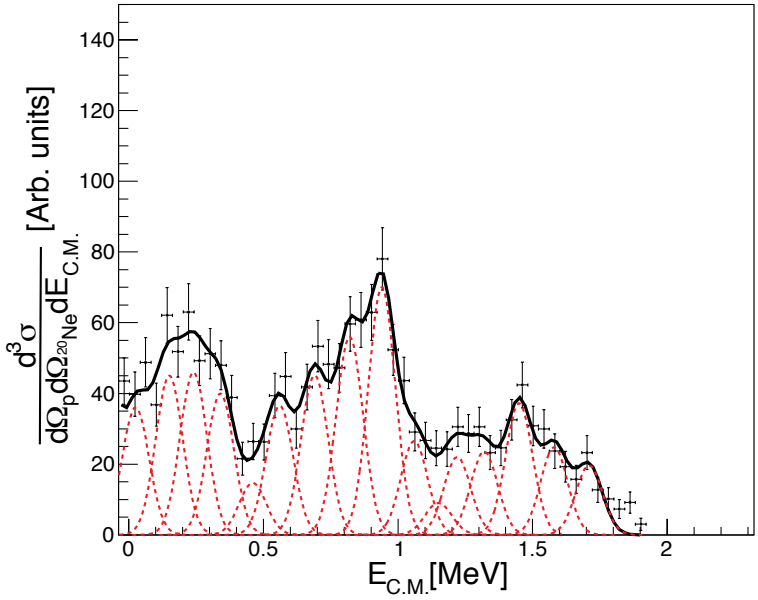

Figure 6.18: Triple-differential cross section over the variables $d\Omega_\alpha$, $d\Omega_{^{20}Ne}$, $dE_{C.M.}$, in arbitrary units. The Gaussian fits correspond to the one in figure 6.16.

Again, this value depends from the kinematic factor and the momentum distribution (of the neutron inside the deuterium, in this case) inside the TH nucleus. The quantity $KF|\Phi(p_s)|^2$ in the experimental conditions of this experiment can be calculated using a proper Monte Carlo simulation. The two-body differential cross-section can therefore be calculated by dividing the triple differential cross-section with such simulation. As can be seen, the cross-section covers both the Gamow window (50÷200 keV) and the energy region where direct data are present in literature [Mowlavi, 1999; Hale et al., 2004; Rowland et al., 2004].

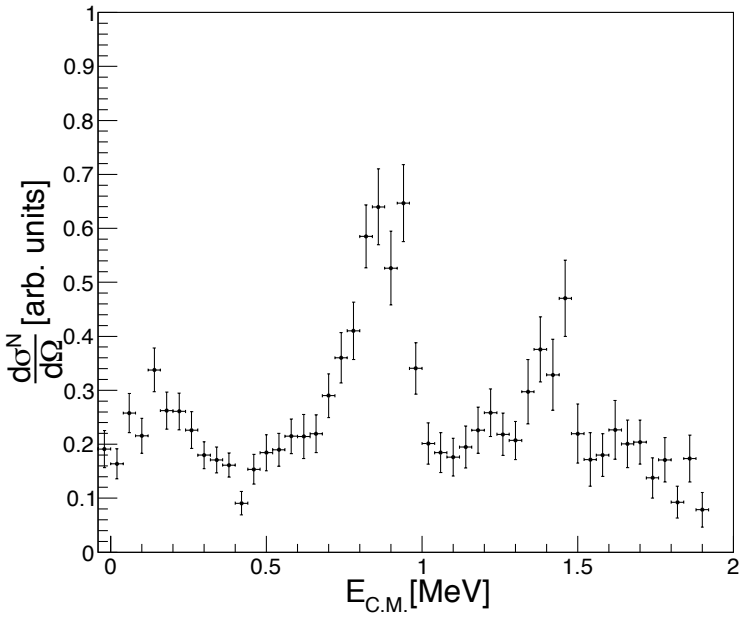

Figure 6.19: Experimental differential cross-section for the ^{23}Na(p,α)^{20}Ne two-body reaction.

6.5 Conclusions

In this chapter, the ^{23}Na(p,α)^{20}Ne was studied using the THM, at the energies of astrophysical interest ($E_{C.M.}$=50÷200 keV). In this region, no definitive information about the cross-section is present, but only speculations based on indirect methods. Anyway, such measurement at low energies is fundamental in the study of the NeNa cycle, and in its implications on ^{23}Na abundances in globular clusters. For this reason, an experiment was performed at LNS-Laboratori Nazionali del Sud, using a ^{23}Na at 58 MeV impinging on a CD_2 target, with the aim to induce the ^{23}Na(d,p^{20}Ne)n reaction: under the TH conditions, the ^{23}Na(p,α)^{20}Ne reaction was then studied.

After the selection of the quasi-free process, it was possible to obtain preliminary informations on the half-off-energy-shell two-body cross section, still in arbitrary units, in the energy interval 0÷2 MeV. During the analysis, many resonances corresponding to ^{24}Mg levels were guessed, resembling what is present in literature [Firestone, 2007b]. Further steps in data analysis have still to be made: at first, a systematic study (similar to the one performed in chapter 5) must be performed, with the aim to detect and isolate the J^π and l for each resonance and the possible interference between different levels. With such information, angular integration can

be performed, and the barrier penetrability can also be evaluated. After that, normalization at higher energies through the *Modified R-Matrix* procedure explained and adopted in chapter 5 must be performed, and in this way the experimental cross-section in absolute unit will be obtained. A new reaction rate would be of critical importance to understand the origin of ^{23}Na and its abundance in GCs, as reported in chapter 1 (see [D'Antona et al., 1983; D'Antona and Ventura, 2007, 2016] for references).

Bibliography

Abia, C., Recio-Blanco, A., de Laverny, P., Cristallo, S., Dominguez, I., and Straniero, O. (2009). Fluorine in Asymptotic Giant Branch Carbon Stars Revisited. *The Astrophysical Journal*, 694:971–977.

Adelberger, E. G., Austin, S. M., Bahcall, J. N., Balantekin, A. B., Bogaert, G., Brown, L. S., Buchmann, L., Cecil, F. E., Champagne, A. E., de Braeckeleer, L., Duba, C. A., Elliott, S. R., Freedman, S. J., Gai, M., Goldring, G., Gould, C. R., Gruzinov, A., Haxton, W. C., Heeger, K. M., Henley, E., Johnson, C. W., Kamionkowski, M., Kavanagh, R. W., Koonin, S. E., Kubodera, K., Langanke, K., Motobayashi, T., Pandharipande, V., Parker, P., Robertson, R. G., Rolfs, C., Sawyer, R. F., Shaviv, N., Shoppa, T. D., Snover, K. A., Swanson, E., Tribble, R. E., Turck-Chieze, S., and Wilkerson, J. F. (1998). Solar fusion cross sections. *Reviews of Modern Physics*, 70:1265–1291.

Adelberger, E. G., García, A., Robertson, R. G. H., Snover, K. A., Balantekin, A. B., Heeger, K., Ramsey-Musolf, M. J., Bemmerer, D., Junghans, A., Bertulani, C. A., Chen, J.-W., Costantini, H., Prati, P., Couder, M., Uberseder, E., Wiescher, M., Cyburt, R., Davids, B., Freedman, S. J., Gai, M., Gazit, D., Gialanella, L., Imbriani, G., Greife, U., Hass, M., Haxton, W. C., Itahashi, T., Kubodera, K., Langanke, K., Leitner, D., Leitner, M., Vetter, P., Winslow, L., Marcucci, L. E., Motobayashi, T., Mukhamedzhanov, A., Tribble, R. E., Nollett, K. M., Nunes, F. M., Park, T.-S., Parker, P. D., Schiavilla, R., Simpson, E. C., Spitaleri, C., Strieder, F., Trautvetter, H.-P., Suemmerer, K., and Typel, S. (2011). Solar fusion cross sections. II. The pp chain and CNO cycles. *Reviews of Modern Physics*, 83:195–246.

Aliotta, M., Raiola, F., Gyürky, G., Formicola, A., Bonetti, R., Broggini, C., Campajola, L., Corvisiero, P., Costantini, H., D'Onofrio, A., Fülöp, Z., Gervino, G., Gialanella, L., Guglielmetti, A., Gustavino, C., Imbriani, G., Junker, M., Moroni, P. G., Ordine, A., Prati, P., Roca, V., Rogalla, D., Rolfs, C., Romano, M., Schümann, F., Somorjai, E., Straniero, O., Strieder, F., Terrasi, F., Trautvetter, H. P., and Zavatarelli, S. (2001). Electron screening effect in the reactions ^{3}He(d,p)^{4}He and d(^{3}He,p)^{4}He*. *Nuclear Physics A*, 690:790–800.

Angulo, C., Arnould, M., Rayet, M., Descouvemont, P., Baye, D., Leclercq-Willain, C., Coc, A., Barhoumi, S., Aguer, P., Rolfs, C., Kunz, R., Hammer, J. W., Mayer, A., Paradellis, T., Kossionides, S., Chronidou, C., Spyrou, K., degl'Innocenti, S., Fiorentini, G., Ricci, B., Zavatarelli, S., Providencia, C., Wolters, H., Soares, J., Grama, C., Rahighi, J., Shotter, A., and Lamehi Rachti, M. (1999). A compilation of charged-particle induced thermonuclear reaction rates. *Nuclear Physics A*, 656:3–183.

Aoki, W., Beers, T. C., Christlieb, N., Norris, J. E., Ryan, S. G., and Tsangarides, S. (2007). Carbon-enhanced Metal-poor Stars. I. Chemical Compositions of 26 Stars. *The Astrophysical Journal*, 655:492–521.

Asplund, M., Grevesse, N., Sauval, A. J., and Scott, P. (2009). The Chemical Composition of the Sun. *Annual Review of Astronomy and Astrophysics*, 47:481–522.

Assenbaum, H., Langanke, K., and Rolfs, C. (1987). Effects of electron screening on low-energy fusion cross sections. *Zeitschrift fur Physik A Atomic Nuclei*, 327(4):461–468.

Azhari, A., Burjan, V., Carstoiu, F., Gagliardi, C. A., Kroha, V., Mukhamedzhanov, A. M., Nunes, F. M., Tang, X., Trache, L., and Tribble, R. E. (2001). Asymptotic normalization coefficients and the ^{7}Be(p,γ)^{8}B astrophysical S factor. *Physical Review C*, 63(5):055803.

Bao, Z. Y. and Kappeler, F. (1987). Neutron Capture Cross Sections for s-Process Studies. *Atomic Data and Nuclear Data Tables*, 36:411.

Barbarino, S., Lattuada, M., Riggi, F., Spitaleri, C., and Vinciguerra, D. (1980). Impulse distribution of the α-d motion in ^{6}Li. *Physical Review C*, 21:1104–1106.

Baur, G. and Rebel, H. (1994). Coulomb dissociation studies as a tool of nuclear astrophysics. *Journal of Physics G Nuclear Physics*, 20:1–33.

Berggren, T. and Tyren, H. (1966). Quasi-Free Scattering. *Annual Review of Nuclear Science*, 16(1):153–182.

Bertulani, C. A. (1994). The astrophysical reactions $^{12}C(\alpha,\gamma)^{16}O$ and $^{7}Be(p,\gamma)^{8}B$ and Coulomb dissociation experiments. *Physical Review C*, 49:2688–2694.

Best, A., Beard, M., Görres, J., Couder, M., deBoer, R., Falahat, S., Güray, R. T., Kontos, A., Kratz, K.-L., LeBlanc, P. J., Li, Q., O'Brien, S., Özkan, N., Pignatari, M., Sonnabend, K., Talwar, R., Tan, W., Uberseder, E., and Wiescher, M. (2013a). Measurement of the reaction $^{17}O(\alpha,n)^{20}Ne$ and its impact on the s process in massive stars. *Phys. Rev. C*, 87(4):045805.

Best, A., Falahat, S., Görres, J., Couder, M., deBoer, R., Güray, R. T., Kontos, A., Kratz, K.-L., LeBlanc, P. J., Li, Q., O'Brien, S., Özkan, N., Sonnabend, K., Talwar, R., Uberseder, E., and Wiescher, M. (2013b). Measurement of the reaction $^{18}O(\alpha,n)^{21}Ne$. *Phys. Rev. C*, 87(4):045806.

Blatt, J. M. and Biedenharn, L. C. (1952). The Angular Distribution of Scattering and Reaction Cross Sections. *Rev. Mod. Phys.*, 24:258–272.

Bragaglia, A., Carretta, E., Gratton, R. G., Lucatello, S., Milone, A., Piotto, G., D'Orazi, V., Cassisi, S., Sneden, C., and Bedin, L. R. (2010). X-shooter Observations of Main-sequence Stars in the Globular Cluster NGC 2808: First Chemical Tagging of a He-normal and a He-rich Dwarf. *Astrophysical Journal, Letters*, 720:L41–L45.

Brehm, K., Becker, H., Rolfs, C., Trautvetter, H., Kappeler, F., and Ratynski, W. (1988). The cross section of $^{14}N(n, p)^{14}C$ at stellar energies and its role as a neutron poison forS-process nucleosynthesis. *Zeitschrift fur Physik A Atomic Nuclei*, 330(2):167–172.

Briley, M. M., Cohen, J. G., and Stetson, P. B. (2004a). The Chemical Inhomogeneity of Faint M13 Stars: Carbon and Nitrogen Abundances. *Astronomical Journal*, 127:1579–1587.

Briley, M. M., Harbeck, D., Smith, G. H., and Grebel, E. K. (2004b). On the Carbon and Nitrogen Abundances of 47 Tucanae's Main-Sequence Stars. *Astronomical Journal*, 127:1588–1593.

Briley, M. M., Smith, V. V., Suntzeff, N. B., Lambert, D. L., Bell, R. A., and Hesser, J. E. (1996). Sodium abundance variations in main-sequence stars of the globular cluster 47 Tucanae. *Nature*, 383:604–606.

Broggini, C., Bemmerer, D., Guglielmetti, A., and Menegazzo, R. (2010). LUNA: Nuclear Astrophysics Deep Underground. *Annual Review of Nuclear and Particle Science*, 60:53–73.

Burbidge, E. M., Burbidge, G. R., Fowler, W. A., and Hoyle, F. (1957). Synthesis of the Elements in Stars. *Review of Modern Physics*, 29:547–650.

Busso, M., Gallino, R., and Wasserburg, G. J. (1999). Nucleosynthesis in Asymptotic Giant Branch Stars: Relevance for Galactic Enrichment and Solar System Formation. *Annual Review of Astronomy and Astrophysics*, 37:239–309.

Carretta, E., Bragaglia, A., Gratton, R. G., Lucatello, S., Catanzaro, G., Leone, F., Bellazzini, M., Claudi, R., D'Orazi, V., Momany, Y., Ortolani, S., Pancino, E., Piotto, G., Recio-Blanco, A., and Sabbi, E. (2009). Na-O Anticorrelation and HB. VII. The chemical composition of first and second-generation stars in 15 globular clusters from GIRAFFE spectra. *Astronomy & Astrophysics*, 505(1):117–138.

Castellani, V. (1985). *Astrofisica Stellare*. http://astrofisica.altervista.org/doku.php.

Caughlan, G. R. and Fowler, W. A. (1988). Thermonuclear Reaction Rates V. *Atomic Data and Nuclear Data Tables*, 40:283.

Charbonnel, C., Krause, M., Decressin, T., Prantzos, N., and Meynet, G. (2013). The role of massive stars in the turbulent infancy of Galactic globular clusters: feedback on the intracluster medium, and detailed timeline. *Mem. Societa Astronomica Italiana*, 84:158.

Cherubini, S., Kondratyev, V. N., Lattuada, M., Spitaleri, C., Miljanić, D., Zadro, M., and Baur, G. (1996). Indirect Investigation of the d + ^{6}Li Reaction at Low Energies Relevant for Nuclear Astrophysics. *The Astrophysical Journal*, 457:855.

Chew, G. F. and Wick, G. C. (1952). The Impulse Approximation. *Physical Review*, 85:636–642.

Clayton, D. D. (1983). *Principles of Stellar Evolution and Nucleosynthesis*. The University Chigago Press.

Cohen, J. G. and Meléndez, J. (2005). Abundances in a Large Sample of Stars in M3 and M13. *Astronomical Journal*, 129:303–329.

Costanzo, E., Lattuada, M., Romano, S., Vinciguerra, D., and Zadro, M. (1990). A procedure for the analysis of the data of a three body nuclear reaction. *Nuclear Instruments and Methods in Physics Research Section A: Accelerators, Spectrometers, Detectors and Associated Equipment*, 295(3):373 – 376.

Cottrell, P. L. and Da Costa, G. S. (1981). Correlated cyanogen and sodium anomalies in the globular clusters 47 TUC and NGC 6752. *Astrophysical Journal, Letters*, 245:L79–L82.

Couture, A., Beard, M., Couder, M., Görres, J., Lamm, L., Leblanc, P. J., Lee, H. Y., O'Brien, S., Palumbo, A., Stech, E., Strandberg, E., Tan, W., Uberseder, E., Ugalde, C., Wiescher, M., and Azuma, R. (2008). Measurement of the F19(p,γ)Ne20 reaction and interference terms from $E_{c.m.}$=200-760 keV. *Phys. Rev. C*, 77(1):015802.

Cristallo, S., Di Leva, A., Imbriani, G., Piersanti, L., Abia, C., Gialanella, L., and Straniero, O. (2014). Effects of nuclear cross sections on ^{19}F nucleosynthesis at low metallicities. *Astronomy and Astrophysics*, 570:A46.

Cristallo, S., Piersanti, L., Straniero, O., Gallino, R., Domínguez, I., Abia, C., Di Rico, G., Quintini, M., and Bisterzo, S. (2011). Evolution, Nucleosynthesis, and Yields of Low-mass Asymptotic Giant Branch Stars at Different Metallicities. II. The FRUITY Database. *The Astrophysical Journal Supplement Series*, 197:17.

Cristallo, S., Straniero, O., Gallino, R., Piersanti, L., Dominguez, I., and Lederer, M. T. (2009). Evolution, Nucleosynthesis, and Yields of Low-Mass Asymptotic Giant Branch Stars at Different Metallicities. *The Astrophysical Journal*, 696(1):797.

Crowther, P. A. (2007). Physical Properties of Wolf-Rayet Stars. *Annual Review of Astronomy and Astrophysics*, 45:177–219.

Cunha, K., Smith, V. V., Lambert, D. L., and Hinkle, K. H. (2003). Fluorine Abundances in the Large Magellanic Cloud and ω Centauri: Evidence for Neutrino Nucleosynthesis? *The Astronomical Journal*, 126(3):1305.

D'Antona, F., Gratton, R., and Chieffi, A. (1983). CNO self-pollution in globular clusters - A model and its possible observational tests. *Mem. Societa Astronomica Italiana*, 54:173–198.

D'Antona, F. and Ventura, P. (2007). A model for globular cluster extreme anomalies. *Montly Notices of the Royal Astronomical Society*, 379:1431–1441.

D'Antona, F. and Ventura, P. (2016). Hot CNO and p-capture nucleosynthesis in intermediate-mass AGB stars. *Mem. Societa Astronomica Italiana*, 87:243.

de Mink, S. E., Pols, O. R., and Hilditch, R. W. (2007). Efficiency of mass transfer in massive close binaries. Tests from double-lined eclipsing binaries in the SMC. *Astronomy & Astrophysics*, 467:1181–1196.

de Mink, S. E., Pols, O. R., Langer, N., and Izzard, R. G. (2009). Massive binaries as the source of abundance anomalies in globular clusters. *Astronomy & Astrophysics*, 507:L1–L4.

Decressin, T., Charbonnel, C., and Meynet, G. (2007a). Origin of the abundance patterns in Galactic globular clusters: constraints on dynamical and chemical properties of globular clusters. *Astronomy & Astrophysics*, 475:859–873.

Decressin, T., Meynet, G., Charbonnel, C., Prantzos, N., and Ekström, S. (2007b). Fast rotating massive stars and the origin of the abundance patterns in galactic globular clusters. *Astronomy & Astrophysics*, 464:1029–1044.

Denisenkov, P. A. and Denisenkova, S. N. (1990). Correlation Between the Abundances of NA and the CNO Elements in Red Giants in Omega-Centauri. *Soviet Astronomy Letters*, 16:275.

Denissenkov, P. A. and Hartwick, F. D. A. (2014). Supermassive stars as a source of abundance anomalies of proton-capture elements in globular clusters. *Montly Notices of the Royal Astronomical Society*, 437:L21–L25.

Denissenkov, P. A. and VandenBerg, D. A. (2003). Canonical Extra Mixing in Low-Mass Red Giants. *Astrophysical Journal*, 593:509–523.

Dobrovolskas, V., Kučinskas, A., Bonifacio, P., Korotin, S. A., Steffen, M., Sbordone, L., Caffau, E., Ludwig, H.-G., Royer, F., and Prakapavičius, D. (2014). Abundances of lithium, oxygen, and sodium in the turn-off stars of Galactic globular cluster 47 Tucanae. *Astronomy and Astrophysics*, 565:A121.

D'Orazi, V., Lucatello, S., Gratton, R., Bragaglia, A., Carretta, E., Shen, Z., and Zaggia, S. (2010). Lithium and Proton-capture Elements in Globular Cluster Dwarfs: The Case of 47 TUC. *Astrophysical Journal, Letters*, 713:L1–L5.

D'Orazi, V., Lucatello, S., Lugaro, M., Gratton, R. G., Angelou, G., Bragaglia, A., Carretta, E., Alves-Brito, A., Ivans, I. I., Masseron, T., and Mucciarelli, A. (2013). Fluorine Variations in the Globular Cluster NGC 6656 (M22): Implications for Internal Enrichment Timescales. *The Astrophysical Journal*, 763:22.

Engstler, S., Raimann, G., Angulo, C., Greife, U., Rolfs, C., Schroder, U., Somorjai, E., Kirch, B., and Langanke, K. (1992). Isotopic dependence of electron screening in fusion reactions. *Zeitschrift fur Physik A Hadrons and Nuclei*, 342:471–482.

Fiorentini, G., Kavanagh, R., and Rolfs, C. (1995). Prospects for underground accelerator research. *Zeitschrift fur Physik A Hadrons and Nuclei*, 350(4):289–301.

Firestone, R. B. (2007a). Nuclear Data Sheets for A = 23. *Nuclear data sheets*.

Firestone, R. B. (2007b). Nuclear Data Sheets for A = 24. *Nuclear data sheets*.

Forestini, M., Goriley, S., Jorissen, A., and Arnould, M. (1992). Fluorine production in thermal pulses on the asymptotic giant branch. *Astronomy and Astrophysics*, 261:157–163.

Fowler, W. A., Caughlan, G. R., and Zimmerman, B. A. (1967). Thermonuclear Reaction Rates. *Annual Review of Astronomy and Astrophysics*, 5(1):525–570.

Frost, C. and Lattanzio, J. (1996). AGB Stars: What Should Be Done ? *ArXiv Astrophysics e-prints*.

Fujimoto, M. Y., Ikeda, Y., and Iben, Jr., I. (2000). The Origin of Extremely Metal-poor Carbon Stars and the Search for Population III. *The Astrophysical Journal Letters*, 529:L25–L28.

Gratton, R., Carretta, E., and Bragaglia, A. (2012). Multiple populations in globular clusters.Lessons learned from the Milky Way globular clusters. *Astron Astrophys Rev (2012) 20: 50*.

Gratton, R. G., Bonifacio, P., Bragaglia, A., Carretta, E., Castellani, V., Centurion, M., Chieffi, A., Claudi, R., Clementini, G., D'Antona, F., Desidera, S., François, P., Grundahl, F., Lucatello, S., Molaro, P., Pasquini, L., Sneden, C., Spite, F., and Straniero, O. (2001). The O-Na and Mg-Al anticorrelations in turn-off and early subgiants in globular clusters. *Astronomy & Astrophysics*, 369:87–98.

Gray, D. (2005). *The observations and analysis of stellar photoshere*. Cambridge University Press.

Greife, U., Gorris, F., Junker, M., Rolfs, C., and Zahnow, D. (1995). Oppenheimer-Phillips effect and electron screening in d+ d fusion reactions. *Zeitschrift fur Physik A Hadrons and Nuclei*, 351:107–112.

Grundstrom, E. D., Gies, D. R., Hillwig, T. C., McSwain, M. V., Smith, N., Gehrz, R. D., Stahl, O., and Kaufer, A. (2007). A Spectroscopic Study of Mass Outflows in the Interacting Binary RY Scuti. *Astrophysical Journal*, 667:505–519.

Hale, S. E., Champagne, A. E., Iliadis, C., Hansper, V. Y., Powell, D. C., and Blackmon, J. C. (2004). Investigation of the ^{23}Na (p,γ) ^{24}Mg and ^{23}Na (p,α) ^{20}Ne reactions via (^{3}He ,d) spectroscopy. *Physical Rewiew C*, 70(4):045802.

Hass, M. (1999). A new Measurement of the ^{7}Be(p,γ)^{8}Be cross-section with an implanted ^{7}Be target. *Physics Letters B*, 462:237–242.

Hedrosa, R. P., Abia, C., Busso, M., Cristallo, S., Dominguez, I., Palmerini, S., Plez, B., and Straniero, O. (2013). Nitrogen isotopes in asymptotic giant branch carbon stars and presolar sic grains: A challenge for stellar nucleosynthesis. *The Astrophysical Journal Letters*, 768(1):L11.

Heger, A., Kolbe, E., Haxton, W., Langanke, K., Martinez-Pinedo, G., and Woosley, S. (2005). Neutrino nucleosynthesis. *Physics Letters B*, 606:258–264.

Iliadis, C. (2007). *Nuclear Physics of Stars*. Wiley-VCH.

Iliadis, C., Longland, R., Champagne, A. E., Coc, A., and Fitzgerald, R. (2010). Charged-particle thermonuclear reaction rates: II. Tables and graphs of reaction rates and probability density functions. *Nuclear Physics A*, 841:31–250.

Indelicato, I., Cognata, M. L., Spitaleri, C., Burjan, V., Cherubini, S., Gulino, M., Hayakawa, S., Hons, Z., Kroha, V., Lamia, L., Mazzocco, M., Mrazek, J., Pizzone, R. G., Romano, S., Strano, E., Torresi, D., and Tumino, A. (2017). New improved indirect measurement of the ^{19}f(p,α)^{16}o reaction at energies of astrophysical relevance. *The Astrophysical Journal*, 845(1):19.

Iwasa, N., Boué, F., Surowka, G., Summerer, K., Baumann, T., Blank, B., Czajkowski, S., Forster, A., Gai, M., Geissel, H., Grosse, E., Hellstrom, M., Koczon, P., Kohlmeyer, B., Kulessa, R., Laue, F., Marchand, C., Motobayashi, T., Oeschler, H., Ozawa, A., Pravikoff, M. S., Schwab, E., Schwab, W., Senger, P., Speer, J., Sturm, C., Surowiec, A., Teranishi, T., Uhlig, F., Wagner, A., Walus, W., and Bertulani, C. A. (1999). Measurement of the Coulomb Dissociation of ^{8}B at 254 MeV /nucleon and the ^{8}B Solar Neutrino Flux. *Physical Review Letters*, 83:2910–2913.

Izzard, R. G. and Tout, C. A. (2003). Nucleosynthesis in Binary Populations. *Publications of Astronomical Society of Australia*, 20:345–350.

Jacob, G. and Maris, T. A. J. (1966). Quasi-Free Scattering and Nuclear Structure. *Review of Modern Physics*, 38:121–142.

Jain, M., Roos, P. G., Pugh, H. G., and Holmgren, H. D. (1970). The (p, pα) and (α, 2α) reactions on ^{6}Li and ^{7}Li at 60 MeV. *Nuclear Physics A*, 153:49–81.

Joachain, C. (1987). *Quantum Collision Theory*. North Holland.

Johnson, C. I., McDonald, I., Pilachowski, C. A., Mateo, M., Bailey, III, J. I., Cordero, M. J., Zijlstra, A. A., Crane, J. D., Olszewski, E., Shectman, S. A., and Thompson, I. (2015). AGB Sodium Abundances in the Globular Cluster 47 Tucanae (NGC 104). *Astronomical Journal*, 149:71.

Jorissen, A., Smith, V. V., and Lambert, D. L. (1992). Fluorine in red giant stars - Evidence for nucleosynthesis. *Astronomy and Astrophysics*, 261:164–187.

Karakas, A. I. and Lattanzio, J. C. (2014). The Dawes Review 2: Nucleosynthesis and Stellar Yields of Low- and Intermediate-Mass Single Stars. *Publications of the Astronomical Society of Australia*, 31:e030.

Kartunnen, H., Kröger, P., Oja, H., Poutanene, M., and Donner, K. J. (1987). *Fundamental Astronomy*. Springer.

Keyworth, G. A., Wilhjelm, P., Kyker, G. C., Newson, H. W., and Bilpuch, E. G. (1968). High-Resolution Study of Isobaric Analog Resonances in ^{23}Na. *Phys. Rev.*, 176:1302–1310.

Kippenhahn, R. and Weigert, A. (1990). *Stellar Structure and Evolution*. Springer-Verlag.

Knoll, G. F. (2010). *Radiation Detection and Measurement*. John Wiley & Sons Inc.

La Cognata, M., Palmerini, S., Spitaleri, C., Indelicato, I., Mukhamedzhanov, A. M., Lombardo, I., and Trippella, O. (2015). Updated THM Astrophysical Factor of the ^{19}F(p, α)^{16}O Reaction and Influence of New Direct Data at Astrophysical Energies. *The Astrophysical Journal*, 805(2):128.

La Cognata, M., Spitaleri, C., and Mukhamedzhanov, A. M. (2010). Effect of High-energy Resonances on the ^{18}O(p, α)^{15}N Reaction Rate at AGB and Post-AGB Relevant Temperatures. *Phys. Rev. C*, 723:1512–1522.

La Cognata, M. L., Mukhamedzhanov, A. M., Spitaleri, C., Indelicato, I., Aliotta, M., Burjan, V., Cherubini, S., Coc, A., Gulino, M., Hons, Z., Kiss, G. G., Kroha, V., Lamia, L., Mrazek, J., Palmerini, S., Piskor, S., Pizzone, R. G., Puglia, S. M. R., Rapisarda, G. G., Romano, S., Sergi, M. L., and Tumino, A. (2011). The Fluorine Destruction in Stars: First Experimental Study of the ^{19}F(p, α_0)^{16}O Reaction at Astrophysical Energies. *The Astrophysical Journal Letters*, 739(2):L54.

Lamers, H., Maeder, A., Schmutz, W., and Cassinelli, J. P. (1991). Wolf-Rayet stars as starting points or as endpoints of the evolution of massive stars? *The Astrophysical Journal*, 368:538–544.

Lane, A. M. and Thomas, R. G. (1958). R-Matrix Theory of Nuclear Reactions. *Review of Modern Physics*, 30:257–353.

Langer, G. E., Hoffman, R., and Sneden, C. (1993). Sodium-oxygen abundance anticorrelations and deep-mixing scenarios for globular-cluster giants. *Publications of the Astronomical Society of the Pacific*, 105:301–307.

Lattanzio, J. (2003). Nucleosynthesis in AGB Stars: the Role of Dredge-Up and Hot Bottom Burning (invited review). In Kwok, S., Dopita, M., and Sutherland, R.,

editors, *Planetary Nebulae: Their Evolution and Role in the Universe*, volume 209 of *IAU Symposium*, page 73.

Lattuada, M., Pizzone, R. G., Typel, S., Figuera, P., Miljanić, D., Musumarra, A., Pellegriti, M. G., Rolfs, C., Spitaleri, C., and Wolter, H. H. (2001). The Bare Astrophysical S(E) Factor of the ^{7}Li(p, α)α Reaction. *The Astrophysical Journal*, 562:1076–1080.

Leo, W. R. (1994). *Techniques for Nuclear and Particle Physics Experiments: A How-To Approach*. Springer-Verlag.

Li, H. N., Ludwig, H.-G., Caffau, E., Christlieb, N., and Zhao, G. (2013). Fluorine Abundances of Galactic Low-metallicity Giants. *The Astrophysical Journal*, 765(1):51.

Lombardo, I., Dell'Aquila, D., Di Leva, A., Indelicato, I., La Cognata, M., La Commara, M., A., O., Rigato, V., Romoli, M., Rosato, E., Spadaccini, G., Spitaleri, C., Tumino, A., and Vigilante, M. (2015). Toward a reassessment of the ^{19}f(p,α)^{16}o reaction rate at astrophysical temperatures. *Physics Letters B*, 748:178 – 182.

Lucatello, S., Masseron, T., Johnson, J. A., Pignatari, M., and Herwig, F. (2011). Fluorine and Sodium in C-rich Low-metallicity Stars. *The Astrophysical Journal*, 729(1):40.

Lucatello, S., Tsangarides, S., Beers, T. C., Carretta, E., Gratton, R. G., and Ryan, S. G. (2005). The Binary Frequency Among Carbon-enhanced, s-Process-rich, Metal-poor Stars. *The Astrophysical Journal*, 625:825–832.

Lugaro, M., Doherty, C. L., Karakas, A. I., Maddison, S. T., Liffman, K., Garcia-Hernandez, D. A., Siess, L., and Lattanzio, J. C. (2012). Short-lived radioactivity in the early solar system: The Super-AGB star hypothesis. *Meteoritics and Planetary Science*, 47(12):1998–2012.

Lugaro, M., Ugalde, C., Karakas, A. I., Gorres, J., Wiescher, M., Lattanzio, J. C., and Cannon, R. C. (2004). Reaction Rate Uncertainties and the Production of ^{19}F in Asymptotic Giant Branch Stars. *The Astrophysical Journal*, 615(2):934.

Maeder, A. and Meynet, G. (1994). New models of Wolf-Rayet stars and comparison with data in galaxies. *Astronomy and Astrophysics*, 287:803–816.

Maeder, A. and Meynet, G. (2006). On the origin of the high helium sequence in ω Centauri. *Astronomy & Astrophysics*, 448:L37–L41.

Marchetta, S. and Marletta, S. (2016). Private communication.

Masseron, T., Johnson, J. A., Plez, B., van Eck, S., Primas, F., Goriely, S., and Jorissen, A. (2010). A holistic approach to carbon-enhanced metal-poor stars. *Astronomy and Astrophysics*, 509:A93.

Massey, P. (1984). Absolute spectrophotometry of northern Wolf-Rayet stars - How similar are the colors? *The Astrophysical Journal*, 281:789–799.

Massey, P. and Johnson, O. (1998). Evolved Massive Stars in the Local Group. II. A New Survey for Wolf-Rayet Stars in M33 and Its Implications for Massive Star Evolution: Evidence of the "Conti Scenario" in Action. *The Astrophysical Journal*, 505:793–827.

Meynet, G. and Arnould, M. (2000). Synthesis of ^{19}F in Wolf-Rayet stars. *Astronomy and Astrophysics*, 355:176–180.

Motobayashi, T., Iwasa, N., Ando, Y., Kurokawa, M., Murakami, H., Ruan (Gen), J., Shimoura, S., Shirato, S., Inabe, N., Ishihara, M., Kubo, T., Watanabe, Y., Gai, M., France, R. H., Hahn, K. I., Zhao, Z., Nakamura, T., Teranishi, T., Futami, Y., Furutaka, K., and Delbar, T. (1994). Coulomb dissociation of ^{8}B and the ^{7}Be(p,γ)^{8}B reaction at low energies. *Physical Review Letters*, 73:2680–2683.

Mowlavi, N. (1999). Sodium production in asymptotic giant branch stars. *Astronomy & Astrophysics*, 350:73–88.

Mukhamedzhanov, A. M., Clark, H. L., Gagliardi, C. A., Lui, Y.-W., Trache, L., Tribble, R. E., Xu, H. M., Zhou, X. G., Burjan, V., Cejpek, J., Kroha, V., and Carstoiu, F. (1997). Asymptotic normalization coefficients for ^{10}B$\rightarrow^{9}$Be+p. *Physical Review C*, 56:1302–1312.

Nollett, K. M., Busso, M., and Wasserburg, G. J. (2003). Cool Bottom Processes on the Thermally Pulsing Asymptotic Giant Branch and the Isotopic Composition of Circumstellar Dust Grains. *The Astrophysical Journal*, 582(2):1036.

Norris, J. E. (2004). The Helium Abundances of ω Centauri. *Astrophysical Journal, Letters*, 612:L25–L28.

Palmerini, S., Cristallo, S., Busso, M., Abia, C., Uttenthaler, S., Gialanella, L., and Maiorca, E. (2011a). Deep Mixing in Evolved Stars. II. Interpreting Li Abundances in Red Giant Branch and Asymptotic Giant Branch Stars. *The Astrophysical Journal*, 741:26.

Palmerini, S., La Cognata, M., Cristallo, S., and Busso, M. (2011b). Deep Mixing in Evolved Stars. I. The Effect of Reaction Rate Revisions from C to Al. *The Astrophysical Journal*, 729:3.

Palmerini, S., Sergi, M. L., La Cognata, M., Lamia, L., Pizzone, R. G., and Spitaleri, C. (2013). The RGB and AGB Star Nucleosynthesis in Light of the Recent ^{17}O(p, α)^{14}N and ^{18}O(p, α)^{15}N Reaction-rate Determinations. *ApJ*, 764:128.

Pizzone, R. G., D'Agata, G., La Cognata, M., Indelicato, I., Spitaleri, C., Blagus, S., Cherubini, S., Figuera, P., Grassi, L., Guardo, G. L., Gulino, M., Hayakawa, S., Kshetri, R., Lamia, L., Lattuada, M., Mijatovič, T., M., M., Miljanič, D., Prepolec, L., Rapisarda, G. G., Romano, S., Sergi, M. L., Skukan, N., Soič, N., Tokič, V., Tumino, A., and Uroič, M. (2017). First Measurement of the ^{19}F(α, p)^{22}Ne Reaction at Energies of Astrophysical Relevance. *The Astrophysical Journal*, 836(1):57.

Pizzone, R. G., Spitaleri, C., Cherubini, S., La Cognata, M., Lamia, L., Miljanić, D., Musumarra, A., Romano, S., Tumino, A., Tudisco, S., and Typel, S. (2005). Influence of the α-d motion in ^{6}Li on Trojan horse applications. *Physical Review C*, 71(5):058801.

Pizzone, R. G., Spitaleri, C., Mukhamedzhanov, A. M., Blokhintsev, L. D., Bertulani, C. A., Irgaziev, B. F., Cognata, M. L., Lamia, L., and Romano, S. (2009). Effects of distortion of the intercluster motion in ^{2}H, ^{3}He, ^{3}H, ^{6}Li, and ^{9}Be on Trojan horse applications. *Physical Review C*, 80(2):025807.

Prantzos, N. and Charbonnel, C. (2006). On the self-enrichment scenario of galactic globular clusters: constraints on the IMF. *Astronomy & Astrophysics*, 458:135–149.

Prantzos, N., Charbonnel, C., and Iliadis, C. (2007). Light nuclei in galactic globular clusters: constraints on the self-enrichment scenario from nucleosynthesis. *Astronomy & Astrophysics*, 470:179–190.

Pumo, M. L., D'Antona, F., and Ventura, P. (2008). Self-Enrichment in Globular Clusters: Is There a Role for the Super-Asymptotic Giant Branch Stars? *Astrophysical Journal, Letters*, 672:L25.

Ramírez, S. V. and Cohen, J. G. (2002). Abundances in Stars from the Red Giant Branch Tip to Near the Main-Sequence Turnoff in M71. III. Abundance Ratios. *Astronomical Journal*, 123:3277–3297.

Ramírez, S. V. and Cohen, J. G. (2003). Abundances in Stars from the Red Giant Branch Tip to near the Main-Sequence Turnoff in M5. *Astronomical Journal*, 125:224–245.

Recio-Blanco, A., de Laverny, P., Worley, C., Santos, N., Melo, C., and Israelian, G. (2012). Fluorine abundances in dwarf stars of the solar neighbourhood. *Astronomy and Astrophysics*, 538:A117.

Renda, A., Fenner, Y., Gibson, B., Karakas, A., Lattanzio, J., Campbell, S., Chieffi, A., Cunha, K., and Smith, V. (2004). On the origin of fluorine in the Milky Way. *Monthly Notices of the Royal Astronomical Society*, 354:575–580.

Renda, A., Fenner, Y., Gibson, B., Karakas, A., Lattanzio, J., Campbell, S., Chieffi, A., Cunha, K., and Smith, V. V. (2005). The Evolution of Fluorine in Galactic Systems. *Nuclear Physics A*, 758:324–327.

Renzini, A., D'Antona, F., Cassisi, S., King, I. R., Milone, A. P., Ventura, P., Anderson, J., Bedin, L. R., Bellini, A., Brown, T. M., Piotto, G., van der Marel, R. P., Barbuy, B., Dalessandro, E., Hidalgo, S., Marino, A. F., Ortolani, S., Salaris, M., and Sarajedini, A. (2015). The Hubble Space TelescopeUV Legacy Survey of Galactic Globular Clusters - V. Constraints on formation scenarios. *Monthly Notices of the Rojal Astronomical Society*, 454:4197–4207.

Rolfs, C.E.and Rodney, W. (1988). *Cauldron in the Cosmos*. University of Chicago Press.

Rowland, C., Iliadis, C., Champagne, A. E., Fox, C., José, J., and Runkle, R. (2004). Does an nena cycle exist in explosive hydrogen burning? *The Astrophysical Journal Letters*, 615(1):L37.

Ryan, S. G., Aoki, W., Norris, J. E., and Beers, T. C. (2005). The Origins of Two Classes of Carbon-enhanced, Metal-poor Stars. *The Astrophysical Journal*, 635:349–354.

Santos, N., Israelian, G., Randich, S., Garcia Lopez, R., and Rebolo, R. (2004). Beryllium anomalies in solar-type field stars. *Astronomy and Astrophysics*, 425:1013–1027.

Satchler, G. (1990). *Introduction to Nuclear Reaction*. Oxford University Press.

Schaerer, D. and Vacca, W. D. (1998). New Models for Wolf-Rayet and O Star Populations in Young Starbursts. *The Astrophysical Journal*, 497(2):618.

Sergi, M. L., Spitaleri, C., La Cognata, M., Lamia, L., Pizzone, R. G., Rapisarda, G. G., Tang, X. D., Bucher, B., Couder, M., Davies, P., deBoer, R., Fang, X., Lamm, L., Ma, C., Notani, M., O'Brien, S., Roberson, D., Tan, W., Wiescher, M., Irgaziev, B., Mukhamedzhanov, A., Mrazek, J., and Kroha, V. (2015). Improvement of the high-accuracy ^{17}O(p ,α)^{14}N reaction-rate measurement via the Trojan Horse method for application to ^{17}O nucleosynthesis. *Phys. Rev. C*, 91(6):065803.

Shapiro, I. S., Kolybasov, V. M., and Augst, G. R. (1965). Treiman-Yang criterion for direct nuclear reactions. *Nuclear Physics*, 61:353–367.

Slaus, I., Allas, R. G., Beach, L. A., Bondelid, R. O., Petersen, E. L., Lambert, J. M., Treado, P. A., and Moyle, R. A. (1977). Quasifree processes in the ^{2}H + ^{3}He interaction. *Nuclear Physics A*, 286:67–88.

Smith, L. F. (1968). Absolute magnitudes and intrinsic colours of wolf-rayet stars. *Monthly Notices of the Royal Astronomical Society*, 140:409.

Sousa, S., Santos, N., Israelian, G., Mayor, M., and Monteiro, M. (2006). Spectroscopic parameters for a sample of metal-rich solar-type stars. *Astronomy and Astrophysics*, 458:873–880.

Spitaleri, C., Typel, S., Pizzone, R. G., Aliotta, M., Blagus, S., Bogovac, M., Cherubini, S., Figuera, P., Lattuada, M., Milin, M., Miljanić, D., Musumarra, A., Pellegriti, M. G., Rendic, D., Rolfs, C., Romano, S., Soić, N., Tumino, A., Wolter, H. H., and Zadro, M. (2001). "Trojan horse" method applied to ^{2}H(^{6}Li,α)^{4}He at astrophysical energies. *Physical Review C*, 63(5):055801.

Stancliffe, R., Lugaro, M., Ugalde, C., Tout, C., Gorres, J., and Wiescher, M. (2005). The effect of the ^{19}F(α, p)^{22}Ne reaction rate uncertainty on the yield of fluorine from Wolf-Rayet stars. *Monthly Notices of the Royal Astronomical Society*, 360:375–379.

Straniero, O., Gallino, R., and Cristallo, S. (2006). s process in low-mass asymptotic giant branch stars. *Nuclear Physics A*, 777:311–339.

Tarasov and Bazin (2008). *LISE++*. LISE group at NSCL/MSU.

Trache, L., Azhari, A., Clark, H. L., Gagliardi, C. A., Lui, Y.-W., Mukhamedzhanov, A. M., Tribble, R. E., and Carstoiu, F. (1998). Asymptotic normalization coefficients for ^{13}C+p$\rightarrow^{14}$N. *Physical Review C*, 58:2715–2719.

Trippella, O., Busso, M., Maiorca, E., Käppeler, F., and Palmerini, S. (2014). s-Processing in AGB Stars Revisited. I. Does the Main Component Constrain the Neutron Source in the ^{13}C Pocket? *ApJ*, 787:41.

Trippella, O. and La Cognata, M. (2017). Concurrent Application of ANC and THM to assess the ^{13}C(α, n)^{16}O Absolute Cross Section at Astrophysical Energies and Possible Consequences for Neutron Production in Low-mass AGB Stars. *ApJ*, 837:41.

Tumino, A., Spitaleri, C., di Pietro, A., Figuera, P., Lattuada, M., Musumarra, A., Pellegriti, M. G., Pizzone, R. G., Romano, S., Rolfs, C., Tudisco, S., and Typel, S. (2003). Validity test of the "Trojan horse" method applied to the ^{6}Li(p,α)^{3}He reaction. *Physical Review C*, 67(6):065803.

Tuthill, P., Monnier, J., and Danchi, W. (1998). Diffraction-Limited Infrared Imaging of M-Giants at Keck. In Bradley, P. A. and Guzik, J. A., editors, *A Half Century of Stellar Pulsation Interpretation*, volume 135 of *Astronomical Society of the Pacific Conference Series*, page 322.

Typel, S. and Wolter, H. H. (2000). Extraction of Astrophysical Cross Sectionsin the Trojan-Horse Method. *Few-Body Systems*, 29:75–93.

Ugalde, C., Azuma, R., Couture, A., Gorres, J., Heil, M., Scheller, K., Stech, E., Tan, W., and Wiescher, M. (2005). The reaction rate for the destruction of fluorine in AGB stars. *Nuclear Physics A*, 758:577–580.

Ugalde, C., Azuma, R. E., Couture, A., Gorres, J., Lee, H. Y., Stech, E., Strandberg, E., Tan, W., and Wiescher, M. (2008). Thermonuclear rate for the ^{19}F(α,p)^{22}Ne reaction at stellar temperatures. *Physical Review C*, 77(3):035801.

Uttenthaler, S., Aringer, B., Lebzelter, T., Kaufl, H. U., Siebenmorgen, R., and Smette, A. (2008). The Fluorine Abundance in a Galactic Bulge AGB Star Measured from CRIRES Spectra. *The Astrophysical Journal*, 682(1):509.

Ventura, P. and D'Antona, F. (2006). Does the oxygen-sodium anticorrelation in globular clusters require a lowering of the ^{23}Na(p,α)^{20}Ne reaction rate? *Astronomy & Astrophysics*, 457:995–1001.

Ventura, P. and D'Antona, F. (2010). The role of lithium production in massive AGB and super-AGB stars for the understanding of multiple populations in globular clusters. *Monthly Notices of the Rojal Astronomical Society*, 402:L72–L76.

Ventura, P. and D'Antona, F. (2011). Hot bottom burning in the envelope of super asymptotic giant branch stars. *Monthly Notices of the Rojal Astronomical Society*, 410:2760–2766.

Ventura, P., D'Antona, F., Mazzitelli, I., and Gratton, R. (2001). Predictions for Self-Pollution in Globular Cluster Stars. *Astrophysical Journal, Letters*, 550:L65–L69.

Wasserburg, G. J., Boothroyd, A. I., and Sackmann, I.-J. (1995). Deep Circulation in Red Giant Stars: A Solution to the Carbon and Oxygen Isotope Puzzles? *The Astrophysical Journal Letters*, 447(1):L37.

Williams, W. (1991). *Nuclear and Particle Physics*. Clarendon Press - Oxford.

Woosley, S., Hartmann, D., Hoffman, R., and Haxton, W. (1990). The nu-process. *The Astrophysical Journal*, 356:272–301.

Woosley, S. and Haxton, W. (1988). Supernova neutrinos, neutral currents and the origin of fluorine. *Nature*, 334:45–47.

Woosley, S. E. and Bloom, J. S. (2006). The Supernova Gamma-Ray Burst Connection. *Annual Review of Astronomy and Astrophysics*, 44:507–556.

Zadro, M., Miljanić, D., Lattuada, M., Riggi, F., and Spitaleri, C. (1987). Quasi-free processes in ^{6}Li(^{3}He, pα) ^{4}He reaction at low energies. *Nuclear Physics A*, 474:373–380.

Zadro, M., Miljanić, D., Spitaleri, C., Calvi, G., Lattuada, M., and Riggi, F. (1989). Excitation function of the quasifree contribution in the ^{2}H(^{7}Li,$\alpha\alpha$)n reaction at E_0=28–48 MeV. *Physical Review C*, 40:181–185.